EPFL

Radiation-tolerant Multichannel Dew Point Temperature Monitoring System for High Energy Physics Applications

Amar KAPIC

École
polytechnique
fédérale
de Lausanne

2023

Everything should be made as simple
as possible, but not simpler.
— Albert Eintsein

To my family.

Acknowledgements

I would like to express my heartfelt appreciation to my academic supervisor, Prof. Sandro, for providing me with the opportunity to pursue my PhD in his lab and for guiding me throughout this entire journey. Thanks to Sandro for the countless and valuable scientific discussions, as well as the enthusiasm and positive energy he has consistently shared with me. I hope to keep and pass on this passion to others with the same fervor.

I must extend my deepest thanks to my CERN supervisor, Andromachi, without whose initiative this project would not exist. Without her support and belief in me as the right candidate for this endeavor, none of this would have been achievable. Thank you for nurturing and encouraging my growth under your guidance throughout these years. I am also grateful to Piero, the "walking encyclopedia", and together with Andromachi, they both became my second family.

I would like to express my gratitude to the jury members: Prof. Martinus Gijs, Prof. Edoardo Charbon, Prof. Gerald Gerlach, and Dr Ezio Torassa, for accepting to review this work and for their interest in my research.

A heartfelt gratitude to Giuseppe from the IRRAD team for his invaluable assistance and support throughout the irradiation tests. I extend my thanks to Svetlana, Jean-Francois and Imtiaz for their assistance in building the testing setups.

My second part of the acknowledgment goes to my family: thank you, Mom, Dad, and Šućo, for your endless support and constant presence, even from afar. *Vi ćete uvijek biti moj dom i moj oslonac! Hvala vam na svemu!* I would like to give a special mention to my little niece, Hana, whose innocent and cheerful energy always brings joy to my life.

Then, I would like to thank Slavica and Nemanja, friends that you can only wish for. Despite the distance, I can always rely on them, day or night. I would like to thank to Prof. Nataša, the team leader of the Montenegrin group at CERN, for her caring nature and willingness to help at any moment. I am filled with gratitude for Itana and Jelena, fellow members of the Montenegrin group at CERN, who have become my true friends.

During my time at CERN, I had a chance to meet some remarkable individuals who have become my CERN family and I want to thank all of them. First on the list is Pedja, who, like me, is one of the most senior members of our little CERN family. He has always been there for me, no matter what. Next on the list are Miloš and Milana (M&M), where one is our group philosopher and the other one with immediate answers to all everyday questions, making

i

them a unique couple in our group.

Other thanks go to my Polish friends, Marta and Zosia. Thanks to Marta for being our "mom", organizing our trips and events, and recalling (literally) every moment of our eventful friendship. Thanks to Zoki for the wonderful moments we have shared, and I still claim, after listening to your singing countless times, that you are the voice of Poland. Even if far away, I hope for many more moments together.

Last but certainly not least on my CERN family list are Marjan and Ivan. You both know how thankful I am to have you as my friends. Thanks for the endless brotherly support and discussions that we always had.

Furthermore, my thanks go to the BCI laboratory, especially to Ata and Gian Luca. Thank you, guys, for being wonderful colleagues, and I hope that we were successful in sharing our knowledge with the students.

Finally, the sweetest for the end – Niki. Your selfless support and presence in my life have played a significant role in helping me successfully close this chapter. I am ready to start a new one with you, and I look forward to many yet to come.

Lausanne, 2023 A. K.

Abstract

The next generation of high-energy physics (HEP) detectors will predominantly be silicon-based. As pixel sensor technology gains momentum and the number of channels surpasses one billion (for a volume of approximately 20 m^3) to achieve the high resolution required for "imaging" charged tracks, current densities become very high, resulting in an overall power consumption of hundreds of kilowatts. Additionally, with increased collider luminosity, radiation levels rise, leading to higher sensor leakage current. Therefore, cooling becomes essential for removing the generated heat and preventing thermal runaway caused by temperature increases induced by the sensor leakage current. If not eliminated by cooling, this heat source creates a positive feedback loop with the increasing flow of leakage current due to its exponential temperature dependence.

Cooling the detectors and their environment has been a characteristic of Si HEP detectors since the 1990s. Due to the ever-increasing current requirements, powerful cooling systems capable of operating continuously for years, for cooling the detector components that operate in a high-radiation (1.2 Grad) and strong magnetic field (4 T) environment, have become integral to the detector support structure. Cooling temperatures range between -40 and -25 °C, and as the detectors cannot be permanently in an isolated environment, they are at risk of vapor condensation that may cause severe damage. To prevent damage from vapor condensation, reliable and detailed monitoring of the dew point temperature, and therefore humidity and ambient temperature, is necessary.

Temperature sensors that can survive in the detector environment, such as Resistance Temperature Detectors (RTDs), are commonly used. However, radiation-tolerant humidity sensors that provide the required resolution are not readily available. Therefore, the main objective of this dissertation was to select and characterize a suitable, affordable, and easy-to-integrate humidity sensor for the challenging HEP detector environment.

Several types of humidity sensors have been considered, those not fully ready for the market have been excluded as well as those not suitable for the HEP environment. The chosen sensor is the capacitive humidity sensor MK33-W of the IST AG company. It has demonstrated a linear dependence of its output on high accumulated proton fluence, which can be compensated for using a first-order polynomial function. Sensor responsivity has been tested at temperatures as low as -30 °C, where the sensor reliably provides information on the surrounding humidity

level after calibration. Furthermore, the sensor has been exposed to a strong magnetic field, matching the one of the detectors, and has shown insensitivity to it.

Efficient, easy-to-deploy, and cost-effective multi-channel readout units for both humidity and temperature sensors have been proposed, considering the large number of sensors that will be distributed throughout the entire detector. Lastly, the integration of the developed systems into the CMS Detector Control System/Detector Safety System (DCS/DSS) has been discussed.

Key words: Dew point temperature, relative humidity, temperature, silicon-based detectors, radiation tolerance, strong magnetic field, sub-zero temperatures, multi-channel readout system, detector control system, detector safety system, CERN.

Résumé

La prochaine génération de détecteurs pour la physique des hautes énergies (HEP) sera principalement basée sur le silicium. Alors que la technologie des capteurs à pixels gagne en élan et que le nombre de canaux dépasse le milliard (pour un volume d'environ 20 m^3) afin d'obtenir la haute résolution requise pour "imager" les traces chargées, les densités de puissance deviennent très élevées, entraînant une consommation totale de plusieurs centaines de kilowatts. De plus, avec une augmentation de la luminosité de l'accélérateur, les niveaux de radiation augmentent, entraînant une augmentation des courants de fuite des capteurs. Par conséquent, le refroidissement devient essentiel pour éliminer la chaleur générée et éviter une surchauffe causée par l'augmentation de la température due aux courants de fuite des capteurs. Si cette chaleur n'est pas éliminée par le refroidissement, elle crée une boucle de rétroaction positive avec le flux croissant de courant de fuite en raison de sa dépendance exponentielle à la température.

Le refroidissement des détecteurs et de leur environnement est une caractéristique des détecteurs Si HEP depuis les années 1990. En raison des besoins toujours croissants, des systèmes de refroidissement puissants capables de fonctionner en continu pendant des années dans un environnement, pour refroidir les composants du détecteur fonctionnant dans un environnement à forte radiation (1.2 Grad) et champ magnétique intense (4 T), sont devenus indispensables pour la structure de support du détecteur. Les températures de refroidissement varient entre -40 et -25 °C, et comme les détecteurs ne peuvent pas être en permanence dans un environnement isolé, ils sont exposés au risque de condensation de vapeur qui peut causer des dommages graves. Pour éviter les dommages dus à la condensation de vapeur, une surveillance fiable et détaillée de la température de point de rosée, et donc de l'humidité et de la température ambiante, est nécessaire.

Les capteurs de température capables de survivre dans l'environnement du détecteur, tels que les capteurs de résistance thermique (RTD), sont couramment utilisés. Au contraire, les capteurs d'humidité résistants aux radiations qui fournissent la résolution requise ne sont pas facilement disponibles. Par conséquent, l'objectif principal de cette thèse était de sélectionner et de caractériser un capteur d'humidité approprié, avec un prix abordable et facile à intégrer pour l'environnement exigeant du détecteur HEP.

Le capteur d'humidité choisi, le MK33-W, a démontré une dépendance linéaire de sa reponse

par rapport à une forte dose accumulée, ce qui peut être compensé en utilisant une fonction polynomiale du premier ordre. La sensibilité du capteur a été testée à des températures aussi basses que -30 °C, où le capteur fournit de manière fiable des informations sur le niveau d'humidité environnant. De plus, le capteur a été exposé à un fort champ magnétique correspondant à celui des détecteurs et s'est avéré insensible à celui-ci.

Des unités de lecture multi-canaux efficaces, faciles à déployer et économiques pour les capteurs d'humidité et de température ont été proposées, compte tenu du grand nombre de capteurs qui seront répartis dans l'ensemble du détecteur. Enfin, l'intégration des systèmes développés dans le Système de Contrôle du Détecteur/Système de Sécurité du Détecteur (DCS/DSS) du détecteur CMS a été discutée.

Mots clefs : Température de point de rosée, humidité relative, température, détecteurs à base de silicium, tolérance aux radiations, fort champ magnétique, températures sous zéro, système de lecture multi-canal, système de contrôle du détecteur, système de sécurité du détecteur, CERN.

Contents

List of Figures

List of Tables

1 The CMS detector upgrade for the High Luminosity Large Hadron Collider

We cannot solve our problems with the same thinking we used when we created them.
— Albert Einstein

The question about the fundamental laws governing the Universe and its elementary constituents has persisted for thousands of years. From ancient thinkers to today's scientists using specific tools to answer it, the road has been a very exciting one. High Energy Physics (HEP) and Astrophysics are two scientific disciplines that specialize in the research of the above. When seeking experimental data to verify theoretical predictions, they use different yet often complementary techniques.

The astrophysics approach involves the use of cosmic rays and neutrinos, monitored by experimental apparatus on Earth or satellite- and spaceship-loaded experimental apparatus to observe the entire spectrum of cosmic particles. The HEP approach uses accelerators, a scientific research tool that has been developing for about a century and has numerous applications. Both Astrophysics and HEP approaches combine a particle source with a "matching" detector that captures images of the produced particles, the object of the analysis of the physicists conducting the study and testing certain theoretical predictions [1].

Contrary to Astrophysics, where "nature" provides the objects of study, HEP uses accelerators as a tool to provide the same objects. Accelerators provide to particles the energy at which we would like to study their interactions with other particles. Each approach has its own advantages and disadvantages, and data from both are used to build a coherent picture of the Universe surrounding us [2].
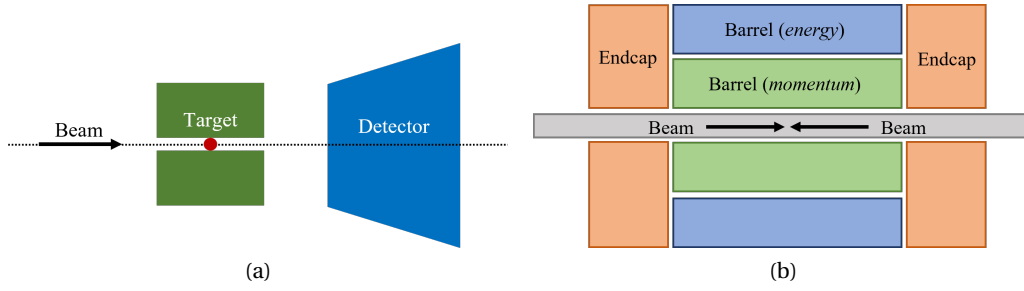
Figure 1.1: Schematic views of (a) an experimental setup for a fixed target experiment, and (b) of a collider experiment. The inner barrel of the detector of the collider experiment determines the direction and the momentum of the particle, while the outer measures the particle energy.

Nowadays, we distinguish between two types of accelerator-based experiments: accelerators with a fixed target and colliders [3]. The accelerators with a fixed target accelerate particles to the desired energy and scatter the beam against the fixed target material. The targets are stationary, material blocks, such as graphite or beryllium. Besides studying the interaction, this approach allows to produce and investigate a secondary beam of particles (stable, unstable, charged, neutral) for a subsequent collision. The whole process is "photographed" by a particle detector. In the second approach, the beams are accelerated separately to desired energies and then brought into collision. The collider accelerators offer higher energy available for the study of different HEP theories where rare phenomena are studied. The schematics of both methods are presented in Fig. 1.1.

Both approaches can be described with two key parameters: energy and luminosity. The center-of-mass energy, usually denoted as $\sqrt{s}$, represents the energy available in collision experiments, whether it involves a stationary and a moving particle or two moving particles. For fixed target experiments, the center-of-mass energy can be approximated as:

$$\sqrt{s} \sim \sqrt{E_{beam}} \tag{1.1}$$

where E_{beam} is the accelerated particle energy, and $\sqrt{s}$ is the available energy given to the (possible) trapped particles that will be able to appear. In the case of a fixed target experiment, the center-of-mass energy grows only with the square root of E_{beam}. On the other hand, in the case of a collider, the center-of-mass energy can be approximated as:

$$\sqrt{s} = 2E_{beam} \tag{1.2}$$

which demonstrates that using two beams in opposite directions is much more efficient.

Louis de Broglie postulated the particle-wave duality as follows:

$$\lambda = \frac{h}{|\vec{p}|} \tag{1.3}$$

where λ is the particle wavelength, p is an impulse of the particle and h is Planck constant. In the case of higher energy, particles probes with small wavelengths can be produced and small objects can be investigated. Thus, by having a higher energy accelerator we can look at smaller things. One of the goals of modern particle accelerators is to see if quarks and leptons, which are the building blocks of present theories, are composed of smaller objects [2].

Together with the centre-of-mass energy, luminosity is related to the number of particles undergoing collisions. From a statistical point of view, more collisions mean a better chance of seeing something rare. Instantaneous luminosity describes how frequently the particles have a chance to interact per unit area. The number of events (collisions) is determined by the instantaneous luminosity and cross-section, the effective area of two particles for a reaction to occur, as follows:

$$\frac{\partial N_{reactions}}{\partial t} = \mathcal{L} \cdot \sigma \tag{1.4}$$

where we assume that the cross-section σ does not depend on the time interval and $\mathcal{L}$ is the instantaneous luminosity. Equation (1.4) quantitatively expresses how the requirement for high statistical accuracy of experimental data translates into the requirement for the high luminosity of an accelerator. However, instantaneous luminosity cannot be increased indefinitely, as it might conflict with the performance of the data acquisition system.

Often integrated luminosity is reported, $L = \int_{t_1}^{t_2} \mathcal{L} \, dt$, which defines the amount of data recorded for the given time-interval $[t_1, t_2]$. The cross-section σ is usually measured in barns, [b], where $1 \text{ b} = 10^{-24} \text{ cm}^2$. The measuring unit for the instantaneous luminosity is $\text{cm}^{-2}\text{s}^{-1}$, while the integrated luminosity is usually expressed in inverse femtobarns [fb^{-1}] or inverse picobarns [pb^{-1}].

After introducing the accelerator key parameters, another aspect of accelerator design that we must take into consideration is the type of particles that will collide. The colliding particles choice is based on the spectrum of phenomena that we want to study. Particles participating in collisions can be composite objects themselves, such as protons or heavy ions. In this case, the particle energy is shared among its constituents, and the energy available to induce new phenomena is lower and determined by the energy in the reference frame of colliding constituents, and not in the frame of the parent particles. Finally, the combination of signs of charges of colliding particles imposes technical restrictions on the configuration and implementation of

the magnetic field in a circular accelerator apparatus.

In addition to these aspects, there are several technical considerations that must be carefully evaluated during the design of an accelerator. These may include the choice between linear and circular accelerator geometry, the radiation energy loss per turn in circular accelerators, the percentage of time that collisions are actually occurring, and the level of various background interactions [4]. All of these factors can significantly impact the performance and effectiveness of the accelerator.

In the following section, the design of the circular Large Hadron Collider (LHC) accelerator and its future upgrade at the *Conseil Européen pour la Recherche Nucléaire* (CERN) will be presented. Key aspects that have influenced the choice of technologies employed at the LHC are discussed. Additionally, this chapter will cover what is called the "Phase-2" upgrade of the Compact Muon Solenoid (CMS) detector, one of two all-purpose detectors functioning at the LHC, followed by a description and analysis of the upgrade plans for its components. The future upgrade will mainly be Silicon(Si)-based and must operate at temperatures well below zero degrees Celsius. Given that the detectors will operate below the dew point temperature of their experimental cavern, it is crucial to monitor the dew point temperature inside the detector in order to avoid condensation, as it can severely damage the detector sensors and electronics. Therefore, the necessity of dew point sensors, and thus the need for temperature and relative humidity sensors, in high-energy physics will be carefully introduced and discussed at the end of this chapter.

1.1   Accelerator Complex

The role of the accelerator is to increase the energy of the charged particles. The energy injection is done using radio-frequency (RF) cavities situated at one point of the beam cyclic trajectory. A magnetic field is used to bend the particles forcing them to move along the circle and to focus them. The world's largest accelerator is the LHC located between 45 m and 170 m below the surface at the Swiss-French border with a circumference of around 27 km. The LHC is a two-ring accelerator (collider) and is part of the more complex CERN accelerator system. It is fed with two counter-circulating proton beams injected by a chain of linear and circular accelerators, depicted in Fig. 1.2.

Prior to their injection into the LHC, the protons undergo a series of pre-accelerations. At the beginning of the injection chain, an electric field is applied to strip electrons of hydrogen atoms to yield protons. This way, the protons are separated and can be injected into the cycle. The protons are subsequently accelerated from 90 keV to a kinetic energy of 50 MeV in the first accelerator in the chain – the Linear Accelerator 4 (LINAC4). The LINAC4 is followed by the Proton Synchrotron Booster (PSB), from which the protons get out with 1.6 GeV of energy. Thereafter, the protons are transferred to the Proton Synchrotron (PS), where the proton beam is pushed to 26 GeV. Next, the Super Proton Synchrotron (SPS) accelerates the beam to a kinetic energy of 450 GeV and transfers it to the LHC or delivers it to fixed target

The CERN accelerator complex
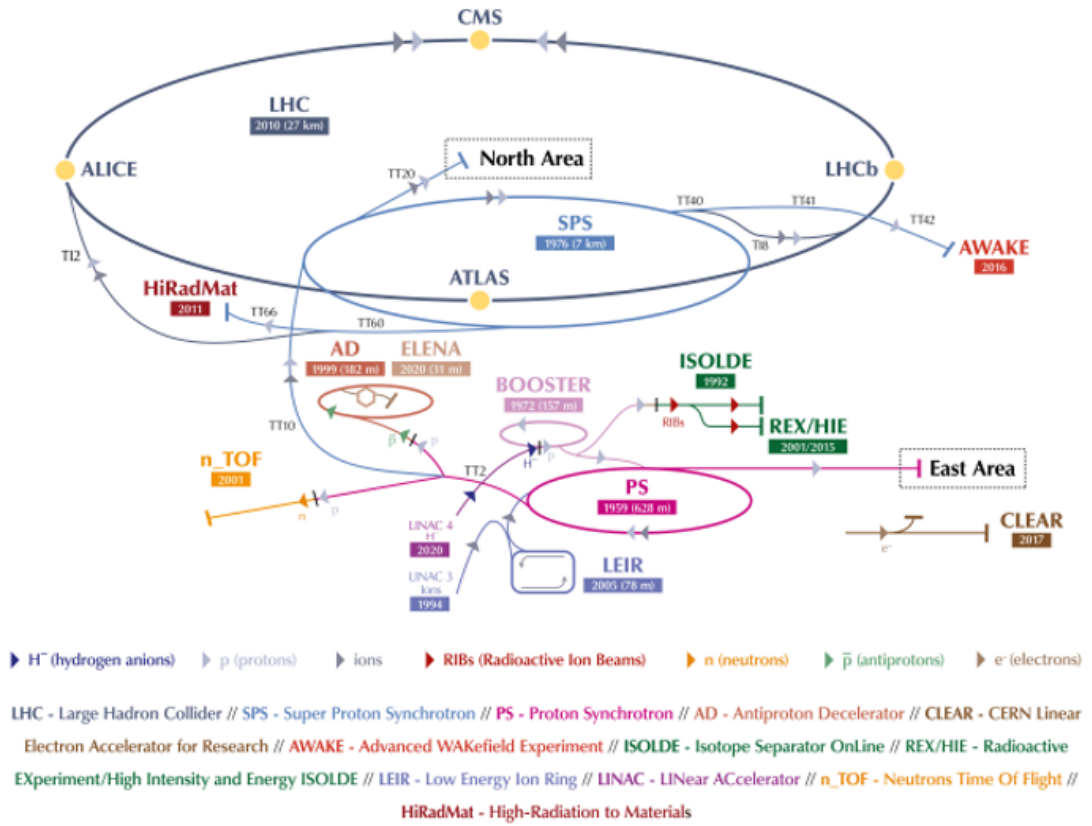
Figure 1.2: The chain of linear and circular machines that accelerates the particle beam until its injection in the LHC, [5].

experiments in the SPS North Area.

1.1.1 Large Hadron Collider

For the LHC circular accelerator with two Gaussian-shaped beams with dimensions σ_x and σ_y colliding almost head-on and with a small crossing angle, the instantaneous luminosity is illustrated as follows:

$$\mathcal{L} = \frac{f N_1 N_2 N_b}{4\pi \sigma_x \sigma_y} \cdot S \tag{1.5}$$

where f is the bunch revolution frequency, N_1 and N_2 are the numbers of particles per bunch, and N_b is the number of bunches per beam. S represents the geometrical luminosity reduction

5

factor ($S < 1$) and it can be expressed as [6]:

$$S = \frac{1}{\sqrt{1 + \left(\frac{\sigma_s}{\sigma_x}\tan\frac{\Phi}{2}\right)^2}} \approx \frac{1}{\sqrt{1 + \left(\frac{\sigma_s}{\sigma_x}\frac{\Phi}{2}\right)^2}} \tag{1.6}$$

where, σ_s is the bunch length, and Φ is the crossing angle. The aforementioned equations, eq.(1.4) – (1.6), show that the luminosity can be increased by reducing the cross-section of the beam, by increasing the number of particles in the beam, or by increasing the bunch revolution frequency. In general, the luminosity of an accelerator gradually increases over time, while accelerator physicists learn how to operate the machine and squeeze the beam size at the intersection point.

In the LHC, the energy of the particles is increased up to 6.8 TeV providing proton-proton collisions with a center of mass energy of up to 13.6 TeV. The beam is split into 2808 bunches, with a revolution frequency of 11245 turns per second, where each bunch is composed of $1.15 \cdot 10^{11}$ particles. The luminosity reduction factor, S, for the LHC results, is 0.835, and the beam size in one direction is 16.7μm resulting in the instantaneous LHC luminosity of 10^{34} cm^{-2} s^{-1} [7].

The bending of the 6.8 TeV proton beam and keeping it on the projected circular trajectory demands a magnetic field of 8.33 T, corresponding to an electrical current of 11.7 kA. Thus, superconductive technology was used as superconductors show no resistance to a current flow below a critical temperature. With superconductive magnets, the current density limitations imposed by Joule heating in standard electromagnets are surpassed. The Niobium-Titanium (NbTi) superconducting coils that are used for the LHC magnets, require a powerful cryogenic system and cryogenic distribution line in the LHC to bring the operating temperature to 1.9 K.

1.1.2   Experiments

The LHC accelerator has eight insertion regions (IRs) as presented in Figure 1.3. These IRs are the locations where the acceleration systems (RF cavities), detectors, and facilities for cleaning and dumping of proton beams are installed. They divide the LHC ring into eight equally long arcs and each of them is equipped with the dipole magnetic system used to bend the beam along the accelerator[I], and quadruple magnetic system used to focus the beam[II] [4]. Additionally, they contain several other systems that provide higher-order multi-pole magnetic fields for fine corrections of the beam orbit

There are four IRs where collisions happen, and in each of them one main detector is installed:

[I]The dipole magnetic system consists of 1232 dipole magnets of 15 meters in length.
[II]The quadruple magnetic system consists of 392 quadrupoles magnets, each 5–7 meter long.

- **IR1 – ATLAS** (**A T**oroidal **L**HC **A**pparatu**S**): The ATLAS detector is one of two general-purpose detectors built to study the Standard Model and beyond, [8].

- **IR2 – ALICE** (**A L**arge **I**on **C**ollider **E**xperiment): The ALICE detector is dedicated to heavy-ion collisions, such as proton-lead (p-Pb) and lead-lead (Pb-Pb). At extremely high temperatures, the quark-gluon plasma is produced, helping to reproduce similar conditions that existed after the Big Bang, [9].

- **IR5 – CMS** (**C**ompact **M**uon **S**olenoid): The CMS is another general-purpose detector, complementary to the ATLAS detector, designed with a very broad scientific program, including both searches for new phenomena and precision measurements in particle physics, [10].

- **IR8 – LHCb** (**L**arge **H**adron **C**ollider **b**eauty): The LHCb detector is the fourth main experiment, designed to study CP violation from the decays of b hadrons, [11].

Additionally, three other small detectors, **LHCf** (**L**arge **H**adron **C**ollider **f**orward), **TOTEM** (**TOT**al **E**lastic and diffractive cross section **M**easurement), and **MoEDAL** (**Mo**nopole and **E**xotics **D**etector **A**t the **L**HC), are located in same caverns as ATLAS, CMS, and LHCb, respectively. LHCf studies the collisions in the forward region [12], while TOTEM measures total cross-section, and studies diffractive processes and elastic scattering [13]. The MoDEAL experiment aims to search for the existence of magnetic monopoles [14].

1.1.3   High Luminosity LHC (HL-LHC)

The number of collisions, and therefore luminosity, must increase to have a better probability of discovering some new physics phenomena and prove the existence of new particles produced in rare events. Figure 1.4 presents the plan, features, and operation parameters of the LHC upgrade for the following years. The LHC upgrade is planned in three phases known as Long Shutdowns (LSs) during which the accelerator is stopped, and the beam instrumentation is maintained, repaired, and/or changed. During the LS3 (between 2026 and 2028), the LHC will be upgraded to the High-Luminosity LHC (HL-LHC), where the luminosity will be increased by a factor of 5 in comparison to the current LHC luminosity, [15], [16].

There are three ways of increasing the luminosity: reducing the crossing angle, reducing the beam size, or increasing the beam density. The current LHC crossing angle is 286 μrad and in the HL-LHC it will be reduced using novel RF cavities (Crab cavities) [15]. They will be made of superconducting material Ni and their main task will be to rotate the bunches at the collision points to reach optimal head-on collisions. In this way, the geometrical luminosity reduction factor, S, will increase from 0.835 to around 1.

The beam size will be reduced using novel quadruple magnets that will help in better beam focusing at the collision points enhancing the luminosity. For the HL-LHC, the beam size will be reduced from 16.7 μm to 8.2 μm. The beam intensity is increased by increasing the total
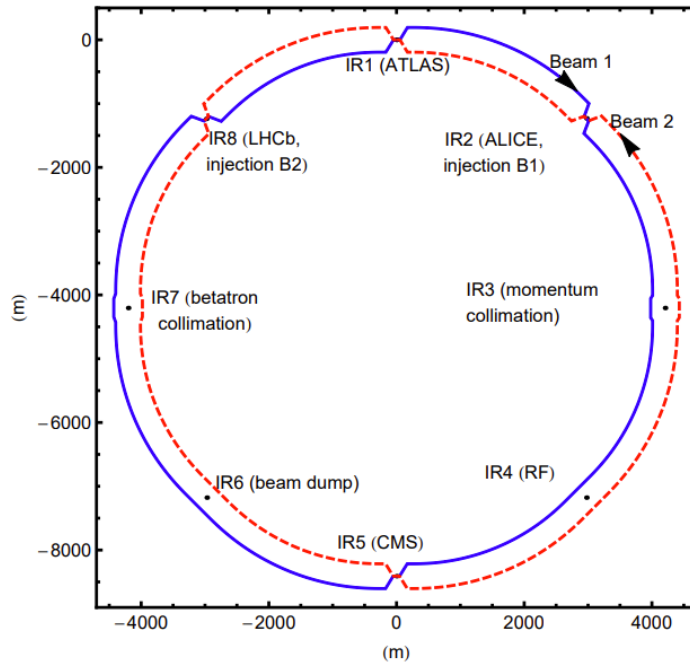
Figure 1.3: The schematic layout of the LHC (the separation of the two rings is not to scale) is shown in a global coordinate system with the origin in the ATLAS collision point. The two beams collide in the four experiments ATLAS, ALICE, CMS, and LHCb. In the other IRs, systems for acceleration (RF cavities – IR4), cleaning (IR3 and IR7), and dumping (IR6) are installed.

number of protons in each beam. As protons are charged particles, the beam represents a current flow. For the present LHC accelerator, the beam intensity is equal to 0.58 A, while for the HL-LHC is almost twice higher and is equal to 1.12 A.

The above-mentioned discussion is summarized in Table 1.1, where a deeper comparison analysis of the current LHC and future HL-LHC collider parameters is given. In the future HL-LHC, the number of protons per bunch will increase up to $2.2 \cdot 10^{11}$, and with the r.m.s. beam size at the interaction point of 8.2 μm will lead to the increase of total inelastic collisions[III] per bunch crossing to 112 mbarn, with the instantaneous luminosity of $5 \cdot 10^{34}$ cm^{-2}s^{-1}.

As previously mentioned, the implementation of a high-luminosity configuration requires several technological advancements. This includes the upgrade of the superconducting magnet and cold powering system, the introduction of new superconductive RF crab-cavities, and the upgrade of the collimation system[IV]. These improvements are necessary to achieve the desired level of luminosity in the accelerator. Therefore, upgrades of the currently existing

---

[III]In an inelastic collision, the number or the nature of the particles after the interaction has changed, while in elastic interaction, the number and the nature of the particles after the interaction remain unchanged.

[IV]The collimation system is a collection of protective devices, used to protect the rest of the accelerator from particles spiraling out of the machine. Furthermore, it can limit the maximum field size of a beam.
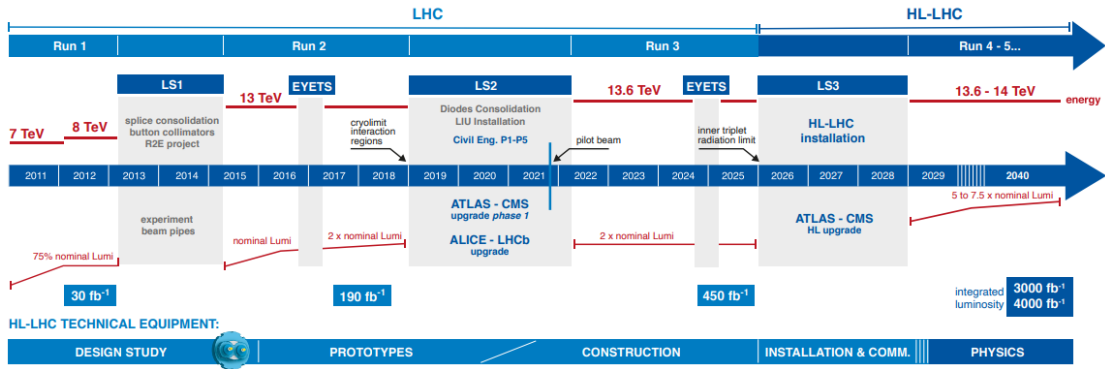
Figure 1.4: Illustration of a bunch crossing with the relative parameters.

Table 1.1: Comparison of collider parameters

Parameter	LHC	HL-LHC	Unit
Collision energy	14	14	[TeV]
Magnetic dipole field	8.33	8.33	[T]
Dipole operating temperature	1.9	1.9	[K]
Circumference	26.659	26.659	[m]
Injection energy	450	450	[GeV]
Total Synchr. radiation power	3.6	7.3	[kW]
Energy loss $\Delta/turn$	6.7	6.7	[keV]
Revolution frequency	11245	11245	[Turns per second]
Bunches per proton beam	2808	2808	–
Protons per bunch	$1.15 \cdot 10^{11}$	$2.2 \cdot 10^{11}$	–
RMS bunch length	7.55	8.1	[cm]
Bunch spacing	25	25	[ns]
Beam current	0.58	1.12	[A]
Stored energy/beam	362	700	[MJ]
RMS beam size at int. point	16.7	8.2	[µm]
Peak luminosity	$1 \cdot 10^{34}$	$5 \cdot 10^{34}$	[cm^{-2}s^{-1}]
Total inelastic cross section	82	112	[mbarn]

facilities must be well planned. Some of the upgrades will imply the entire replacement of some sub-detectors and involve silicon material as a main constituent of the future high-energy physics detectors. The upcoming upgrade is briefly presented in the following section on the example of the CMS detector upgrade scheduled during the LS3 phase.

1.2   The Phase-2 Upgrade of the Compact Muon Solenoid

The increase in the luminosity poses significant challenges for particle detection with the current detectors. The particle detection and energy measurement would be drastically impaired due to the two following reasons:

- **Increased confusion due to pile-up events:**[V] By increasing the luminosity, the number of particles per bunch increases as well followed by adding additional beam-focusing elements. For future HL-LHC experiments, the average number of inelastic collisions per bunch-crossing is even expected to exceed the number of 140 (200)[VI]. Due to the increase, assigning measured energy depositions in the sub-detectors to the particles emerging from the hard collisions of interest becomes more difficult. Pile-up energy depositions could be confused as energy from the showering particles of interest.

- **Degrading sensors due to radiation damage:** The current sensitive material used for particle detection could not cope with the expected radiation levels during the HL-LHC operation. The radiation might have a huge impact on the resolution of some sub-detectors, and, therefore, detectors with a novel radiation hardness will be required, especially for regions with harsher radiation levels.

To address the above-listed constraints, the CERN detector collaborations are planning upgrades and even the entire replacement of some sub-detectors, which will be presented in the example of the CMS detector.

The CMS detector weighs 14000 tons, is 21 meters long and is 15 meters high. It is cylindrical and contains several sub-detector systems as illustrated in Figure 1.5. A large solenoid[VII] envelops the first three layers: the tracker system, the electromagnetic calorimeter (ECAL) and the hadron calorimeter (HCAL). The last layer is muon chambers located outside the magnet. The cylindrical part of the detector is known as a barrel, while the side parts are called endcaps. Figure 1.6 shows the cross-section of the CMS detector as well as the particle trajectories reconstructed from the signals that arise as a result of their interactions with the materials of the detector through which they pass.

The current detector is built to operate at the instantaneous luminosity of $1 \cdot 10^{34}$ cm^{-2}s^{-1} and integrated luminosity of 500 fb^{-1}, [17], while, after the foreseen upgrade of the LHC, the instantaneous luminosity will be $5 \cdot 10^{34}$ cm^{-2}s^{-1} and the target value of the integrated luminosity is 3000 fb^{-1} [18], [19]. The current equipment and instrumentation are not designed for the radiation dose expected at such high luminosity, thus, the detector upgrade is necessary

---

[V]Pile-up is defined as the average number of particle interactions per bunch-crossing. There are different types of pile-up. In-time pile-up is additional proton-proton collisions occurring in the same bunch-crossing as the collision of interest. Out-of-time pile-up is additional proton-proton collisions occurring in bunch-crossings just before and after the collision of interest.

[VI]The 140 is the average number of inelastic proton-proton collisions per bunch-crossing that corresponds to the instantaneous luminosity of HL-LHC of $5 \cdot 10^{34}$ cm^{-2}s^{-1}, while 200 is the average number of inelastic proton-proton collisions per bunch-crossing estimated for the instantaneous luminosity of $7.5 \cdot 10^{34}$ cm^{-2}s^{-1}

[VII]The solenoid magnet represents the core and "muscles" of the CMS detector and it is the only part of the detector that does not require upgrade. The purpose of the CMS magnet is to bend the trajectories of the high-energy particles arising from the proton-proton collision making it a vitally important part for the identification of the charge and momentum of the detected particles. The solenoid magnet is a 12.5 m long cylinder with a 6.3 m diameter and its coils are made of the niobium-titanium (NbTi) wires with 2180 turns. It is a superconducting magnet that operates at a temperature of 4.5 K. The solenoid magnet can carry an electric current up to 18 kA, creating a uniform magnetic field of 3.8 T along its length, slightly lower than the 4 T design value.

CMS DETECTOR

Total weight   : 14,000 tonnes
Overall diameter : 15.0 m
Overall length   : 28.7 m
Magnetic field   : 3.8 T

STEEL RETURN YOKE
12,500 tonnes

SILICON TRACKERS
Pixel (100x150 μm²) ~1 m² ~66M channels
Microstrips (80–180 μm) ~200 m² ~9.6M channels

SUPERCONDUCTING SOLENOID
Niobium titanium coil carrying ~18,000 A

MUON CHAMBERS
Barrel: 250 Drift Tube, 480 Resistive Plate Chambers
Endcaps: 540 Cathode Strip, 576 Resistive Plate Chambers

PRESHOWER
Silicon strips ~16 m² ~137,000 channels

FORWARD CALORIMETER
Steel + Quartz fibres ~2,000 Channels

CRYSTAL
ELECTROMAGNETIC
CALORIMETER (ECAL)
~76,000 scintillating PbWO₄ crystals

HADRON CALORIMETER (HCAL)
Brass + Plastic scintillator ~7,000 channels

Figure 1.5: A 3D drawing of the CMS detector. The LHC beams travel along the length of the detector before colliding at the center. The interaction point is surrounded by the silicon tracker (blue), followed by the ECAL (tan) and HCAL (yellow) which are all enveloped by the superconducting solenoid (white). The steel return yoke of the magnet (red) doubles as an absorber for the muon tracking system and it contains the various muon tracking stations (white).

as planned during the LS3, also known as a CMS Phase-2 upgrade.

Phase-2 of the CMS detector upgrade is a major upgrade project that is currently underway. This is being achieved through the installation of new detector layers and the upgrade of existing detector components with new sensors and readout electronics, [19]. Fig. 1.7 presents a cross-section of the CMS detector with an overview of the upgrades foreseen for the HL-LHC.

One of the key features of the Phase-2 upgrade is the installation of a new detector layer called the High-Granularity Calorimeter (HGCAL). This layer will provide improved accuracy in the measurement of the energy of particles produced in collisions. It will replace the current ECAL and HCAL endcaps and will be made up of about six million individual sensor cells that are capable of measuring the energy of particles with high precision.

The Phase-2 upgrade also includes the installation of new tracking detectors called the Inner Tracking System (ITS) and the Outer Tracking System (OTS). These detectors will provide improved accuracy in the measurement of the momentum of particles produced in collisions
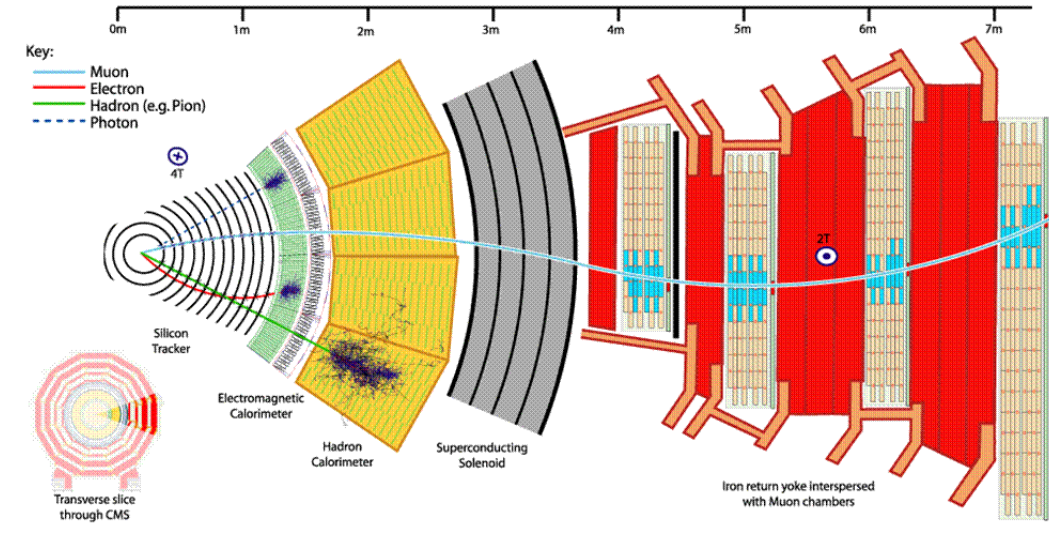
Figure 1.6: Cross-section of CMS detector with reconstructed particle trajectories. The charged particles such as electrons, muons, and charged pions ($\pi^\pm$) are bent inside and outside the solenoid whereas the neutral particles such as photons and neutral pions (π^0) traverse without being bent. The silicon tracker is mainly for measuring the momentum of particles whereas the ECAL and HCAL measure the energy deposits. The electrons and photons deposit their energy inside the ECAL whereas the hadrons deposit in both ECAL and HCAL. The muons are the only particles that traverse all the way to the muon chambers.
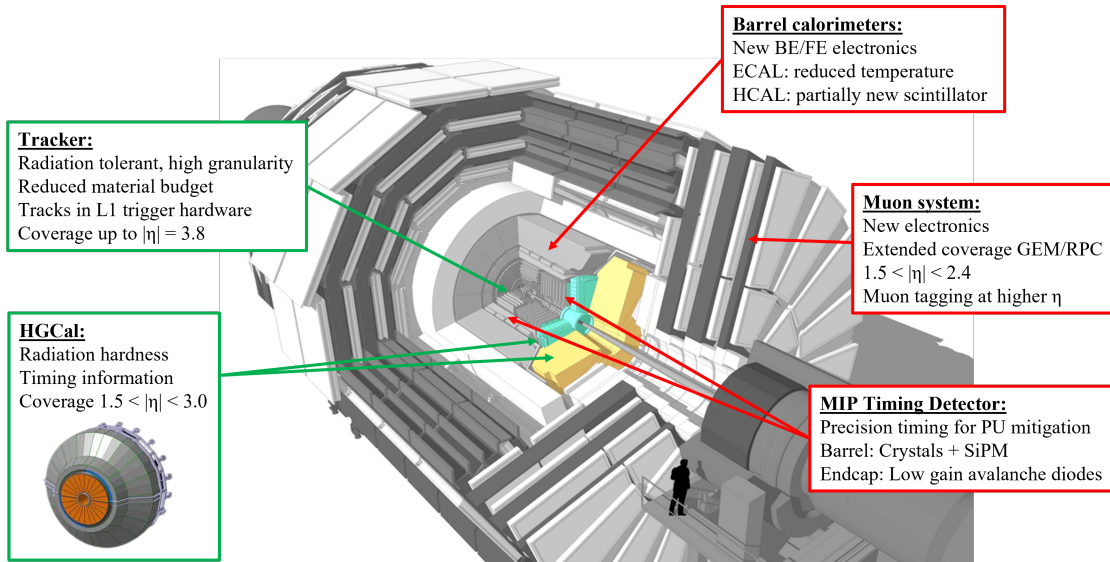
Figure 1.7: Cross-section of the CMS detector showcasing planned upgrades for the HL-LHC. The green boxes represent the sub-detectors that will be completely replaced, while the red boxes indicate either new modules or extensions of the current ones. The HGCAL sub-detector is going to replace the ECAL and HCAL endcaps represented in blue and yellow, respectively.

by measuring the trajectories of charged particles with high precision.

Other important features of the Phase-2 upgrade are the upgrades of the existing Barrel Calorimeters (ECAL and HCAL) and the Minimum Ionising Particle Timing Detector (MTD). The upgraded ECAL will operate at a reduced temperature, while the HCAL upgrade will contain the implementation of partially new scintillators. The upgrades of both calorimeters are followed by the integration of new back-end and front-end electronics.

The MTD is used to measure the time of arrival of particles produced in proton-proton collisions at the LHC with a resolution of about 50 picoseconds. It is divided in Barrel Timing Layer (BTL) and Endcap Timing Layer (ETL). The foreseen upgrade of the MTD is based on the integration of new silicon photomultipliers (SiPMs) in the detector barrel (BTL) and low-gain avalanche diodes in the detector endcap (ETL). Finally, the Phase-2 upgrade involves the upgrade of the existing muon detectors.

The new data acquisition and trigger systems are required to improve the speed and detection efficiency of the CMS detector. This will allow researchers to collect data from more LHC collisions and study a wider range of physics phenomena.

1.2.1 Silicon Detectors in High-Energy Physics

Silicon material is selected as a major constituent of the detector upgrades (especially for the Tracker and for the HGCAL). Silicon is a widely used detector material in a variety of radiation detection applications in particle, nuclear, and atomic physics due to its ability to produce a large number of free charge carriers per incident radiation. This allows for excellent resolution, even when the deposited energy is low. In particle tracking applications, silicon detectors can be made very thin while still providing a good signal-to-noise ratio. The ability to micro-pattern the material using lithographic methods also allows for excellent spatial resolution. Among semiconductor materials that offer similar characteristics, silicon is the primary material used in the microchip industry and thus has the advantage of low cost and extensive manufacturing experience.

Silicon as an Active Material

Silicon is a semiconductor material belonging to group IV of the periodic table, with a band gap energy of E_g = 1.12 eV. Table 1.2 gives an extensive overview of the silicon material properties. The electrons in a crystal lattice of silicon can occupy either localized states associated with individual atoms or delocalized states within the lattice itself. The latter set of states is known as the conduction band, and electrons occupying these states are not bound to fixed lattice locations and can move freely through the crystal. The probability that an electronic state of energy E at a temperature T is occupied by an electron is given by the Fermi-Dirac distribution:

Table 1.2: Properties of silicon material

Parameter	Value	Parameter	Value
Energy Bandgap [eV]	1.12	Density [gm/cm^3]	2.328
Electron Mobility [cm^2/Vs]	1500	Melting Point [°C]	1420
Hole Mobility [cm^2/Vs]	600	Dielectric Constant	11.8
Thermal Conductivity [W/(cm · K)]	1.5	Resistivity [Ωcm]	10^3
Breakdown [Vcm^{-1}]	$3 \cdot 10^5$	Absorption Edge [µm]	1.4
Lattice Constant [Å]	5.43	Refractive Index	3.5
Thermal Expansion Coefficient [°C^{-1}]	$2.6 \cdot 10^{-6}$	Hardness [kg/mm^2], $T = 300$ K	1000

$$f_e(E) = \frac{1}{e^{(E-E_F)/k_b T} + 1} \tag{1.7}$$

where k_B is the Boltzmann constant and E_F is the Fermi energy, which is the point at which the probability of a state being occupied is 50%.

Electrons (e) in a crystal lattice can be promoted to the conduction band through thermal excitation or the deposit of external energy. This process leaves a vacancy in the crystal lattice, which can be described as a quasi-particle known as a hole (h). On average, approximately $W \sim 3.65$ eV of energy is required to create a single electron-hole pair, although the exact value depends on the specific nature of the energy deposition. By applying an electric field, electrons and holes can be separated spatially, a principle that forms the basis for the use of silicon (or any other semiconductor) as detector material.

In pure silicon crystals, the intrinsic charge carrier density is roughly 10^{10} cm^{-3} at room temperature. This is significantly higher than the number of charge carriers created by ionization from a charged particle traversing the same volume. To reduce the intrinsic charge carrier density and make silicon a viable detector material, dopants are introduced.

From a Crystal to a PN Junction

Dopants, which are atoms from group III (e.g. boron) or group V (e.g. phosphorous) added to the silicon crystal lattice, introduce additional energy levels into the band gap due to their different number of valence electrons. The introduction of a group V dopant results in the creation of a loosely bound state in the band gap just below the edge of the conduction band, which can be easily promoted to the conduction band through a process known as n-type doping. This process results in an abundance of quasi-free electrons, referred to as majority charge carriers, and holes, referred to as minority charge carriers. Group III dopants result in the introduction of a state in the band gap just above the edge of the valence band through a process known as p-type doping, creating an abundance of holes and electrons. When a p-type and an n-type doped material come into contact, they form a PN-junction in which
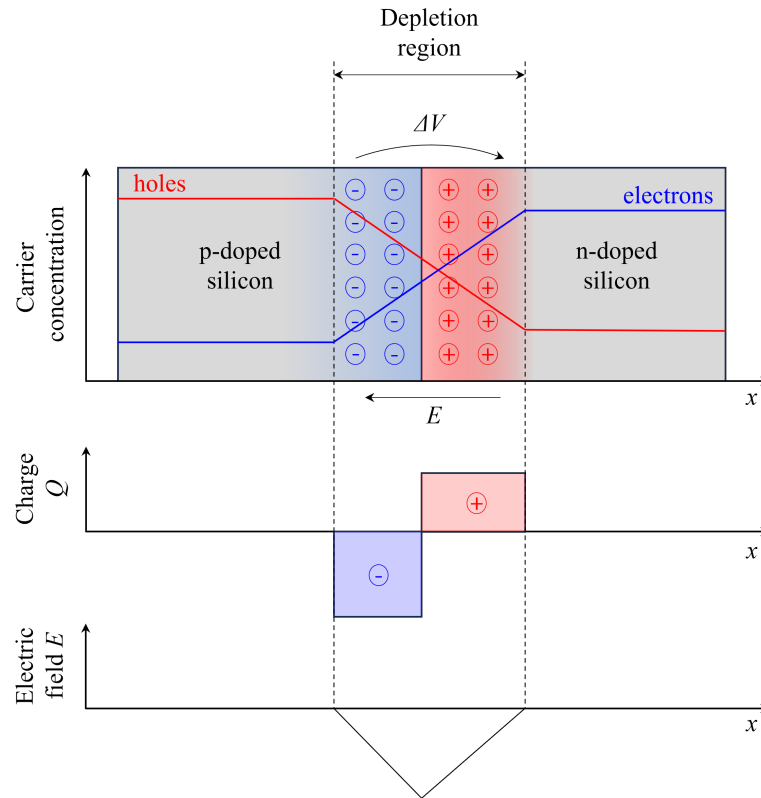
Figure 1.8: Schematic of p- and n-type doped silicon regions forming a PN-junction. Once the PN-junction is established, the mobile charge carriers recombine in the contact region. The resulting concentrations of free charge carriers, space charge density, and electric field are illustrated.

the acceptor states in the p-type region are filled by the electrons from the donor states in the n-type region, resulting in a negatively charged p-type region and a positively charged n-type region, creating a potential difference ΔV across the junction (see Fig. 1.8). In equilibrium, the contact region is free of intrinsic charge carriers.

From a PN Junction to a Detector

The size of the depleted volume is determined by the doping concentration and is limited to at most a few micrometers. It can be controlled by adjusting the external voltage V_{bias}. This voltage is applied to the contact electrodes in a reverse direction and the depleted region expands proportionally to the square root of the sum of the applied bias voltage and internal junction voltage. The effective voltage, V_{eff}, is defined as $V_{eff} = V_{bias} + \Delta V$, where ΔV is typically well below 1 V. This is known as reverse biasing, which is the way HEP detectors operate. This mode of operation allows for the efficient detection of particles by creating a large depletion zone for the charges produced by the incident particle to be collected. Examples of such sensors include silicon strip and silicon pixel sensors, which are used in the Tracker
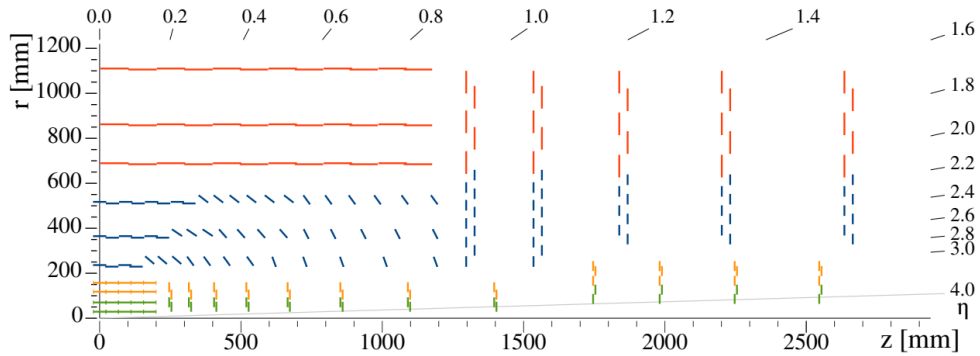
Figure 1.9: One-quarter view of the tracker layout in r-z projection. The Inner Tracker contains pixel modules made of two readout chips (green lines) and pixel modules with four readout chips (yellow lines), while the Outer Tracker exhibits the pixel-strip (PS) and 2-strip (2S) modules denoted by blue and red lines, respectively.

sub-detector.

1.2.2 The Phase-2 Upgrade of the Tracking System

The tracker is located in the innermost part of the CMS detector, placed around the interaction point. The tracker is a detector system, with a volume of 5.6 m in length and 2.4 m in diameter, that serves to reconstruct the path of particles and determine the momentum of particles, [20], [21]. Due to the presence of the magnetic field, charged particles travel in a curved trajectory and the bending of the trajectory depends on the momentum of particles. The greater the particle's momentum, the less curved is their trajectory.

The detectors used for this purpose are semiconductor detectors made of silicon as active material, [22]. Particles passing through semiconductor detectors create electron-hole pairs. In the external field, the charges are separated, returning an electrical signal that is proportional to the energy of the incident particle. The signal left by the particle is very precisely located, with a precision of up to 10 μm. Based on a large amount of collected data, the paths are reconstructed in software and the corresponding impulse is attached to the particle.

The primary goal of the new Tracker System is to ensure adequate track reconstruction performance at the much higher pileup levels of the HL-LHC. The tracking system is subdivided into two parts: the Inner Tracking System (ITS), placed directly around the interaction point, and the Outer Tracking System (OTS). The layout of the Phase 2 Tracker is depicted in Fig. 1.9. The granularity of the outer tracker and inner detector in the new system will be roughly 4 and 6 times greater, respectively, than the current systems, to achieve at HL-LHC similar levels of occupancy as at a luminosity of 10^{34} cm^{-2}s^{-1}, [23].

The Inner Tracker in the CMS detector will be equipped with pixel modules. The high-luminosity operation poses challenges for the design of the Inner Tracker in terms of radiation
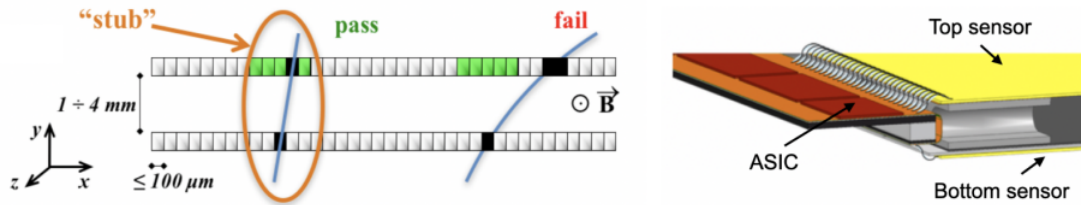
Figure 1.10: Illustration of the pT module concept. The correlation of signals in closely-spaced sensors enables the rejection of low-pT particles; the channels shown in green represent the selection window to define an accepted stub. A low-momentum track falls outside the acceptance window and produces no stub. [24]

tolerance of sensors and readout electronics, as well as data volume to be stored in the front-end pipelines and sent out at high trigger rates. Thin silicon sensors (of thickness 100-150 μm), segmented into pixel sizes of 25 × 100 μm² or 50 × 50 μm², are expected to exhibit the required radiation tolerance and to deliver the desired performance in terms of detector resolution, occupancy, and two-track separation. ATLAS and CMS are carrying out a common development to design a pixel chip with 2500 μm² cell size, in 65 nm CMOS technology. The Inner Tracker is composed of a barrel part with four cylindrical layers and eight small plus four large disc-like structures in each forward direction. The Inner Tracker is designed to allow for the replacement of degraded parts during an extended technical stop, without requiring the removal of the CMS beam pipe. This is achieved by using inclined rails that enable the detector to be extracted and inserted.

The use of tracking information in the Level 1 trigger implies that the Outer Tracker has to send out self-selected information at every bunch crossing, using local data reduction in the front-end electronics to limit the volume of data that has to be sent out at 40 MHz. This is achieved by pT modules that are capable of rejecting signals from particles below a certain pT threshold. The principle of operation of the pT modules is illustrated in Fig. 1.10.

These modules come in two versions: 2-strip modules (2S) and pixel-strip modules (PS). The 2S modules have strips that are 5 cm long and are used in the outermost three layers of the Outer Tracker, while the PS modules have strips that are 2.4 cm long and one of the sensors is segmented into macro-pixels, providing measurement of the z (r) coordinate in the barrel (endcaps). These PS modules are used in the first three layers of the Outer Tracker and in the radial region of 200-600 mm. In the endcaps, the modules are arranged in rings, with PS modules in the rings at low radii and 2S modules at larger radii. To connect the upper and lower sensors of the module, each module is read out independently by front-end electronics, preventing communication between the sensor halves, which leads to a geometrical inefficiency of stub[VIII] finding. To overcome this limitation, CMS has developed an innovative layout where the first three barrel layers are populated with progressively tilted modules, which are nearly perpendicular to incident particles over the entire barrel length.

[VIII]A local track segment.
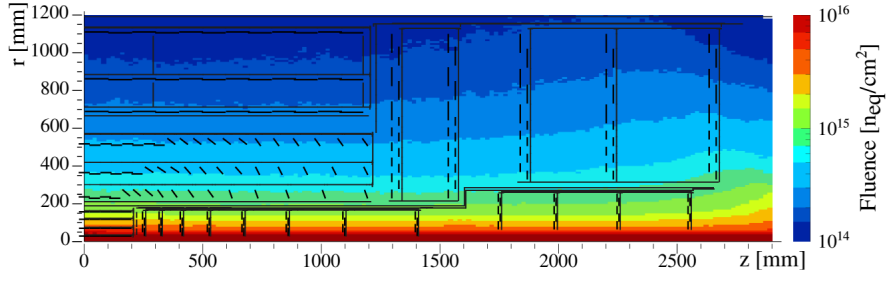
Figure 1.11: Integrated particle fluence in 1 MeV neutron equivalent per cm^2, for the Phase-2 Tracker sub-detector. The estimates shown correspond to a total integrated luminosity of 3000 fb^{-1} of pp collisions at $\sqrt{s}$ = 14 TeV, and have been obtained with the FLUKA software.

Table 1.3: Maximum expected fluence for selected detector regions or components of the tracker. Values are for 3000 fb^{-1} of pp collisions at $\sqrt{s}$ = 14 TeV assuming a total cross-section, σ_{pp}, of 80 mb. The positions in r and z at which the quoted maximum fluence levels for the respective region or component type are reached are also given.

Region or component	Max. fluence [n_{eq}/cm^2]	r [mm]	z [mm]
IT barrel layer 1	$2.3 \cdot 10^{16}$	28	0
IT barrel layer 2	$5.0 \cdot 10^{15}$	69	0
IT barrel layer 4	$1.5 \cdot 10^{15}$	156	89
IT forward, ring 1	$1.0 \cdot 10^{16}$	51	252
IT service cylinder	$1.3 \cdot 10^{15}$	170	260
OT PS modules	$9.6 \cdot 10^{14}$	218	129
OT 2S modules	$3.0 \cdot 10^{14}$	676	2644

The upgraded Tracker must be fully efficient for a target integrated luminosity of 3000 fb^{-1}, with an appropriate margin of 50% to accommodate uncertainties in the FLUKA simulations, [25], and the potential delivery of additional integrated luminosity. This requirement must be fulfilled without any maintenance intervention for the Outer Tracker. The Inner Tracker, which uses pixel detector modules, is planned to maintain the current accessibility concept, allowing for regular extraction and replacement of modules and other elements as they accumulate substantial radiation damage. FLUKA simulations have been performed to estimate the radiation exposure of the different detector regions, which is about one order of magnitude higher compared to the requirements used for the design of the existing Tracker, reaching a 1 MeV neutron equivalent fluence[IX] of $2.3 \cdot 10^{16}$ n$_{eq}$/cm^2 in the innermost regions of the Inner Tracker (Fig. 1.11). The particle fluence depends primarily on r, while the variation with z is very moderate. The maximum fluence levels expected for various parts of the new Tracker are summarized in Table 1.3.

The minimization of material in the tracker has been a primary goal in the optimization process. Improvements to the configuration, special module design, and new cooling and

---

[IX]Fluence = the particle flux integrated over time [particles/cm^2]. Flux = the number of particles passing through a unit area perpendicular to the beam, in one second [particles/cm^2/s].
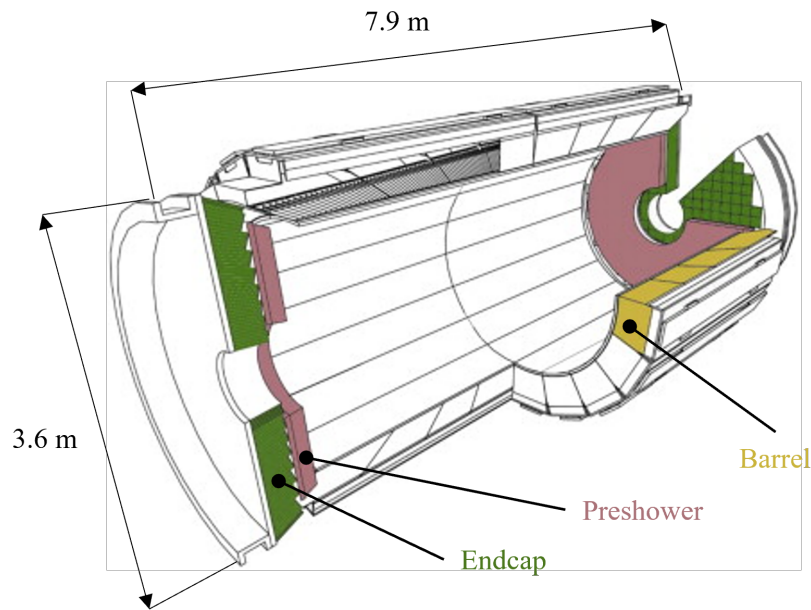
Figure 1.12: Schematic view of the ECAL sub-detector. The barrel consists of 61 200 PbWO$_4$ crystals divided into 36 supermodules, while there are 14 648 PbWO$_4$ crystals in the endcaps.

power distribution techniques have greatly reduced the mass in the tracking volume. The support structures will hold the detectors in place and provide mechanical stability, while the cooling systems will remove the heat generated by the detectors and readout electronics.

1.2.3   Phase-2 Upgrade of the Barrel Calorimeters

ECAL Barrel Calorimeter

The Electromagnetic Calorimeter (ECAL) plays a crucial role in measuring the energy of particles that interact through electromagnetic interactions, such as photons, electrons, and positrons, during the collision of proton beams, [26]. The ECAL is constructed from layers of lead tungstate (PbWO$_4$) scintillator tiles, emitting light when particles strike. These tiles are arranged in a matrix of cells, with each cell covering a small area of the calorimeter. When a particle passes through the ECAL, it deposits some of its energy in the scintillator tiles, causing them to emit light. This light is then detected by photomultiplier tubes (PMTs) located behind the tiles, which convert the light into an electrical signal. The signal is then amplified and used to determine the energy of the particle. Figure 1.12 depicts the schematic view of the ECAL structure marking its main constituents: preshower, endcaps and barrel supermodules.

Figure 1.13 shows the total accumulated fluence for the ECAL Barrel region for an integrated luminosity of 3000 fb^{-1}. The accumulated neutron equivalent dosage for the ECAL Barell region will be in the range from $1.2 \cdot 10^{14}$ n$_{eq}$/cm^2 to $2.5 \cdot 10^{14}$ n$_{eq}$/cm^2.

19
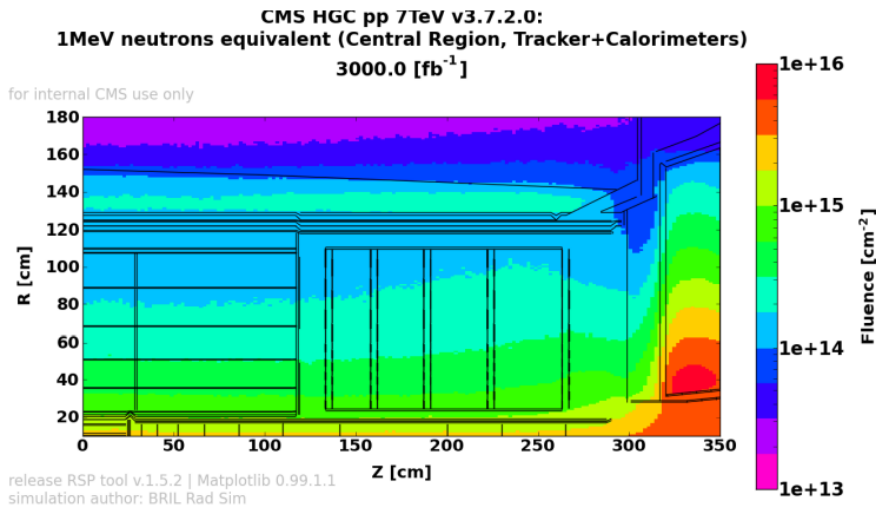
Figure 1.13: Integrated particle fluence in 1 MeV neutron equivalent per cm^2, in the ECAL Barrel region. The estimates shown correspond to a total integrated luminosity of 3000 fb^{-1} of pp collisions at $\sqrt{s}$ = 14 TeV, and have been obtained with the FLUKA software.

The Phase-2 upgrade of the CMS ECAL is needed to maintain the ability to trigger efficiently on electrons and photons via the improved rejection of anomalous signals in the photodetectors, to mitigate radiation-induced effects that would degrade the energy resolution, and to satisfy the upgraded hardware trigger requirements. During the Phase-2 upgrade, the front-end electronics will be replaced. The data will be transferred off-detector at 40 MHz, simultaneously overcoming present limitations in trigger latency and acceptance rate. The supermodules will be operated at a lower temperature during Phase-2, 9 °C, which will significantly reduce the aging-induced noise increase in the avalanche photodiodes (APD) and further mitigate the APD noise and provide better out-of-time (OOT) pileup rejection. A new front-end chip will be designed with a shorter shaping time, better anomalous signal rejection in APDs, and capability for precision timing as well.

HCAL Barrel Calorimeter

The purpose of the Hadron Calorimeter (HCAL) is to measure hadrons energy depositions, [27]. The active material, the scintillators and fibers, is not expected to have a significant impact on the physics performance of CMS for the full HL-LHC period. Therefore, the replacement of HCAL Barrel scintillators and fibers will not be necessary. The Phase-1 front-end electronics with Silicon Photomultipliers (SiPMs) will continue to be used for the HL-LHC period. However, the current HCAL Barrel back-end electronics, based on the μTCA standard, will not be able to sustain the 750 kHz Level-1 trigger rate planned for Phase-2, new back-end electronics based on the design developed for the ECAL Barrel will be produced and installed.
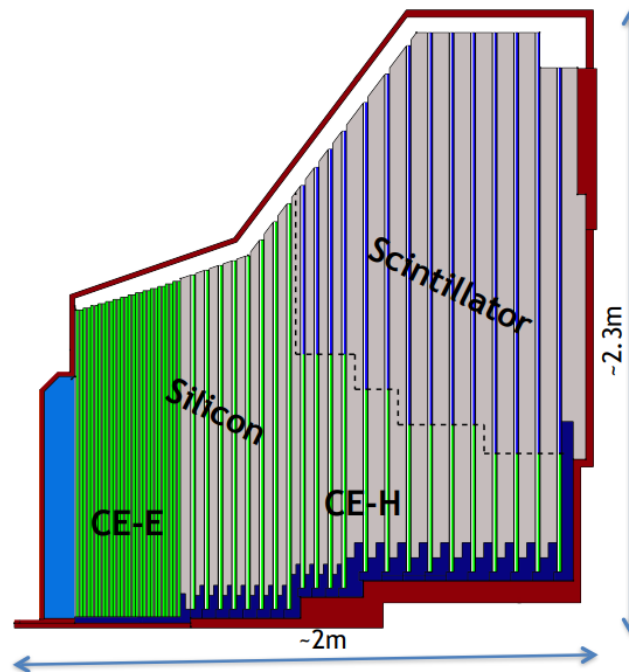
Figure 1.14: Overview of the CMS calorimeter endcap upgrade design.

1.2.4   The High Granularity Calorimeter

The CMS High Granularity Calorimeter (HGCAL) is a high-resolution calorimeter that is being developed for the Phase-2 upgrade of the CMS experiment at the LHC. The primary goal of the HGCAL is to replace the current ECAL and HCAL endcaps, which use degraded $PbWO_4$ crystals, due to decreasing crystal performance and increasing ambiguity in the association of energy depositions to particles, [28].

The HGCAL is designed to be radiation tolerant, particularly in regions with harsh radiation levels, and to have a more granular measurement of energy depositions to treat pile-up in the offline event reconstruction. Furthermore, the additional recording of the time of each energy deposition with $\mathcal{O}(50\ \mathrm{ps})$ precision is helpful in the rejection of pile-up. The HGCAL design is aimed at offering robustness and good performance through the full HL-LHC operational lifetime.

The HGCAL is designed with an electromagnetic (CE-E) and hadronic section (CE-H), both of which have excellent transverse and longitudinal segmentation for 3D measurement of shower topologies. An overview of the CMS calorimeter endcap design is presented in Figure 1.14. The electromagnetic compartment, CE-E, will be made of 28 sensitive layers interspersed with Cu, CuW, and Pb absorber plates, equivalent to a total depth of 25 radiation lengths (X_0) or 1.3 nuclear interaction lengths (λn). The hadronic compartment, CE-H, will comprise 22 sensitive layers with steel as passive material in between, adding another 8.5 (λn) to the total depth of HGCAL. This section is designed to measure the hadronic shower maximum.
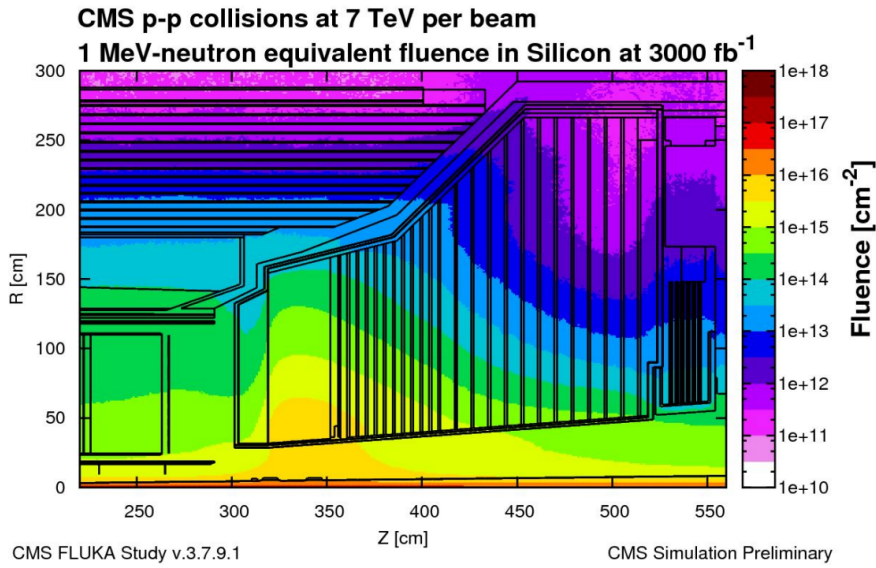
Figure 1.15: Integrated particle fluence in 1 MeV neutron equivalent per cm^2, accumulated in HGCAL after an integrated luminosity of 3000 fb^{-1}.

The simulation, presented in Figure 1.15, indicates that the highest fluence is around 10^{16} n$_{eq}$/cm^2 and the highest dose around 2 MGy. Research has shown that silicon sensors can tolerate these levels, and even fluences up to $1.5 \cdot 10^{16}$ n$_{eq}$/cm^2 (50% higher than expected for an integrated luminosity of 3000 fb^{-1}) without losing adequate charge collection. Therefore, silicon was chosen as the active material throughout the CE-E.

The sensors are divided into three different active thicknesses, depending on their radius and radiation doses. Figure 1.16 depicts a sketch of the silicon module and its integration in the CE-E and CE-H. Each sensor has a pad of approximately 0.5 cm^2 or 1.0 cm^2, depending on its thickness. This is chosen to ensure a sufficient signal-to-noise ratio for a Minimum Ionizing Particle (MIP) measurement. This also allows for proper calibration of the system, and at the same time, the range of transverse size is well suited to eliminate pileup energy along the longitudinal development of the shower.

The total area of silicon in the HGCAL is more than 600 m^2. To cover this area cost-effectively, a hexagonal geometry for the silicon sensors was chosen and the baseline of the sensor size has been adjusted from 6" design to 8" (Fig. 1.17). Each of the approximately six million diodes will be read out individually. In total, 30 000 silicon-based modules will be made.

In regions with relatively low levels of radiation in the hadronic compartment, square scintillating tiles with SiPM readout will be used as sensitive material. Their size will start at 4 cm^2 and will increase with increasing detector radius up to 30 cm^2. The total number of associated readout channels is $4 \cdot 10^5$, which is more than one order of magnitude less than the silicon-based channels.
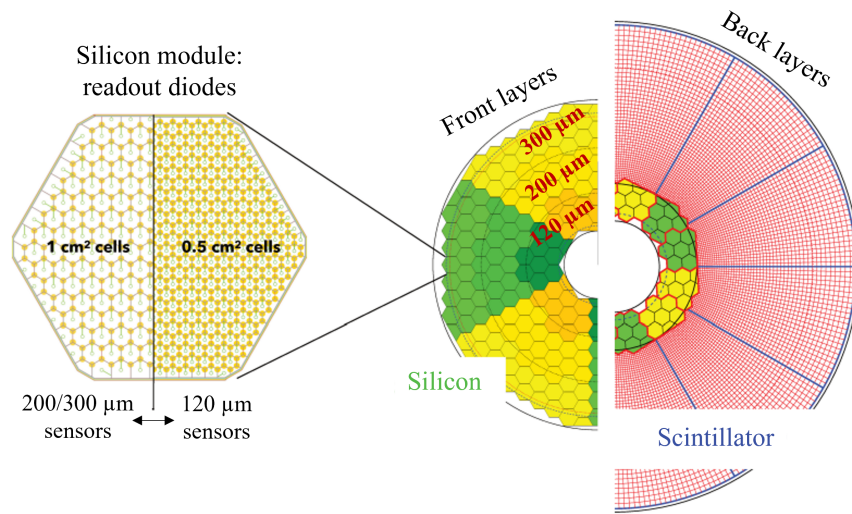
Figure 1.16: Left: Subdivision into readout diodes of a silicon module. The left part of this sketch shows the 1.0 cm^2 cells used for 200 and 300 μm sensors, while the right part shows the 0.5 cm^2 cells used in 120 μm sensors. Right: The left part shows the arrangement of the silicon modules in the CE-E and in the front part of the CE-H, while the right part shows the mixed structure of silicon- and scintillator-based modules used in the back part of the CE-H.
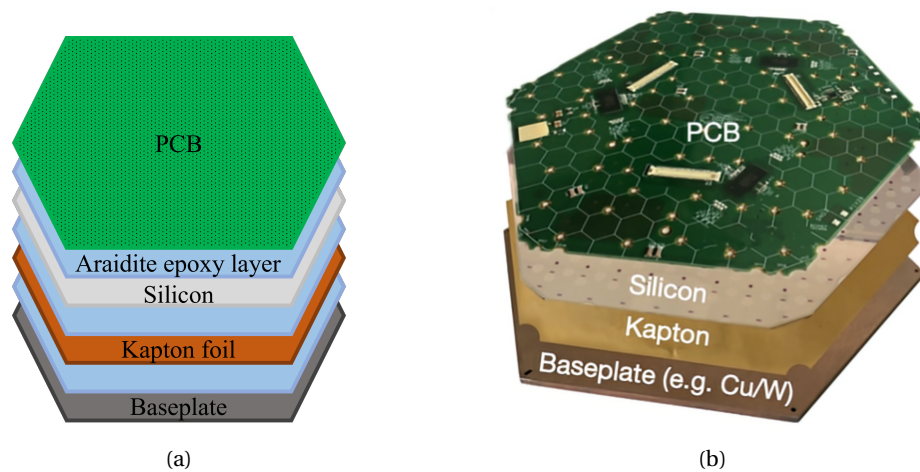
Figure 1.17: (a) Schematic view of the stacked layers of a CE-E silicon module. (b) 8" prototype module.

The fine granularity of the HGCAL will also allow precise timing measurements, which will further help mitigate the pileup effects. This will be possible by implementing an entirely new reconstruction software in the framework of the CMS particle flow reconstruction.
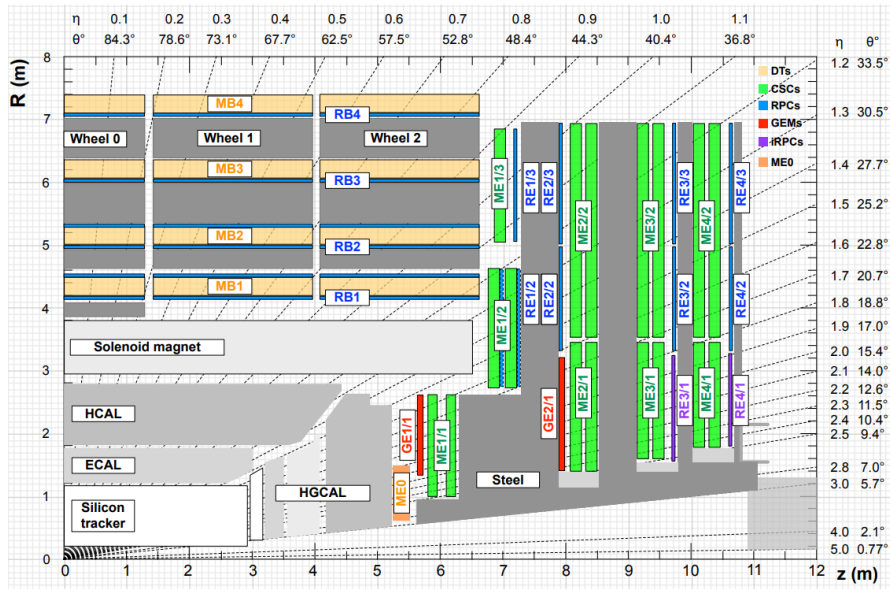
Figure 1.18: An R-z cross-section of a quadrant of the CMS detector, including the Phase-2 upgrades (RE3/1, RE4/1, GE1/1, GE2/1, ME0). The acronym iRPCs in the legend refers to the newly improved RPC chambers RE3/1 and RE4/1. The locations of the various muon stations are shown in color (MB = DT = Drift Tubes, ME = CSC = Cathode Strip Chambers, RB and RE = RPC = Resistive Plate Chambers, GE and ME0 = GEM = Gas Electron Multiplier). M denotes Muon, B stands for Barrel and E for Endcap.

1.2.5   Phase-2 Upgrade of the Muon Chambers

The muon chambers are used to measure the trajectory of muons, which are heavy particles that are similar to electrons but much more massive, [29]. Muons pass through all the detector layers without interacting with them, thus muon chambers are placed at the very end of the detector, outside of the calorimeters.

The muon system of the CMS detector will not undergo a major upgrade during Phase-2 of the HL-LHC. The muon system in the CMS detector comprises several different types of detectors, including Drift Tubes (DT) and Resistive Plate Chambers (RPC) in the barrel, and Cathode Strip Chambers (CSC) and RPCs in the endcaps. These systems are expected to be able to tolerate the increased radiation levels during Phase-2 without significant degradation, and as a result, there are no plans to replace them. However, measurements are ongoing to confirm their radiation tolerance margins. The only exception is the readout electronics of the DTs, which will be replaced due to radiation damage and this change will also remove the current trigger rate limitation of the system at 300 kHz. Additionally, some of the CSC chambers readout electronics will also be upgraded due to new trigger specifications.

Additionally, to address the issue of lack of redundant coverage in some regions, new detector technologies will be used in this region to improve efficiency for the muon trigger. To maintain good efficiency for the muon trigger in these regions, four stations are being complemented
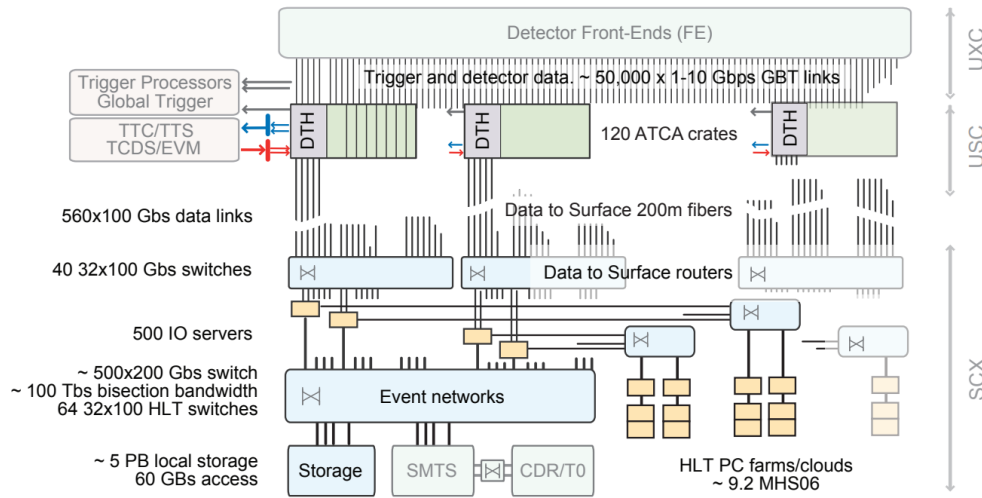
Figure 1.19: Principle architecture of the Phase-2 CMS DAQ.

with additional chambers that make use of new detector technologies with higher rate capability. The first two stations (named GE1/1 and GE2/1) will use Gas Electron Multiplier (GEM) chambers for their high granularity and good position resolution, while the last two stations (named RE3/1 and RE4/1) will use low-resistivity RPCs with lower granularity but good timing resolution (Figure 1.18). An additional GEM station will be installed in the space that becomes free behind the new endcap calorimeters, allowing for muon tagging with a matching track in the tracker extension.

Phase-2 upgrade of the muon chambers will also include new tracking algorithms and software tools to improve the reconstruction and identification of muon tracks. These algorithms and tools will make use of the increased granularity provided by the new CSCs to improve the accuracy of the muon momentum measurements.

1.2.6   Trigger and Data Acquisition System

The Trigger and Data Acquisition (DAQ) System of the CMS detector at the LHC is responsible for collecting and processing the data produced by the detector and selecting the most interesting events for further analysis, [30]. The trigger and data acquisition system play a critical role in the operation of the CMS detector, as it must handle a large volume of data produced in the LHC collisions and select the events that are most likely to be of scientific interest.

The proposed new hardware trigger scheme includes a feature that uses track information, which is mandatory to maintain the present physics acceptance of the system. Without this feature, the data transfer rate needed would be 4 MHz at 200 pileups. This data transfer rate is beyond the capabilities of foreseeable technologies, given the constraints on the space available for data transfer links. Additionally, this would also imply a significant increase in computing power and DAQ bandwidth for the online event selection process.

To allow sufficient time for the hardware track reconstruction, matching of tracks to muons, and gathering calorimeter information, the latency of the trigger must be increased to 12.5 µs. This change requires an upgrade of the readout electronics in the ECAL Barrel, as well as a proper design of the front-end electronics to overcome the latency limitations and eliminate hardware trigger rate restrictions.

Based on the expected performance of the trigger with track information, a trigger acceptance rate of 750 kHz is needed for beam conditions yielding 200 pileups to maintain similar physics acceptance as in Phase I. This specification can be easily accommodated in the design of all new detector readout electronics. However, an additional upgrade in the inner rings of the CSC stations 2 to 4 will be necessary to overcome data losses that will appear at trigger rates beyond 500 kHz.

The DAQ system is also being upgraded to implement the increase of bandwidth and computing power required to accommodate the larger event size and trigger rate, as well as the greater complexity of the reconstruction at high pileup. Figure 1.19 shows the principle schematics of the baseline Phase-2 CMS DAQ. Compared to Phase I, the bandwidth and computing power requirements are increased by factors of about 10 (15) and 15 (30) respectively, for operation at pileups of 140 (200). These increases are well within the projected network technology capabilities expected at the time of Phase-2. Assuming an online event selection of 1/100 event at the high-level trigger (HLT), as is the case in the current system, the subsequent rate of recorded data will increase to 5 (7.5) kHz from LHC Run I levels of about 1 kHz at pileup of 140 (200) respectively.

1.3   Need for Dew Point Measurements in High-Energy Physics Applications

The high radiation dose resulting from the LHC operation at full luminosity and the CMS Phase-2 upgrade may pose a loss of performance of the sensors and the following electronics due to the following reasons:

- **Increased leakage currents:** Radiation-induced defects can significantly impact the performance of a detector. These defects increase the reverse-bias leakage current, leading to the emission of both electrons and holes. Large leakage currents I_{leak} in the sensor are generally undesired because they result in the reduction of the effective bias voltages and worsen the sensor noise behavior. It is proportional to the acquired equivalent fluence Φ_{eq} and the depleted volume V as:

$$I_{leak} = \alpha \cdot \Phi_{eq} \cdot V \tag{1.8}$$

  where α is a current-related damage factor that represents the contributions of constant

and decaying defects in time after irradiation.

The most important impact of leakage current characteristics on detector operation conditions results from the strong temperature dependence of the current. The current at a temperature T is obtained from a reference measurement at a room temperature T_{ref} as:

$$I_{leak}(T) = I_{leak}(T_{ref}) \cdot \left(\frac{T}{T_{ref}} \right)^2 \exp\left(-\frac{E_G}{2 \cdot k_B} \cdot \left(\frac{1}{T} - \frac{1}{T_{ref}} \right) \right) \tag{1.9}$$

where E_G is the band gap. It can be concluded that it is very important to cool down the sensor during operation as in that case the leakage current is strongly suppressed and thus also the noise is reduced.

- **High power dissipation due to the increased granularity:** The downside of having such a finely segmented detector is the increased need for readout electronics and power supply components, causing the total power dissipation in hundreds of kW. To remove heat from electronics and sensors, a large cooling capacity is required.

Due to the aforementioned constraints, powerful cooling systems are indispensable detector parts used to distribute coolant (even at subzero temperatures) throughout the detector structure. The CMS sub-detectors, such as the Tracker and the HGCAL, are going to operate at a temperature of -35 °C, while the operating temperature of the ECAL sub-detector will be reduced to 9 °C instead of the present 18 °C.

Consequently, the dew point temperature must be carefully monitored and controlled in CMS. This is due to several factors. The presence of moisture can cause corrosion and other types of damage to detector components. Maintaining a low dew point minimizes the likelihood of moisture accumulating on these components, thereby reducing the risk of damage. Moisture can also impact the performance of certain detector components, such as PMTs. PMTs are sensitive to humidity and may produce false signals if the humidity level is too high. In some cases, moisture can interfere with the measurement process itself. For example, in a calorimeter, a device used to measure the energy of particles, the presence of moisture can affect the way the detector absorbs and measures the energy of the particles. Therefore, by carefully monitoring and controlling humidity and temperature, researchers can help ensure that their experimental apparatus is functioning correctly and that the data they collect is accurate and reliable.

In the present CMS detector, the Tracker sub-detector is the only one functioning at the subzero temperature at the moment given that it is already built out of silicon. The dew point measurements are done far from the detector, at about 100 meters away, using a sniffer system. The system extracts gas samples from different positions inside the detector and transfers them to a gas analysis rack in an underground service cavern. Dew point analysis is performed

(a) Wet Mirror dew point sensor   (b) Vaisala DMT242 dewpoint transmitter

Figure 1.20: The most reliable dew point sensors present in the market.

using industrial Vaisala DMT242 transmitters and Wet Mirror dew point sensors, known for their reliable performance in dry environments (Figure 1.20). The number of sniffer points to be added in the CMS detector is clearly limited due to space limitation, complexity of piping to reach the service cavern and economic reasons. Consequently, distributed sensing with the "sniffing" solution, which is able to provide only time-averaged dew point measurements, must be complemented by more detailed dew point temperature mapping throughout the detector volume.

1.3.1   Dew Point Sensor Requirements

Any dew point sensor to be introduced in the CMS detector volume should ideally comply with the following requirements:

(a) Be radiation tolerant. The sensor performance can degrade after radiation but in a relatively slow and well-modeled (possible to "correct") way.

(b) Be insensitive to a magnetic field (up to 4 T), or have a well-established parameterization of the effect of the magnetic field on its performance.

(c) Have small dimensions (mm size or surface mount device—SMD) in order to be easily integrated into the detector environment.

(d) Provide reading across several tens of meters long distances, as the powering and readout stations are several tens of meters away from the measurement point.

(e) Any drift of the sensor operation parameters should be known in advance as no recalibration can happen in situ.

(f) Be capable of integration in detector control systems, based on the industrial standard hardware, and be capable of providing reliable data quasi-online since it is used as a

safety check of the detector environment.

For what follows, we distinguish between two categories of dew point sensors: (1) direct dew point measurements and (2) those combining relative humidity and temperature measurements leading to a dew point temperature calculation. Vaisala DMT242 and Wet Mirror dew point sensors belong to the first category of instruments. However, it is not possible to install these sensors in the very limited (mm) space that Si-detectors have available for services although there are efforts to miniaturize them.

Modules of the second category calculate the dew point temperature using appropriate approximation-based measurements of relative humidity and temperature. In these modules, both temperature and relative humidity sensors can fulfill dimensional requirements. However, it is currently only possible to find standard industrial temperature sensors, and not humidity sensors, that are radiation tolerant at the radiation levels of interest. Therefore, our research target is the selection of the humidity sensor candidates and the verification of their performance under radiation.

1.3.2   Temperature Sensors in High-Energy Physics Applications

Temperature measurement is a crucial aspect in high-energy physics detectors, where the temperature of various components and systems must be monitored. Several types of temperature sensors are commonly employed in these applications, including thermocouples, resistance temperature detectors (RTDs), and thermistors. Each of these sensors has distinct advantages and disadvantages, and the selection of the most appropriate sensor for a given application requires a thorough consideration of these factors.

Thermistors are temperature-sensitive resistors that exhibit a significant change in resistance with a small change in temperature. They are commonly used in applications that require a fast response time and high accuracy in a narrow temperature range. Thermistors are relatively inexpensive, and they are capable of measuring a wide range of temperatures, but they can be sensitive to mechanical stress. In 2005, several negative temperature coefficient (NTC) thermistors from EPCOS, Siemens, and BTC, together with the positive temperature coefficient (PTC) temperature sensor produced by Infineon were exposed to the 64 MeV proton beam for 8 hours [31]. The equivalent cumulative dose of about 200 kGy ($2 \cdot 10^{14}$ n_{eq}/cm^2) was reached for the characterization of the sensors during the 8-hour irradiation process. NTC thermistors showed no shift in parameters during the beam period, while PTC sensors showed abnormal behavior due to the radiation-induced effects. A comparison of the readout of EPCOS NTC and Infineon PTC temperature sensors during the irradiation period is shown in Fig. 1.21.

Thermocouples are temperature sensors consisting of two dissimilar metals joined together at one end. They work by measuring the voltage difference between the two metals, which is proportional to the temperature difference between the two ends. They are widely used in industrial applications due to their robustness, wide temperature range, and fast response
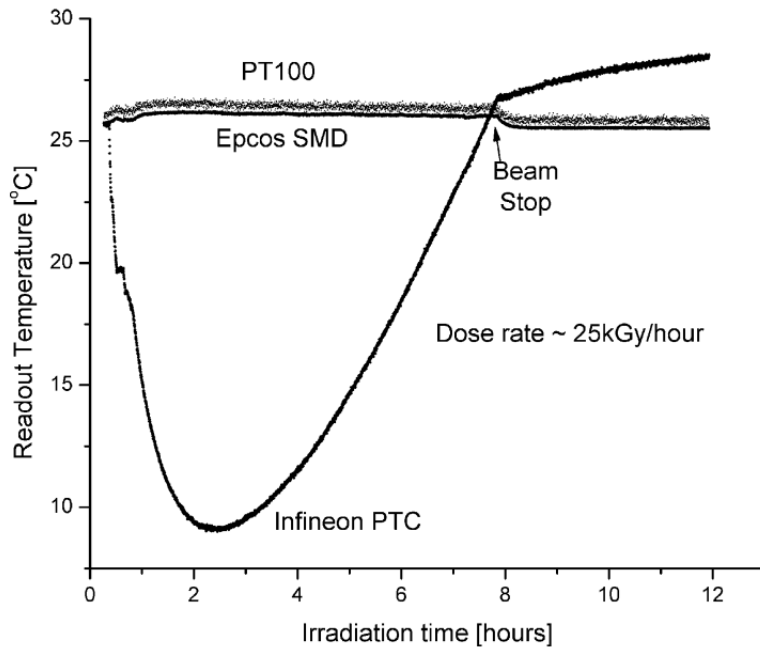
Figure 1.21: Comparison of the readout of NTC and PTC temperature sensors during the 8 h irradiation period. One PT100 temperature sensor (radiation tolerance verified) was placed nearby for the control of beam-induced local heat-up of the test board and material, [31].

time. However, thermocouples require a reference junction, which can limit their accuracy in extreme temperatures, and they can also be sensitive to electromagnetic interference.

RTDs are temperature sensors consisting of a resistor made of a material with a high-temperature coefficient of resistance. They are commonly made of platinum (Pt), nickel-chromium (NiCr), or copper (Cu) and have a linear resistance-temperature relationship. RTDs are highly accurate, with very stable and repeatable output, making them ideal for applications that require precise temperature measurements. Platinum RTDs have been demonstrated to be capable of withstanding the challenging conditions in the CMS detector environment, including exposure to high levels of irradiation and magnetic field up to 4 T. Pt RTDs have been used in the Tracker since its inception, and their usage has been significantly expanded in the design of the LS3 CMS detector upgrade. The main challenge with utilizing these sensors is the need for a cost-effective, multi-platform, and easy-to-deploy monitoring system.

1.3.3   Humidity Sensors in High-Energy Physics Applications

The demand for compact and low-cost sensors for humidity monitoring has driven the development of miniaturized electronic sensors, with capacitive-based sensors being the most widely used, accounting for nearly 75% of the commercial market.

In the CMS experiment, several miniaturized commercial sensors have been evaluated and
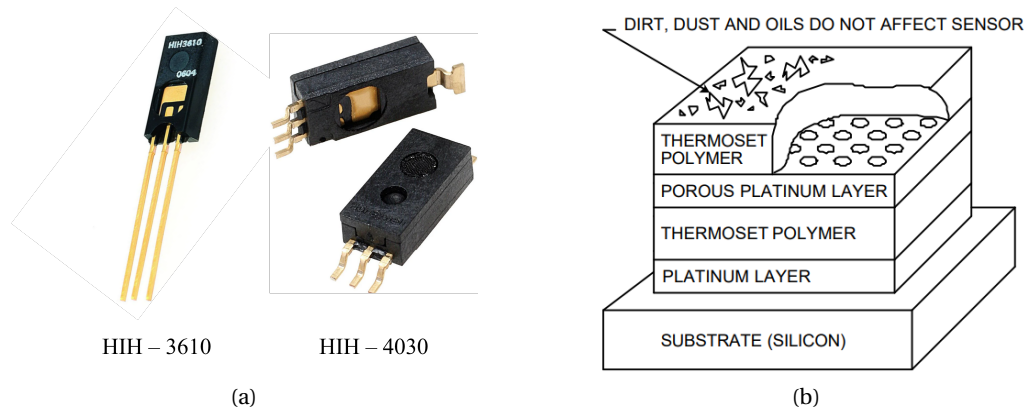
Figure 1.22: (a) Photos of the HIH - 3610 and HIH - 4030 humidity sensors produced by Honeywell and (b) their scheme of the construction elements.

used, but none have fully met the requirements. For instance, the Honeywell HIH-3610, [32], and HIH-4030, [33], series (Fig. 1.22) have been considered due to their small size, low cost, and fast response, [34], [35]. These sensors are based on polymer capacitive sensing elements and require at least three wires and an adequate voltage supply for each measurement point, [36]. Additionally, a separate measurement of the local temperature must be taken as the output of these hygrometers is influenced by temperature (typically requiring four more wires for each standard thermometer). These devices are also vulnerable to damage from radiation as they are not designed for radiation hardness. Furthermore, detailed analysis at CERN showed that these sensors have an estimated absolute error in relative humidity measurement of at least ± 2 %rh even after individual calibration. This error increases to $\pm 3 - 5$ %rh when operating at temperatures below $0°$C.

During the first long shutdown of the LHC machine, the HIH-4030 sensors were integrated into the Tracker Bulkhead area of the CMS experiment. These sensors were read out using Arduino microcontrollers, but they were not expected to survive once an operation with a beam starts. Nonetheless, they were integrated into the detector online monitoring to provide cross-checks for the readings of other hygrometers and gain a better understanding of the humidity situation in the experiment during the LS1 phase.

Another capacitive-polymer technology-based sensor is the Precon HS-2000 (Fig. 1.23 (a)), [37], which integrates the relative humidity and temperature measurements on the same small chip, providing a direct reading of the dew point and reducing the number of wires needed for each measurement point to four (Fig. 1.23 (b)). However, studies at CERN in 2012 showed that the Precon HS-2000 is not resistant to radiation and is sensitive to the magnetic field.

Finally, the HMX2000 sensor was selected for relative humidity monitoring in CMS. Front and backside pictures of a sensor are presented in Fig. 1.24. The HMX2000 is a piezoresistive device that consists of four cantilever silicon beams connected to form a Wheatstone Bridge. The

(Front View)

Pin # 1 2 3 4

Pin 1	Temperature Out (0 to Vsupply)
Pin 2	Power (2 to 5.5 volt)
Pin 3	RH Out (0 to Vsupply)
Pin 4	Ground

(a)   (b)
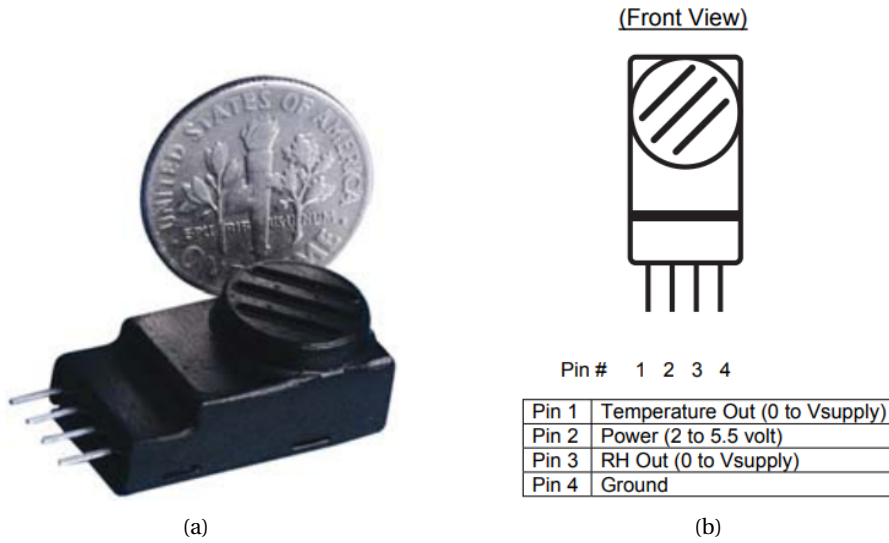
Figure 1.23: (a) A photo of Precon sensor HS2000 and its (b) pin diagram (front view).
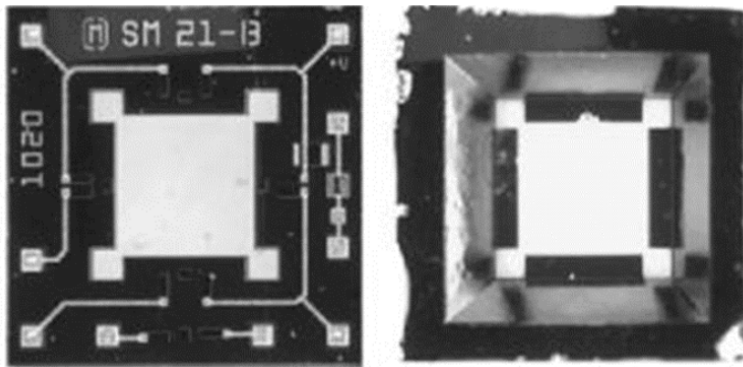
Figure 1.24: Photographs of the front and backside of a HMX2000 humidity sensor.

beams are coated with a polymeric material and the electrical resistance of the piezoresistors changes in response to humidity-induced changes in the size of the polymeric resistive elements. Studies at CERN in 2005 showed that these sensors provide a non-linear response with long-term drifting and a low response (0-100 %rh in 100 mV), requiring complex amplification and power to be operated and read-out over a long distance. The HMX2000 has good radiation tolerance characteristics and is insensitive to strong magnetic fields. For these reasons, 16 HMX2000 sensors were integrated in 2012 in the Tracker Bulkhead area of CMS, coupled with miniaturized analog Pt100 temperature sensors, requiring 4+4 wires to provide a dew point temperature reading for each measurement point. However, the proper operation of these hygrometers and their calibration and readings have never been documented over the years.

Additionally, the R&D research at CERN explored the use of fiber optic humidity sensors. The work of Makovec et. al. focused on the development of a radiation-tolerant optical
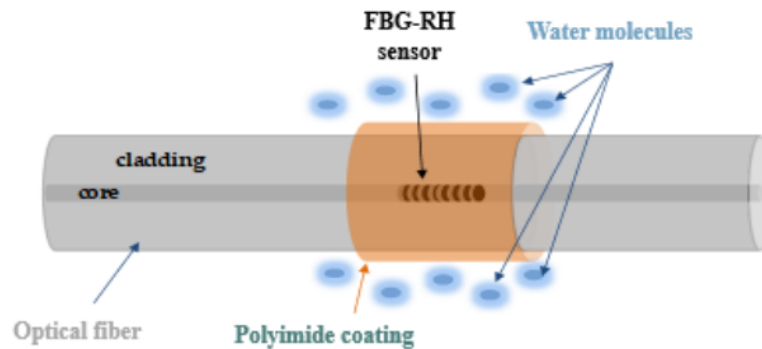
Figure 1.25: Schematic of the proposed radiation-tolerant optical hygrometer based on FBG

hygrometer based on fiber Bragg gratings (FBGs) and coated with a polyimide polymer overlay (as illustrated in Fig. 1.25), [38]. The sensors were characterized across a temperature range of -20 °C to 20 °C and, furthermore, exposed to the gamma beam. The results indicated that their performance was impacted by exposure to strong gamma-ionizing radiation, with a shift in the natural wavelength peak of each sensor being observed as a result.

In addition to their work on FBG-based humidity sensors, Makovec et. al. also investigated the use of long-period gratings (LPGs) for humidity sensing, [39]. Their LPG sensor was coated with a TiO_2 layer and subjected to the same radiation dose used for the FBG hygrometer. The sensitivity of the LPG sensors was found to be non-linear, making calibration more challenging. Despite their radiation tolerance, these sensors are still susceptible to mechanical stress and temperature changes, which can affect the lattice distance of the fiber. A further limitation of these sensors is that they are not easily integrated into standard industrial processes or high-energy physics experiments.

1.4   Summary

Using Si-based sensors in HEP detectors is becoming more and more common and technological solutions assuring the smooth functioning and long survival of the sensors are important. Cooling at subzero temperatures and monitoring the dew point temperature is challenging due to space, radiation and magnetic field issues. Cooling is important for two main reasons:

(i) **to remove the heat** produced by millions of densely packed bias and readout channels that dissipate hundreds of kW of power in a closed volume,

(ii) **to limit the increase of leakage currents in silicon**. Leakage currents increase linearly with the received radiation dose and decrease exponentially as a function of the temperature drop.

Cooling the detector structures at below-zero temperatures should be carefully done to avoid vapour condensation. As dew point temperature measurement is the measure of the detector

"dryness", it is an essential parameter to monitor. The dew point temperature of a volume can be calculated knowing the measurements of relative humidity and temperature. Temperature sensors that can survive inside the detector environment are common (RTDs) but not humidity sensors that can be radiation tolerant and provide the required resolution. Thus, the objectives of this Ph.D. dissertation are the selection and characterization of the radiation-tolerant humidity sensor followed by the development of the radiation-tolerant dew point monitoring system for high-energy physics applications.

2 Humidity Sensors: Methods and Materials [I]

Nothing is softer or more flexible than water,
yet nothing can resist it.
— Lao Tzu

Humidity measurement is a crucial aspect in a variety of fields, ranging from meteorology and agriculture to domestic appliances, biomedical applications, and the automotive industry [41]–[43]. It is also required as part of various industrial processes, e.g., for high-quality chemical production in the food/beverage industry, in the mining sector, in the cement industry, and in industrial chemistry [44]–[46]. It is used as well in pharmaceutical applications, e.g., during the manufacturing of tablets and capsules to avoid additional humidity, which would damage the quality of the product [47]. Furthermore, the necessity for humidity sensors in high-energy physics applications is discussed in the preceding chapter, making it one of the most challenging domains for future generations of humidity sensors.

As a result of industrialization, the demand for accurate and reliable humidity sensors has increased, making it one of the most important fields in modern sensor technology. However, measuring humidity is not "simple", as the sensors must satisfy a number of requirements, including short response time, high sensitivity, negligible hysteresis, and a large operating range for both humidity and temperature, [48], [49]. Furthermore, the materials used in humidity sensors must exhibit good long-term properties, making the search for stable humidity-sensitive materials ongoing [50]–[52].

This chapter will delve deeper into the topic by examining relevant definitions in relation

---

[I]Part of this chapter has been published in [40].
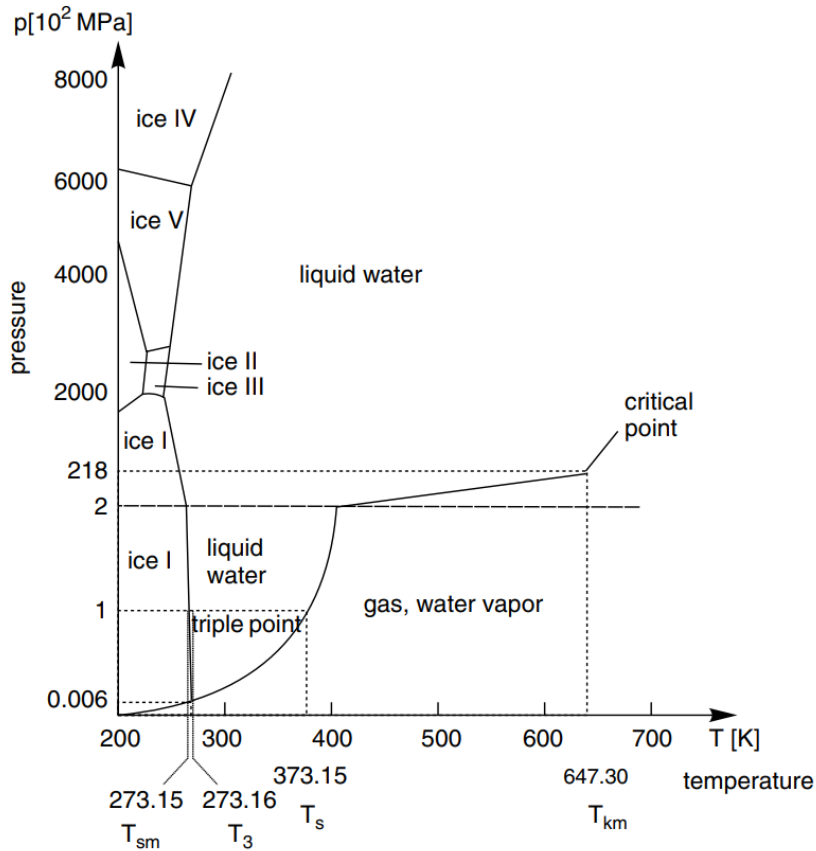
Figure 2.1: Phase diagram of water [53]. T_3 is the triple point where all three phases coexist in equilibrium. T_{sm} and T_s are melting and boiling temperatures of water, respectively. The critical point is determined by the critical temperature T_{km} and the critical pressure of $218 \cdot 10^2$ MPa.

to humidity measurement, exploring the most advantageous transduction principles, and comparing the properties of commercial humidity sensors. An overview of these sensors is necessary to fully understand the possibilities and limitations of presently available humidity sensors in the market and to make informed decisions about the selection of the potential candidate for use in the HEP environment.

2.1 Concept of Humidity

Water exists in three distinct phases - liquid, gas (vapor), and solid (ice) - and its phase is determined by the temperature and pressure of its environment (Fig. 2.1). In the study of water in the atmosphere, two important terms are used: humidity and moisture. Humidity refers to the amount of water vapor present in gases, while moisture refers to the water content in liquids and solids due to adsorption or absorption.

The humidity may be expressed as specific humidity[II], absolute humidity, relative humidity, or as mixing ratio[III]. In a system of moist air, the ratio of the mass of water vapor to the volume of the system is called the absolute humidity AH:

$$AH = \frac{n \cdot M_w}{V} \tag{2.1}$$

where n is the number of water molecules with molecular mass M_w, and V is the volume. The AH is normally expressed in g/m^3.

The relative humidity is defined as the ratio of the actual water vapor pressure[IV], p_w, at a given temperature to the saturation water vapor pressure, p_{sat}, at the same temperature and it is expressed in percentages:

$$RH = \frac{p_w}{p_{sat}} \cdot 100 \tag{2.2}$$

The saturation pressure p_{sat} defines the maximum amount of water vapor that can be present in the air at a given temperature before condensation occurs. According to the International Association for the Properties of Water and Steam (IAPWS), for the range of temperatures from 273 K to 673 K, the saturation vapor pressure can be calculated as follows [54]:

$$p_{sat} = p^* \cdot \beta^4 \tag{2.3}$$

where p* = 1 MPa and

$$\beta = \frac{2C}{-B - \sqrt{(B^2 - 4AC)}} \tag{2.4}$$

with

[II]The specific humidity is defined as the mass of water vapor per unit mass of humid air.

[III]The mixing ratio is defined as the water vapor per unit mass of dry air.

[IV]The actual water vapor pressure can be calculated as a product of absolute humidity, given temperature and a specific gas constant (= 461.5 J/(kg · K))

$$A = (\theta + n_1) \cdot \theta + n_2$$

$$B = (n_3 \cdot \theta + n_4) \cdot \theta + n_5$$

$$C = (n_6 \cdot \theta + n_7) \cdot \theta + n_8$$

$$\theta = \frac{T_s}{T^*} + \frac{n_9}{(T_s/T^*) - n_{10}} \tag{2.5}$$

where T_s is the saturation temperature and $T^* = 1$ K. Values of the coefficients n_1 to n_{10} are listed in Table 2.1. The saturation temperature T_s is also known as dew (frost) point temperature, another commonly used term in the field of hygrometry. The dew (frost) point temperature is defined as the gas temperature above the surface of the water (ice) at which the water vapor pressure and the saturation water vapor pressure are equal. Equations (2.3)-(2.5) can be written as an implicit quadratic equation describing the saturation line. This equation is a function of saturation pressure and saturation temperature, and it provides exact solutions using p_{sat} and T_s as variables.

Table 2.1: Coefficients used in the formula to compute the saturation vapour pressure over water [54]

i	n_i	i	n_i
1	$0.11670521452767 \cdot 10^4$	6	$0.14915108613530 \cdot 10^2$
2	$-0.72421316703206 \cdot 10^6$	7	$-0.48232657361591 \cdot 10^4$
3	$-0.17073846940092 \cdot 10^2$	8	$0.40511340542057 \cdot 10^6$
4	$0.12020824702470 \cdot 10^5$	9	-0.23855557567849
5	$-0.32325550322333 \cdot 10^7$	10	$0.65017534844798 \cdot 10^3$

According to the International Temperature Scale of 1990 (ITS-90) standard, in the range from 123 K to 273 K, the saturation pressure can be computed as follows [55], [56]:

$$ln(p_{sat}) = \sum_{i=0}^{5} k_i T^{i-1} + k_5 \cdot ln(T) \tag{2.6}$$

where the values of coefficients k_0 to k_5 are presented in Table 2.2[V].

From equation (2.2), the saturation pressure is a non-linear function of relative humidity, thus, it can be concluded that the dew (frost) point is, as well, a non-linear function of relative humidity at a constant temperature.

The dew (frost) point temperature can be computed by knowing the locally measured relative

---

[V]The values of coefficients are taken from [56]. Their derivation is not a topic of this dissertation and for more information refer to [57].

Table 2.2: Coefficients used to compute p_{sat} over ice according to ITS-90 standard [56]

i	k_i
0	$-5.8666426 \cdot 10^3$
1	$2.232870244 \cdot 10^1$
2	$1.39387003 \cdot 10^{-2}$
3	$-3.4262402 \cdot 10^{-5}$
4	$2.7040955 \cdot 10^{-8}$
5	$6.7063522 \cdot 10^{-1}$

humidity and ambient temperature in the following steps:

Step 1: Compute p_{sat} according to equations (2.3)-(2.5) (or equation (2.6)) for a measured ambient temperature.

Step 2: Compute p_w from equation (2.2) for a measured relative humidity, using the p_{sat} computed in step 1.

Step 3: Use p_w as p_{sat} in equations (2.3)-(2.5) (or equation (2.6)) and solve the equation for T_s using one of the iterative approaches (e.g. Newton-Rapson method). The T_s represents the dew (frost) point temperature.

2.1.1   Properties of Water

The properties of water in the gaseous phase differ from those in the liquid phase. In the liquid phase, water molecules form clusters rather than existing as individual H_2O molecules (Figure 2.2). The size of these clusters is temperature dependent, leading to the constant formation and breaking of hydrogen bonds between the molecules. The bound charges within the H_2O molecule contribute to both a large dipole moment ($\sim 6.1 \cdot 10^{-30}$ Cm) and a high relative permittivity ϵ_w, which is dependent on the cluster size and, thus, on the temperature. This dependence is estimated using the formula [58]:

$$\epsilon_w = 87.74 - 0.4 \cdot \left(\frac{T}{T^*}\right) + 9.398 \cdot 10^{-4} \cdot \left(\frac{T}{T^*}\right)^2 - 1.41 \cdot 10^{-6} \cdot \left(\frac{T}{T^*}\right)^3 \tag{2.7}$$

where $T^* = 1$ K. At positive temperatures, the dielectric constant of water decreases as the temperature increases. This can be explained by the increase in the mobility of the water molecules at higher temperatures, which reduces the polarizability of the water and thus the dielectric constant. Conversely, at negative temperatures, the dielectric constant of water increases as the mobility of the water molecules decreases.

Water molecules in the solid state are fixed into position, held together by hydrogen bonds

(a) Ice   (b) Water   (c) Steam
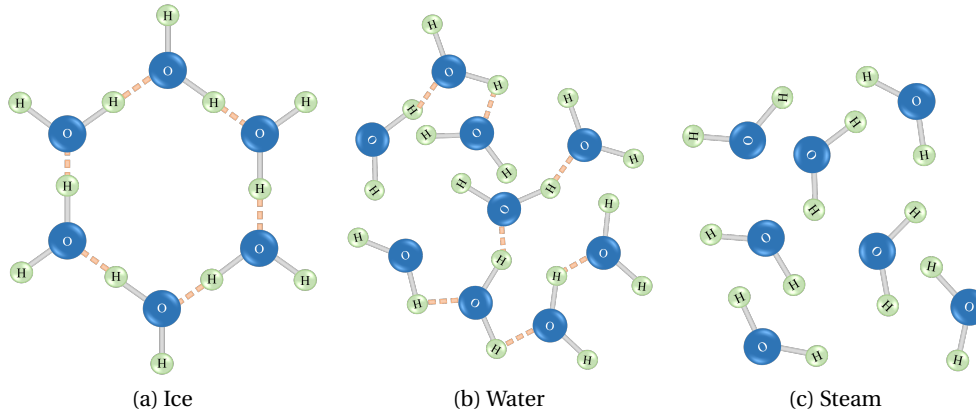
Figure 2.2: Hydrogen bonds are strongest at subzero temperatures when they hold six oxygen atoms in a tight hexagonal molecule of ice (a). In its liquid form oxygen atoms are loosely linked in chains (b), whereas at temperatures above 100 °C, they are separated in steam (c).

holding adjacent water molecules together. These bonds maintain a fixed distance between water molecules, resulting in a lattice structure. The high number of hydrogen bonds in this state causes the water molecules to be held farther apart than in their liquid form, which in turn makes solid ice less dense than liquid water.

Dielectric materials exhibit a loss factor due to the inability of bound charges to resonate at the frequency of the applied electric field. The dielectric properties of liquid water, as a function of frequency, can be described using the Debye relaxation theory [59]. The Debye theory allows the permittivity to be represented by the following formula:

$$\epsilon_w(\omega) = \epsilon_w(\infty) + \frac{\epsilon_w(0) - \epsilon_w(\infty)}{1 + j\omega\tau_r} = \epsilon'_w(\omega) - j\epsilon''_w(\omega) \tag{2.8}$$

where the real- and imaginary parts are respectively:

$$\epsilon'_w(\omega) = \epsilon_w(\infty) + \frac{\epsilon_w(0) - \epsilon_w(\infty)}{1 + (\omega\tau_r)^2} \tag{2.9}$$

$$\epsilon''_w(\omega) = \frac{(\epsilon_w(0) - \epsilon_w(\infty)) \cdot \omega\tau_r}{1 + (\omega\tau_r)^2} \tag{2.10}$$

where $\epsilon_w(\infty)$ is the high-frequency dielectric constant, $\epsilon_w(0)$ is the static dielectric constant, ω is the angular frequency of the electric field, and τ_r is the relaxation time of the water
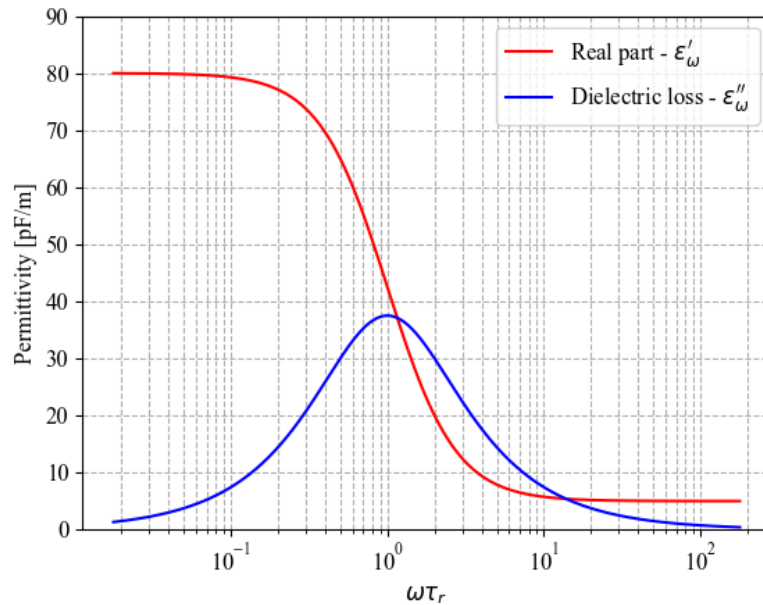
Figure 2.3: Real and imaginary parts of the permittivity of H_2O as a function of the normalized frequency, assuming Debye relaxation as described by eq. (2.8)-(2.10).

molecules.

For liquid water, the high-frequency limit is $\epsilon_w(\infty) \approx 5$ and the low-frequency limit is $\epsilon_w(0) \approx 80$. The dielectric relaxation time[VI], τ_r, has an estimated value of $17.8 \cdot 10^{-12}$ s, meaning that the dielectric properties of water are frequency-independent up to approximately 100 MHz. This implies that relaxation is only expected in the GHz range. Both the real and imaginary parts are plotted as a function of the normalized frequency, $\omega\tau_r$, in Fig. 2.3 and are related to each other by the Kramers-Kronig relations[VII].

The permittivity of adsorbed vapor in general exhibits a frequency dependence that differs from that of pure liquid water, as calculated above. This is due to two factors: first, adsorbed water vapor does not exist in an extended phase, unlike the unlimited clusters assumed in eq. (2.7), and second, the nature of the interaction between thin films in humidity sensors and adsorbed water results in permittivity that is dependent on mobility. This means that, for example, the first and second adsorbed layers can be treated as having different permittivity and relaxation mechanisms.

[VI]For spherical dipoles with radius a, the relaxation time is estimated with $\tau_r = 4\pi\eta a^3/kT$, with η the viscosity and k the Boltzmann constant.

[VII]Kramers-Kronig relations are $\chi'(\omega) = \frac{1}{\pi}\int_{-\infty}^{\infty}\frac{\chi''(\omega)}{x-\omega}dx$ and $\chi''(\omega) = -\frac{1}{\pi}\int_{-\infty}^{\infty}\frac{\chi'(\omega)}{x-\omega}dx$, with χ the susceptibility $\chi(\omega) = \epsilon(\omega) - 1$.
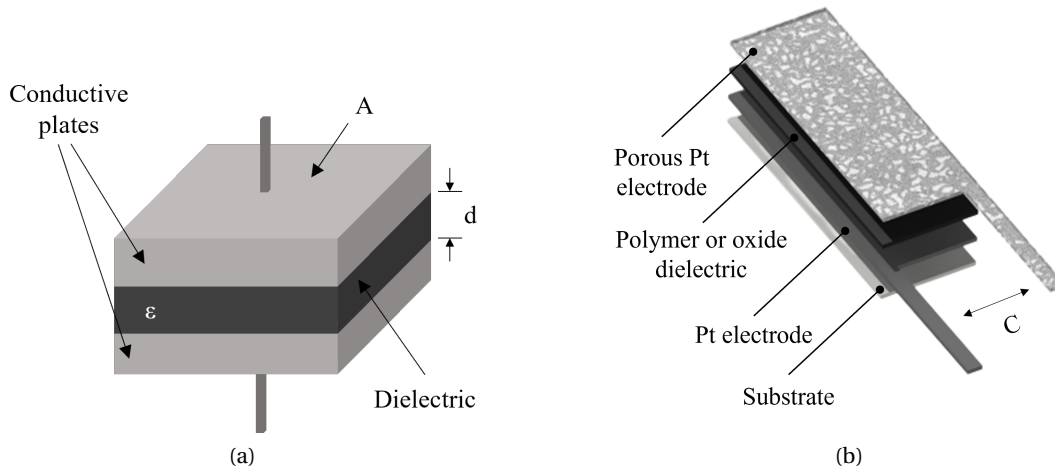
Figure 2.4: (a) Schematic representation of a capacitive humidity sensor, showing the area of the electrodes, A, and the thickness of the water-absorbing layer, d, between them. (b) Layers in capacitive humidity sensors.

2.2   Methods for Humidity Measurements

This section provides an overview of the fundamental principles of humidity sensing. The sensor in a hygrometer must be selective to water molecules and have internal properties that change with water concentration, allowing it to convert H_2O vapor pressure into an electrical signal. Capacitance and resistance-based sensors are commonly used types, where their capacitance/resistance values change when exposed to moisture. Furthermore, this section introduces alternative techniques, such as the piezoresistive method, fiber-optic approach, and thermal conductivity technique, which have been tested for use in HEP applications. Finally, the section discusses the optical method of measuring humidity using the Wet Mirror dew point sensor as an example. The latter is used as a reference sensor in the tests discussed in subsequent chapters.

2.2.1   Capacitive Humidity Sensors

Capacitive humidity sensors are typically composed of a water-absorbing (dielectric) material, deposited between two electrodes Fig. 2.4. The presence of moisture in the dielectric results in a gradual increase in its relative permittivity. This change in permittivity affects the capacitance of the sensor as follows:

$$C_s = \epsilon \frac{A}{d} \tag{2.11}$$
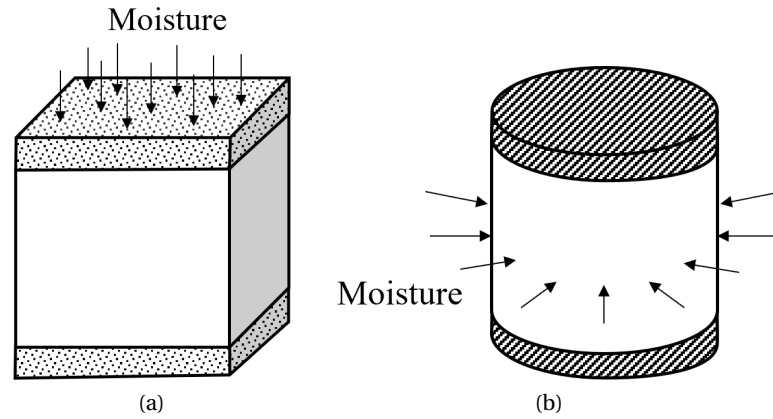
Figure 2.5: Schematic representation of (a) a traditional porous capacitive sensor and (b) a capacitive sensor with cylindrical electrode structure.

where C_s is sensor capacitance, ϵ is the dielectric constant of the water-absorbing material, A is area of electrodes and d is the thickness of the water-absorbing layer. Equation (2.11) illustrates that, besides the type of used hygroscopic material, the properties of capacitive humidity sensors are determined by the electrode configuration as well. Different electrode designs impact the rate at which vapor diffuses into the dielectric. For instance, a cylindrical electrode structure (shown in Fig. 2.5 b)) has been proposed to improve vapor diffusion time and increase the time-response of the device down to 1 second compared to the traditional porous electrode depicted in Fig. 2.5 a), [60]. In addition, there are more electrode geometries to choose from, with interdigitated electrodes being the most favorable for rapid responses (Fig. 2.6), [61]. However, a thin top electrode can result in a more uniform field distribution, and an intermediate solution is to provide the top electrode with small meshes 2.6 d).

The capacitance change of the sensor does not always have a strong correlation with permittivity change and it can be instead described as a nonlinear function as follows [62]:

$$\frac{C_s}{C_0} = \left(\frac{\epsilon_w}{\epsilon_d}\right)^n \tag{2.12}$$

where ϵ_w is the permittivity of the dielectric in a humid state, and ϵ_d is the permittivity of the dielectric in a dry state. The factor n is associated with the dielectric morphology.

Porous dielectrics are often used in humidity sensors to enhance device sensitivity by reducing the dielectric constant [63]. When exposed to humid air, the pores in the porous dielectric fill with moisture in a process called capillary condensation. This phenomenon occurs when the droplet radii are less than the Kelvin radius given as [64]:
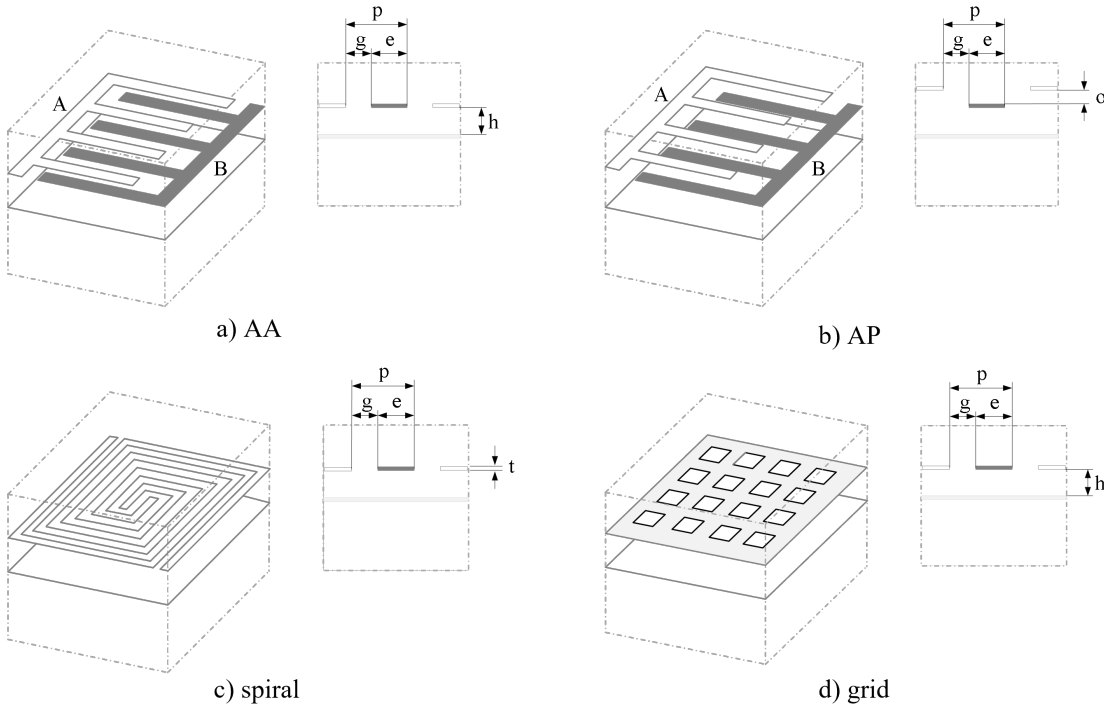
Figure 2.6: Electrode configurations for capacitive humidity sensors.

$$r_k = \frac{2\gamma M_\omega \cos\theta}{\rho RT \ln(p_\omega/p_{sat})} \tag{2.13}$$

where γ is the liquid/vapor surface tension, M_ω the molar mass of the liquid, θ the contact angle, ρ the density of the liquid, R the universal gas constant, and T the temperature.

As industrial fabrication of multi-performant materials becomes more accessible, several combinations of materials are used in order to achieve better relative humidity sensors. Ceramics are popular porous materials due to their mechanical strength and high-temperature resistance, but they are susceptible to contamination [65], [66]. Therefore, lead-free electro-ceramics sensors have been proposed to avoid this issue and improve response and recovery times [67]. Porous silicon is also used as a sensing layer for humidity sensors [68], [69] and can be paired with an integrated resistor to refresh the sensor performance [70], [71].

Polymer materials are another choice for the hygroscopic part of the sensors. Polymer materials offer a linear response to humidity and easy integration into the device but have limitations with high humidity levels or temperatures [42]. However, a mixture of polymer with TiO_2 microparticles has succeeded in measuring humidity in the range of 10 to 90 %rh [72]. Polyimides are a popular choice for hygroscopic material in humidity sensors due to their high sensitivity to humidity and thermal stability [73]–[75]. They are resistant to most chemical
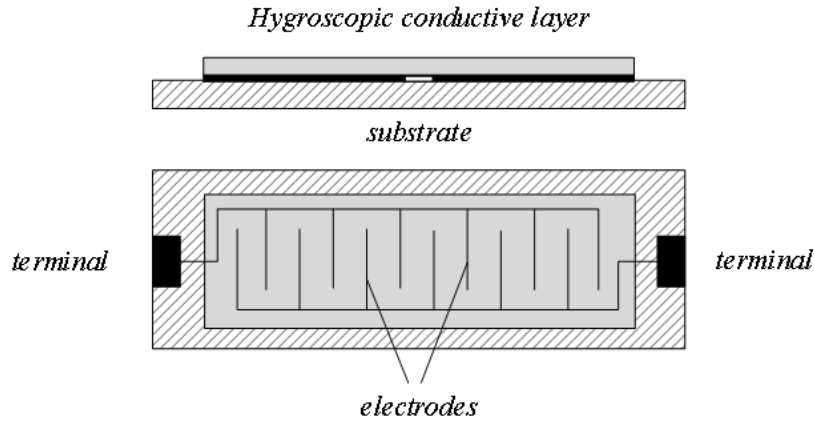
Figure 2.7: Schematic representation of a resistive humidity sensor showing the substrate, integrated electrodes, and hygroscopic conductive layer. The hygroscopic conductive layer plays a crucial role in changing the resistivity between the electrodes upon absorbing water droplets.

contaminants and fully compatible with silicon technology [76].

2.2.2 Resistive Humidity Sensors

Resistive humidity sensors are devices whose impedance changes in the presence of humid air. The change can be measured by resistance, voltage, or current. The typical design of a resistive humidity sensor consists of a substrate, integrated electrodes, and a hygroscopic conductive layer as depicted in Fig. 2.7. The substrate provides mechanical support and electrical insulation, while the integrated electrodes serve as conductive pathways. The hygroscopic conductive layer is the most important part of the sensor, as it changes the resistivity between the electrodes when water droplets are absorbed.

There are three main groups of materials used for resistive humidity sensors: ceramics, polymers, and electrolytes. Ceramic materials are suitable for high-temperature applications, while polymers and electrolytes are more sensitive to temperature changes. Ceramic materials are commonly used for humidity sensors operating at high temperatures [77], while polymers are preferred for applications requiring high sensitivity. As a working principle, the resistance of ceramic material changes as [78]:

$$\log\left(\frac{R(RH)}{R_0}\right) = \frac{\log a - \log RH^n}{1 + b/RH^n} \tag{2.14}$$

where $R(RH)$ is the resistivity at RH, and a and b are constants depending on the composition and porosity of the ceramic. Electrolytes are a relatively new class of materials that have gained

popularity due to their excellent conductivity and high sensitivity [79], [80].

In recent years, several advancements have been made in the field of resistive humidity sensors. Carbon nanotubes have been presented as a way to minimize the dimensions of the resistive humidity sensor to the nanoscale [81]. Multiwalled carbon nanotubes (MWCNTs) have been investigated to obtain resistive sensors operating in ranges of frequency from 600 MHz to 2 GHz [82]. Nano-crystalline Si has been tested for its performance in resistive humidity sensors at different filament temperatures [83]. These advancements have led to the development of more sensitive, reliable, and cost-effective resistive humidity sensors.

2.2.3 Piezoresistive Humidity Sensors

The piezoresistive principle is based on the change in electrical resistivity of a material under mechanical stress. In this case, the presence of humid air causes the expansion of the material, which leads to a stress change. Piezoresistors then transduce the stress into an electrical signal.

Piezoresistive humidity sensors are a relatively less common type of humidity sensor. However, piezoresistive humidity sensors offer several advantages over other types of humidity sensors [84]. One of the primary advantages of piezoresistive humidity sensors is their high sensitivity. These sensors can detect even small changes in humidity levels and can provide accurate readings in a wide range of relative humidity values. Additionally, piezoresistive humidity sensors consume relatively little power and have fast response times, making them ideal for many applications.

Despite these advantages, piezoresistive humidity sensors may also have some drawbacks. For example, they may be sensitive to temperature variations, which can affect their accuracy. Additionally, these sensors may require careful calibration to ensure accurate measurements, particularly over a wide range of relative humidity values.

Piezoresistive humidity sensors have been the subject of relatively few publications in the literature. One of the earliest investigations of this type of sensor was conducted by Gerlach and Sager, who used a polymer layer as a conductive material on top of a silicon-bending plate [85]. More recent studies have focused on improving the performance of piezoresistive humidity sensors. For example, one paper proposes a miniaturized version of a piezoresistive humidity sensor with a sensitivity of 0.25 mV/%rh and a non-linearity of only 3.1% full scale, in a range between 30% and 80% of relative humidity [86]. Another publication presents a comparative study between bare piezoresistive silicon cantilevers and those covered by ZnO nanorods [87]. The use of ZnO nanostructure significantly increases the sensitivity of the sensor.
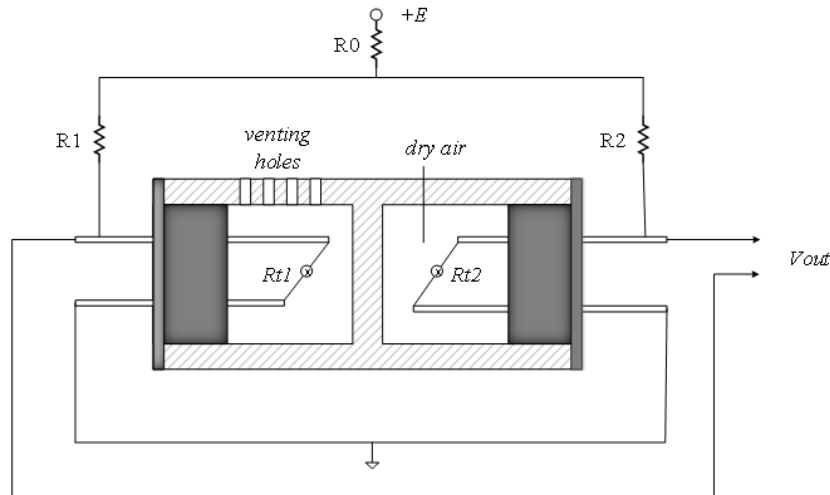
Figure 2.8: Design and electrical connection of an absolute humidity sensor with self-heating thermistors.

2.2.4 Thermal Conductivity Humidity Sensors

Thermal conductivity humidity sensors are designed to measure absolute humidity by detecting the difference in thermal conductivity between dry air and air containing water vapor. These sensors typically include two negative temperature coefficient thermistor elements that are matched and arranged in a bridge circuit. One thermistor is encapsulated in dry nitrogen, while the other is exposed to the environment as shown in Fig. 2.8.

When a current flows through the thermistors, resistive heating increases their temperatures. Because the sealed sensor dissipates more heat than the exposed sensor, the difference in resistance between the two thermistors is proportional to the absolute humidity. This information can be used to calculate relative humidity if temperature and pressure are known.

Absolute humidity sensors are highly durable and can operate at temperatures as high as 300 °C [88]. They are also resistant to chemical vapors due to the use of inert materials such as glass, semiconductor material for thermistors, high-temperature plastics, or aluminum in their construction. These sensors generally provide better resolution at temperatures above 100 °C than capacitive and resistive sensors and can be used in applications where these sensors would not be suitable.

The typical accuracy of an absolute humidity sensor is ± 3 g/m^3, which converts to about ± 5 %rh at 40 °C and ± 0.5 %rh at 100 °C. In addition, thermal conductivity sensors respond to any gas that has thermal properties different from those of dry nitrogen, which can affect the accuracy of the measurements. To ensure accurate measurements, it is crucial to conduct measurements on this device in an area with minimal air flow through the venting holes, as any air convection can lead to extra cooling and result in measurement errors.

2.2.5   Fiber Optic Humidity Sensors

Over the past two decades, there has been a significant increase in the use of fiber optic technology for humidity sensors, with many different implementations and variants discussed in detailed review papers [89]–[91]. While these reviews cover technological advancements over the last century, this present subsection's focus is to review the general technologies used for optical fiber-based humidity sensors. As such, we will only briefly introduce the working principles of the main types of humidity sensors based on optical fibers, as they are not typically well-suited for detection setups in modern HEP. Additionally, many of them are in the R&D phase and still not available in the humidity sensor market.

The first group of optical humidity sensors we will summarize is based on the interaction of an evanescent field. This group of sensors uses the interaction of an evanescent field with a sensitive coating material to detect changes in humidity [92]. When water molecules are absorbed by the coating material, the refractive index of the coating changes, which alters the evanescent wave and causes changes in the transmitted optical power across the spectrum. Research on this type of sensor focuses on developing more sensitive coating materials and improving response time.

The second group of sensors is based on the in-fiber grating. Here, this group is divided into two categories depending on its refraction index: short-period gratings or Fiber Bragg Gratings (FBG), and Long Period Gratings (LPG). FBG humidity sensors work as filters that reflect light signals at a specific wavelength, known as the Bragg wavelength. According to the so-called Bragg condition, the Bragg wavelength λ_B is determined by the effective refractive index of the fiber n_{eff} and the grating period Λ as follows [92]:

$$\lambda_B = 2 \cdot n_{eff} \cdot \Lambda \tag{2.15}$$

The effective refractive index and grating pitch are affected by strain and temperature, which can cause shifts in the Bragg wavelength making this group suitable for temperature and strain measurements. This shift can be computed as follows [93]:

$$\frac{\Delta \lambda_B}{\lambda_B} = (1 - P_e) \cdot \epsilon + [(1 - P_e)\alpha + \xi]\Delta T \tag{2.16}$$

where P_e is the photoelastic constant of the fiber, ϵ is its dielectric constant, α is the thermal-expansion coefficient, and ξ is the thermo-optic coefficient of the fiber.

An example of an FBG humidity sensor is shown in Fig. 2.9. When water molecules are absorbed by the hygroscopic coating material, the dielectric constant changes, and so does
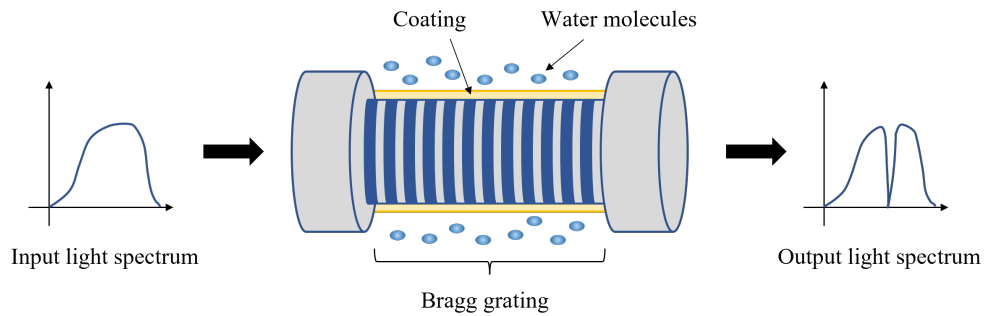
Figure 2.9: A sketch of the principle of operation of an FBG-coated relative humidity sensor [92]. Water molecules absorbed by a hygroscopic coating material affect the Bragg wavelength in a fiber Bragg grating (FBG) through the swelling effect, which induces strain on the FBG and causes a shift in its wavelength.

the Bragg wavelength. The expansion in the fiber hygroscopic coating, known as the "swelling effect," causes strain induced on FBG, resulting in a Bragg wavelength shift.

LPGs may have a periodic perturbation along the fiber with periodicity ranging from 100 μm to 1 mm. They are more sensitive to temperature and strain than FBG sensors [94]. Different types of materials have been explored as coatings for the development of LPG-based RH sensors, including polymers [95], hydrogels [96], gelatin [97], cobalt-chloride-based materials [98], and SiO_2 nanospheres [99].

Both in-fiber grating approaches have been tested for HEP applications. Makovec et al. proposed an optical hygrometer based on FBG that is radiation-tolerant and coated with a polyimide polymer layer [38]. These sensors were fully characterized in a temperature range of -20 °C to 20 °C. After exposure to strong γ-ionizing radiation, the sensor performance was affected only in terms of the natural wavelength peak of each sensor that was shifted due to radiation. The same authors also proposed an LPG as a humidity sensor, which was coated with a TiO_2 layer and then exposed to the same radiation dose as their FBG hygrometer [39]. Despite their radiation tolerance, these sensors are sensitive to mechanical stress applied to the fibers and thermal changes, as changes in temperature result in changes in the lattice distance of the fiber. Additionally, integrating these sensors into standard industrial processes or HEP detectors using as many as possible industrial tools as the basis of the environmental protection systems is challenging.

Optical interferometry is another way to detect the presence of moisture. The interferometric sensing mechanism relies on detecting the perturbation in the phase of the light signal propagating through the fiber caused by external humidity. This detection is done by continuously mixing the acquired signal with a reference signal and converting their phase difference into an optical intensity change. Various types of optical interferometers can be used as humidity detectors, such as Fabry-Pèrot [100], Sagnac [101], Michelson [102], and Mach-Zehnder [103].

In 2011, a novel fiber optic humidity sensor based on the near-field Fabry-Perot configuration for use in high radiation experiments at CERN was proposed [104]. The device was constructed by depositing a layer of SnO_2 particles onto the distal end of cleaved optical fibers. Although the sensor yielded promising results, such as high sensitivity, low response time, and limits of detection below 0.1% in the low humidity range of 0-10 %rh, it was found to be limited in terms of multiplexing capability due to the inability to integrate multiple sensors on the same fiber. As a result, this configuration was abandoned, and the focus shifted towards more innovative fiber optic sensor-based solutions.

The final type of humidity optical sensor considered is based on evanescent wave scattering (EWS) phenomena. Several papers in the literature discuss this type of optical humidity sensor based on porous silica fibers [105]–[107]. The electromagnetic field generated at the interface, which propagates through the optical fiber, is not completely limited within the fiber. Any change in the refractive index of the surrounding material due to the adsorption of humid air alters the evanescent wave, which can be detected by analyzing the scattered light [108].

2.2.6 Optical Humidity Sensors

This subsection analyses the main representative of the optical humidity sensor - the dew point mirror sensor. The dew point mirror sensor is a precise and accurate method for measuring humidity and is often used as a reference sensor in laboratory applications.

A dew point mirror sensor consists of a sensitive surface that is cooled in a defined manner, resulting in a decrease in the amount of water that can be absorbed. At a certain temperature, the saturation water vapor pressure is reached, causing water vapor to condense at the surface as liquid or crystalline water. This temperature corresponds to either the dew point or the frost point of the gas. Other parameters related to gas humidity such as absolute humidity, relative humidity, water vapor pressure, and so on, can be derived from the dew point temperature of a gas.

Dew point instruments typically consist of (Fig. 2.10):

- a sensitive surface (such as an optical mirror, ceramic capacitor, or semiconductor),

- a cooling and heating unit (typically a Peltier element) with precise temperature control,

- a signal (such as light, electrical current, or voltage at a resistor, capacitance, or semi-conductor device) that changes rapidly when condensation occurs,

- temperature sensors for precise measurement of the surface temperature and gas temperature,

- analysis and signal processing devices,

- and a control unit for automatic cleaning, data analysis, measuring time reduction, gas flow velocity control, etc.
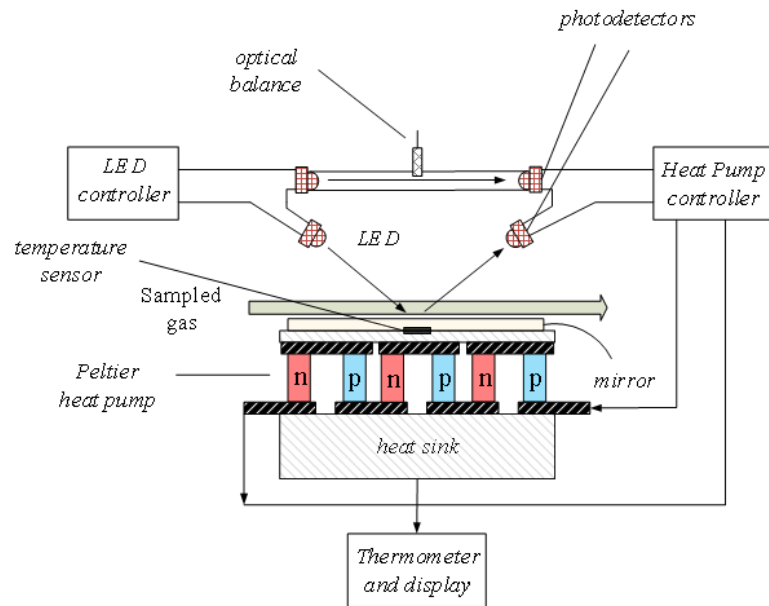
Figure 2.10: Chilled mirror dew point sensor with the optical bridge.

In order to reach very low dew point temperatures of T_d < -80 °C, a combination of several Peltier elements or coolants can be used. The quality of the temperature control is the main determinant of the precision of the measurement, and proportional–integral–derivative (PID) controllers are often used for this purpose. Dew point mirrors operate in a quasi-continuous mode, meaning that a certain settling time is required until the final value is reached, so they cannot resolve rapid humidity changes.

Visual observation of condensation is important to differentiate between liquid and crystalline condensation, which determines if the condensation temperature is interpreted as the dew point temperature or the frost point temperature. The dew point mirror sensor is a valuable tool for precise and accurate humidity measurements in laboratory settings.

2.3   Commercial Humidity Sensors

In this section, we explore the challenges of selecting the ideal humidity sensor for the CMS sub-detectors operating in restrictive environmental conditions. While thermal conductivity humidity sensors perform excellent performance at temperatures above 100 °C, they exhibit limited effectiveness at much lower temperatures. On the other hand, fiber optic-based humidity sensors show great radiation tolerance, but suffer from inherent losses, dispersion, and low reproducibility. The latter makes it challenging to integrate fiber optic-based humidity sensors into the system, particularly when considering the need for important geometrical spread with sensors to be scattered throughout the detector. Furthermore, integrating these sensors into the readout system demands significant effort. Thus, we must carefully consider the advantages and disadvantages of commercially available, mass-produced devices to identify

the ideal candidate for the CMS sub-detectors.

The previously conducted tests of detectors at LHC have revealed a significant obstacle - the absence of appropriate miniature relative humidity sensors suitable for local, distributed monitoring within harsh and difficult-to-access environments. Commercial humidity sensors available in the market are generally tailored to function at ambient temperatures and their technical specifications usually refer to the standard operating temperature (such as 20 °C or 25 °C). Additionally, their tolerance to radiation and magnetic interference, and the possibility of implementation in high-energy physics applications, are not commonly documented or demonstrated.

2.3.1 Piezoresistive sensors

Piezoresistive-based humidity sensors are rare in the market. The HMX2000-HT humidity-temperature sensor, produced by limited-size Hygrometrix company, was particularly note-worthy, utilizing volumetric changes in polymeric films caused by water vapor (Fig. 2.11). The sensor was tested for radiation and it demonstrated high radiation tolerance [109]. The sensing element is made up of a thin polymer film, which is deposited and bonded to four cantilever beams that are bulk micromachined from the silicon substrate of a chip. Each microbeam had an electrically isolated and diffused-in semiconductor strain gauge that uses a piezoresistive effect to measure the beam stress. Water vapor adsorption and desorption cause the polymer film to expand and contract, creating stress in the underlying silicon microbeam through surface shear stress coupling at the polymer-silicon interface. The response of this structure to water vapor is similar to a classical bimorph structure, with water vapor concentration transmitted and linearly measured as mechanical strain. One advantage of the Hygrometrix sensor design over conventional capacitive and resistive sensors is that the polymeric film is electrically isolated from the sensing electrodes. This design ensures long-term stability and accuracy, with a nitride and oxide passivation layer separating the polymer film from the strain gauges and associated metallization.

The HMX2000-HT humidity-temperature sensor could accurately determine relative humidity levels between 0 and 100 %rh with 1.5 %rh accuracy, even after being exposed to various harsh environments such as freezing, water immersion, air pollution, and diesel fumes. The sensor measured full RH levels, including 100 %rh with water condensation, within a temperature range of -40 °C to 85 °C and can be stored for long periods at temperatures between -55 °C and 125 °C without damage. Unfortunately, this sensor is not available in the market anymore and, even in the first attempt to use them at CERN, it became evident that the sensors were rather experimental and not fully ready for the market yet. Therefore, the decision was that the search should be focused on resistive and capacitive humidity sensors, that are fully ready and established in the market.
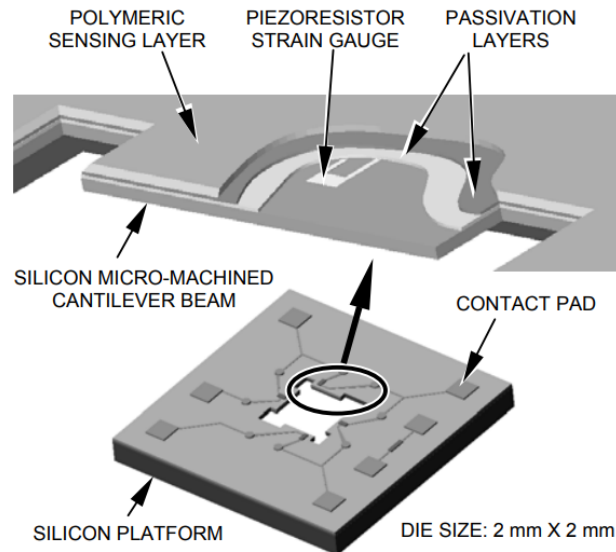
Figure 2.11: The Hygrometrix RH sensor is a piezoresistive device with four semiconductor strain gauges and a full Wheatstone Bridge all on one chip [110].

2.3.2 Resistive sensors

Resistive humidity sensors typically consist of noble metal electrodes deposited on a substrate or wire-wound electrodes on a plastic or glass cylinder, coated with a salt or conductive polymer. Resistive humidity sensors have several advantages, including their interchangeability, which allows for calibration by a resistor at a fixed RH point, eliminating the need for humidity calibration standards [110]. They also have a response time ranging from 5 to 30 seconds for a 63 % step change and are generally field replaceable. However, they do have significant temperature dependencies and suffer from hysteresis and long-term drift, particularly between high and low humidity levels. Additionally, they are not suitable for measuring low humidity values below 5 %rh due to high impedance change and difficult dynamics control.

The CHS-UPS [111], produced by TDK is a typical example of resistive-based humidity sensors, with an operating range of 5 to 95 %rh and 0 °C to 50 °C (Fig. 2.12). The sensor accuracy for the humidity range from 5 to 95 %rh and at 25 °C is ± 3 %rh. While resistive humidity sensors do not require complex circuitry for signal processing, they are less commonly used than capacitive sensors due to their inherent drift and temperature effects.

2.3.3 Capacitive sensors

The market benchmark for high-performance relative humidity sensors includes the SHT85 [112] module and HUMICAP 180 sensor [113] developed by Sensirion and Vaisala, respectively (Fig. 2.13). The SHT85 module exhibits the optimal performance within the recommended temperature and humidity range of 5 – 60 °C and 20 – 80 %rh, respectively. However, prolonged exposure to conditions outside this range, particularly at high humidity levels, may cause a
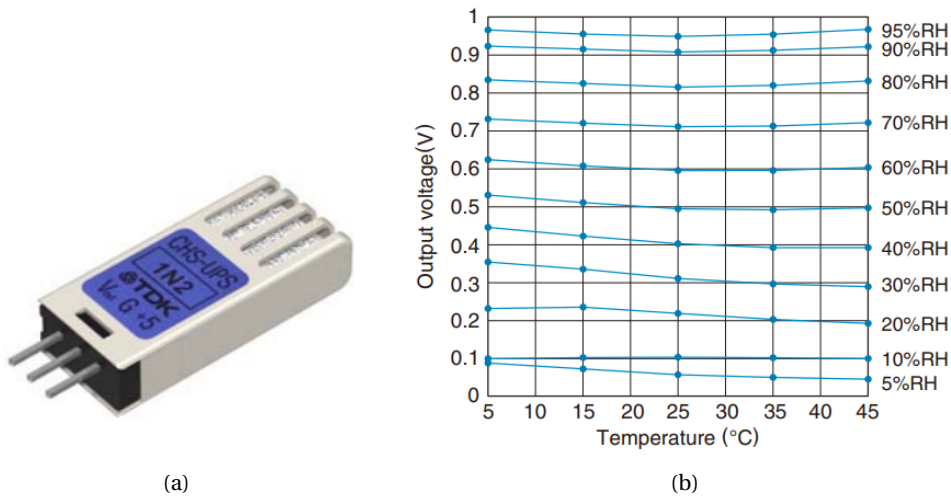
Figure 2.12: (a) Photo of the CHS-UPS humidity sensor, and (b) thermal dependency of the sensor output at different humidity levels.

temporary offset in the RH signal.

In terms of accuracy, the Sensirion module has a declared uncertainty of approximately ±1.5 %rh at 25 °C within the range of 10 to 80 %rh. This error may increase up to ±2 %rh outside of this range, with an additional 1 %rh uncertainty arising from hysteresis and repeatability. Nevertheless, the data sheet does not specify the accuracy of the RH measurement at temperatures below 0 °C, as shown in Fig. 2.14 a). Besides the RH sensor, the SHT85 module consists of a temperature sensor as well. The temperature measurement has an error of ±0.15 °C between 5 and 60 °C, which increases up to ±0.3 °C when operating below 0 °C or above 60 °C, as reported in Fig. 2.14 b). The module provides the digital output and it comes together with off-the-shelf readout electronics on the same chip. Unfortunately, the integrated-solution sensor that combines the sensing element with the appropriate conditioning and digitization circuitry is not suitable for use inside a HEP detector due to the lack of radiation-hardness of the electronics components.

On the other hand, Vaisala's HUMICAP 180 sensor exhibits the fastest response time of all the evaluated sensors, taking only 40 seconds to move from 50 %rh to 70 %rh and 55 seconds to reach 90 %rh [114]. The sensor gives an analog signal and it can be separated from the signal conditioning unit by a cable of a specific length (2 m, 5 m, or 10 m). However, as the cable length cannot be extended, and the company does not sell the "bare" sensor, it has been eliminated from further consideration.

After a thorough investigation, we identified another sensor-building company - IST AG, with a proven track of tailoring their offerings to meet unique customer requirements. In particular, their innovative MK33-W humidity sensor is engineered to operate in harsh environments. The sensor operating relative humidity range is from 0 to 100 %rh, with a hysteresis of less

(a)   (b)
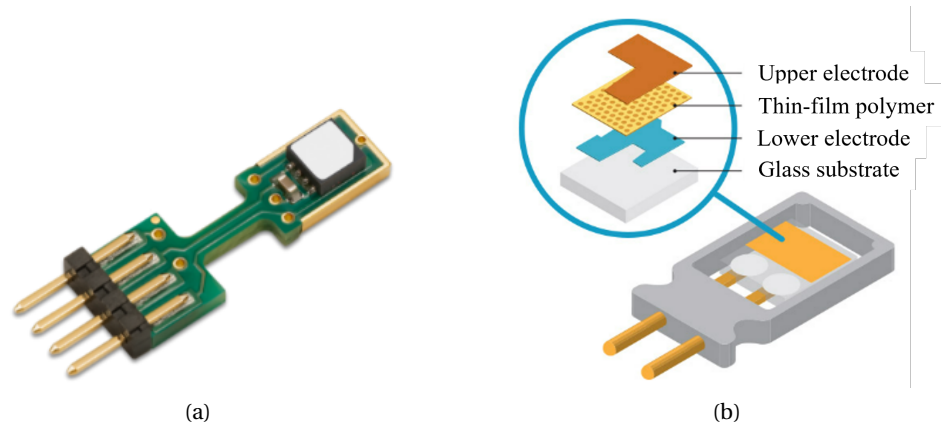
Figure 2.13: (a) A photo of the SHT85 RH/T module and (b) a schematic of the HUMICAP 180 sensor layer-by-layer.

(a)   (b)
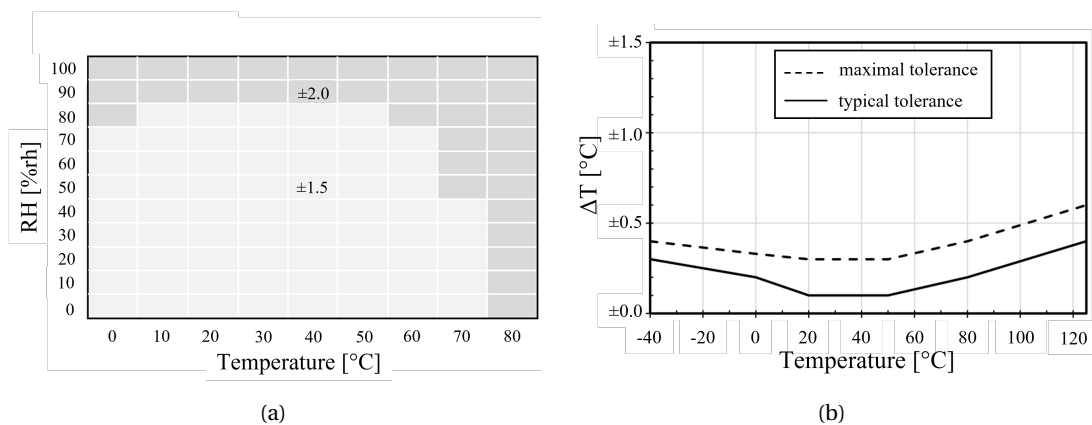
Figure 2.14: SHT85 RH/T module: (a) Typical accuracy of relative humidity measurements given in %rh for temperatures 0 – 80 °C. (b) Typical and maximal tolerance for a temperature sensor in °C.

than 2 %rh (Fig. 2.15 a)).

Figure 2.15 (b) depicts the linear relationship between the sensor's capacitance and the relative humidity changes. Additionally, the sensor comes together with a Pt1000 temperature sensor for temperature recompensation purposes and they are mounted on the same module. Although the module electronics limit the sensor operating temperature range between -40 °C to 190 °C, the IST AG offers bare sensors that are separated from the readout electronics and can withstand even more extreme temperatures.
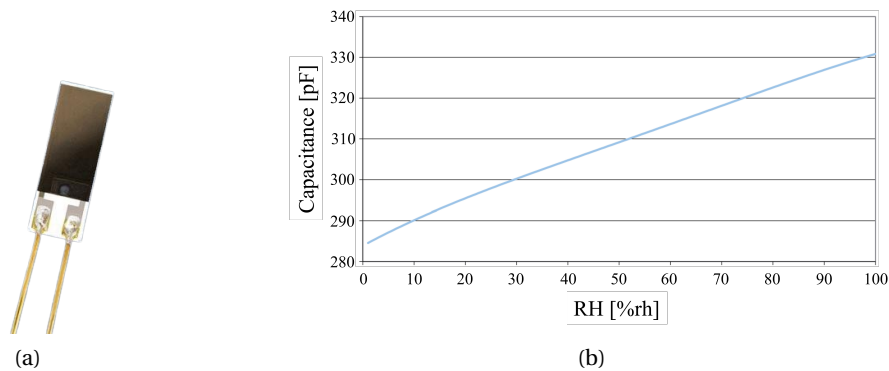
Figure 2.15: (a) A photo of the MK33-W capacitive-based relative humidity sensor and (b) sensor capacitance with the change in the relative humidity

2.3.4 Overview of the considered commercial humidity sensors

Table 2.3 provides a comprehensive overview of the discussed devices, including their respective operating ranges in terms of relative humidity and temperature, typical levels of accuracy and hysteresis, response time, as well as the type of output signal produced. Moreover, this table also indicates the availability of each sensor in the market, as well as whether or not the sensor can be procured without the accompanying readout electronics.

Table 2.3: Overview of the discussed devices.

Product name	HMX2000-HT	CHS-UPS	SHT85	Humicap 180	MK33-W
Technique	piezoresistive	resistive	capacitive	capacitive	capacitive
RH range [%rh]	0-100	5-95	0-100	0-100	0-100
T range [°C]	-40 to 85	0 to 50	-40 to 105	-70 to 180	-40 to 190
Typical accuracy [%rh]	1.5	3	1.5	1	< 2
Hysteresis [%rh]	1.7	≈ 0	1	–	< 2
Signal output	Analog	Analog	Digital	Analog	Analog
Bare sensor	yes	yes	no	no	yes
Available in the market	no	yes	yes	yes	yes

2.4 Summary

This chapter has provided an extensive investigation into the world of humidity sensors. Several transduction principles, humidity-sensitive materials, and required technologies were introduced and discussed. Table 2.4 provides a comprehensive overview of the advantages and disadvantages of the principles discussed for humidity detection.

Moreover, we have compared the properties of various commercial humidity sensors, and based on our findings, the MK33-W humidity sensor appears to be a potential candidate for HEP applications. The reasons for this are its large RH range, ability to operate in sub-

zero temperatures, and the possibility to purchase a bare sensor from the manufacturer with possible modifications if needed.

However, before thinking about integrating the MK33-W sensor into HEP detectors, we must subject it to rigorous testing. Such testing should include evaluating its temperature dependence at negative temperatures, as the sensors are usually tested at typical temperatures of 20 °C or 25°C, and its ability to withstand certain levels of radiation and magnetic field exposure. With these challenges in mind, Chapter **4** will delve into the testing procedures required to evaluate the MK33-W sensor performance and suitability for its use in HEP environments.

Table 2.4: Comparative characteristics of methods used for humidity measurements.

Sensor Type	Advantages	Disadvantages
Capacitive	Small in size; low cost; mass-production possible; require very little maintenance; wide measurement range 0–100 %rh; wide temperature range (up to 200 °C); low-temperature dependence; low hysteresis (below 1%rh); low drift; good linearity; relatively fast response; highly resistant to contaminants; auto-calibration is possible	Can be limited by distance from electronics to the sensor; loss of relative accuracy at the low end (< 5 %rh); requires electronics to convert capacitance to relative humidity; significant drift; may suffer calibration shifts and hysteresis if used at high temperatures and or high humidities; degradation under influence of electrical shocks
Resistive	Small and cheap; mass production possible; high sensitivity; low cost; often easy to use	Nonlinear characteristics; limited range (typically 15 to 95 %rh); difficulties in measuring low values (< 5 %rh); High-temperature dependence; poor stability, significant drift; sensitive to contamination, condensation and interference;
Piezoresistive	Polymeric film can be electrically isolated from the sensing electrodes; high linearity and low hysteresis; wide measurement range 0 – 100 %rh; simple signal conditioning	Low response; difficult to find it in the market
Thermal Conductivity	Very durable, operate at temperatures up to 300 °C; great resolution at temperatures > 100 °C; resistant to chemical vapors	Low accuracy at lower temperatures; sensitive to any gas different than dry nitrogen; higher air flow can affect the measurement accuracy
Fiber Optic	Low cost; high sensitivity; small size; robustness; flexibility; the ability for remote monitoring as well as multiplexing; used even in the presence of unfavorable environmental conditions such as noise, strong electromagnetic fields, high voltages, nuclear radiation, in explosive or chemically corrosive media, at high temperatures; low hysteresis	Inherent losses; dispersion; nonlinearity; birefringence; reproducibility
Dew point mirror	Broad measuring range; high precision and accuracy; no hysteresis; good long-term performance; long-term calibration stability; fundamental measurement	High cost; not for in-situ use; can be slow in response; contamination (last variants have automatic calibration); dew points below 0 °C require careful interpretation; usually required some skill to operate

3 Radiation effects in the HEP detector environment

Knowledge leaves no regrets except for radiation.
I wish I'd never messed with it.
— Marie Curie

As particles (photons, leptons, hadrons) interact with matter, they lose energy through interactions with the electrons and nuclei of material atoms. The effects of these interactions on the material depend on the energy-loss processes (the type of interaction varies with the energy of the incoming particle) and the structure of the material.

This chapter begins with an introduction to the interaction mechanisms between particles and matter, followed by a description of the radiation damage mechanisms in silicon-based sensors. The displacement damage mechanism is presented, referring to both microscopic defects and macroscopic effects. The second type of radiation damage mechanism, surface damage, is also briefly addressed. Furthermore, since the selected humidity sensor candidate is a polymer-based sensor, this chapter provides an overview of the radiation damage on the polymer material.

Additionally, the chapter provides an overview of the effects of radiation on electronics in LHC detectors. Although the physics of energy loss is similar to that of silicon-based sensors, the radiation quantities used to evaluate damage differ between these categories. Radiation degradation in silicon sensors typically relies on bulk displacement damage, while electronics degradation is mainly influenced by ionizing dose effects.

3.1 Interaction Mechanisms of Particles with Matter

The fundamental mechanisms through which particles interact with the material they traverse are ionization and excitation, which are interactions occurring within the atomic shell. The action of nuclear forces, which could lead to interactions between the nucleus and the transversing particles with subsequent energy exchange, is limited to a very small portion of space. Table 3.1 summarizes the particle types, their rest mass and mean lifetime of subatomic particles important for the HEP environment.

Table 3.1: Particle properties at HEP environment [115].

	Particle type	Rest mass [MeV/c]	Mean life [s]
Photons	(γ)	0	Stable
Leptons	Electron (e^-), positron (e^+)	0.511	Stable
	Muon (μ^+, μ^-)	105.66	$2.2 \cdot 10^{-6}$
Hadrons	Proton (p)	938.27	Stable
	Neutron (n)	939.57	880
	Charged pion (π^+, π^-)	139.57	$2.6 \cdot 10^{-8}$
	Neutral pion (π^0)	134.98	$8.5 \cdot 10^{-17}$

The nucleus is protected by an electronic shell, which can only be penetrated by charged particles possessing sufficiently high energy. Positively charged particles must also overcome a repulsive potential, which can reach up to 30 MeV for heavy nuclei, in order to reach the nucleus [116]. Photons can also interact with the nucleus, but the probability of such a process is very low until the photons possess energy levels corresponding to wavelengths of the order of the nucleus dimensions. This means that photon-nucleus interactions and energy exchange occur only at energies of several MeV.

Due to the different mechanisms through which charged particles, photons and neutrons interact with matter, they must be studied separately. However, it has been observed that significant differences exist even among different charged particles. For example, heavy and light charged particles can interact with matter in completely different ways. Thus, radiation effects are divided into four distinct categories depending on the incoming particle: heavy charged particles, light charged particles, photons, and neutrons.

3.1.1 Interaction Mechanisms of Heavy Charged Particles with Matter

The heavy charged particles in HEP environment are the muons, the protons and the charged pions. The basic mechanisms through which all these mentioned particles interact with matter and lose energy during their trajectory are completely identical. The energy loss of heavy particles, in range $0.1 \leq \beta\gamma \leq 1000$, when traveling through a material can be described by the Bethe-Bloch formula as follows [117]:

$$\left[-\frac{dE}{dx}\right]_{ion} = Kz^2\frac{Z}{A}\frac{1}{\beta^2}\left[\frac{1}{2}\ln\frac{2m_ec^2\beta^2\gamma^2 T_{max}}{\bar{I}^2} - \beta^2 - \frac{\delta(\beta\gamma)}{2} + \frac{C}{Z}\right] \tag{3.1}$$

where $K = 4\pi N_A r_e^2 m_e c^2$, N_A is the Avogadro constant, r_e the classical electron radius, m_e the electron mass, c the speed of light in vacuum. Z is atomic number and A is molar mass of the material, z is charge of the incident particle, δ corrects for the density effect necessary for highly relativistic particles and C/Z accounts for shell corrections due to the structure of the atom. $\bar{I}$ is the mean ionization potential of the atoms in the material through which the particle is passing, β is the ratio of the particle velocity to the speed of light ($= v/c$), and γ is Lorentz factor ($= 1/\sqrt{1-\beta^2}$). T_{max} is the maximum energy transfer and it is approximated as [118]:

$$T_{max} = \frac{2m_ec^2\beta^2\gamma^2}{1 + 2\gamma m_e/m + (m_e/m)^2} \tag{3.2}$$

where m is the particle mass. The energy loss is also referred as mass-stopping power and it is expressed in $\text{MeV}\cdot\text{cm}^2/\text{g}$.

Based on the Bethe-Bloch formula, it can be concluded that the energy lost per unit path length by a heavy charged particle is directly proportional to the square of its charge and the atomic number of the material. Furthermore, the energy lost by a heavy charged particle per unit path length is inversely proportional to the square of its velocity and the molar mass of the material. Since the Coulomb interaction is transmitted at the finite speed of light, it is clear that at high velocities, the energy transfer distance is not sufficient to impart sufficient momentum to the electron.

Figure 3.1 presents the dependence of energy loss per unit length of a positively charged muons in copper on its energy. In the segment of the curve from B to C, a clear inverse proportionality to the particle energy can be observed, as predicted by the Bethe-Bloch formula. In the part from C to D, the slight increase can be attributed to the fact that at higher energies, the logarithmic term contributes significantly, while the first part of the curve, from A to B, is not described by the Bethe-Bloch formula. Specifically, the ionization losses of heavy charged particles sharply decrease to zero as their energy decreases. This can be explained by the fact that at very low energies, heavy charged particles capture as many electrons as needed to transform into neutral atoms. Since the primary interaction between a heavy charged particle and orbital electrons occurs through the electric field, it is evident that neutral atoms cannot cause ionization, leading to a rapid decrease in the energy loss per unit path length as the energy decreases.

Attempts to analytically determine the track length (or range) of a heavy charged particle
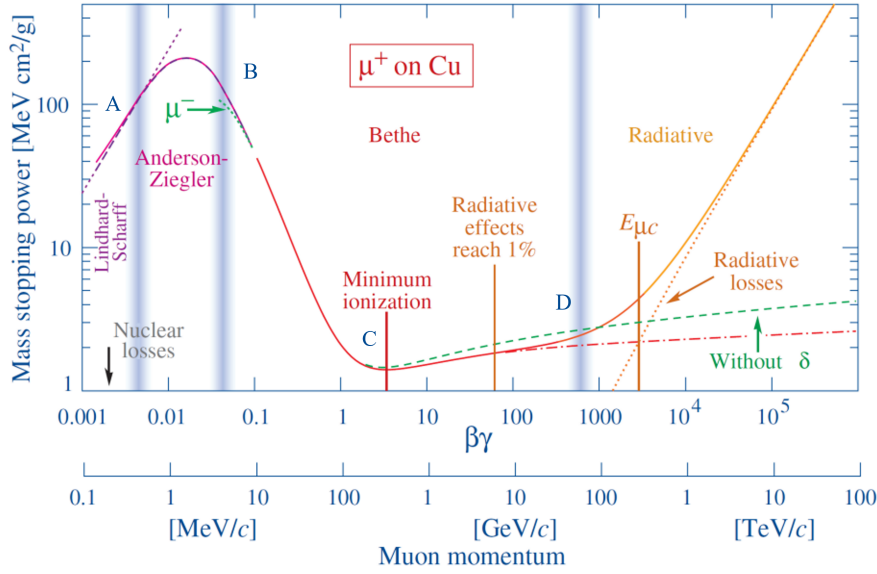
Figure 3.1: Mass stopping power of positively charged muons in copper (solid line: total stopping power, dotted line: radiative stopping power, dash-dotted line: electronic stopping power according to Bethe-Bloch formula) [119].

based on the Bethe-Bloch formula have unfortunately not yielded the desired results. The track length of a heavy charged particle could be calculated as [120]:

$$R = \int_{E_0}^{0} \frac{dE}{(-dE/dx)} \tag{3.3}$$

where the expression in the denominator of the integrand would be given by the Bethe-Bloch formula. However, since it fails to describe the interaction of heavy charged particles with matter at low energies, estimates for the range obtained in this way have not proven to be sufficiently accurate. For the range of alpha particles[I] in the air, a more reliable estimation is still obtained based on a well-known empirical relation [121]:

$$R_\alpha = 0.318 \cdot E_\alpha^{3/2} \tag{3.4}$$

If the energy of an alpha particle is expressed in MeV, the range in air can be obtained in centimeters. The above relation provides a good estimation for alpha particle energies in the range of 3 to 7 MeV.

[I]Alpha particles, also called alpha rays or alpha radiation, consist of two protons and two neutrons tightly bound together into a particle identical to a helium-4 nucleus.

3.1.2 Interaction Mechanisms of Light Charged Particles

The light charged particles are electrons and positrons. These two types of particles interact with matter in almost identical ways. The only significant difference is that when electrons lose all their energy, they are captured by an atom and transform into ordinary orbital electrons, whereas positrons, when they lose energy, they annihilate with an electron. During this process, both particles disappear, and two gamma rays of 511 keV are emitted, moving apart at 180 degrees. Therefore, when studying the effects of positron passage through a medium, it should be kept in mind that eventually, the process will finish by the creation of penetrating electromagnetic radiation.

As for heavy charged particles, the relation describing the energy loss of light charged particles per unit path length is similar to expression (3.1). The fundamental difference between heavy and light particles lies in the fact that light particles have a much smaller mass than heavy particles, the interaction between light charged particles and electrons must take into account quantum-mechanical phenomena, and light charged particles exhibit relativistic effects at much lower energies than heavy charged particles. The expression for the energy loss of a light particle per unit path length is obtained in the following form [122]:

$$\left[-\frac{dE}{dx}\right]_{ion} = K\frac{Z}{A}\frac{1}{\beta^2}\ln\frac{m_e c^2 \beta^2 \gamma^2 T}{2\bar{I}^2} \tag{3.5}$$

where T is the kinetic energy of the electron. Similar to heavy charged particles, the energy loss of light charged particles is inversely proportional to the square of their velocity, especially at lower energies when the contribution of the logarithmic term is not significant.

Since the mass of a heavy charged particle is a few thousands times greater than the mass of a light charged particle, if both particles have the same kinetic energy, the squares of their velocities would differ by that factor. This means that the heavy charged particle would have a much lower velocity, resulting in a much higher energy loss per unit path length compared to light charged particles of the same energy. Hence, heavy charged particles lose their energy much faster than light charged particles of the same energy, leading to a significantly shorter range.

Due to the small mass of electrons, radiative losses[II] are possible, and light charged particles can also lose their energy through the emission of so-called bremsstrahlung radiation. The energy losses of light charged particles due to radiation can be represented as [118]:

[II]Radiative energy loss is the radiation produced by an interaction of a charged particle with the atomic nucleus.

$$\left[\frac{dE}{dx}\right]_{rad} \sim nZ^2 E_0 \tag{3.6}$$

The energy losses of light charged particles due to radiation are directly proportional to the number of atoms per unit volume, n. However, unlike ionization losses, radiative losses are directly proportional to the energy of the light charged particle. It should also be noted that radiative losses increase with the square of the atomic number of the material through which light charged particles are moving.

Since radiative losses of light charged particles increase with energy, it can be expected that at higher energy values, radiative losses become dominant, meaning that at higher energies, light charged particles lose more energy per unit length due to radiation than due to ionization.

Furthermore, any charged particle can emit Cherenkov radiation. The only condition that needs to be met is that its velocity is greater than the phase velocity of light in that medium [123]. The energy lost by a particle in this way is larger as the velocity of the particle increases, but the overall losses are small compared to ionization and radiative losses. Only for relativistic particles do energy losses through Cherenkov radiation reach a few percent of the total losses. While this effect is not as significant for analyzing the energy losses of a charged particle when moving through a medium, it has provided numerous possibilities for detecting relativistic particles.

3.1.3   Interaction Mechanisms of Photons

Between gamma and X-ray radiation, there is no difference in terms of their interaction with matter. In both cases, we are dealing with electromagnetic radiation of small wavelength, and they only differ in their place of origin. Gamma radiation originates from the nucleus, while X-ray radiation arises from processes occurring in the vicinity of the nucleus. At the same time, both types of radiation can be treated as beams of photons moving at the speed of light [124].

The fundamental mechanisms of interaction between electromagnetic radiation and matter can only be described by quantum electrodynamics. Photons have no charge and thus cannot interact with electrons through electric fields at larger distances, as was the case with heavy and light charged particles. The primary ways in which a photon can be removed from a beam are:

- **Electron-positron pair production:** If the energy of the photon is sufficiently high, it is possible to create an electron-positron pair, and the photon completely disappears (Fig. 3.2 (a) (i)). In order for electron-positron pair production to occur, the energy of the photon must be greater than $2m_e c^2$, which is equal to 1.022 MeV. This process requires the presence of another body to accept the portion of the photon momentum

that completely disappears in this process. The most common case is pair production in the Coulomb field of the nucleus. Pair production can also occur in the field of an electron, in which case the electron absorbs a portion of the photon momentum. This process can only happen if the energy of the photon is higher than $4m_ec^2$ or 2.044 MeV. If the electron and positron have sufficiently high energy, they can ionize matter, similar to light charged particles.

- **Photoelectric effect:** The photoelectric effect is a process in which a photon transfers its entire energy to an orbital electron. The photon ceases to exist at that moment, and the electron is ejected from the atom with energy, which is equal to the photon energy before the interaction, minus the binding energy of the orbital electron.

  The photoelectric effect can only occur with bound electrons. This is dictated by the conservation of momentum, where another body must also accept a portion of the photon momentum. That third body is the atom, which shares the photon momentum with the electron in this process. However, since energy is inversely proportional to mass in such situations, it is clear that the recoil energy of the entire atom will be negligibly small compared to the energy gained by the electron. The recoil energy of the nucleus is several orders of magnitude smaller than the recoil energy of the electron. If the photoelectric effect involves an inner shell, the emission of an electron is typically followed by atomic relaxation. This means that the vacancy is filled by an electron from an outer shell and characteristic X-rays or Auger electrons[III] are emitted (Fig. 3.2 (a) (ii)).

- **Rayleigh scattering and Compton effect:** When passing through a material, gamma or X-ray photons can be scattered from their original path. This scattering can be coherent (Rayleigh scattering) when there is no energy exchange, and photons with the same energy continue moving in a different direction, or it can be incoherent (Compton effect) when both the direction and energy of the incident photon change (Fig. 3.2 (a) (iii) and (iv) respectively). Rayleigh scattering occurs on orbital electrons when the photon has less energy than the binding energy. If the energy of the photon is significantly higher than the binding energy of the orbital electrons, the Compton effect occurs. In this process, the photon transfers a portion of its energy to the electron and continues moving in a different direction with lower energy or longer wavelength. Rayleigh processes are much less likely to occur compared to Compton scattering.

Fig. 3.2 (b) illustrates the regions where each of the three major types of photon interactions with matter dominates. At lower photon energies, the photoelectric effect is the dominant mechanism, while Compton scattering becomes dominant at intermediate energies. The Compton scattering also increases with decreasing atomic number of matter. Therefore the interval of domination is wider for light nuclei. Finally, electron-positron pair production dominates at high energies.

[III]Auger electrons are electrons that are emitted when an electron from a higher energy level falls into a vacancy in an inner shell. The process usually occurs when the atom is bombarded with high energy electrons.
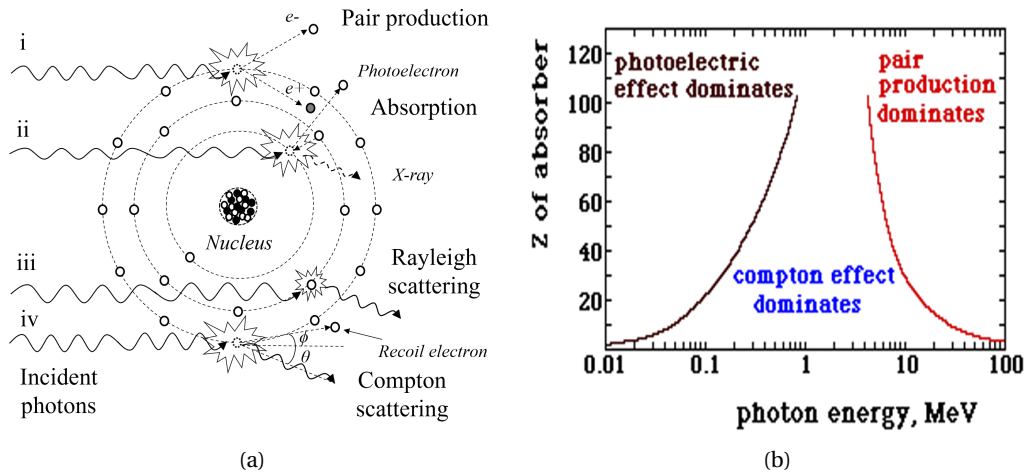
Figure 3.2: (a) Illustrative summary of photons interactions: (i) Pair production - the electron and positron are emitted in the direction of the photon motion; (ii) Photoelectric absorption results in total removal of the incident photon with energy greater than the binding energy of the electron in its shell, with subsequent x-ray emission; (iii) Rayleigh scattering is interaction with an electron (or whole atom) in which no energy is exchanged and incident photon energy equals scattered photon energy with a small angular change in direction; (iv) Compton scattering interactions occur with essentially unbound electrons, with a transfer of energy shared between recoil electron and scattered photon. (b) The curves demarcate the regions where three major types of photon interaction with matter effect are dominant.

3.1.4   Nuclear Interactions

The interactions discussed earlier are related to atomic interactions. However, when hadrons travel through matter, they can experience elastic and inelastic collisions with nuclei. Inelastic nuclear collisions take place when new particles are generated or when the internal structure of the target nucleus or the projectile is changed.

During the initial fast phase of a hadron-nucleus interaction (lasting approximately 10^{-22} s), the incoming hadron interacts with the nucleons, potentially resulting in the creation of new particles, particularly pions, if the energy of the projectile is sufficiently high (typically in the GeV range or higher). Pion production can take place when a nucleon collides with a free nucleon, provided that the energy exceeds 290 MeV. The energy threshold is slightly lower for nucleons bound within a nucleus. These hadrons can initiate intranuclear cascades, and the more energetic particles may have the ability to exit the nucleus. The high-energy particles predominantly travel in the forward direction. Other particles can deposit their energy within the nucleus, leaving it in an excited state. Subsequently, the nucleus undergoes a slow de-excitation process (lasting approximately 10^{-16} s). During this evaporation phase, lower-energy (MeV) neutrons, protons, or light fragments (such as alpha particles) are emitted in an isotropic manner. Additionally, the residual nucleus may undergo γ de-excitation. In heavy elements, evaporation competes with fission, where the nucleus breaks up into larger

66

fragments. Fission products can also undergo particle evaporation. The remaining nuclei resulting from evaporation or fission can exhibit radioactive properties [115].

Neutrons, being the only "stable" neutral hadrons, have a relatively long mean lifetime of approximately 15 minutes. Neutrons with low energies (a few MeV) primarily decelerate through elastic scattering until they become thermalized and are captured by a nucleus. The likelihood of neutron capture is inversely proportional to the neutron velocity, making thermal neutrons more prone to absorption compared to fast neutrons. Capture is often followed by gamma emission, known as radiative capture. In heavier materials, neutrons can also induce fission. The absorption of neutrons depends significantly on the nuclear isotopes present in the material.

3.2   Radiation Effects on Silicon-based Sensors

This section provides an overview of the radiation-induced performance degradation of the sensors used in the silicon-based HEP experiments. The main cause of this degradation is displacement damage effects that occur in the silicon bulk of the devices.

3.2.1   Displacement Damage

Microscopic Defects

Displacement damage (DD), also known as bulk damage, is a phenomenon that occurs when high-energy particles, such as protons, neutrons, or heavy ions, impinge on a target material, causing displacement of atoms from their lattice sites and creating irregularities in the crystal structure (Fig. 3.3). The ejected atom from its lattice site is called *primary knock-out atom* (PKA). This displacement of atoms is caused by the transfer of kinetic energy from the impinging particle to the target, either through elastic or inelastic scattering, resulting in interstitials and vacancies. Vacancies and interstitials either recombine (in $\sim 90\%$ of cases) or migrate and form stable defects known as the *Frenkel pairs*. The process can lead to entire damage cascades, which result in the formation of clusters of lattice defects [125]. The maximum transferred energy $E_{R,max}$ of an incoming particle of mass m_p and kinetic energy E_p to produce PKAs and clusters (by elastic scattering) can be calculated from non-relativistic collision kinematics as [126]:

$$E_{R,max} = 4E_p \frac{m_p m_l}{(m_p + m_l)^2},$$
(3.7)

where the lattice atom has a mass m_l.

The number of Frenkel pairs N_F induced by a PKA with energy E_R, can be calculated by the
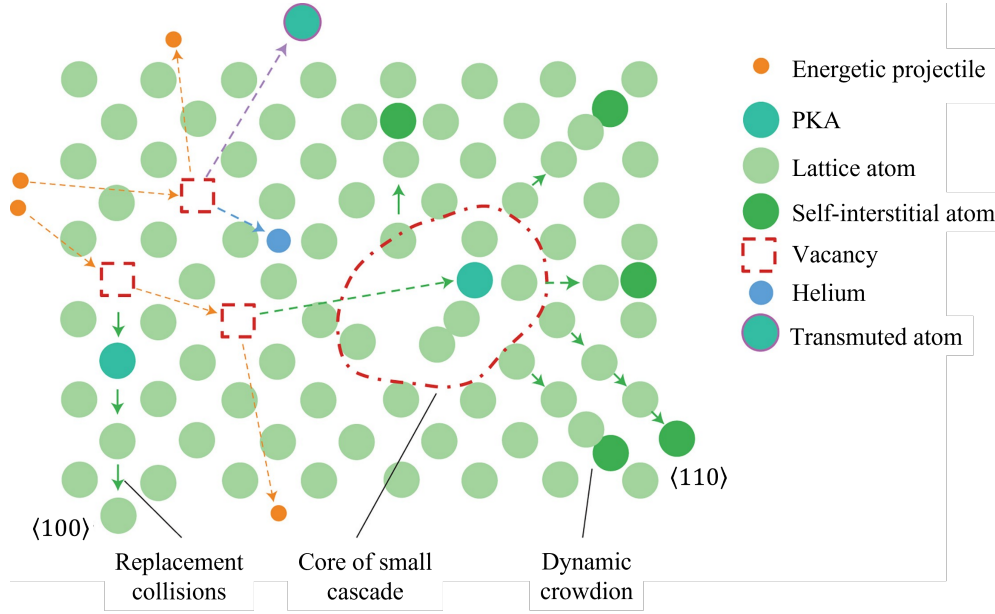
Figure 3.3: Primary damage induced by incoming particles [127].

theoretical Norgett, Robinson and Torrens (NRT) model as follows [128]:

$$N_F = \beta_e \frac{\xi(E_R) E_R}{2 E_p},$$

(3.8)

where $\xi(E_R)$ is the Lindhard partition function describing the fraction of energy going into a nuclear displacement. The displaced atoms can indeed lose energy also by means of electronic losses, which do not feed the collision cascade. The term β_e is the displacement efficiency and takes into account a more realistic potential to describe the scattering (other than the hard-sphere potential). The adopted value for β_e is 0.8 and it is close to the analytically derived asymptotic value used in the Robinson-Sigmund analysis [129]. The term $2E_p$ comes from the assumption that the energy is equally split between the two colliding atoms, according to the hard-sphere model.

The non-ionizing energy loss (NIEL)-scaling hypothesis

The non-ionizing energy loss (NIEL)-scaling hypothesis is a principle used to estimate the radiation damage caused by non-ionizing energy loss in materials. The NIEL refers to the portion of energy lost by a traversing particle that does not go into ionization and eventually leads to displacement damage. However, only a fraction of the NIEL leads to displacements

as part of the energy is dissipated in phonons[IV]. This fraction depends on the energy of the impinging particle. The NIEL is defined in units of MeVcm^2/g and can be calculated as follows [130]:

$$NIEL(E) = \frac{N_A}{A} \sum_i \int_{E_{min}}^{E_{max}} \left(\frac{d\sigma(E)}{dE_R}\right)_i \cdot E_R \cdot \xi(E_R) \cdot dE_R,$$ (3.9)

where N_A is the Avogadro number, A is the atomic mass of the target atom, E is the energy of the impinging particle and E_R is the energy given to the recoil atom. Term $(d\sigma(E)/dE_R)_i$ is the differential partial cross section for a particle with energy E to create a recoil atom with energy E_R in the $i - th$ reaction.NIEL can also be presented as displacement damage function D (NIEL cross-section) as follows [130]:

$$D(E) = \frac{A}{N_A} \cdot NIEL(E) = \sum_i \int_{E_{min}}^{E_{max}} \left(\frac{d\sigma(E)}{dE_R}\right)_i \cdot E_R \cdot \xi(E_R) \cdot dE_R,$$ (3.10)

where the displacement damage $D(E)$ is presented in units of MeV mb. An often-used standard metric for displacement damage is the *1 MeV-equivalent neutron fluence*, abbreviated with Φ_{eq}. This metric describes the damage produced in a material by neutrons having an energy of 1 MeV and it is usually normalized to 95 MeV mb. The calculated displacement functions for neutrons, protons, pions and electrons in the energy range from some meV to 10 GeV are plotted in Fig. 3.4.

The NIEL hypothesis assumes that radiation damage effects scale linearly with NIEL. For the simulated examples shown in Fig. 3.5 the number of vacancies should give a measure of the damage irrespective of their distribution, whether homogeneously scattered over a relatively wide volume (as for the case of low energetic proton damage) or clustered in high density in small regions (as in the case of neutron damage). Therefore, different particles or particles with different energies should be scalable using their NIEL (i.e., the number of displacements), and the damage can be normalized using the data in Fig. 3.4.

NIEL scaling is a powerful method for predicting displacement damage parameters in complex radiation fields. However, it has some limitations, such as differences in point-like and clustered defects contribution to device damage parameters [132]. The displacement damage functions in Fig. 3.4 are currently used to calculate the 1 MeV neutron equivalent fluence radiation fields in LHC and HL-LHC experiments.

[IV]At the quantum scale, phonons are waves of oscillatory atomic vibrational energy.
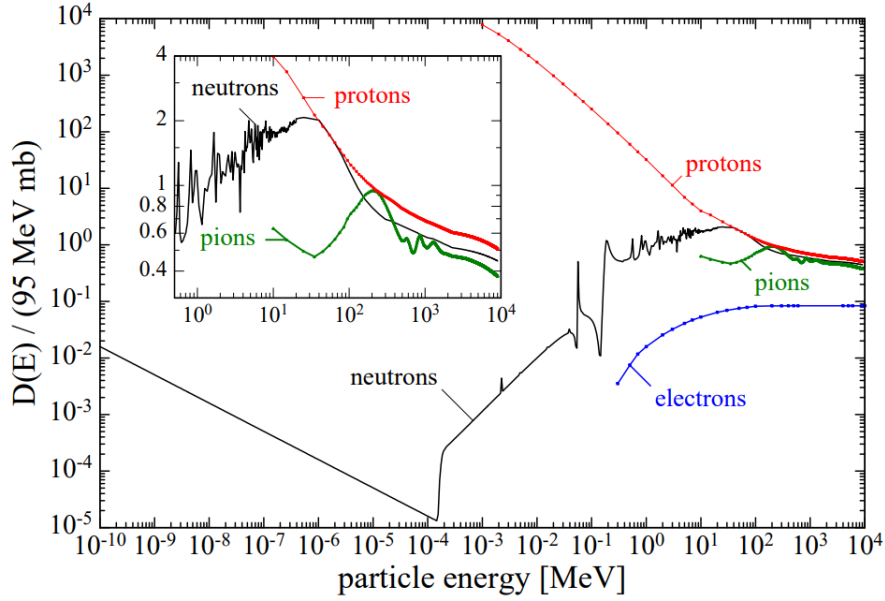
Figure 3.4: Non-ionizing energy loss (NIEL) cross-sections normalized to 95 MeV mb. The insert shows magnified D(E) for the most damaging particles at LHC [130].

Hardness factors

The damage effects of different types of irradiation with the same fluence vary significantly. Thus, it is useful to normalize the damage effects to a "standard irradiation". With the help of the displacement damage $D(E)$ it is possible to define a hardness factor κ allowing to compare the damage effects of different radiation sources with different particles and individual energy spectra $\phi(E)$. It is common practice to define the hardness factor κ in such a way that it compares the damage produced by specific irradiation to the damage which would have been produced by monoenergetic neutrons of 1 MeV and the same fluence [133]:

$$\kappa = \frac{1}{D_n(1MeV)} \cdot \frac{\int_0^\infty \frac{d\phi(E)}{dE} D(E) dE}{\int_0^\infty \frac{d\phi(E)}{dE} dE},$$

(3.11)

The $D_n(1$ MeV$)$ is set to 95 MeV mb to assure the independence of different calculations from the used binning of the spectra. The equivalent 1 MeV neutron fluence Φ_{eq} can be calculated by [133]:

$$\Phi_{eq} = \kappa \cdot \Phi = \kappa \int_0^\infty \frac{d\phi(E)}{dE} D(E) dE.$$

(3.12)
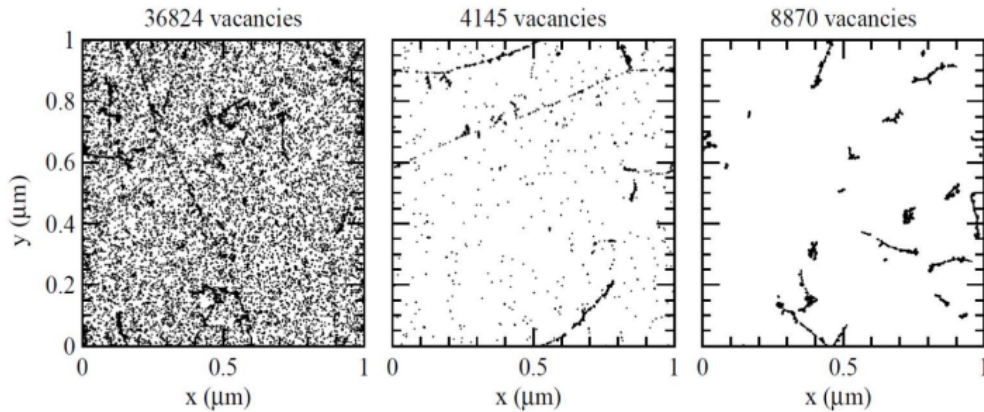
Figure 3.5: Simulation of microscopic defect formation with radiation and diffusion [131]. The vacancy distribution is produced with 10 MeV protons (left), 24 GeV protons (middle), and 1 MeV neutrons (right). The plots are projections over 1 μm of depth (z) and correspond to a fluence of 10^{14} n_{1MeV}/cm^2.

The hardness factors for the most commonly used irradiation facilities are given in Table 3.2.

Table 3.2: Measured hardness factors of commonly used irradiation particles [133].

	26 MeV protons	23 GeV protons	200 MeV pions	reactor neutrons
κ	1.85	0.62	1.14	0.92

Macroscopic Effects

Radiation-induced electrically active defects in the semiconductor bandgap can impact device performance in various ways. To quantify this impact, the Shockley-Read-Hall (SRH) framework can be used [134]. The effect of each defect can be calculated if certain information is known, such as the capture cross sections for holes (σ_p) and electrons (σ_n), position in the bandgap, type of defect, and concentration of the defect (N_t) [135]. On the device performance level, three main effects can be identified and formulated in the SRH framework: leakage current, effective space charge, and trapping, and they are illustrated in Fig. 3.6. These effects are discussed in depth in the following subsections.

Leakage Current

Leakage current (bulk generation current) is primarily caused by defect levels that are near the middle of the bandgap. This follows the NIEL hypothesis scaling for hadron damage, indicating that defect engineering (e.g. impurities in the silicon) does not affect it. The thermally generated electron-hole pairs are separated in the electric field before they can recombine, which gives rise to the bulk generation current (see Fig. 3.6 (c)). An increase in the
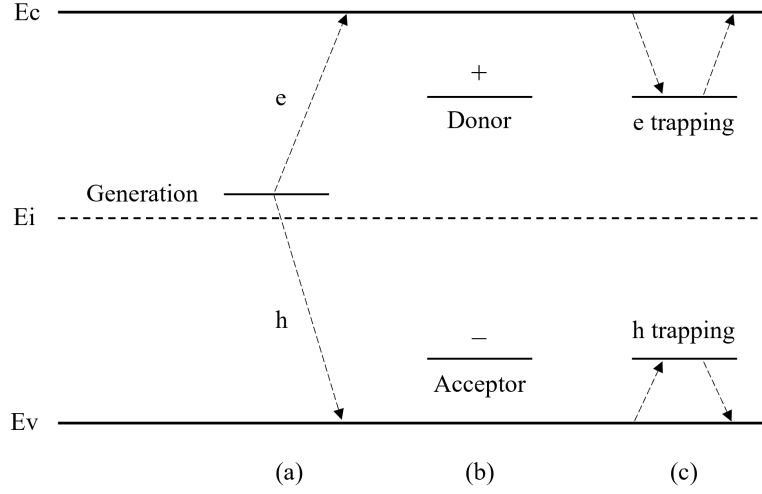
Figure 3.6: Consequences of deep energy levels to the operation of semiconductor detectors: (a) charged defects alter the space charge and therefore the electric field, (b) defects can trap and de-trap free carriers and (c) defects act as generation-recombination centers. Electrons and holes are denoted by e and h.

leakage current leads to an increase in the noise of the amplifiers and to an increase in power consumption as well.

The total leakage of the device is determined by summing the generation rate of all defect types, accounting for the active volume of the sensor. The equation for the total leakage takes into account the depletion width d and area A of the sensor and is given as follows [136]:

$$I_{leak} = q_0 d A \sum_{defect} G_t,$$ (3.13)

where q_0 is the elementary charge, and G_t is the generation rate of a single defect type t. In the case of neglectable free carrier concentrations (assuming that the generation rates of electrons and holes are equal), G_t is given as [136]:

$$G_t = N_t f_t e_n = N_t (1 - f_t) e_p = N_t \frac{e_n e_p}{e_n + e_p},$$ (3.14)

where f_t is defect occupancy with electrons, e_n and e_p represent the electron and hole emission rates of the detects.

Effective Space Charge

Depletion voltage is an important parameter in semiconductor detectors, and it can be affected by radiation-induced changes to the effective space charge as follows [137]:

$$V_{dep} = \frac{q_0 d^2}{2\epsilon\epsilon_0} \left| N_{eff} \right|,$$ (3.15)

where N_{eff} is the effective space charge, ϵ is the relative permittivity of semiconductor (e.g. silicon), ϵ_0 is the vacuum permittivity, d detector thickness, and q_0 is the elementary charge. The change in the effective space charge can result in a shift of the depletion voltage to lower or higher values. In the latter case, higher operation voltages may need to be applied to establish an electric field throughout the full sensor volume to avoid underdepletion and loss of active volume. Furthermore, inhomogeneous distribution of the space charge might lead to double junction effects or the shift of the highest electric field towards regions that are unprofitable for segmented sensors [132]. High local fields can lead furthermore to impact ionization effects or breakdown.

It has been shown that the change of the space charge in silicon is strongly material-dependent (e.g., oxygen content) and depends on the particle type used for the irradiation experiment (e.g., neutron versus proton damage) [138]. This implies that this damage effect does not directly scale with NIEL and can be altered or mitigated by defect engineering approaches (e.g., change of impurity content). Defects in the material can contribute to the space charge by either donating or accepting charges, which alters the electric field distribution and the depletion voltage of a device. The effective space charge N_{eff} (neglecting free carriers) is then given by the sum of all positively charged donors N_D and all negatively charged acceptors N_A as follows [130]:

$$N_{eff} = \sum_{donors} (1 - f_t)N_t - \sum_{acceptors} f_t N_t,$$ (3.16)

where the index t is running over all donor and acceptor such as defect types t with concentration N_t.

Charge Collection Efficiency (Trapping)

Electrons and holes generated by an ionizing particle in the silicon bulk drift to the electrodes if a field is applied (charge collection). However, the charge carriers can be trapped in the radiation-induced defects or impurities in the silicon material (see Fig 3.6 (b)). If the release

(detrapping) time is longer than the collection time of the system or if the concentration of defects is very high, the overall signal of the sensor is reduced. This is a major problem in high-fluence applications, where trapping becomes the limiting factor.

To mitigate this problem, device modifications leading to faster collection times can be made. In segmented sensors, electrons could be collected instead of holes at the sensing electrodes due to their higher mobility and the possibility to exploit charge multiplication by impact ionization in lower fields and without device breakdown.

The trapping is defined by the trapping time (inverse capture rate) τ_e for electrons and τ_h for holes that are calculated as [132]:

$$\frac{1}{\tau_e} = c_n(1 - f_t)N_t \tag{3.17}$$

$$\frac{1}{\tau_h} = c_p f_t N_t, \tag{3.18}$$

where N_t is the concentration of the traps, and c_n and c_p are the capture coefficients for electrons and holes. The effective trapping probability $1/\tau_{eff,e/h}$ for electrons and holes can be calculated by summing over the trapping probabilities of all traps with emission times longer than the integration time of the electronics, as follows [132]:

$$\frac{1}{\tau_{eff,e}} = \sum_{defects} c_{(n,t)}(1 - f_t)N_t \tag{3.19}$$

$$\frac{1}{\tau_{eff,h}} = \sum_{defects} c_{(p,t)} f_t N_t. \tag{3.20}$$

The effective trapping time constants depend on the energy levels of the defects or impurities, with electron traps having energy levels in the upper part of the band gap and hole traps having energy levels in the lower part of the band gap. Traps close to the mid-gap have a dominant contribution to the effective trapping times, as their emission times are long enough to be included in eqs. (3.19) and (3.20). Therefore, the depletion voltage must be chosen carefully to ensure that the depletion region extends deep enough into the bulk material to minimize the trapping of charge carriers by defects and impurities.

3.2.2 Surface Damage

In semiconductor detectors, the non-ionizing energy loss is responsible for bulk damage only. However, ionization can also cause permanent changes in the surface properties of the crystal. The surface of silicon material for example is characterized by a periodic lattice structure that abruptly terminates, leaving Si atoms without covalent bonds to their neighboring atoms. These so-called *dangling bonds* make the atoms highly active electrically and chemically. To prevent this issue, a silicon oxide film is thermally grown on the wafer to passivate the surface and prevent impurities from diffusing into the highly pure silicon bulk [139]. However, ionizing radiation can alter the number and properties of electronic states at the Si/SiO_2 interface.

Figure 3.7 depicts the cross-section of the silicon detector surface divided into silicon/oxide interface and silicon and oxide bulks. The border region between oxide and silicon crystal is characterized by a large defect density due to bond stress. In general, surface defects can be caused by growth and irradiation. According to their position in the oxide, the traps are divided into oxide bulk traps, border traps and interface traps [133]. The latter two are located close to the interface and can exchange charges with underlying silicon (switching traps). The oxide traps are mostly donors, which is the reason that net oxide charge density is always positive. The most important oxide defects are trivalent Si ($\equiv$Si·, donor), interstitial oxygen (OI, donor) and non-bridging oxygen ($\equiv$Si-O·, acceptor). Other important defects include hydrogen-related defects (all donors) [140]. Hydrogen is particularly important since it passivates the dangling bonds by attaching to them. The build-up of interface traps is not fully understood yet and there are different models explaining it [141]. The bulk and interface traps formed during the processing of the oxide can be passivated by annealing (350-500 °C) in a hydrogen-rich environment [133].

In contrast to the silicon bulk, electron-hole pair creation is not fully reversible in an insulator, and recombination rates can vary (between several percent and almost 100 %) depending on the oxide quality. In addition to recombination, generated charge carriers can also be captured by existing defects, where the emission is highly suppressed since the band gap is much larger in oxide and nitride layers ($E_g = 8.8$ eV in SiO_2 and $E_g = 5$ eV in Si_3N_4). In the oxide, the mobility of electrons ($\mu_{e,SiO_2} \approx 20$ cm^2/(V·s)) is several orders of magnitude higher than that of holes ($\mu_{h,SiO_2} \approx 2 \cdot 10^{-5}$ cm^2/(V·s)). This leads to a fast separation of electron-hole pairs. Electrons drift to the metal electrode, while the holes drift by a hopping mechanism via shallow levels to the Si - SiO_2 interface, especially when a voltage is applied. The effect is enhanced for a positive voltage applied on the metal side during radiation; electron movement is accelerated to the metal side and holes drift to the interface, a standard mode for a transistor.

3.3 Radiation Effects on Polymer-based Sensors

Covalent bonds are the main type of chemical bond in polymers and they are highly susceptible to ionizing radiation. As a result, radiation not only affects the physico-chemical properties of polymeric materials but also impacts their mechanical and other macroscopic characteristics.
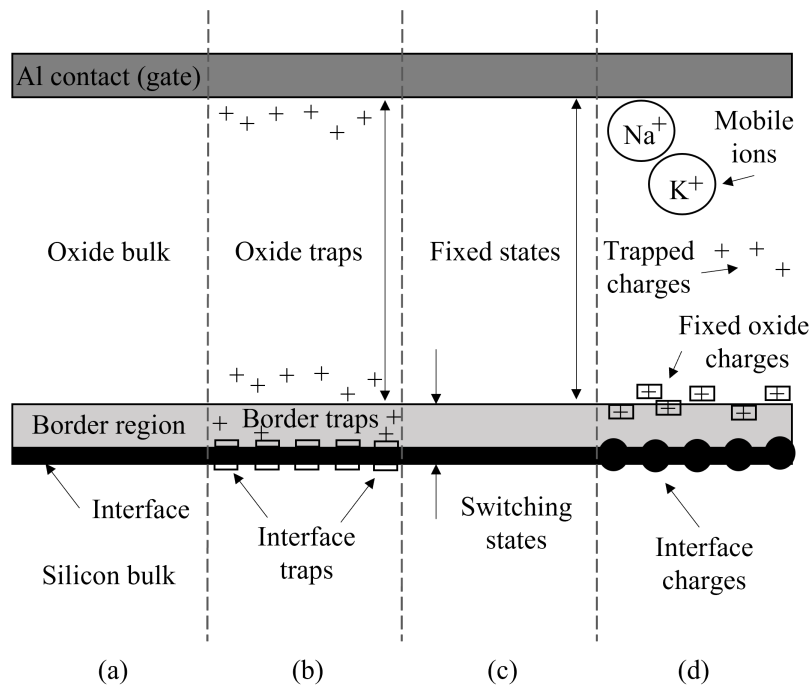
Figure 3.7: Schematic view of the surface of a silicon detector; (a) surface regions, (b) trap locations, (c) states, (d) oxide charges [133].

When a high-energy particle collides with an electron, an inelastic scattering process can occur, leading to the ejection of an electron from the atom or molecule and the formation of an ion or radical. Radicals are molecules or ions with unpaired valence electrons, which make them highly reactive in chemical reactions. This reactivity can result in the breaking of chemical bonds, breaks in polymer chains, structural rearrangements of the polymer in affected areas, and the ejections of hydrogen or small molecules.

Reactions initiated by radiation can be classified into two main types [142]:

i) **Cross-linking:** Cross-linking is the intermolecular bond formation of polymer chains, as shown in Fig. 3.8 (a). The commonly accepted mechanism involves the cleavage of a C-H bond on one polymer chain to form a hydrogen atom, followed by abstraction of a second hydrogen atom from a neighboring chain to produce molecular hydrogen. Then the two adjacent polymeric radicals combine to form a cross-link. This process increases the average molecular weight of polymer. The mechanism of cross-linking generally varies with the different types of polymers. The degree of cross-linking is proportional to the radiation dose.

ii) **Scission:** Scission is the opposite process of cross-linking and involves the breaking of C-C bonds, as shown in Fig. 3.8 (b). This process reduces the average molecular weight of polymer. Cross-linking usually increases tensile strength properties and reduces elongation, while scission leads to a decrease in both tensile strength and elongation.

(a)

(b)
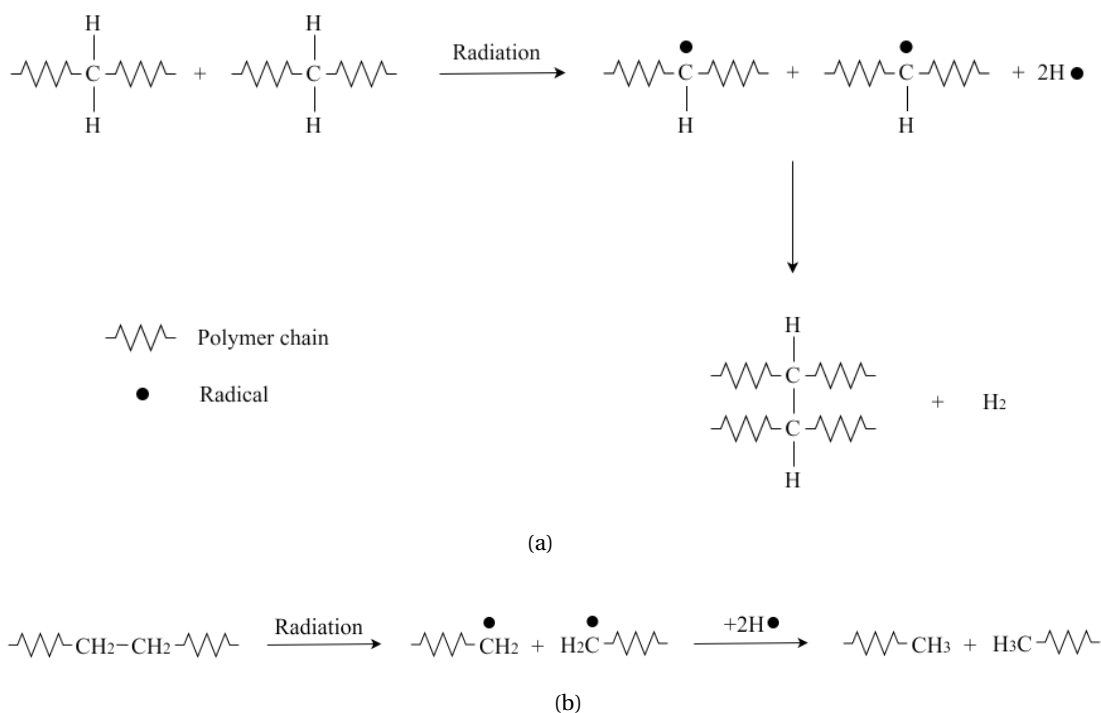
Figure 3.8: Radiation-induced (a) cross-linking and (b) scission in the polymer material [142].

As depicted in the degradation reactions in Fig. 3.8, radiation exposure can result in the generation of small molecules. The specific molecules produced depend on the type of polymer and the energy of the radiation.

However, the dominant effect of radiation on polymers depends on factors such as molecular structure, the presence and type of additives, and the surrounding environment (inert or oxidative). When oxygen is present, it rapidly reacts with the radicals produced by irradiation, leading to oxidation chemistry dominating the free-radical reaction pathways and molecular products. The reaction between oxygen and radicals follows a chain reaction mechanism involving radical multiplication. Consequently, the effects of radiation on the physical properties of macromolecular materials are significantly different under oxidizing conditions compared to non-oxidizing conditions [143].

Furthermore, under radiation-oxidation conditions, the extent of radiation-induced degradation in certain polymers can be strongly influenced by environmental factors other than just the absorbed dose. Time/temperature phenomena, including dose-rate effects and post-irradiation effects, are equally important as molecular structural differences for determining the radiation resistance of many polymers. It is generally admitted that irradiating polymers below their glass transition temperature does not result in a synergistic effect between radiation and temperature. The degradation observed is not significantly different from irradiation at room temperature and temperature ageing.

At cryogenic temperatures, organic materials become stiffer and more brittle while losing plasticity and impact strength. Irradiation of these materials, whether at low or room temperature, does not affect their degradation. The mechanical properties of polymer-based materials are more influenced by the test temperature rather than the irradiation temperature [143].

When studying the effects of radiation on adhesive systems, it is important to note that the adhesive-adherend interface is typically not sensitive to radiation. As the interface is responsible for the strength of the bonding (the bonding fails at the interface), no degradation will be observed until the polymer starts to degrade. Polymer degradation leads to a reduction in deformation at break, and of the modulus at higher absorbed doses. This effect is particularly pronounced in soft adhesives such as silicone. However, this remark about the non-degrading interface is not applicable in cases where poorly prepared surfaces contain pollutants and oxidants.

3.4 Radiation Effects on Electronics

Understanding the impact of radiation on microelectronic systems in LHC experiment radiation environments is crucial for designing and testing electronics that meet reliability requirements. Additionally, selecting and qualifying commercial-off-the-shelf (COTS) electronics requires knowledge of their performance in radiation environments for which they may not have been designed. However, reproducing all radiation conditions in test facilities is not possible, and the response of CMOS and bipolar electronics can depend on various factors. Radiation affects microelectronic devices in three ways: total ionizing dose (TID) effects, single event effects (SEE), and non-ionizing energy loss (NIEL) effects [132].

3.4.1 Total ionizing dose (TID) effects

The effects of Total Ionizing Dose (TID) can lead to device degradation and failure over time. TID is associated with trapped charge states that accumulate in the oxide layer or at the oxide-bulk interface, resulting in changes in electric fields and affecting electrical characteristics. TID affects the threshold voltage, charge mobility, and leakage current in Metal-Oxide-Semiconductor (MOS) transistors.

During irradiation, electrons and holes are generated in pairs by ionizing radiation, and while they are typically transported through the usual mechanisms of diffusion and drift, charges in insulating oxide layers are less mobile than those in doped semiconductor regions. This can result in an accumulation of positive charge during irradiation, causing CMOS and bipolar devices to experience shifts in threshold voltages, opening of parasitic conductive paths, and decreased current gains. CMOS structures can also experience degradation due to migrating holes that initiate defects close to the oxide-bulk interface. The build-up and annealing of these effects depend on dose rate and temperature, and the non-monotonic behavior of the leakage current in NMOS transistors is a well-known example of this effect.

Tests to qualify electronic components for TID in LHC radiation environments should be performed in similar radiation and environmental conditions to minimize errors, but high dose rates can cause *low dose-rate* (LDR) effects that complicate the prediction of long-term behavior. Irradiating at high dose rates causes a negative shift in the threshold voltage, while low dose rates allow for more annealing of oxide traps, leading to the impact of interface traps and positive shifts in the threshold voltage. Test methods have been developed to take LDR effects into account for radiation hardness assurance (RHA), and the qualification of bipolar components is more challenging due to enhanced LDR sensitivity (ELDRS), which makes it difficult to predict real-life application behavior from laboratory results [144].

In addition to low dose-rate (LDR) effects, experiments also need to consider the sensitivity of TID response in different wafer production batches (so-called *Lot-to-lot effects*) [145]. Application-Specific Integrated Circuits (ASICs) are designed using a specific technology process and are manufactured by a single company across multiple production plants. This reduces variability in their radiation resistance since they can be fabricated at a particular plant upon request. On the other hand, COTS components are typically purchased from distributors, and purchasing lots are made up of samples of unknown origin. Unless specific arrangements are made with the supplier to guarantee a common and known origin of the components, the purchased lot is assumed to be inhomogeneous, meaning that the components may come from various production lots. Differences in radiation damage have been observed among samples from various manufacturing plants or even different lots produced at the same Fab (see Fig. 3.9) [146]. In addition to the natural variability in their characteristics, which is normal even in tightly controlled processes due to the complex nature of modern CMOS technologies, manufacturers may introduce modifications to the processing sequence without prior notification. As a result, it is risky to assume comparable radiation response even for ASICs manufactured at the same Fab at different times. Similarly, for COTS of unknown origin, significant variation can be observed within the same purchase lot. Therefore, it is important to conduct sample testing for each batch or lot.

3.4.2   Single event effects (SEE)

The term Single Event Effects (SEE) refers to a group of radiation effects on electronic circuits that occur when a single particle passes through the device. Examples of SEE include Single Event Upset (SEU), Single Event Latch-up (SEL), Single Event Gate Rupture (SEGR), and Single Event Burnout (SEB) [147]. SEEs can be divided into three categories based on their impact on the system:

i) **soft SEEs** (also called soft SEUs) - refer to radiation-induced bit flips that corrupt data or system configurations. These effects are non-permanent and can be corrected by resetting the system or rewriting data in memory,

ii) **hard SEEs** (also called hard SEUs) - they are permanent and cannot be fixed by resetting or rewriting data (e.g. a bit stuck in a memory cell),
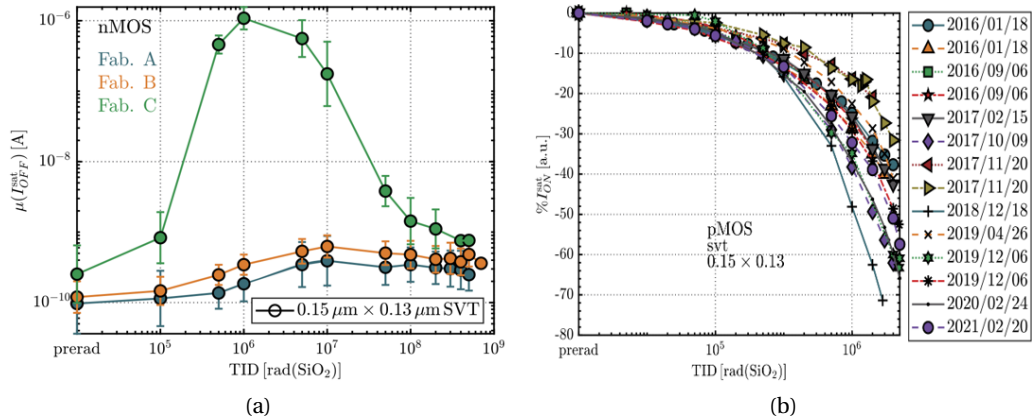
Figure 3.9: (a) Mean and standard deviation of the leakage current as a function of TID for nMOS transistors in 130 nm CMOS technology. The leakage current peak at about 1 Mrad(SiO2) is observed in samples from Fab. C. (b) Lot-to-lot variability of 0.15 μm × 0.13 μm pMOS transistors in 130 nm CMOS technology, coming from the same Fab., as a function of TID [146].

iii) **destructive SEEs** (SELs, SEBs, and SEGRs) - cause permanent damage to the circuit. SELs are destructive SEEs, unless a robust architectural solution protects the circuit against thermal destruction resulting from latch-up. SEBs and SEGRs are always destructive SEEs typically affecting high-power and/or high-voltage circuits.

SEEs are caused by the deposition of ionizing energy in a small sensitive area of the chip by a single particle. SEUs, for instance, typically affect the drain of a transistor, and the charge required for the event is usually less than that needed for destructive SEE. Fragments from hadronic collisions of protons, neutrons, and pions with atoms in the circuit can trigger SEE, but only if they have a large linear energy transfer (LET) and are produced close enough to the sensitive area. As the feature size of integrated circuits decreases and the operating voltage reduces, circuits become more sensitive to smaller amounts of deposited charge. However, this is offset by the reduction in sensitive area size, reducing the probability of fragments traversing the sensitive area and its path length within it. Nevertheless, the vulnerability of modern chips to low-energy neutron interactions could increase their susceptibility to SEE. Finally, while the SEU cross-section per node may decrease, the SEU cross-section per chip will increase substantially due to the higher node density.

3.4.3 Non-ionizing energy loss (NIEL) effects

As mentioned in previous sections, the Non-ionizing energy loss (NIEL) effects, also known as displacement damage, refer to the cumulative degradation caused by particles interacting with semiconductor material. This interaction displaces atoms and creates defects and clusters of defects in the crystal lattice, resulting in changes to the device electrical and optical properties.

The accumulation of NIEL defects can cause increased leakage currents and changes in the effective doping concentrations. Although CMOS devices are typically less susceptible to NIEL effects than TID due to their high majority charge carrier doping, the impact of NIEL can still be significant in some MOS devices with low doping features such as LDMOS. Compared to CMOS, bipolar electronics are generally more sensitive to bulk defects.

3.5 Summary

The performance of semiconductor particle detectors is significantly impacted by radiation damage to the crystal lattice and surface structure. We can distinguish between two radiation damage mechanisms: displacement damage and surface damage. Displacement damage is produced by non-ionizing energy loss and it can be characterized by microscopic defects such as vacancies, interstitials, Frenkel pairs, and clusters of lattice defects. These defects can further lead to macroscopic effects on detector performance such as charge levels, space charge, electric field, leakage current, and trapping probability. Surface damage represents the permanent changes in the surface properties of crystals and it is caused by ionization.

In the case of polymer-based sensors, radiation exposure can lead to two types of damage processes: cross-linking and scission. The cross-linking process increases the average molecular weight of the polymer, while scission reduces it. Cross-linking usually enhances tensile strength properties and reduces the elongation of the polymer material, whereas scission leads to a decrease in both tensile strength and elongation.

Radiation also affects electronics through total ionizing dose (TID) effects, single event effects (SEE), and non-ionizing energy loss (NIEL) effects. Understanding these radiation effects is required for selecting and qualifying COTS sensors and electronics for use in the HEP environment.

4 Empirical Models of Humidity and Temperature Sensor Candidates [I]

I think it's much more interesting to live in uncertainty
than to have answers that could be wrong.
— Richard Feynman

As discussed in Chapter **1**, the HL-LHC is set to significantly increase the present instantaneous luminosity by a factor of five, resulting in higher radiation doses that current materials cannot withstand. To ensure the equipment's ability to withstand this challenging environment, all materials entering the detector environment must undergo rigorous testing and examination for harsh radiation doses.

In addition to radiation tolerance, the equipment must be capable of functioning efficiently in sub-zero temperatures and under a strong magnetic field of 4 T. This chapter presents the findings from irradiation experiments, temperature dependence tests, and behavior of the humidity sensors in a strong magnetic field. Furthermore, the results from exposing the temperature sensor candidate to the proton beam are analyzed and discussed.

To better understand the environmental conditions of the detector, the following section provides a summary of the expected integral fluences and operating temperatures of the upcoming CMS sub-detectors, as well as the mapping of the magnetic field in the CMS detector.

[I]Part of this chapter has been published in [148] and [149].

Tracker
Temperature: -35 ℃
Fluence: $3 \cdot 10^{14}$ to $2.3 \cdot 10^{16}$ n_{eq}/cm^2

ECAL
Temperature: 9 ℃
Fluence: $1.2 \cdot 10^{14}$ to $2.5 \cdot 10^{14}$ n_{eq}/cm^2

HGCAL
Temperature: -35 ℃
Fluence: $1 \cdot 10^{13}$ to $2 \cdot 10^{16}$ n_{eq}/cm^2
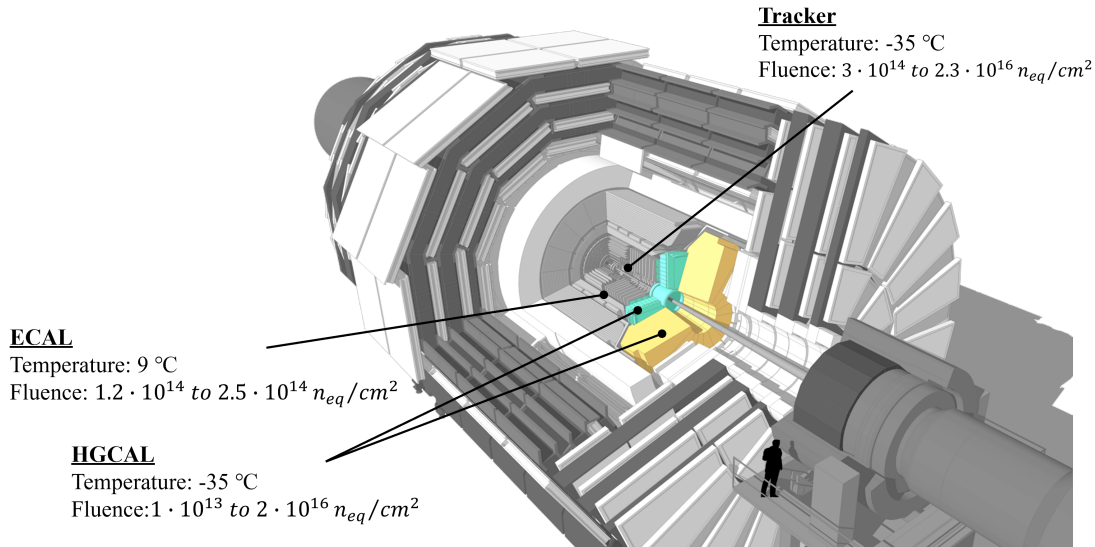
Figure 4.1: A 3D overview of the CMS detector with the corresponding integral fluences, anticipated for the period of over ten years of the detector operation, and operating temperatures for sub-detectors that require dew point temperature measurements. The replacement of the ECAL and HCAL endcaps by the HGCAL is indicated by a blue and yellow colour, respectively.

4.1 Environmental conditions in the CMS detector

As the LHC prepares for its next phase, the HL-LHC, the CMS detector must be upgraded to handle the higher radiation levels that will be generated. The upgrade involves replacing and improving several sub-detectors. The endcaps of the ECAL and HCAL are going to be replaced by the HGCal as shown in Figure 4.1. The figure gives an overview of the expected equivalent 1 MeV neutron fluences (Φ_{eq}) obtained by FLUKA software for each sub-detector where dew point temperature measurements are necessary, as well as their foreseen operating temperatures. The Tracker, which is closest to the collision point, will receive the highest radiation dose, followed by the HGCal sub-detector. To withstand this radiation, these sub-detectors will be primarily made of silicon and operate at temperatures as low as minus 35 degrees Celsius.

The expected radiation dose for the Tracker is estimated to range from $3 \cdot 10^{14}$ n_{eq}/cm^2 to $2.3 \cdot 10^{16}$ n_{eq}/cm^2, while the HGCal is anticipated to gradually receive from $1 \cdot 10^{13}$ n_{eq}/cm^2 to $2 \cdot 10^{16}$ n_{eq}/cm^2. The ECAL sub-detector will also receive high levels of radiation, with expected integrated fluences ranging from $1.2 \cdot 10^{14}$ n_{eq}/cm^2 to $2.5 \cdot 10^{14}$ n_{eq}/cm^2. The ECAL sub-detector will operate at a temperature of 9 degrees Celsius.

As for the magnetic field, Fig. 4.2 provides a mapping of the magnetic flux density predicted on a longitudinal section of the CMS detector [150]. The CMS solenoid generates a magnetic field of around 4 T. Approximately two-thirds of the magnetic flux return through the barrel yoke, half of which enters directly into the barrel without passing through the endcap disks.
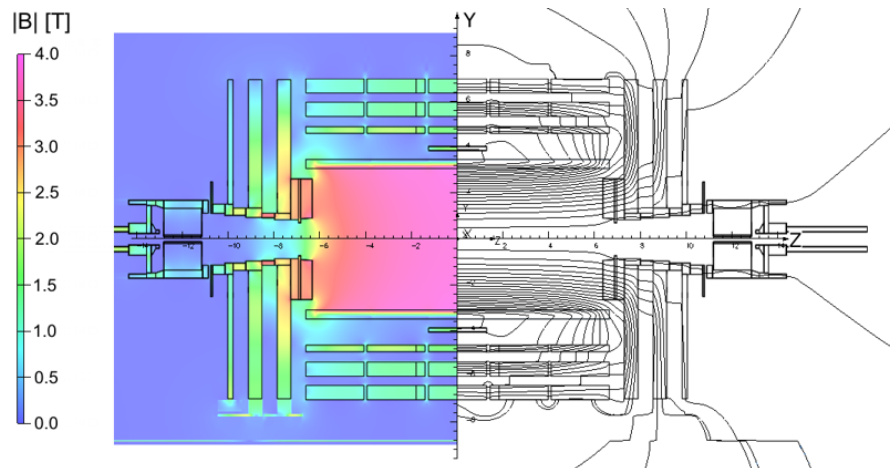
Figure 4.2: Value of the magnetic field (left) and field lines (right) predicted on a longitudinal section of the CMS detector, at a central magnetic flux density of 3.8 T. Each field line represents a magnetic flux increment of 6 Wb [150].

One-third of the total flux escapes radially, returning outside the steel yoke.

4.2 Radiation Tolerance of the Selected Humidity and Temperature Sensor Candidates

To assess the radiation tolerance of materials entering CERN accelerator complex and detectors, several irradiation facilities have been established at CERN: i) the **irrad**iation proton (IRRAD) facility, [151], ii) the **C**ERN **H**igh energy **A**ccele**R**ator **M**ixed field (CHARM) facility, [152], and iii) **G**amma **I**rradiation **F**acility (GIF++) facility [153]. The IRRAD facility exposes samples directly to the proton beam, whereas the CHARM facility uses secondary particles (known as showers), generated by proton interaction with a metallic target. The GIF++ facility combines high energy charged particle beams, primarily muon beam with momentum up to 100 GeV/c, with a 14 TBq^{137}Cesium source to produce a background gamma field. In addition to these facilities, numerous X-ray beams are available at CERN, and they are commonly used to emulate electronics and cable aging, [154], [155].

The radiation field of high-energy physics detectors is complex, with the presence of various leptons and hadrons of different types, masses, and energies. This environment can lead to three failure mechanisms for detector devices: ionization damage, single-event effects, and displacement damage effects (see Chapter **3**). Some devices may even be susceptible to two or all three of these mechanisms. Therefore, it is critical to investigate the radiation hardness of detectors, electronics components, systems, and materials prior to using them in real-detector systems.

To replicate all of these failure scenarios, a source beam of protons is employed for testing.
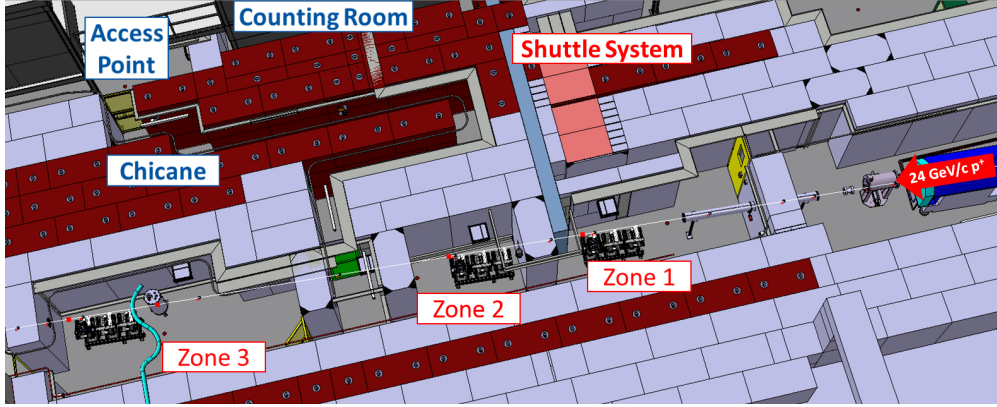
Figure 4.3: The 3D schematic drawing of the IRRAD proton facility. The material is placed in different zone depending on the device nature and the dose needed to receive. A shuttle system is used to insert the samples in the radiation area.

The below-discussed experiments are conducted at the IRRAD facility.

4.2.1   IRRAD proton facility

The IRRAD proton facility is located along the T8 beam-line at CERN, where the primary proton beam is extracted from the Proton Synchrotron (PS) ring. The IRRAD facility is divided into three separate zones, based on the particular nature of the samples to be irradiated, as depicted in Figure 4.3. To minimize radiation background during sample irradiation, each zone is demarcated by an 80 cm thick wall, perforated to allow the beam to pass through. The first zone is positioned closest to the beam-line and is designated for sample placement to receive the maximum feasible dosage [156].

The proton beam has a Gaussian distribution, with a standard deviation of 12 x 12 mm^2 full width at half maximum. It has a momentum of 24 GeV/s, and is delivered in 400 ms intervals or "spills". There is a minimum 2.4 s gap between each spill, with an average of $5 \cdot 10^{11}$ particles per spill [157].

The required proton fluence (Φ_P) for sensor exposure can be computed by the ratio of the equivalent 1 MeV neutron fluence Φ_{eq} and hardness factor κ:

$$\Phi_P = \frac{\Phi_{eq}}{\kappa} \tag{4.1}$$

where, for the 24 GeV/c proton beam, the estimation of the hardness factor from the experimental measurements is $\kappa = 0.62$ [158]. Having the value of the proton fluence, the effective dose D can be computed as follows:

$$D = 1.602 \cdot 10^{-10} \cdot \left(\frac{dE}{dx} \right)_{min} \cdot \Phi_P \tag{4.2}$$

where D is expressed in Gy^{II}. Term $\left(\frac{dE}{dx} \right)_{min}$ refers to the energy loss per unit path length of a charged particle as it passes through a medium. In the case of silicon, it has a value of 1.664 $MeV/(g/cm^2)$.

4.2.2   Radiation Effects on Humidity Sensors - 1st irradiation campaign

The first irradiation campaign was conducted on a mini version of the MK33-W relative humidity sensor to evaluate its performance under radiation [159]. The MK33-W mini relative humidity sensor is a capacitive type sensor with a capacitance of 200±40 pF at 30 %rh and 23 °C, and a sensitivity of 0.3 pF/%rh, allowing for an operational range of 30 pF from 0 to 100 %rh. The first irradiation tests were conducted using the split sensor electronic version, where the sensors were separated from the readout electronics by cable. This module version was calibrated by the company to minimize the cable parasitic effects.

Experimental Setup

The schematic of the experimental setup is presented in Fig. 4.4. Five sensors have been placed in the irradiation zone connected to the readout electronics over 40-meter-long cables. The readout electronics were positioned in a non-irradiated room with the reference sensor. The exposed samples and the reference sensor were kept at a stable temperature of 20 °C, controlled by the air conditioning unit, and the same, but not controlled, relative humidity levels.

The sensor conditioning and readout were implemented in a programmable logic controller (PLC)-based system, similar to all detector safety systems used in the CMS detector. A supervisory control and data acquisition (SCADA) interface was used to provide the user with quasi "real-time" access to data and easy visualization while storing data in a proper database. In order to visualize data, there was a delay of some seconds between data acquisition and displaying. However, this delay is typically insignificant when measuring relative humidity.

Results and Discussion

The proton fluence reached for sensor characterization was $7.5 \cdot 10^{15}$ protons/cm^2, with a deviation of ± 7%. The accumulated proton fluence is equivalent to $4.65 \cdot 10^{15}$ n_{eq}/cm^2 of the equivalent 1 MeV neutron fluence.

[II]Gy is defined as the absorption of one Joule of radiation energy by one kilogram of matter. As an alternative, the absorbed radiation dose may be expressed in rad, where 1 rad corresponds to 0.01 Gy
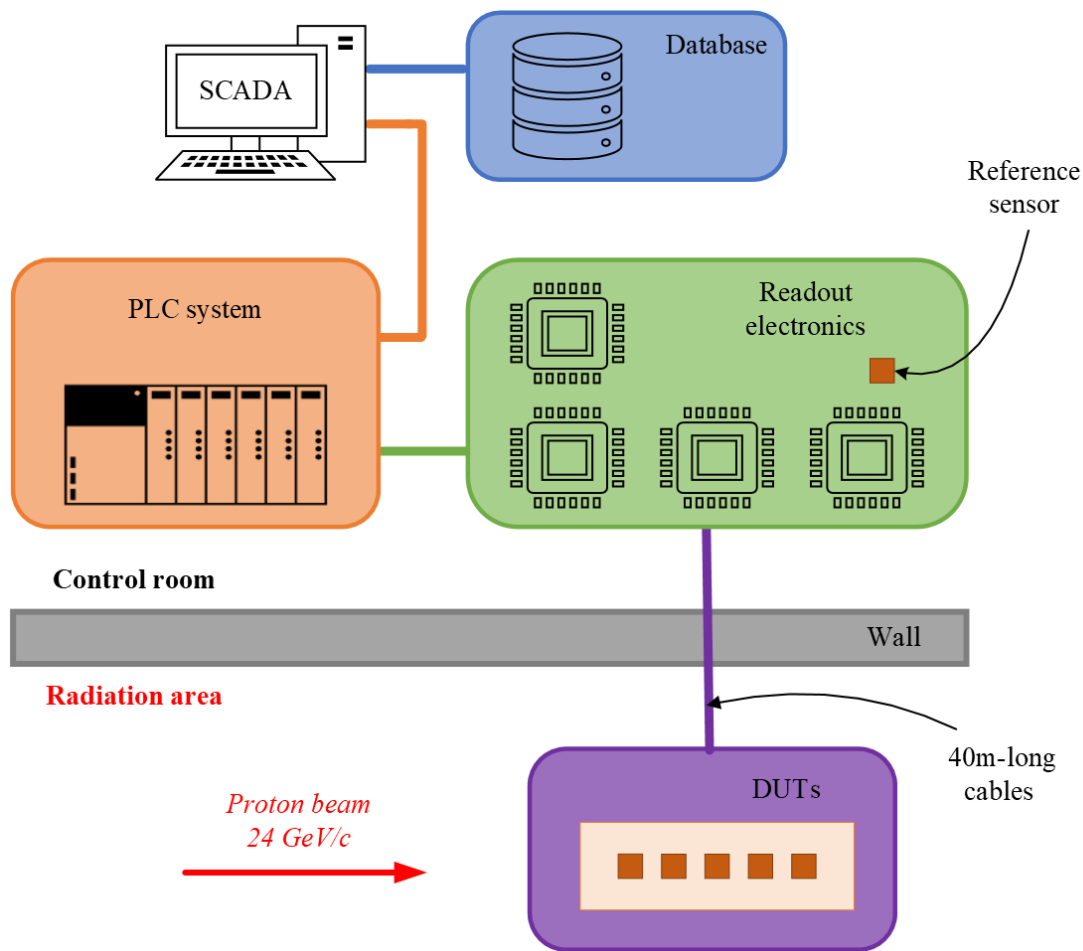
Figure 4.4: Schematic of the first irradiation campaign. Sensors were placed in the irradiation zone, while the readout electronics were located in the non-radiation-affected area. The readout electronics were implemented in the PLC-based system, and the SCADA interface for data visualization was provided to the user.

Fig. 4.5 depicts the reference sensor measurements taken during the irradiation campaign, with the relative humidity values fluctuating between 28 %rh and 42 %rh. Fig. 4.6 shows the outputs of the sensors with respect to the received fluence, where is demonstrated that the outputs do not completely depend on the change in relative humidity. Specifically, for a period between 200 to 245 hours, the relative humidity measured by the reference sensor ranged from 28 to 41 %rh. For the same period, the accumulated fluence of the exposed sensors increased from $6 \cdot 10^{15}$ to $7.5 \cdot 10^{15}$ protons/cm^2, causing around a 30 %rh variation in the outputs of the sensors (Fig. 4.6). This suggests that the output is influenced by the amount of received dose in addition to humid air.

Furthermore, considering the difference between the exposed sensors and the reference one, a linear relationship between the output signal of the exposed sensors and the received fluence was observed, as evident in Fig. 4.7. Fitting with a first-degree polynomial confirms the
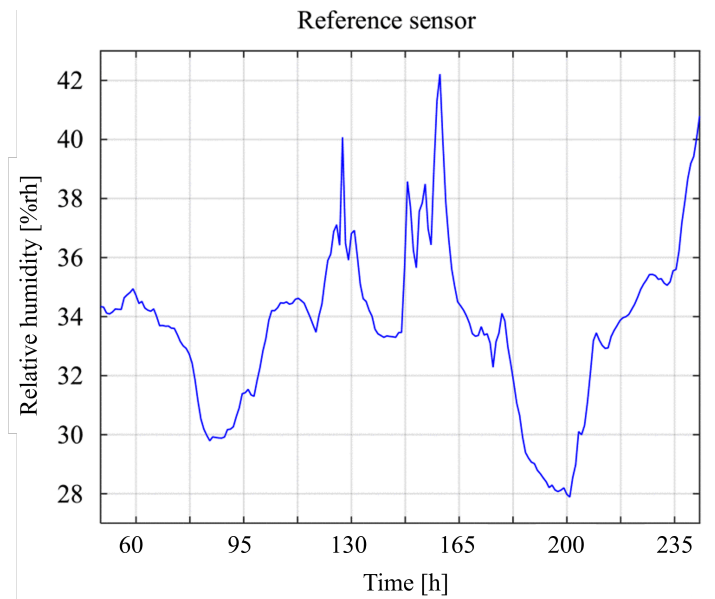
Figure 4.5: Continuous measurements of the reference sensor during the first irradiation campaign. The relative humidity measured with the reference sensor ranged between 28 %rh and 42 %rh.
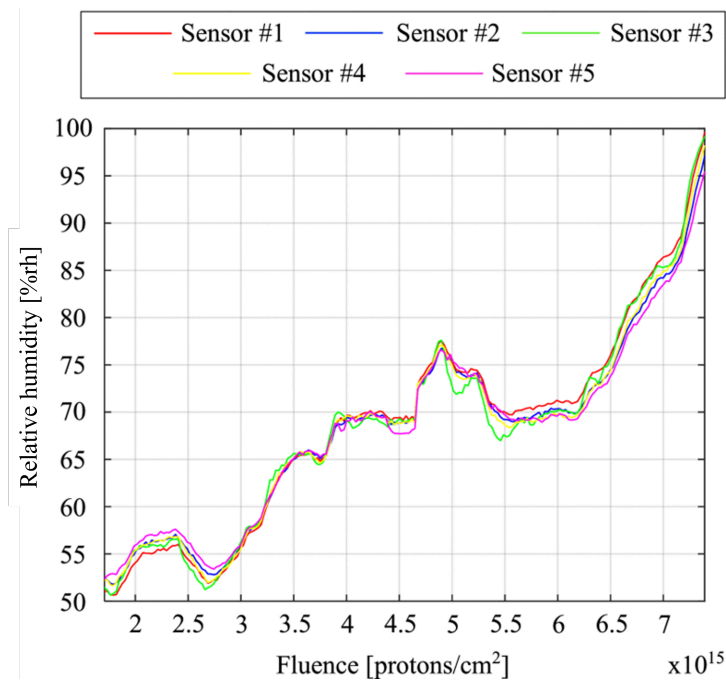
Figure 4.6: Continuous measurements of the sensors subjected to the direct proton beam. The measurements were taken in the controlled temperature and non-controlled humidity environment.
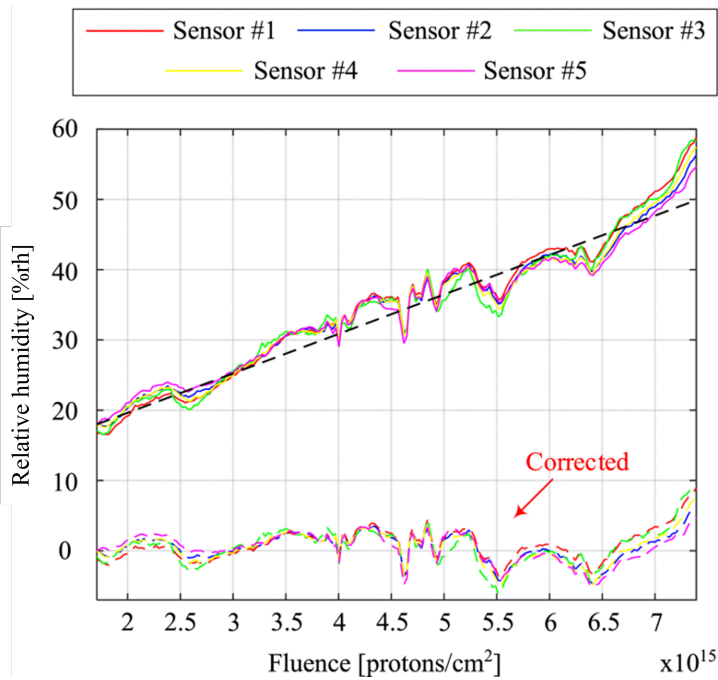
Figure 4.7: Comparison of measurements between the sensors exposed to the proton beam and the reference sensor. The dashed lines represent the deviation of the exposed sensors after recompensating for the radiation effects.

linearity of the effect, with the sensitivity of the sensor output being approximately $5.61 \cdot 10^{-15}$ %rh/(protons/cm^2). After applying correction, the deviation in relative humidity between the irradiated sensors was around 3 %rh, as demonstrated in the same figure. In the beginning, output change is almost constant with respect to radiation, while for large (accumulated) radiation the gradient of the output of the sensor function becomes significantly larger.

The radiation tolerance test at the IRRAD facility provided the initial data for identifying a relative humidity sensor capable of functioning in the current and future detectors in the LHC. The experiment has demonstrated enough good radiation tolerance at high doses after correction, and hence, this type of humidity sensor is a promising candidate for future tests regarding its accuracy and sensitivity before and after the irradiation campaign.

4.2.3   Radiation Effects on Humidity Sensors - 2nd irradiation campaign

Following the promising results obtained in the first radiation campaign, the "bigger" version of the MK33-W sensor has been considered and tested under radiation. The sensitivity of the sensor is 0.45 pF/%rh, and its capacitance at 30 %rh and room temperature is 300 pF ± 40 pF. The second irradiation campaign was conducted in controlled environmental conditions, whereby the samples were placed in a cold box to achieve and regulate subzero temperatures. Furthermore, a special gas system comprising pre-calibrated gas mixtures was used to regulate the humidity levels inside the cold box. The obtained results from the irradiation tests are

Figure 4.8: A photograph of the cold box with the cooling elements. The samples that are going under irradiation are attached to the lid of the cold box. The cold box contains a special opening for the insertion of the pre-calibrated gas mixture to avoid having condensation inside when operating at negative temperatures.

discussed herein.

Experimental Setup

In the LHC experiments, silicon-based detectors are kept at low temperatures to avoid annealing effects, reduce leakage current, and prevent thermal runaway of sensors and electronics [160]. Therefore, samples are held at low temperatures to simulate the real detector operational environment during irradiation experiments. For this purpose, a specially designed cold box with a volume of 0.05 m^3 was used to maintain a constant and low temperature throughout the second irradiation process (see Fig. 4.8).

The IRRAD proton facility is equipped with compressed and nitrogen gas lines. The compressed gas is used to supply the cooling system, while nitrogen (or dry air) is flushed inside the cold box to ensure a dry atmosphere and the absence of condensation during irradiation. Additionally, other gas lines are available for users to switch from nitrogen (or dry air) to other pre-calibrated gas mixtures.

The signal conditioning units were located in the IRRAD control room, which is a radiation-free zone situated 30 meters away from the sensors. This distance allowed for the simulation of the real system expected in the CMS detector. The experimental setup is schematically depicted in Fig. 4.9. The sensor conditioning units were implemented in the PLC-based system through analog modules. The SCADA interface provided quasi "real-time" data access,

easy visualization, and data storage in the Oracle database.

Results and Discussion

The sensor samples were directly subjected to the proton beam for more than 33 days. Three sensors, coming from the same wafer, were inserted in a customized 3D printed structure, made of the radiation-resistant Accura 25 material, and affixed to the lid of the cold box. The cold box was positioned in Zone 1 of the radiation area as depicted in Fig. 4.10. The temperature in the cold box was between -19 °C and -21 °C during the entire experiment. Several pre-calibrated gas mixtures were used to test the responsivity of the sensors.

Measurements were taken prior to the irradiation, throughout the irradiation process, and during the sensor relaxation phase (annealing) at different environmental conditions, and they are briefly analyzed and discussed in the following subsections.

Evaluation of sensor responsiveness before irradiation

To evaluate the responsiveness of the sensors prior to the irradiation experiment, 100 ppm (parts per million) calibrated gas mixture (99.9 % argon) and compressed dry air were used. The flow rate and gas flow pressure were controlled using a flow meter and flow pressure controller. The flow rate was adjusted between 3 l/min and 5 l/min with a pressure flow of 1 bar for the 100 ppm gas mixture to ensure the durability of the gas bottle. Compressed dry air was used throughout the entire experiment.

The Edgetech Dew Point Meter, one of the most reliable instruments for dew point temperature measurements presently available in the market, was used to measure the dew point temperatures of these gas mixtures before entering the cold box. The dew point temperature of the dry air was around -60 °C, while in the case of 100 ppm gas, the dew point temperature was -45 °C. The ambient temperature inside the cold box was around -20 °C.

The measurements were taken for a 40-minute interval at two different humidity conditions, as shown in Fig. 4.11. The mean value of the sensors' measurements in dry air was 310.72 pF, with a standard deviation of 0.46 pF, while the mean value for the 100 ppm was 318.63 pF with a standard deviation of 0.59 pF. The difference in mean values between dry air and 100 ppm conditions was 7.91 pF and this value was used as an initial reference for further analysis.

Sensor responsiveness during the radiation process

During the irradiation experiment, the sensor samples were exposed to a high proton fluence over a period of 33 days. The sensor samples received a proton fluence of $3 \cdot 10^{16}$ protons/cm^2, which is equivalent to $1.86 \cdot 10^{16}$ n$_{eq}$/cm^2. This fluence represents the highest dose that the upcoming CMS sub-detectors will receive during a 10-year period of operation.
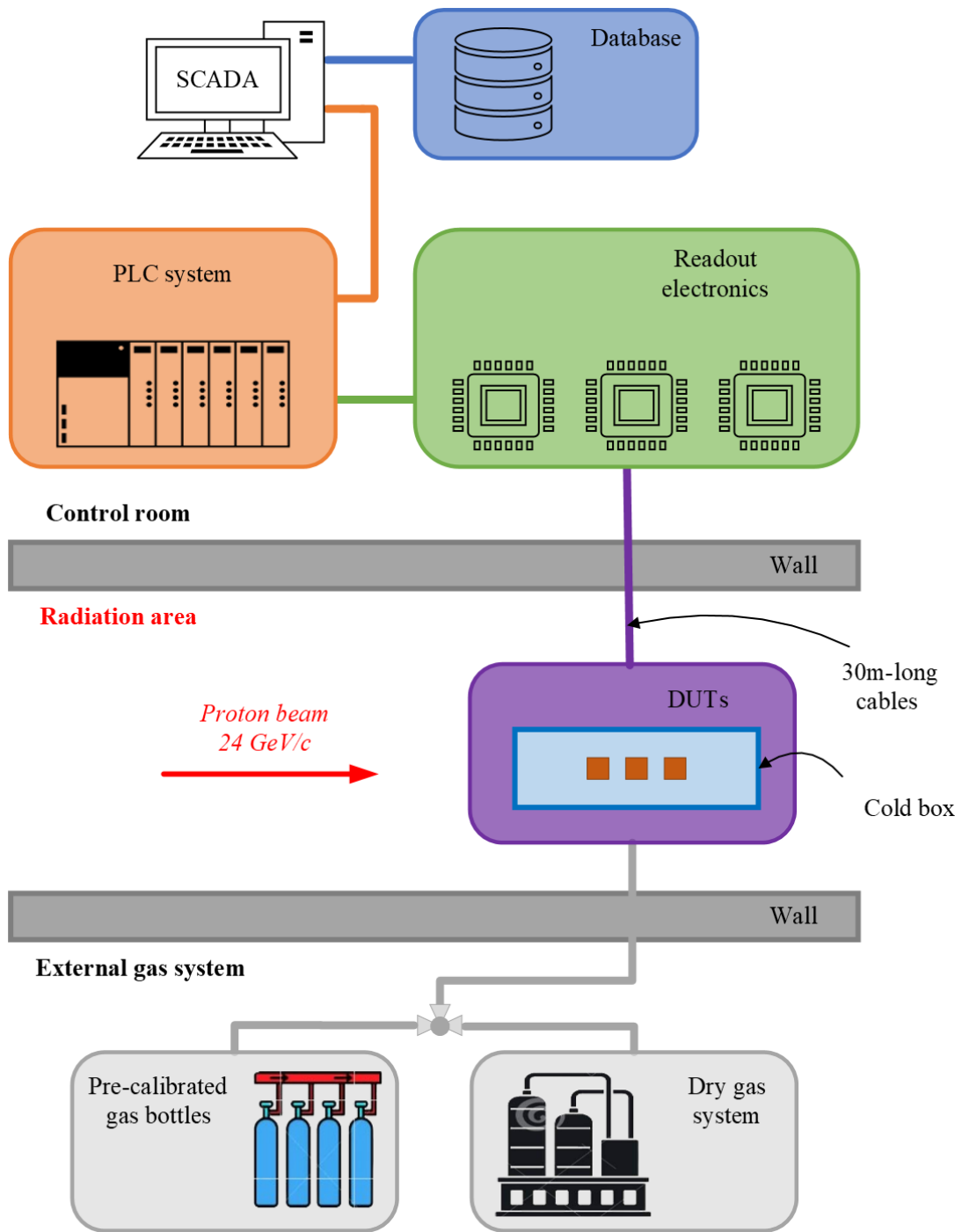
Figure 4.9: Schematic view of the experimental setup in the IRRAD proton facility. Sensor samples are placed inside the cold box and directly exposed to the proton beam. The environmental conditions of the cold box are controlled by the chiller and pre-calibrated gas mixtures. Sensors are separated from the readout electronics by 30-meter-long cables. Data acquisition is done by the PLC-based system and the SCADA system.

Figure 4.10: A photograph of the cold box with the samples inside positioned on one of the tables in the radiation area. The lasers show the center of the incoming proton beam.
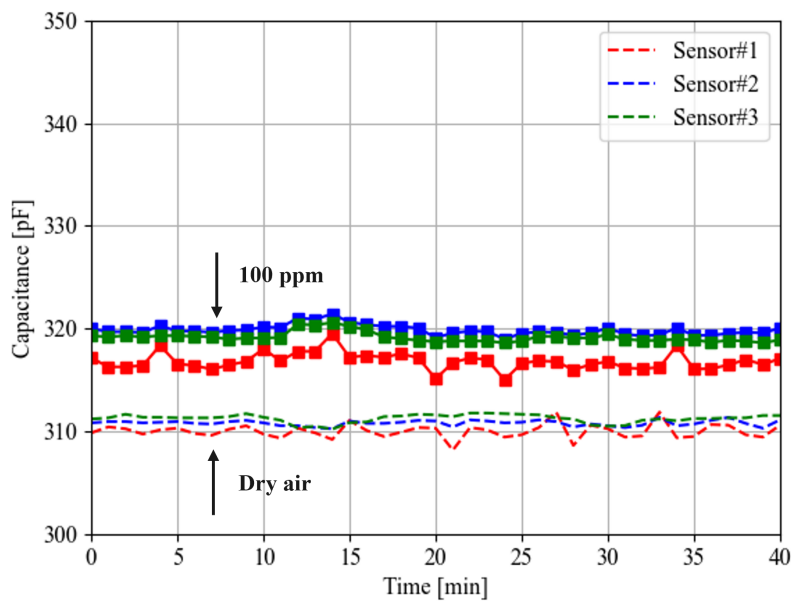
Figure 4.11: Measurements are taken prior to sensors exposure to radiation. Two different environmental conditions were considered: dry air and 100 ppm calibrated gas.

The data acquisition system actively stored measurements in the Oracle database throughout the entire experiment. Fig. 4.12 shows the measurements taken from the sensors over a period of 33 days. The presented graph clearly demonstrates the linear dependence of the outputs of the sensors on the received dose. The dependency of the exposed sensors can be characterized using a first-order polynomial function as follows:
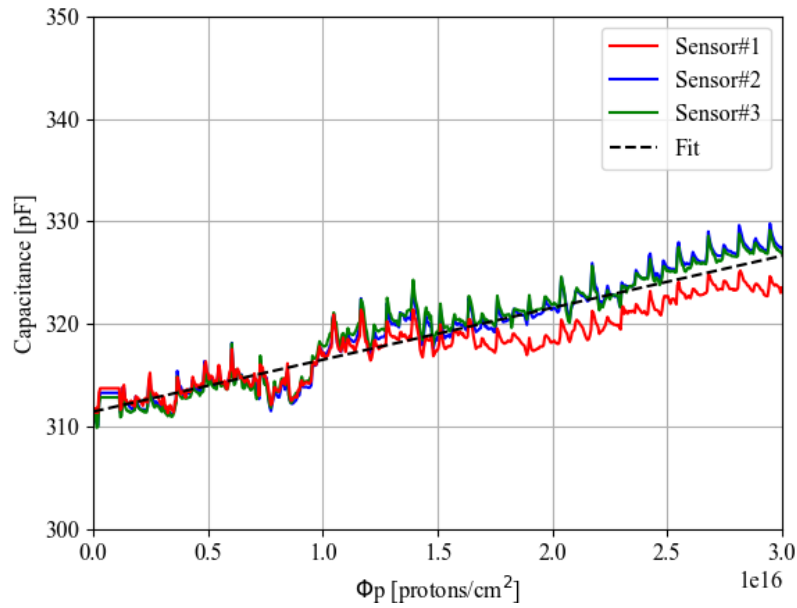
Figure 4.12: Measurements were continuously taken during the irradiation of the samples. During the 33-day irradiation period, the ambient condition was dry air, and the temperature was -20 °C. The dependence of the sensor capacitance on the fluence can be described by a linear fit.

$$C = m_h \cdot \Phi_p + C_0. \tag{4.3}$$

where C is the sensor capacitance expressed in pF and Φ_p denotes the received fluence expressed in protons/cm^2. m_h is a "damage" factor due to irradiation. It has a constant value of $5.01 \cdot 10^{-16}$ pF/(protons/cm^2) and it represents the slope of the linear relationship. C_0 is the sensor capacitance at dry conditions. In this case, for three sensors originating from the same wafer, the sensor capacitance at dry air conditions before exposure to radiation had a value of around 311 pF.

The mean value of the difference in capacitance between the measurements performed in dry air before and after the radiation experiment is 13.42 pF (σ = 1.03 pF) for Senosor#1 and 15.94 pF (σ = 0.77 pF) Sensor#2, whereas for the Sensor#3 the mean difference is 16.14 pF (σ = 0.81 pF). The measurements were taken with the on-purpose designed readout unit for humidity monitoring over long distances[III]. To validate the measurements and ensure their accuracy, the difference in capacitance between the initial and final measurements was confirmed using an LCR meter Agilent 4263B. The results from the LCR meter aligned with the measurements

---

[III]The designed readout electronics effectively nullify the effects of the internal sensor parasitic resistance and cable parasitic capacitance. More on the readout unit in Chapter **5**.

Table 4.1: Comparison of mean values and standard deviations of the sensors measurements before and after radiation period at dry air and 100 ppm.

Period	Gas mixture	Mean [pF]	σ [pF]
Before	Dry air	310.72	0.46
irradiation	100 ppm	318.63	0.59
After	Dry air	325.32	0.25
irradiation	100 ppm	333.29	0.14

Table 4.2: Sensors measurements at dry air and 100 ppm conditions before the irradiation period and after the annealing processes.

Parameter	Before irradiation	After irradiation	Annealing
$\Delta_{100ppm-dryair}$	7.91 pF	7.97 pF	6.16 pF
Temperature	-19 °C	-21 °C	-15 °C

obtained from the designed signal conditioning units, further confirming the reliability of the data.

After the radiation exposure, the response of the sensors was evaluated using a 100 ppm gas mixture. The acquired results are compared to measurements conducted before the irradiation period at dry air and 100 ppm conditions. The results are presented in Table 4.1. Notably, the difference in capacitance between the measurements at dry air and 100 ppm states, both before and after the radiation exposure, was found to be 7.91 pF and 7.97 pF, respectively. These results demonstrate the capability of the sensor to reliably measure environmental conditions even after undergoing such a high radiation exposure.

Annealing period

Following the radiation exposure, the sensors were subjected to an annealing procedure at room temperature. The annealing process was performed over a period of 60 days in dry state conditions. After the completion of the annealing procedure, the responsivity of the sensors was evaluated by using a 100 ppm gas mixture. The impact of the annealing process on the responsivity of the sensors was analyzed and compared to the measurements taken before and after the irradiation campaign and the results are summarized in Table 4.2.

The decrease observed in $\Delta_{100ppm-dryair}$ after the annealing period, compared to the measurements taken before and after the irradiation campaign, can be attributed to temperature variations. The temperatures recorded were -19 °C, -21 °C, and -15 °C before the irradiation campaign, after the irradiation campaign, and after the annealing process, respectively. The increase in the temperature to -15 °C resulted in a drop in humidity, which was effectively measured as a decrease in the capacitance change by the tested samples.

(a)   (b)
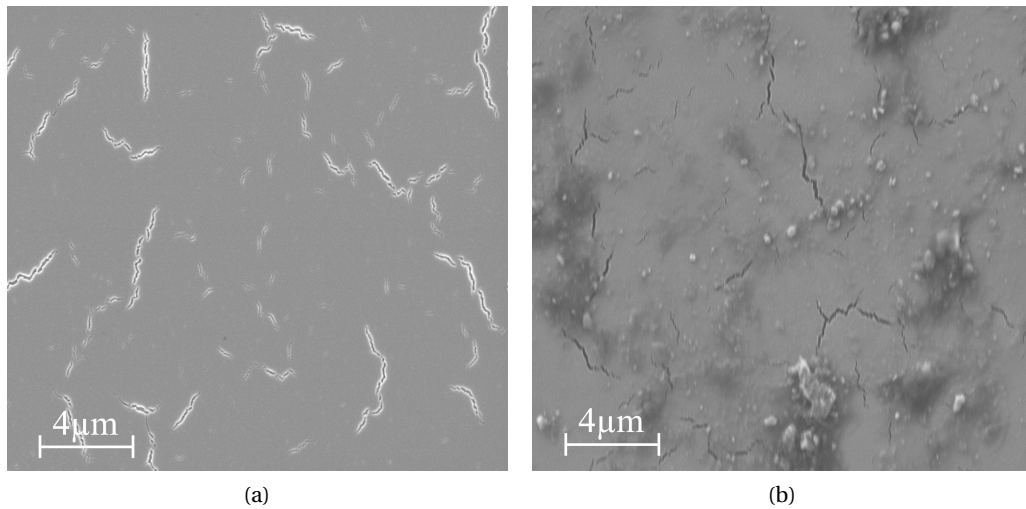
Figure 4.13: Microscopic images of the (a) reference sensor surface and (b) irradiated sensor surface.

FIB/SEM microscopy

The Focused Ion Beam/Scanning Electron Microscopy (FIB/SEM) technique was performed using a Zeiss XB540 instrument to examine the irradiated samples. One irradiated sample was subjected to microscopy analysis, while a non-irradiated sample served as a reference to assess any material alterations caused by irradiation. The Secondary Electron Secondary Ion (SESI) Detector was used for conventional imaging. SEM imaging of the sample surface was performed at an imaging current of 1 nA and an imaging voltage of 5 kV. Images were captured at magnifications of 5000× and 10000×.

Figure 4.13 shows the microscopic images of the surfaces of the reference sensor and the irradiated sample. The visible cracks, intentionally introduced in both samples during the fabrication process, aim to enhance the sensor sensitivity. The dots observed in the microscopic images of the irradiated sample surface represent dust particles. Furthermore, no disparities were detected in the surface of the sensors during the microscopic investigation.

To explore any potential modifications in the sensor dielectric material resulting from irradiation, a FIB cross-sectional milling technique was employed (Figure 4.14). A Pt deposition barrier was initially deposited on the surface of the sample at a milling current of 300 pA in order to protect the sample surface and ensure a sharp cross-sectional surface was revealed. Coarse milling at 7 nA was then used to remove material and polishing of the resulting cross-sectional surface was performed at 1.5 nA. Microscopic images of the cross-sections of the reference and irradiated samples reveal no discernible changes in the material caused by the high-energy proton beam. The deposited layer between the substrate and dielectric exhibits a non-uniform shape resulting from the fabrication process.
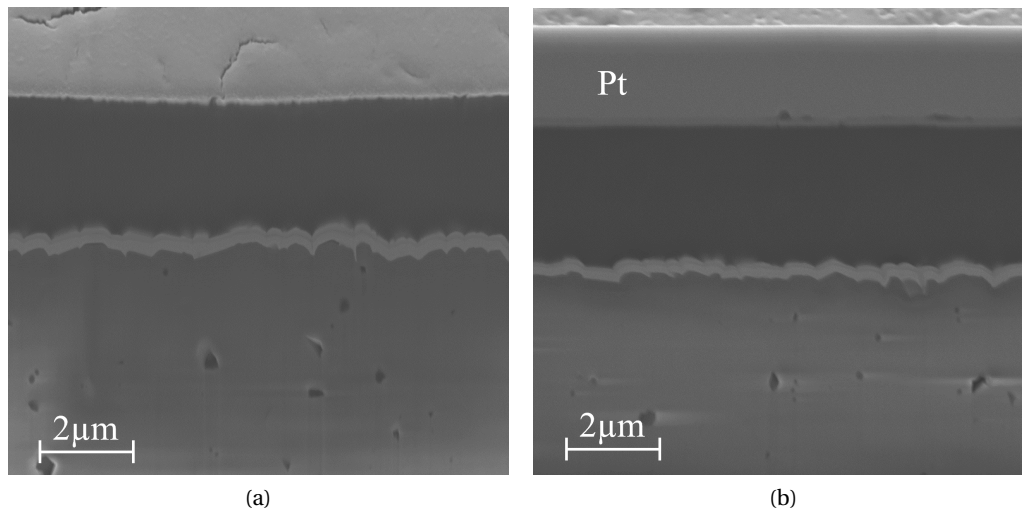
Figure 4.14: Microscopic images of the (a) reference sensor cross-section and (b) irradiated sensor cross-section.

4.2.4 Radiation Effects on Temperature Sensors

Pt (Platinum) RTDs are temperature sensors that have been demonstrated to withstand the harsh detector environment, including exposure to high levels of irradiation and magnetic fields of up to 4 T [31], [161], [162]. However, with the forthcoming HL-LHC project and its anticipated higher radiation doses, it became necessary to verify the capability of Pt1000 temperature sensors to function effectively in the most demanding areas of the detector. This subsection presents the experimental investigation conducted to assess the response of Pt1000 temperature sensors under the highest expected radiation dose.

Experimental setup

In this experiment, ten Pt1000 temperature sensors were used and divided into two groups of five sensors each, designated as "Group 1" and "Group 2". These sensors were placed on a metal block (copper plate) to ensure uniform temperature distribution among them, as illustrated in Figure 4.15 a). A thermal paste was applied to enhance the connection between the sensors and the plate. Then, the samples were inserted into a climatic chamber which facilitated precise temperature control, as shown in Figure 4.15 b).

Results and Discussion

The climatic chamber enabled temperature variations between 20 °C and -30 °C during the experiment. Measurements were recorded at specific temperature intervals: 20 °C, 10 °C, 0 °C, -10 °C, -20 °C, and -30 °C. The results from both groups are depicted in Figure 4.16, while the mean values and standard deviations are presented in Table 4.3. The analysis reveals no

(a)   (b)
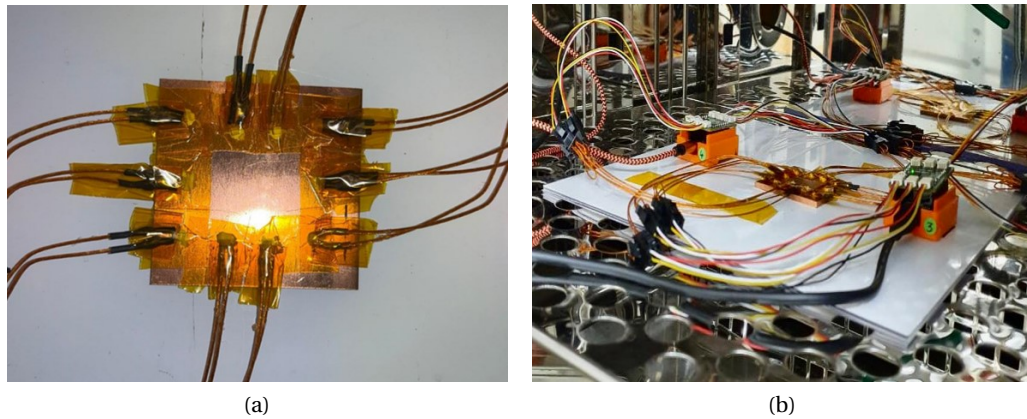
Figure 4.15: Photos of (a) Pt1000 temperature sensors positioned on a copper plate with thermal paste applied to ensure optimal sensor-plate connection and (b) the sensors inserted into the climatic chamber for precise temperature regulation.

Table 4.3: Mean values and standard deviations of non-irradiated Pt1000 temperature sensors measurements at different temperatures.

	Group 1		**Group 2**	
Temperature [°C]	Mean [°C]	σ [°C]	Mean [°C]	σ [°C]
20	17.28	0.08	17.26	0.11
10	7.61	0.08	7.6	0.11
0	-1.86	0.08	-1.87	0.11
-10	-11.66	0.06	-11.67	0.04
-20	-21.41	0.06	-21.43	0.03
-30	-31.44	0.06	-31.47	0.03

significant difference in the mean values between the two groups. For Group 1, the standard deviation reaches up to 0.08 °C, whereas for Group 2, it ranges from 0.11 °C for positive temperatures to 0.04 °C for negative temperatures.

Following the initial test, sensors from Group 2 were subjected to direct proton beam exposure for more than 30 days, resulting in an accumulated fluence of approximately $4 \cdot 10^{16}$ protons/cm^2 [IV]. After the irradiation campaign, the experiment in the climatic chamber was repeated at the same temperature intervals. The histograms of the measurements from the two observed groups are presented in Figure 4.17, and the corresponding mean values and standard deviations are summarized in Table 4.4.

The sensors in Group 2 exhibited slight deviations in temperature measurements compared to the reference measurements obtained from Group 1 sensors. The difference in mean values between Group 1 and Group 2 remained relatively consistent at approximately 2.3 °C across

---

[IV]The accumulated proton fluence is equivalent to $2.5 \cdot 10^{16}$ n_{eq}/cm^2. This dose is the highest expected dose in the regions of the Tracker sub-detector that are nearest to the collision point after 10 years of the HL-LHC operation.
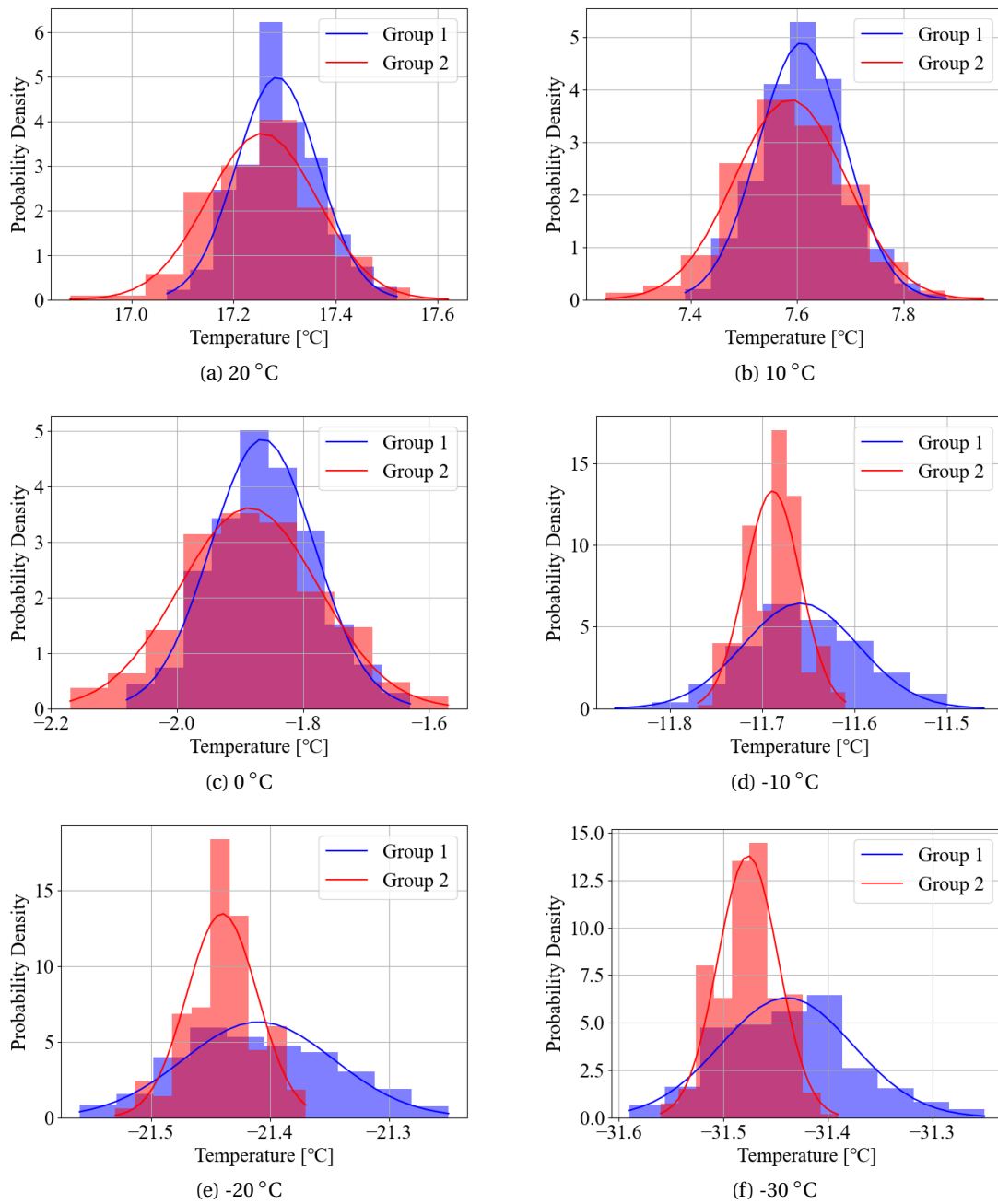
Figure 4.16: Histograms and Gaussian fit of non-irradiated Pt1000 temperature sensor measurements at different temperatures.

Table 4.4: Mean values and standard deviations of non-irradiated Pt1000s measurements (Group 1) and irradiated Pt1000s measurements (Group 2) at different temperatures.

	Group 1		**Group 2**	
Temperature [°C]	Mean [°C]	σ [°C]	Mean [°C]	σ [°C]
20	16.86	0.08	19.18	0.13
10	7.51	0.07	9.83	0.13
0	-1.98	0.06	0.33	0.13
-10	-11.61	0.06	-9.31	0.13
-20	-21.2	0.06	-18.89	0.13
-30	-30.77	0.08	-28.46	0.13

different temperatures. Therefore, these deviations in measurements from Group 2 sensors are easily compensated for. Moreover, the standard deviation of the irradiated samples slightly increased, particularly at negative temperatures, reaching 0.13 °C.

The conducted experiment demonstrated the ability of the Pt1000 temperature sensors to operate effectively in high-radiation environments. However, it is crucial to consider the deviation observed in measurements after exposure to such high doses, particularly when computing the dew point temperature. At -30 °C and under dry air conditions (relative humidity around 0 %rh), the 2 °C deviation in temperature measurements would lead to a corresponding 2 °C deviation in dew point temperature measurements. Hence, it is imperative to account for the sensor radiation dependence when aiming for accurate dew point temperature measurements. The dependence of the temperature sensors on radiation is then described by a linear function in terms of the accumulated fluence, as follows:

$$\Delta T = m_T \cdot \Phi_p, \tag{4.4}$$

where m_T has a value of $5.75 \cdot 10^{-17}$ °C/(protons/cm^2). By determining the appropriate value of m_T, the deviation caused by radiation can be effectively compensated, thus reducing the error associated with dew point temperature measurements.

4.3   Temperature Dependence of the Humidity Sensor Candidate

Humidity (and radiation in our case) is not the only factor affecting the dielectric properties. The sensor dielectric properties also vary with temperature [163]. Paper [164] shows that if the temperature increases, the dielectric constant will increase as well, while if the temperature decreases, the dielectric constant will decrease. This effect is demonstrated for the positive temperature range from 10 °C to 65 °C. Paper [165] highlights the sensor performance limitations and the subsequent calibration compensation due to the temperature effect at temperatures up to 150 °C. In [166], the authors investigated the sensor temperature dependence in the range of 10 °C to 60 °C and reported a 5 % deviation from the reference values.
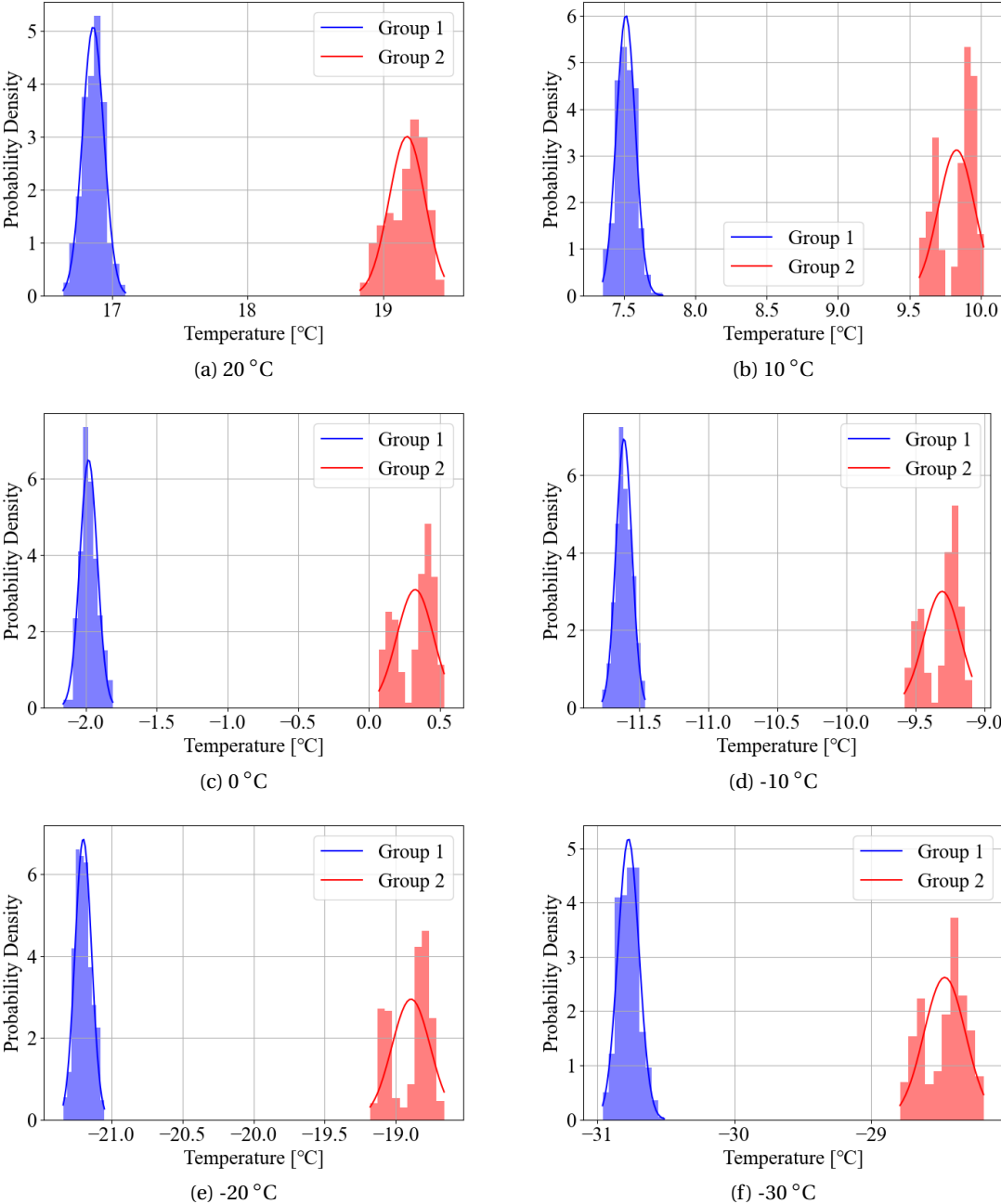
Figure 4.17: Histograms and Gaussian fit of Pt1000 temperature sensor measurements at different temperatures. Group 1 consists of the non-irradiated samples, while Group 2 consists of the irradiated samples.

However, all the listed papers present results at temperatures above the freezing point of water and within the "comfortable" humidity levels (range from 15 %rh to 90 %rh). This is perfectly well understood because these are the environmental conditions for most processes where this form of sensor will be used. Instead, in this study, we present the behavior of the relative humidity sensor at temperatures below the freezing point of water and at low (< 10 %rh) relative humidity levels. As both humidity and temperature have an effect on the sensor's electrical properties, to express the exact humidity value as a function of capacitance change it is necessary to determine its temperature dependence. This effect might be of small importance when the capacitive relative humidity sensors are functioning at stable temperatures (most applications). However, for future silicon-based High Energy Physics (HEP) detectors, the temperature of operation will vary from 20 °C to -35 °C during several temperature steps imposed by the detector operational needs.

Therefore, in the following sub-sections, we present the possible methods for generating various humidity levels and the selected approach, as well as the measurements, the applied calibration procedures, and the uncertainty analysis of the measurements at negative temperatures.

4.3.1   Humidity generators

There are four standard systems for generating humidity: fixed-point humidity generator, two-pressure humidity generator, two-temperature humidity generator, and two-flow humidity generator. The fixed-point humidity system can be easily established using vapour-saturated salts [167]. This method is inexpensive and easily reproducible in research facilities. Nevertheless, the relative humidity ranges are limited, and the process is time-consuming as one has to wait until a stable state has been reached. The other limitation is that the method is inherently affected by the ambient temperature, which is a parameter that we want to change during our tests for the reasons stated before (see Fig. 4.18)[V].

In the case of the two-pressure method, a gaseous mixture is vapour saturated at pre-set temperature and at a pressure higher than atmospheric (Fig. 4.19) [168]. Then, the saturated high-pressure air flows from the saturator, through a pressure-reducing valve, where the air is isothermally reduced to test pressure, usually normally atmospheric pressure, at the test temperature. The relative humidity is calculated using the temperature and pressure of the saturator and the test chamber as follows:

$$RH = \frac{p_c \cdot p_{sat}(T_s) \cdot f(p_s, T_s)}{p_s \cdot p_{sat}(T_c) \cdot f(p_c, T_c)},\qquad(4.5)$$

where p_s and p_c are the pressure in the saturator and chamber, respectively. $p_{sat}(T_s)$ and

---

[V]Furthermore, the saturated salt solutions cannot be used for sensor calibration at the negative temperatures.
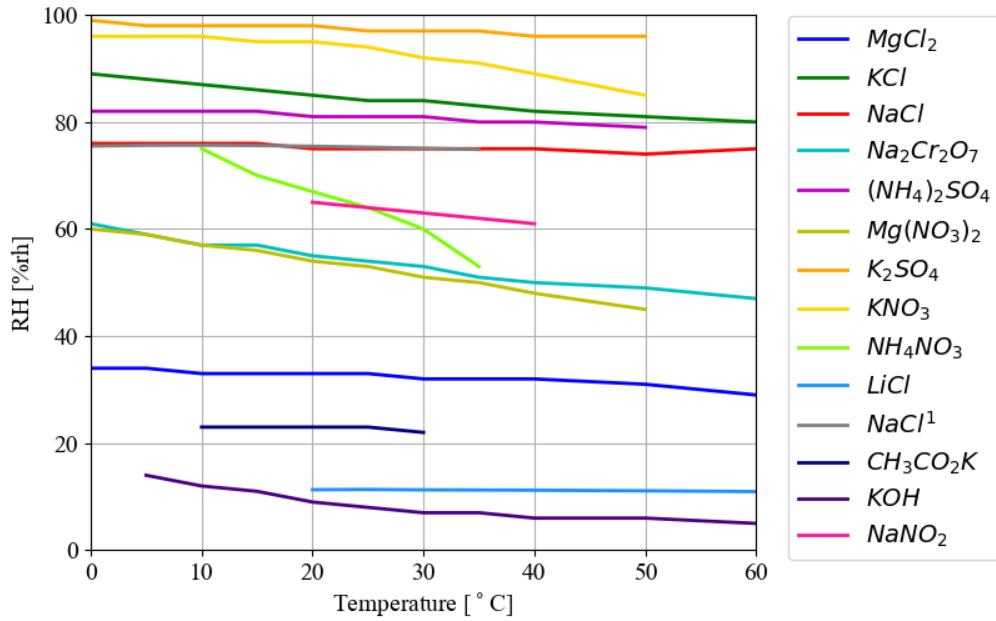
Figure 4.18: Relative humidity over different saturated salt solutions. LiCl and NaCl[1] are saturated aqueous solutions of inorganic salts.

$p_{sat}(T_c)$ are saturation vapor pressure at temperature T_s and T_c in the saturator and chamber, respectively, while $f(p_s, T_s)$ and $f(p_c, T_c)$ are enhancement factors at corresponding temperature and pressure. The benefit of such a system is lower uncertainties, while the trade-offs are in cost-effectiveness and the requirement of clean, high-pressure air.

In the two-temperature method, the air must be saturated with water vapour at a fixed temperature, and then its temperature is increased to a preset value (Fig. 4.20) [169]. To determine the resulting humidity content of the gas stream, measurements of the temperature and pressure of both the cool, saturated-gas stream and the warmer test chamber stream are required. This method has been efficiently tested at temperatures as low as -40 °C and -50 °C but not for the relative humidity levels below 10 %rh. Although this method is very accurate, it is typically slow, with only one measurement point per day.

The two-flow method is based on controlling the ratio of flow rates of two gaseous mixtures [170], [171]. One stream is dry air, while the other stream is saturated air with water at a known temperature. The resulting vapor concentration (absolute humidity) X_i can be calculated from the two flow rates as follows:

$$X_i = X_s \frac{v_s \cdot t_s}{v_s \cdot t_s + v_a \cdot t_a},$$

(4.6)

where X_s is the concentration of water vapor in saturated air, v_s and v_a are the flow rates
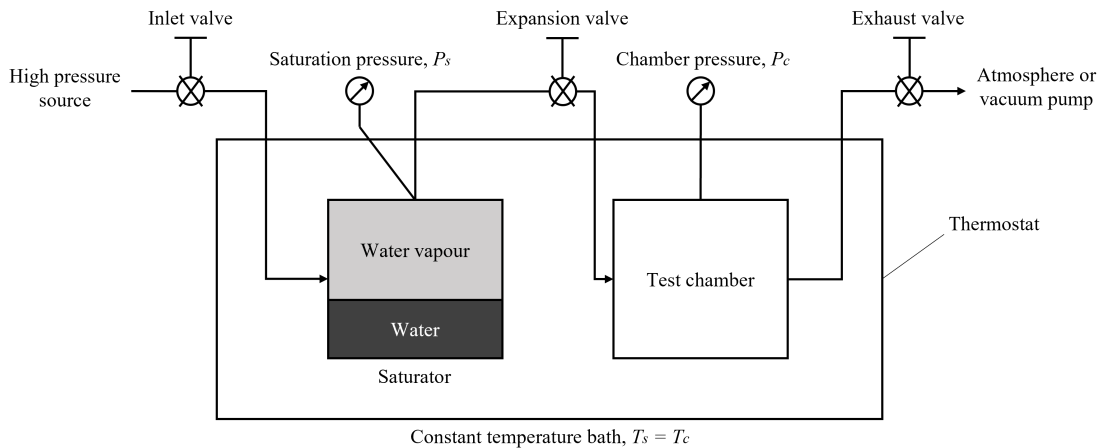
Figure 4.19: Schematic diagram of two-pressure humidity generator.
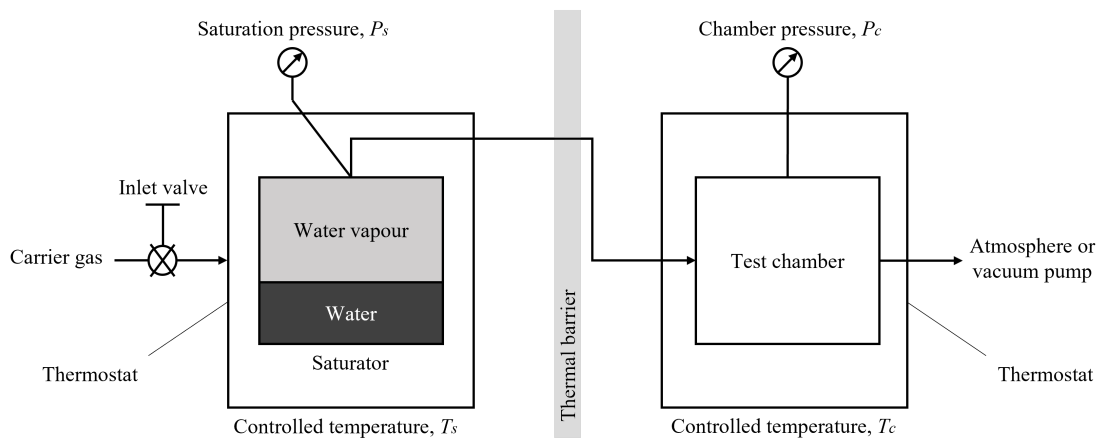
Figure 4.20: Schematic diagram of two-temperature humidity generator.

of saturated and dry air, and t_s and t_a are the working time of the corresponding channels, respectively.

All of the above methods used to create the necessary atmosphere for calibration and testing of humidity sensors are static. The main disadvantage of using static methods for preparing humidity standards is the absorptive losses on surfaces such as bags and gas cylinder walls [172]. This loss is difficult to explain, especially in the parts-per-billion range and is particularly significant for water vapor with low vapor pressures.

To overcome this problem, the dynamic mixing flow method is used where a constant gas flow is provided to the test chamber as shown in Fig. 4.21. The main benefits of this method are that a constant gas flow avoids any problem with gas consumption by the sensor itself, and also minimizes problems with adsorption and desorption at the walls of the test system [110]. In addition, a constant gas flow prevents any distortion of the measurement due to changes in gas-exchange time constants, forced cooling of heated sensors, and other flow-dependent

105

effects.

In this dynamic mixing flow method, the flows q_i of gases are mixed continually at constant pressure p and constant temperature T. The concentration of water vapor in the output stream of the dilution system depends on the initial concentration of water vapor in the calibration flow and the ratio of gas flows in the channels. If the values of flows q_i are known, the reference relative concentration X_i can be calculated from eq. (4.7):

$$X_i = \frac{q_i}{q_i + q_n} \tag{4.7}$$

or provided by a chilled mirror. This last method allows the user to reach various temperature ranges and low humidity levels, hence, it is used for the sensor characterization in this thesis.

4.3.2 Experimental Setup

A special setup was designed to characterize the sensors at low temperatures and various humidity levels. The schematic of the used setup is shown in Fig. 4.21. Two gas mixtures with different moisture contents were used to provide the final mixture. One stream of gas was dry air, while the other was an Argon-calibrated gas mixture with 100 ppm water. One gas stream would be flushed through a water-filled bubbler to obtain the saturated air. The latter would be mixed with the other air stream and forwarded to the testing box containing the devices under test (DUTs). Different humidity levels were achieved by controlling the mass flow rate. The climatic chamber, produced by the ESPEC company [173], was used to control the environmental temperature. Inside the climatic chamber, a metal box with a copper pipe coil was placed (as shown in Fig. 4.22). The function of a long copper pipe coil was to cool down the incoming air to the temperature of the climatic chamber before it entered the metal box. The DUTs, together with PT1000 temperature sensors were inserted into the metal box. The external chilled mirror dew point sensor, connected in series with the DUTs, provided a reference measurement.

4.3.3 Calibration procedure

The purpose of calibration is to establish a connection between the values returned by the device under test and those returned by the reference value. Here, we consider two mathematical methods for defining the calibration equation.

The classical method

In the classical method, the measured value is a function of the true value as follows:
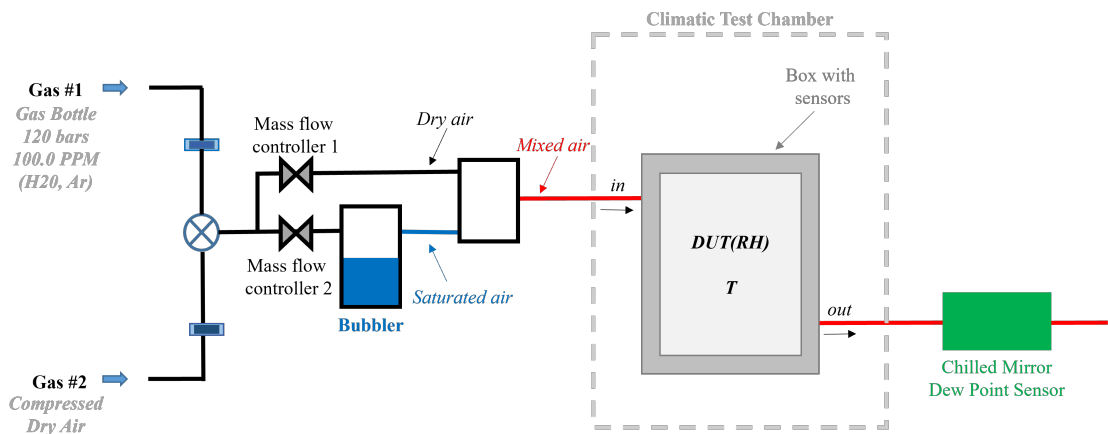
Figure 4.21: Schematic view of the setup for humidity and temperature control with two gaseous mixtures, mass flow controllers, bubbler and chilled mirror as a reference sensor. A climatic chamber is used for temperature control.

(a) Inside of the climatic chamber   (b) Inside of the metal box
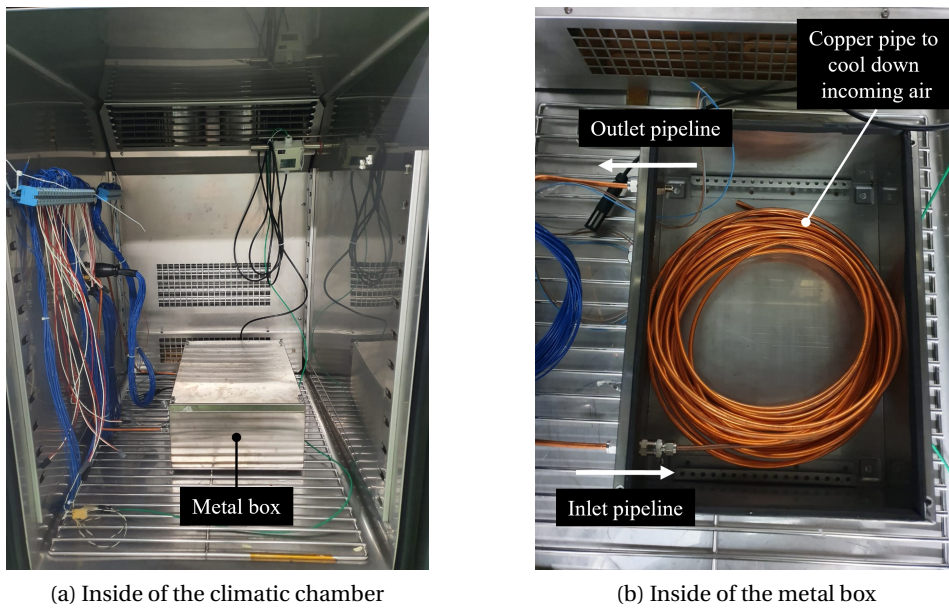
Figure 4.22: (a) A photo of the climatic chamber and of the metallic box containing the sensors and (b) a "long" copper pipe coil used to cool down the incoming air by forcing it to circulate in the cold volume. The sensors were placed at the output of the copper pipe.

$$y_{meas} = f(x_{true}), \tag{4.8}$$

where y_{meas} is the measured value by DUT, and x_{true} is the true value.

The relationship between measured and reference values can be linear, polynomial or non-linear. The true sensor value can be expressed as a function or computed using the iterative numeric analysis technique.

The inverse method

In the case of the inverse method, the true value is presented as a dependent variable, while the measured value is an independent variable:

$$x_{true} = g(y_{meas}), \tag{4.9}$$

According to the literature, the inverse method has better prediction ability compared to the classical method [174]. This statement was also confirmed by Monte Carlo simulations in [175].

4.3.4   Uncertainty Analysis

According to the ISO GUM [176], the uncertainty evaluation of measurements can be decomposed using two methods: Type A and Type B. The Type A approach of the standard uncertainty evaluation is based on the statistical analysis of measurements. The Type B evaluation is a method based on the information given by the device manufacturer.

There are many uncertainty sources that have to be taken into consideration, and they are discussed in more detail in the following subsections.

Uncertainty of humidity generation

The relative humidity reference value is measured by the calibrated chilled mirror dew-point sensor. Hence, the uncertainty from the humidity generation is determined by the deviation of the measured reference value.

The main uncertainty constituents of humidity generation are the instability and inhomogeneity of the produced gas mixture. The instability in generated humidity is typically a less significant component and it might be caused due to instability of the dew point temperature, the ambient temperature, and the pressure, in the case of two-pressure systems.

The second uncertainty contributor, inhomogeneity of generated humidity, becomes an issue in the case of the serial connection of the DUT and dew-point meter, as is the case in Fig. 4.21. The presence of a temperature gradient inside the testing environment causes a significant influence on relative humidity calibration. Therefore, many Pt1000 temperature sensors were spread at several box locations to quantify the temperature inhomogeneity in the presented

relative humidity calibration system.

Uncertainty of the reference chilled mirror dew-point sensor

The uncertainty of the reference sensor depends on the type of reference standard used. In the case of a chilled mirror dew point sensor, the ambient temperature and dew-point temperature have to be considered separately as follows:

$$u_{ref}(RH_{ref}) = \sqrt{\left(\frac{\partial RH_{ref}}{\partial t_d} u(t_d)\right)^2 + \left(\frac{\partial RH_{ref}}{\partial t_a} u(t_a)\right)^2}, \tag{4.10}$$

where $u_{ref}(RH_{ref})$ is the uncertainty of relative humidity measurement of the reference sensor, RH_{ref} is measured relative humidity by the reference sensor, t_d and t_a are dew-point temperature and ambient temperature measured by the dew point meter, respectively. This is a Type A uncertainty and is for the case of a set of individual values which can be randomly distributed meaning that the mean value is also a random quantity. For every random quantity, it is possible to find the standard deviation of all obtained mean values. The latter is approximated as follows:

$$u_{ref}(RH_{ref}) = \frac{s(RH_{ref})}{\sqrt{n}} \tag{4.11}$$

where $s(RH_{ref})$ is the standard deviation divided by the square root of the number of repeated measurements n.

The analog output signals of the chilled mirror dew-point sensor were digitized using a 16-bit ADC, hence, the reading uncertainty is negligible.

Uncertainty of the device under test

The uncertainty of DUT is determined by sensor non-linearity, repeatability, resolution, hysteresis, and calibration procedure. The uncertainty due to temperature variation is important in the case of capacitive-based sensors.

Uncertainty due to nonlinearity and repeatability:

The information about the sensor nonlinearity is given by the manufacturer and it is less than 2 %rh for the range between 15 %rh and 90 %rh. The uncertainty due to nonlinearity is a Type

B uncertainty with rectangular distribution and is derived as follows:

$$u_{non} = \frac{HW}{\sqrt{3}},$$

(4.12)

where, u_{non} is the uncertainty of DUT due to nonlinearity, and HW is a half-width of the rectangular distribution. In the case of the considered relative humidity sensor, this uncertainty is equal to 0.577 %rh.

Information on the repeatability uncertainty is not given by the manufacturer, hence, it was not taken into consideration for the analysis of the uncertainty of DUT.

Uncertainty due to resolution:

As in the case of a chilled mirror sensor, the analog output of the sensor is digitized using an ADC 16-bit, therefore, the resolution uncertainty of the DUT is negligible.

Uncertainty due to hysteresis:

The hysteresis for the DUT is <2 %rh. The uncertainty caused by hysteresis for the uniform, rectangular distribution is calculated as for the previous cases and is equal to 0.577 %rh.

Uncertainty due to temperature variation:

The temperature dependence manufacturer has represented with the linear function:

$$u_{temp} = (B_1 \cdot \%rh + B_2) \cdot T[^{\circ}C] + (B_3 \cdot \%rh + B_4),$$

(4.13)

where, u_{temp} is the relative humidity shift due to temperature effects and B_1, B_2, B_3 and B_4 are constants and have values of 0.0011 1/°C, 0.0892 %rh/°C, -0.0268 and -2.079 %rh respectively. The equation and constants, provided by the sensor manufacturer, work well for positive temperatures. The performed experiments show that this assumption is instead not valid for negative temperatures and this will be elaborated on in more detail in the Results and Discussion section.

The uncertainty due to the temperature variations defines the stability of the measurement chamber. It is determined by the values of standard deviations of the temperature monitoring Pt1000 sensors. The temperature sensitivity factor of the DUT is defined as:

$$S_T = \frac{\partial RH}{\partial T},$$ (4.14)

Uncertainty of calibration procedure:

The uncertainty of the calibration procedure is Type A uncertainty. The uncertainty of the true value, $u(x_{true})$, can be calculated as follows:

$$u(x_{true}) = \frac{\partial x_{true}}{\partial y_{meas}} \cdot u(y_{meas}),$$ (4.15)

where, y_{meas} is measured value by the DUT, and $u(y_{meas})$ is the uncertainty of the DUT.

In this analysis, the uncertainty of classical and inverse methods is considered. In both approaches, the linear and polynomial regressions are evaluated.

Classical method:

In the case of linear regression, the predicted value can be determined as follows:

$$x_{true} = \frac{y_{meas} - n}{k},$$ (4.16)

where, x_{true} is predicted value, y_{meas} is observed value, while n and k are coefficients of linear equation. Based on the equation (4.15), the uncertainty of the calibration procedure can be derived as:

$$u(x_{true}) = \frac{1}{k} \cdot u(y_{meas})$$ (4.17)

In the case of quadratic regression, the predicted value is calculated as follows:

$$x_{true} = -\frac{b}{2a} + \sqrt{\frac{b^2}{4a^2} - \frac{c}{a} + \frac{y_{meas}}{a}}$$ (4.18)

111

Table 4.5: Overview of Type B uncertainties.

Uncertainty	u_{non}	u_{res}	u_{hys}
DUT	0.577 %rh	-	0.577 %rh

where, a, b, and c are coefficients of the quadratic calibration function.

The calibration uncertainty is evaluated from:

$$u(x_{true}) = \frac{1}{2a\sqrt{\frac{b^2}{4a^2} - \frac{c}{a} + \frac{y_{meas}}{a}}} \cdot u(y_{meas}) \tag{4.19}$$

Inverse method:

Here, the measured value is independent, while the true value is a dependable variable. The uncertainty, in both cases of linear and quadratic regression, can be simply written as:

$$u(x_{true}) = s(y_{meas}) = \sqrt{\frac{\sum_{i=1}^{n}(x - \overline{x})^2}{n-1}} \tag{4.20}$$

4.3.5   Results and discussion

Several capacitive humidity sensors were tested in the previously described setup[VI]. The experiments were done at three different temperatures: -10 °C, -20 °C, and -30 °C. At each temperature, different humidity levels were obtained. The measurements of the tested sensors were subtracted from the measurements of the reference chilled mirror sensor for the error analysis. The below presented calibration curves are the mathematical formulas expressing the true relative humidity as a function of the measured relative humidity and the measured ambient temperature.

To complete the analysis of DUTs at different negative temperatures, the uncertainties are calculated and discussed. Type B uncertainties are listed in Table 4.5, and Type A uncertainties, due to calibration procedure and due to temperature variations, are deeply analyzed in the following subsections.

[VI]The influence of the pressure change has not been considered.

Calculation of Type A uncertainties

The first test was conducted at -10 °C with 5 different humidity levels reached: 2 %rh, 49 %rh, 63 %rh, 71 %rh and 78 %rh. The relationship between the average measurements of the 3 DUTs and the reference sensor is presented in Fig. 4.23 (a)[VII] in green squares. The deviation of the average DUTs values from the reference measurement are presented in Fig. 4.23 (b) and it can be seen that at -10 °C, it reaches 3 %rh when measuring in the comfort zone for the sensor (from 15 %rh to 90 %rh). The same figures present the average values of the DUTs at other negative temperatures, -20 °C, and -30 °C, with respect to the measurements obtained with the reference sensor. In the second experiment, at -20 °C, 4 humidity points were obtained: 5 %rh, 15 %rh, 78 %rh and 86 %rh. It is noticeable that at 15 %rh the deviation is around 5 %rh, while for the higher humidity levels, the deviation increases noticeably. For example, at 85 %rh the difference between the reference value and the DUT measured value is around 12 %rh.

The third run was conducted at -30 °C. With the designed setup, 3 humidity levels were considered: 15 %rh, 35 %rh and 78 %rh. At 15 %rh the deviation is slightly different than at the temperature of -20 °C and has a value of around 6 %rh. As was the case with the second experiment, the deviation from the reference measurement is significantly larger at high humidity levels and at 78 %rh is around 12.5 %rh.

From the tests, it can be concluded that with decreasing the temperature, the difference between the reference measurements and DUTs measured values increases. This means that with temperature decrease, the dielectric constant of polymer material decreases. If the temperature increases, the dielectric constant will increase and this conclusion is in agreement with the results reported in [164] for the positive temperatures.

In this study, two calibration procedures were considered to estimate the true value: the classical method and the inverse method. In both approaches, linear and quadratic regression functions have been applied.

<u>The classical method</u>

In the case of the classical method, the measured value is in the function of the independent true value. Linear regression functions for the experiments can be written as:

$$y_{meas,i} = k_i \cdot x_{true} + n_i \tag{4.21}$$

[VII]The maximum error for all measurements goes up to 1 %rh making the error bars invisible in the graphs as the entire range of relative humidity is presented (from 0 %rh to 100 %rh). However, those values are included in the uncertainty analysis of the measurements, and their values are presented in the analysis for each temperature separately.

(a)

(b)
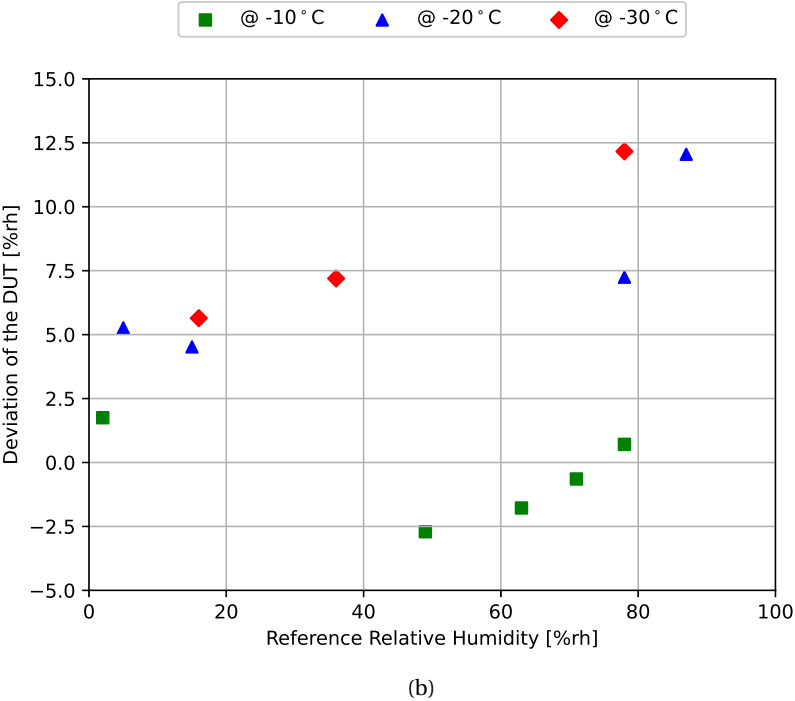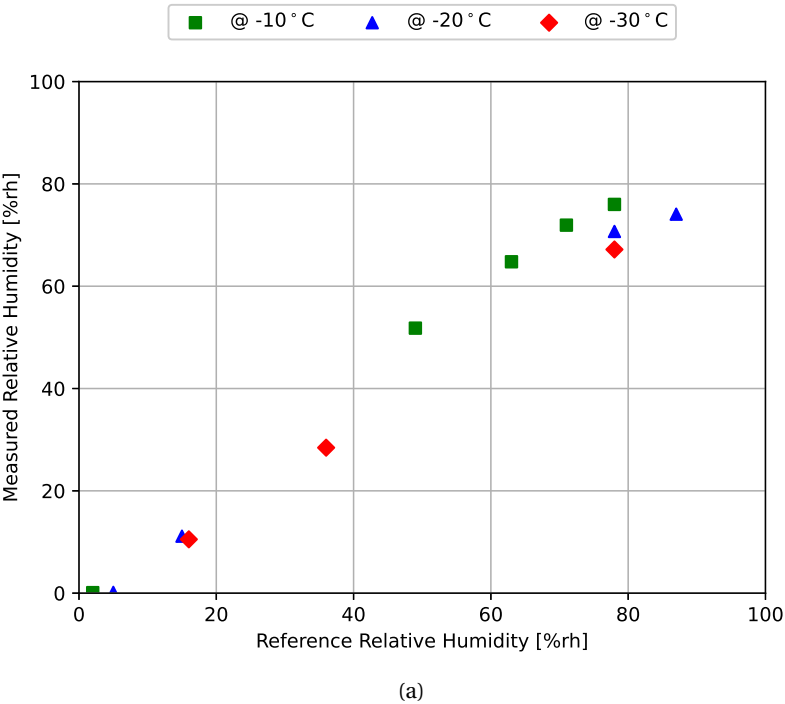
Figure 4.23: Average deviations of the devices under test with respect to the reference chilled mirror sensor (a) and the average difference between the reference chilled mirror and DUTs (b). The measurements were done at three different negative temperatures and various humidity levels.

where, k_i and n_i are the temperature dependant variables, and i is the number of the experiment. The k_i and n_i variables can be presented as linear functions of temperature as follows:

$$\begin{cases} k_i = k_1 \cdot T_i + k_2 \\ n_i = n_1 \cdot T_i + n_2 \end{cases} \tag{4.22}$$

where, k_1, k_2, n_1 and n_2 are constants of the linear functions. Inserting the previous system of equations in (4.21), the linear calibration function for estimating the true value becomes as follows:

$$x_{true} = \frac{y_{meas} - n_1 \cdot T - n_2}{k_1 \cdot T + k_2} \tag{4.23}$$

From (4.14) and (4.23) is easy to determine the temperature sensitivity factor S_T:

$$S_T = \frac{k_1(n_2 - y_{meas}) - n_1 k_2}{(k_1 \cdot T + k_2)^2} \tag{4.24}$$

The residual plot of the predicted values of relative humidity at three different negative temperatures for classical linear regression is presented in Fig. 4.24. A systematic pattern is noticeable indicating that the linear calibration equation is not an adequate model. At negative temperatures, -10 °C and -20 °C, the nonlinearity of the sensor polymer material is increased, while at -30 °C the polymer material has more linear behaviour with respect to humidity. The coefficient of determination, R^2, has a value of 0.995 meaning that 99.5% of the dependent output can be explained by the model.

Analogously, a second-order polynomial calibration curve, as a function of measured relative humidity and temperature, is derived from (4.18), where a, b and c are temperature dependent variables and they are approximated with linear equations in the function of temperature ($a = a_1 \cdot T + a_2$, $b = b_1 \cdot T + b_2$ and $c = c_1 \cdot T + c_2$). The temperature-sensitive factor, S_T, is determined as the first derivative of the polynomial calibration curve.

The residuals of the second-order calibration curve are shown in Fig. 4.25. The distribution of scattered points is more uniform compared to linear regression and indicates that this method is more adequate as a calibration model for the DUTs. The coefficient of determination, R^2, is 0.998 showing that 0.2% of the dependent output cannot be explained by the model.

The uncertainty of the classical method calibration procedure is calculated according to
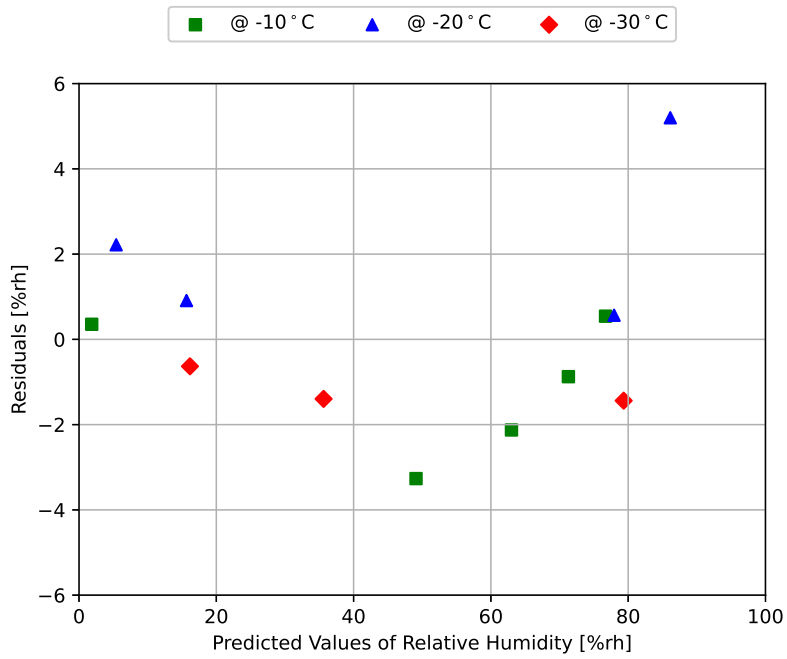
Figure 4.24: Residuals for linear calibration equation of classical method at three different negative temperatures.
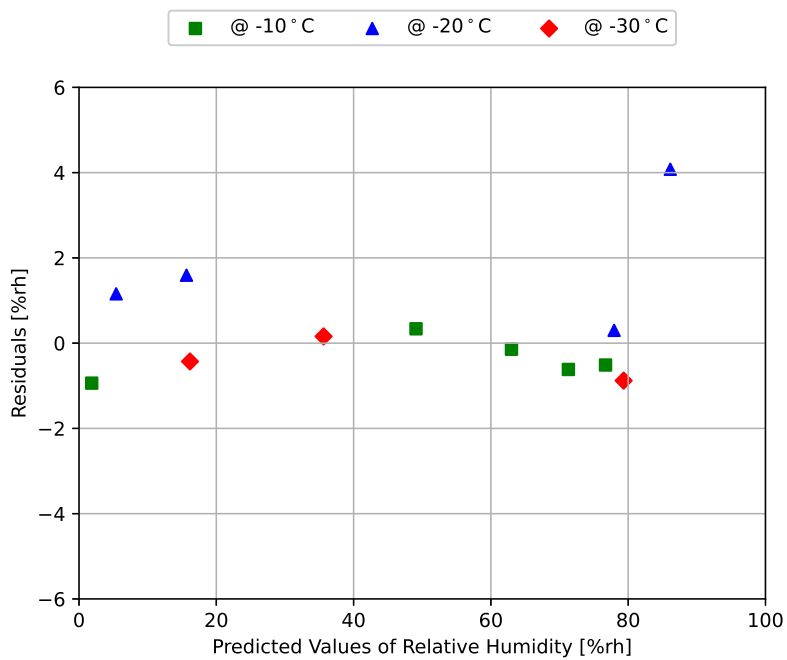
Figure 4.25: Residuals for quadratic calibration equation of classical method at three different negative temperatures.

(4.17) and (4.19) for the linear and polynomial regressions, respectively, and their values are
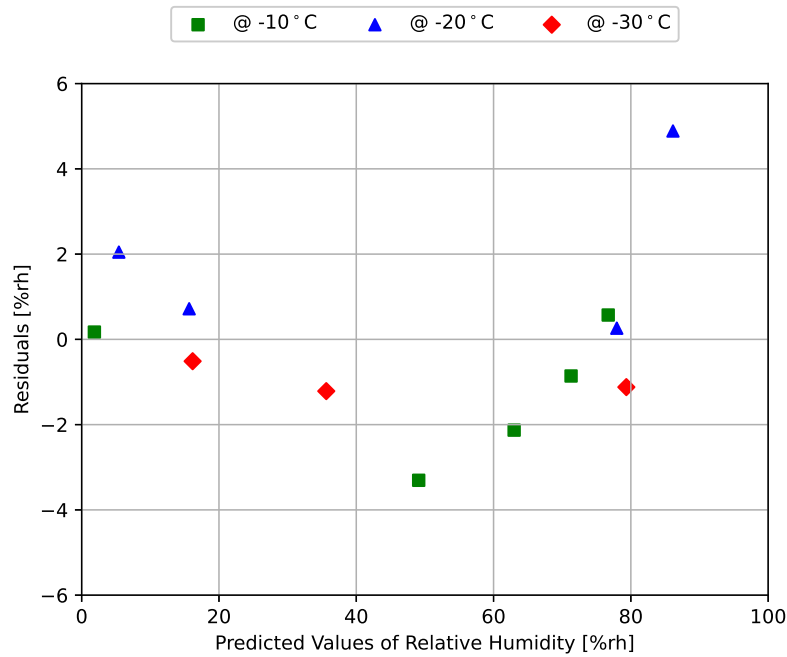
Figure 4.26: Residuals for linear calibration equation for the inverse method at three different negative temperatures.

presented later in the discussion.

The inverse method

The linear calibration curve as a function of measured relative humidity and temperature is written as follows:

$$x_{true} = (p_1 \cdot y_{meas} + m_1) \cdot T + p_2 \cdot y_{meas} + m_2 \tag{4.25}$$

where, p_1, p_2, m_1 and m_2 are constants of linear temperature functions. The sensitive temperature factor S_T is derived as follows:

$$S_T = p_1 \cdot y_{meas} + m_1 \tag{4.26}$$

The residual plot for the linear regression of the inverse method is presented in Fig. 4.26. The systematic pattern is observed and, hence, the polynomial regression is considered. The calculated coefficient of determination, R^2, is equal to 0.996.
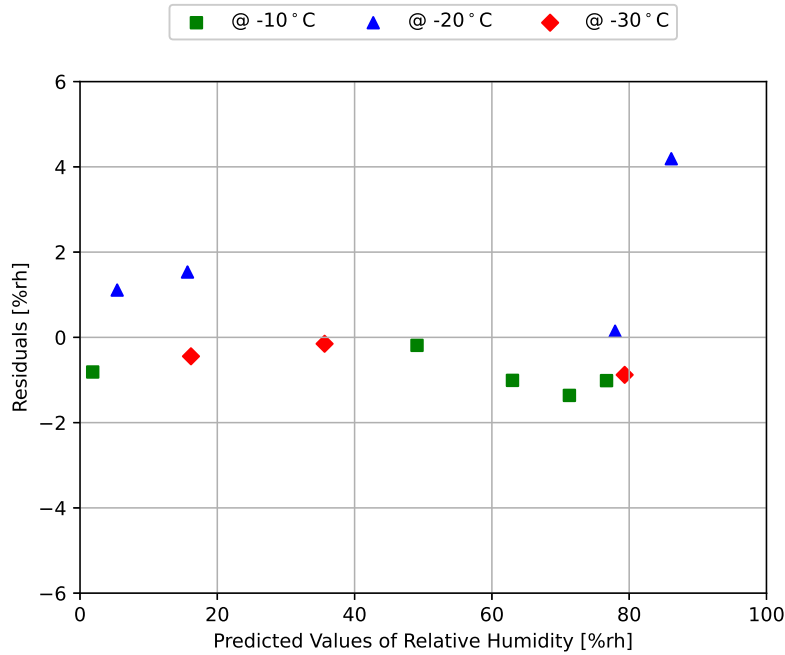
Figure 4.27: Residuals for quadratic calibration equation of inverse method at three different negative temperatures.

The second-degree calibration function to predict the true value is written as:

$$x_{true} = (d_1 \cdot y_{meas}^2 + e_1 \cdot y_{meas} + f_1) \cdot T + d_2 \cdot y_{meas}^2 + e_2 \cdot y_{meas} + f_2 \tag{4.27}$$

where d_1, d_2, e_1, e_2, f_1 and f_2 are constants of linear temperature-dependant functions ($d = d_1 \cdot T + d_2$, $e = e_1 \cdot T + e_2$ and $f = f_1 \cdot T + f_2$).

The temperature sensitivity factor, S_T, is derived as:

$$S_T = d_1 \cdot y_{meas}^2 + e_1 \cdot y_{meas} + f_1 \tag{4.28}$$

The residual plot after the second-order calibration curve is shown in Fig. 4.27. The residuals are uniformly distributed making the second-order polynomial model more adequate. The high value of R^2 is obtained and is equal to 0.998. The uncertainty is calculated using (4.20).

The constants of the linear and polynomial functions in both cases of classical and inverse methods are presented in Table 4.6.

The uncertainties due to calibration procedure and temperature variations for both methods,

Table 4.6: Constants of linear and quadratic calibration functions of classical and inverse methods.

Method	Regression	Constants					
Classic	Linear	k_1	k_2	n_1	n_2		
		0.00655	1.082	0.1465	0.0432		
	Quadratic	a_1	a_2	b_1	b_2	c_1	c_2
		-0.0001192	-0.004883	0.0149	1.464	0.1228	-2.311
Inverse	Linear	p_1	p_2	m_1	m_2		
		-0.00724	0.9086	-0.1625	-0.04307		
	Quadratic	d_1	d_2	e_1	e_2	f_1	f_2
		0.0001126	0.004734	-0.01515	0.5629	-0.1581	1.011

classical and inverse, and linear and quadratic regressions at different negative temperatures are presented in Tables 4.7-4.9. The uncertainty due to calibration with linear and quadratic models of the inverse method has the same value. At -10 °C, the classical linear method shows slightly smaller uncertainty due to the calibration procedure and temperature variations compared to the inverse method. For -20 °C and -30 °C, the inverse method offers smaller uncertainty due to calibration procedure and temperature variations. Thus, the inverse method is selected as the calibration procedure when humidity sensors operate well below 0 °C. There is no significant difference between the linear and quadratic approaches in the case of the inverse method. However, when using the second-order polynomial model, residuals are uniformly distributed, making it a more suitable calibration model.

Table 4.7: Uncertainties due to calibration procedures and temperature variations at -10 °C

Method	Regression	2 %rh		49 %rh		63 %rh		71 %rh		78 %rh	
		u_{cal}	$S_T \cdot u_{temp}$	u_{cal}	$S_T \cdot u_{temp}$	u_{cal}	$S_T \cdot u_{temp}$	u_{cal}	$S_T \cdot u_{temp}$	u_{cal}	$S_T \cdot u_{temp}$
Classic	Linear	0.181	0.003	0.24	0.01	0.228	0.011	0.134	0.012	0.414	0.013
	Quadratic	0.142	0.002	0.255	0.012	0.273	0.014	0.173	0.015	0.565	0.015
Inverse	Linear	0.184	0.003	0.244	0.011	0.232	0.013	0.136	0.014	0.421	0.014
	Quadratic	0.184	0.003	0.244	0.013	0.232	0.013	0.136	0.013	0.421	0.013

Table 4.8: Uncertainties due to calibration procedures and temperature variations at -20 °C

Method	Regression	5 %rh		15 %rh		78 %rh		87 %rh	
		u_{cal}	$S_T \cdot u_{temp}$	u_{cal}	$S_T \cdot u_{temp}$	u_{cal}	$S_T \cdot u_{temp}$	u_{cal}	$S_T \cdot u_{temp}$
Classic	Linear	0.157	0.004	0.089	0.005	0.146	0.014	0.16	0.015
	Quadratic	0.13	0.003	0.078	0.006	0.179	0.015	0.201	0.015
Inverse	Linear	0.149	0.003	0.085	0.005	0.139	0.014	0.152	0.015
	Quadratic	0.149	0.003	0.085	0.007	0.139	0.014	0.152	0.014

Table 4.9: Uncertainties due to calibration procedures and temperature variations at -30 °C

Method	Regression	16 %rh		36 %rh		78 %rh	
		u_{cal}	$S_T \cdot u_{temp}$	u_{cal}	$S_T \cdot u_{temp}$	u_{cal}	$S_T \cdot u_{temp}$
Classic	Linear	0.161	0.005	0.23	0.008	0.298	0.015
	Quadratic	0.147	0.007	0.221	0.01	0.327	0.013
Inverse	Linear	0.143	0.004	0.204	0.007	0.264	0.012
	Quadratic	0.143	0.006	0.204	0.009	0.264	0.013

Calculation of combined uncertainty

The combined standard uncertainty considers every uncertainty source and in our case is affected by reference sensor uncertainty and DUT uncertainties. It is derived as follows[VIII]:

$$u_c^2 = u_{ref}(RH_{ref})^2 + u_{non}^2 + u_{rep}^2 + u_{res}^2 + u_{hys}^2 + S_T^2 \cdot u_{temp}^2 + u_{cal}^2, \tag{4.29}$$

The values of combined uncertainty are presented in Tables 4.10-4.12 for temperatures of -10 °C, -20 °C and -30 °C, respectively. For the temperature of -10 °C, the linear classical method and inverse method show similar values of the combined uncertainty. At lower temperatures, -20 °C and -30 °C, the inverse method shows better performances. In all three experiments, the combined uncertainty is mostly influenced by Type B uncertainties. The uncertainty due to the calibration procedure is the most significant Type A uncertainty, while uncertainty due to temperature variations has a small value and it has negligible influence on the combined uncertainty. The uncertainty of the reference sensor is practically negligible, except at -10 °C and at 78 %rh.

Table 4.10: Uncertainty of measurements at -10 °C

Uncertainty	2 %rh	49 %rh	63 %rh	71 %rh	78 %rh
$u_{ref}(RH_{ref})$	0.006	0.034	0.059	0.083	0.417
$u_{c,clas,lin}$	0.836	0.851	0.849	0.831	1.005
$u_{c,clas,qua}$	0.828	0.856	0.863	0.838	1.076
$u_{c,inv,lin}$	0.836	0.852	0.85	0.831	1.008
$u_{c,inv,qua}$	0.836	0.852	0.85	0.831	1.008
$U_{k=2,clas,lin}$	1.672	1.702	1.698	1.662	2.01
$U_{k=2,clas,qua}$	1.656	1.712	1.726	1.676	2.152
$U_{k=2,inv,lin}$	1.672	1.704	1.7	1.662	2.016
$U_{k=2,inv,qua}$	1.672	1.704	1.7	1.662	2.016

Besides the combined uncertainty, Tables 4.10-4.12 present the expanded uncertainty U as well. The expanded uncertainty is defined as a product of the combined uncertainty and the coverage factor k. The coverage factor, k, is chosen to be 2, giving a level of confidence of 95.45%. The expanded uncertainty is considered as long as the number of effective degrees of freedom, ν_{eff}, is large. To calculate the effective degrees of freedom, the Welch-Satterthwaite equation is used as follows [176]:

$$\nu_{eff} = \frac{u_c(y)^4}{\sum_{i=1}^{n} \frac{u(x_i)^4}{\nu_i}} \tag{4.30}$$

[VIII]Assuming no correlation between the considered parameters.

Table 4.11: Uncertainty of measurements at -20 °C

Uncertainty	5 %rh	15 %rh	78 %rh	87 %rh
$u_{ref}(RH_{ref})$	0.006	0.019	0.05	0.051
$u_{c,clas,lin}$	0.831	0.821	0.83	0.833
$u_{c,clas,qua}$	0.826	0.819	0.837	0.842
$u_{c,inv,lin}$	0.829	0.821	0.829	0.832
$u_{c,inv,qua}$	0.829	0.821	0.829	0.832
$U_{k=2,clas,lin}$	1.662	1.642	1.66	1.666
$U_{k=2,clas,qua}$	1.652	1.638	1.674	1.684
$U_{k=2,inv,lin}$	1.658	1.642	1.658	1.664
$U_{k=2,inv,qua}$	1.658	1.642	1.658	1.664

Table 4.12: Uncertainty of measurements at -30 °C

Uncertainty	16 %rh	36 %rh	78 %rh
$u_{ref}(RH_{ref})$	0.019	0.034	0.059
$u_{c,clas,lin}$	0.832	0.848	0.871
$u_{c,clas,qua}$	0.829	0.846	0.881
$u_{c,inv,lin}$	0.829	0.842	0.86
$u_{c,inv,qua}$	0.829	0.842	0.86
$U_{k=2,clas,lin}$	1.664	1.696	1.742
$U_{k=2,clas,qua}$	1.658	1.692	1.762
$U_{k=2,inv,lin}$	1.658	1.684	1.72
$U_{k=2,inv,qua}$	1.658	1.684	1.72

The effective degrees of freedom are in the range from 116 to 181, presenting enough large value to allow the use of coverage factor ($k = 2$) for the expanded uncertainty according to the [177]. The conducted tests have shown that the combined (and consequently, expanded) uncertainty is lower when employing the inverse calibration procedure for negative temperatures. Therefore, the inverse calibration method is chosen to be used in our application.

4.4 Humidity Sensor Performance Under Strong Magnetic Field

A capacitive humidity sensor typically consists of two electrodes separated by a dielectric material. In the specific case of the MK33-W humidity sensor, the dielectric material is composed of a mixture of non-ferromagnetic polymers, indicating that the magnetic field should not affect its functionality. However, it is necessary to evaluate the behavior of capacitive sensors in the presence of strong magnetic fields before entering the detector complex. In this regard, we conducted tests to investigate the effect of magnetic fields on the performance of the capacitive sensor, and the results are discussed in the following subsections.
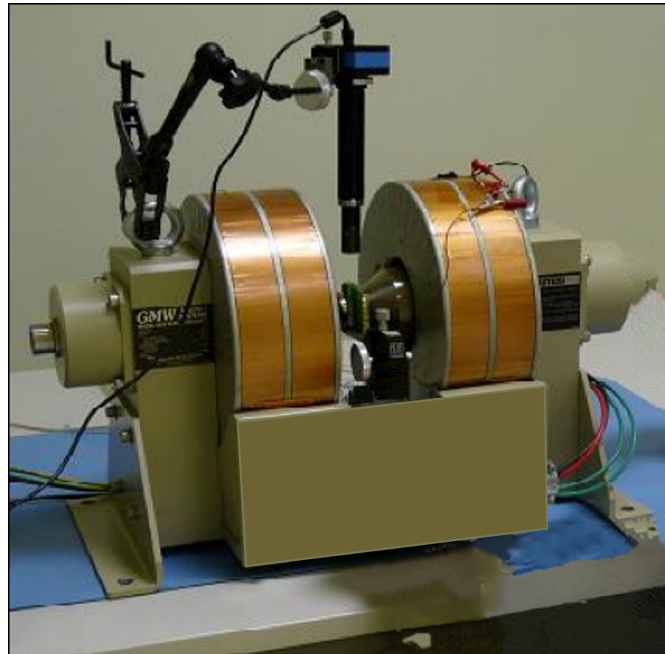
Figure 4.28: This small aperture laboratory electromagnet is capable of producing a 2 T field - the same field strength as in the ATLAS solenoid magnet and about 50 % of that in the CMS magnet.

4.4.1   Experimental setup

The experiment was performed at the **Q**uality **A**ssurance and **R**eliability **T**esting (QART) laboratory in CERN. The photo of the used electromagnet is depicted in Fig. 4.28. The electromagnet has dimensions of 604 mm in width, 282 mm in-depth, and 359 mm in height, with a pole diameter of 38 mm. Depending on the current flowing through the coil and the distance between the poles, the electromagnet could produce a magnetic field ranging from 0 to 2 T. The magnetic field excitation plots are displayed in Fig. 4.29 with respect to the pole gap and the current flowing through the coil. To attain the highest magnetic field, the pole gap had to be minimized, while the current flowing through the coil had to be maximized.

4.4.2   Results and Discussion

In this experiment, a non-irradiated sample and an irradiated sample were used. The irradiated sample was coming from the second irradiation campaign where it received accumulated fluence of $3 \cdot 10^{16}$ protons/cm^2. Besides the devices under test (DUTs), a reference SHT30 humidity sensor [178], was placed in close proximity to the DUTs, but outside of the magnetic field. Its purpose was to provide a reference measurement of the relative humidity, while the DUTs were being tested.

During the experiment, the sensors were placed between the poles of the electromagnet,
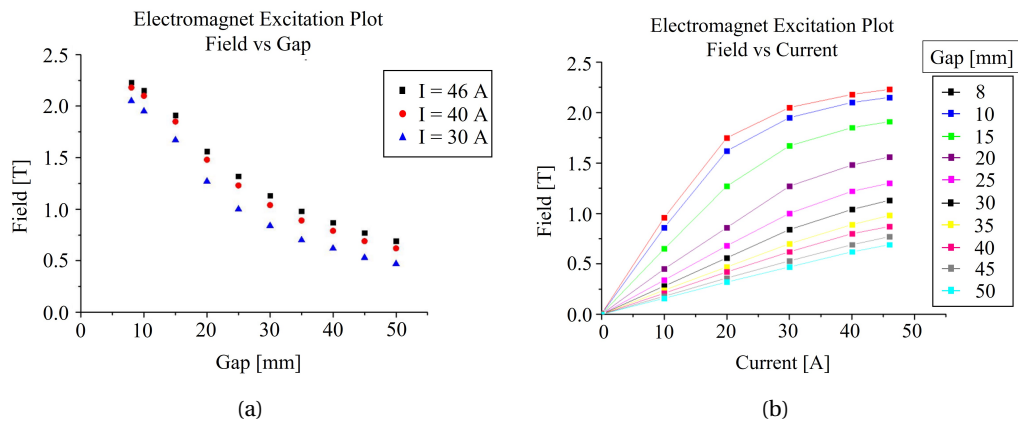
Figure 4.29: (a) Magnetic field with respect to the pole gap. (b) Magnetic field with respect to the current.
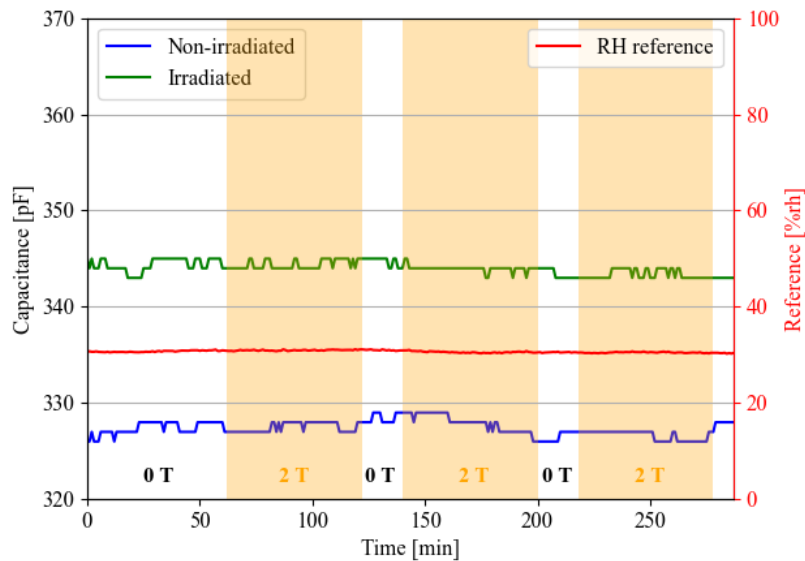
Figure 4.30: Capacitance measurements of non-irradiated and irradiated humidity sensors under alternating magnetic fields ranging from 0 T to 2 T. The measurements from the reference sensor indicate consistent environmental humidity throughout the experiment

with the magnetic field alternating between 0 T and 2 T. Separate experimental runs were conducted with the sensors oriented both perpendicularly and vertically to the magnetic field. Figure 4.30 depicts the outcomes of the magnetic test conducted on the sensors where it can be noticed that no alterations in the sensor outputs were observed.

4.5 Final Models

In the HEP environment, the capacitance of a humidity sensor can be influenced by several factors, including humidity, radiation, temperature, and magnetic fields. The resulting sensor capacitance can be expressed as a function of these variables as follows:

$$C_{out} = f(RH, \Phi(t), T, B) \tag{4.31}$$

where C_{out} is the measured sensor capacitance, RH represents the impact of humidity on the sensor output, $\Phi(t)$ represents the influence of radiation on the measured capacitance, T represents the influence of temperature on the sensor output, and B corresponds to the effect of the magnetic field on the sensor output.

Radiation tests have demonstrated that the MK33-W sensor output exhibits a linear dependence on the accumulated fluence over time. The accumulated fluence during the second irradiation campaign is equivalent to the operational lifespan of HEP detectors in the HL-LHC over 10 years. The change in capacitance due to irradiation over time can be expressed by a factor of $5.01 \cdot 10^{-16}$ pF/(protons/cm^2) (see eq. (4.3)).

Furthermore, tests conducted on both non-irradiated and irradiated sensors under strong magnetic fields did not show any significant effect. Therefore, the contribution of the magnetic field can be neglected. The sensitivity of the MK33-W sensor can change at lower temperatures, as observed in tests conducted at negative temperatures. Thus, the sensor output must be corrected accordingly as shown in eq. (4.27).

Finally, the true capacitance value, solely influenced by humidity and compensated for temperature and radiation effects, can be expressed as follows:

$$C_{true}(rh) = S \cdot RH + C_0 \tag{4.32}$$

where C_0 is the sensor capacitance value in a dry state (~ 0 %rh), S is sensor sensitivity (= 0.45 pF/%rh for the positive temperatures), and RH is the relative humidity, which can be easily calculated from the previous equation.

The observed uncertainty after the irradiation campaign was 1.05 pF, which is equivalent to 2.3 %rh. In the temperature dependence test, the uncertainty of the second-degree inverse calibration function was approximately 1 %rh.

As for the temperature sensor, Pt1000 has proven to be immune to the strong magnetic field. The Pt1000 output can be recompensated for the radiation effects using eq. (4.4). The

uncertainty of the measurements, after receiving the highest expected dose, was 0.13 °C.

4.6   Summary

This chapter presents a comprehensive overview of the tests conducted on a humidity sensor candidate suitable for the HEP environment. The sensors were subjected to high radiation doses equivalent to the dosage expected in the innermost parts of the CMS detector during ten years of operation in the HL-LHC. The test results reveal that the sensor output exhibits a linear dependence on accumulated fluence and can be effectively compensated using a first-order polynomial function. Furthermore, the effects of negative temperatures on the sensor sensitivity can be compensated using an inverse calibration method. Additionally, the tests demonstrate that the strong magnetic field has negligible influence on the sensor measurements.

As the ultimate objective of the project is to determine the environmental dew point temperature, this requires selecting a temperature sensor in addition to the humidity sensor as discussed in Chapter **1**. The tests indicate that Pt1000 temperature sensors are minimally affected by radiation and can be reliably used in the HEP environment.

In summary, these results highlight the tested sensors resilience in harsh environments and their suitability for sub-detectors requiring dew point temperature measurements. This study offers valuable insights for researchers and engineers in the field of HEP, providing guidance in employing reliable and robust environmental sensors in their experiments.

5 Multi-Channel Readout Systems for Humidity and Temperature Monitoring [I]

Without data, you're just another person with an opinion.
— W. Edwards Deming

Given the size of the CMS detector and, thus, the number of sensors required, it is necessary to design multi-channel platforms that are both cost-effective and space efficient for conditioning humidity and temperature sensors.

This chapter details the development of a robust multi-channel readout system designed for the remote conditioning of the capacitive humidity sensors. The circuit effectively mitigates the impact of leakage resistance which arises due to the effects of condensation and pollution on the sensor. Furthermore, the conditioning/readout system is capable of nullifying the cable parasitic capacitance and generating a signal proportional to the observed relative humidity, resulting in a highly accurate humidity-sensing system.

Although Si-based detectors are equipped with in-built Si-based temperature sensors, a significant amount of individual RTD sensors is used as they function independently of the status of the detector. Here, we propose a cost-effective, multiplatform, and easy-to-deploy temperature monitoring system.

[I]Part of this chapter has been published in [179] and [180].

5.1   Equivalent Electrical Circuit of the Capacitive-based Humidity Sensor

Based on the design, capacitive sensors are divided into two groups: grounded capacitive sensors, where one terminal is always grounded; and floating capacitive sensors, where both electrodes are available to the signal conditioning circuit [181]. In both cases, the change in capacitance has to be converted to voltage, current, time/frequency, or pulse width modulation to be measured. This conversion is obtained using an appropriate signal conditioning circuit.

In this study, the focus is given to the floating type of lossy capacitive sensors, such as our selected sensor candidate, and related signal conditioning circuits. The design of the signal conditioning circuit strongly depends on the type of sensor. Some of the proposed interface circuits for capacitive floating sensors are based on bridge architectures (e.g. depletion or auto-balancing configuration) [182], charging/discharging technique [183], synchronous modulation and demodulation [184], and capacitive to digital converters (e.g. charge balancing, dual-slope, and sigma-delta) followed by an analog-to-digital converter (ADC) [185]. Some of the proposed interfaces are designed considering the sensor as a pure capacitor. However, this assumption is not valid for many sensing applications such as the measurement of liquid level, proximity, humidity, as well as in fingerprint sensing [186].

In several cases, including humidity measurements, the simplified electrical equivalent model consists of a parallel connection of the sensing capacitor, C_s, and of an internal leakage resistor, R_s, as shown in Fig. 5.1. In this configuration, the leakage resistor may be present due to improper structure on the substrate or influenced by environmental factors (e.g. temperature, condensation, and pollution) [187]. Stray capacitance C_{p1} and C_{p2} occur as a result of the connection to the sensor electrodes, while $C_{cables1}$, $C_{cables2}$, and $C_{cables3}$ are parasitic capacitance introduced by the cables used to connect the sensor to the signal conditioning circuit. In our application, the signal conditioning unit, which is not radiation tolerant, is going to be placed in a non-radiation affected zone and it is going to be separated from the sensor by a cable which length is of the order of 100 m. The capacitance of the typical coaxial cable is 100 pF/m, thus, a 100 m long cable will make the sensor "invisible" to readout electronics making the monitoring pF changes in sensor capacitance over cables non-trivial. In such cases, the circuit output no longer contains only the information about the sensing capacitance and it has to be accordingly modified in such a way that the information produced is not affected either by the leakage resistor or by the stray capacitance due to the sensor leads, including the parasitic capacitance introduced by the cables.

5.2   State-of-the-Art

The output signal of the lossy capacitive sensor is presented as the complex impedance, containing the real and imaginary parts due to the parallel connection of the sensor capacitance
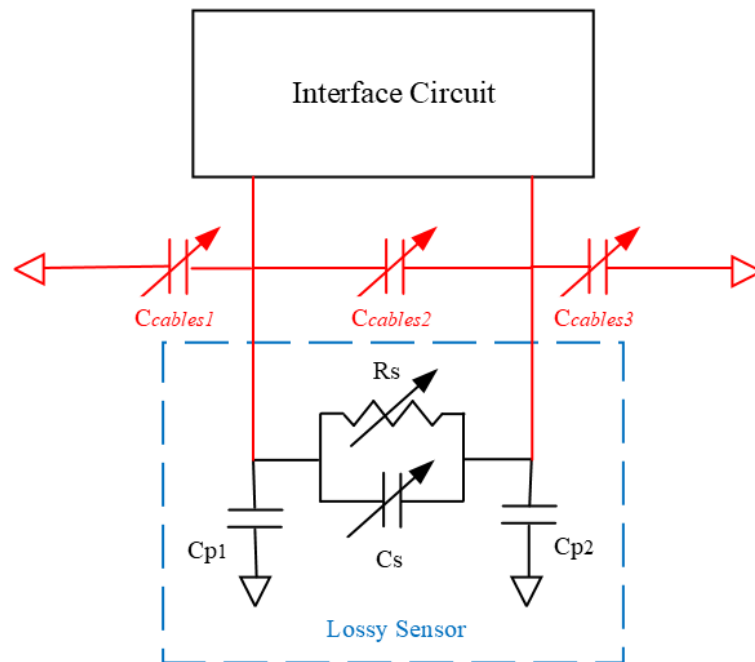
Figure 5.1: Equivalent electrical circuit for the leaky capacitive-based relative humidity sensor, where C_s represents the sensor capacitance, R_s is the internal sensor leakage resistance, and C_{p1} and C_{p2} are parasitic capacitance due to the sensor leads, while $C_{cables1}$, $C_{cables2}$, and $C_{cables3}$ are parasitic capacitance caused by the presence of cables.

and leakage resistance.

Table 5.1 presents a comparison of some of the measurement circuits for the lossy capacitive sensors (without the presence of the cables) available in the literature. Many of the proposed solutions offer low relative error, high immunity to stray capacitance caused by the sensor leads, and measure the capacitance in the pF range that is necessary for the capacitive humidity sensors. However, in the case of high radiation effects, the conductance losses cannot be predicted and neglected. Therefore, a measurement circuit with high immunity to conductance losses is needed. In such a case, a widely used method to separate the sensor capacitance from the leakage resistance is quadrature detection [188].

The quadrature detection method is used in sine-wave-based bridge architectures where the sensor signal is amplified before it reaches the phase-sensitive detectors (PSD). It usually consists of two phase-sensitive circuits, where one manages a signal in phase with the excitation signal and returns the real part of the measured impedance, while the second circuit manages a signal that is phase-delayed by 90 degrees with respect to the excitation and returns only the imaginary part of the signal.

Table 5.1: Comparison of measurement circuits

Ref	Capacitance Range	Circuit Topology	Output Type	Immunity to Stray Capacitance	Immunity to Conductance Losses	Relative Error
[182]	900 pF - 1.1 µF	Bridge	Analog	Medium	High	< 10%
[189]	100 pF - 2 nF	Bridge	Digital	High	33 kΩ- 3 MΩ	< 6%
[190]	1 pF - 619 pF	Relaxation Oscillator	Digital	High	Medium	2.33%
[191]	9.6 pF - 597.8 pF	Relaxation Oscillator	Digital	High	270 kΩ- 9.6 MΩ	1.1%
[192]	66 pF - 506 pF	Dual-Slope + PSD	Digital	High	270 kΩ- 100 MΩ	±1%
[193]	50 pF - 800 pF	Multi-Slope	Digital	High	50 kΩ- 950 kΩ	< 0.6%
[194]	6 pF - 22 pF	Bitstream/Average	Digital	High	Medium	< 0.2%
[195]	47 pF - 668 pF	Bridge + PSD	Analog	High	High	< 0.18%

5.3   Auto-balancing Bridge Circuit for Capacitive-based Sensors

In [195], a PSD-based capacitance-to-voltage converter is presented. The signal conditioning schematic of the proposed solution is shown in Fig. 5.2. It consists of two circuits: an auto-balancing bridge circuit, and a quadrature phase shifter circuit. The principle of operation of the auto-balancing bridge circuit is based on the demodulation of the bridge output and separation of the capacitive component. The demodulation of the bridge output signal is done by the switch controlled by the quadrature phase-shifted signal. The quadrature phase shifter is designed using a voltage-controlled all-pass filter and a quadrature detector in a feedback loop. The quadrature detector is implemented with an analog multiplier, a low-pass filter, and an integrator.

By solving the quadrature phase shifter circuit, the phase shift φ between the excitation sine signal ($V_i(t) = V_m \sin(\omega t)$) and all-pass filter output is defined as [195]:

$$\varphi = \pi - 2\arctan\left(\omega C_p \frac{K_2 R_p}{K_2 - V_{int}(t)}\right), \tag{5.1}$$

where ω is the angular frequency of the excitation signal, C_p and R_p are the capacitor and resistor of the all-pass filter, respectively, K_2 is the gain factor of the multiplier M_2 and $V_{int}(t)$ is the output voltage of the integrator. The ratio in the equation has the dimension of a (voltage-controlled) resistor. We notice from eq. (5.1) that the phase shift φ depends on the parameters of the all-pass filter R_p and C_p as well as on the frequency $f(=\frac{\omega}{2\pi})$ of the excitation signal. Therefore, the operating frequency range of the proposed circuit is determined by choosing the values of the components of the RC network.

The shifted signal is used as a control signal for the switch of the auto-balancing bridge circuit. The output voltage of switch $V_{SW}(t)$ can be derived as follows [195]:

$$V_{SW}(t) = \begin{cases} -V_m R_m \left[\frac{1}{R_S}\sin\omega t + \omega(C_S - \frac{V_{sens}}{K_1}C_r)\cos\omega t\right], \\ \varphi < \omega t < \pi + \varphi \\ V_m R_m \left[\frac{1}{R_S}\sin\omega t + \omega(C_S - \frac{V_{sens}}{K_1}C_r)\cos\omega t\right], \\ \pi + \varphi < \omega t < 2\pi + \varphi \end{cases} . \tag{5.2}$$

where V_m is the magnitude of the input signal, R_m is the resistor used in the current-to-voltage configuration, C_s is the sensor capacitance, V_{sens} is the measured output voltage, K_1 is the gain factor of the multiplier M_1, and C_r is the reference capacitor. The low-pass filter is added at the output of the switch to remove the high-frequency components. The output voltage of this configuration is, [195]:
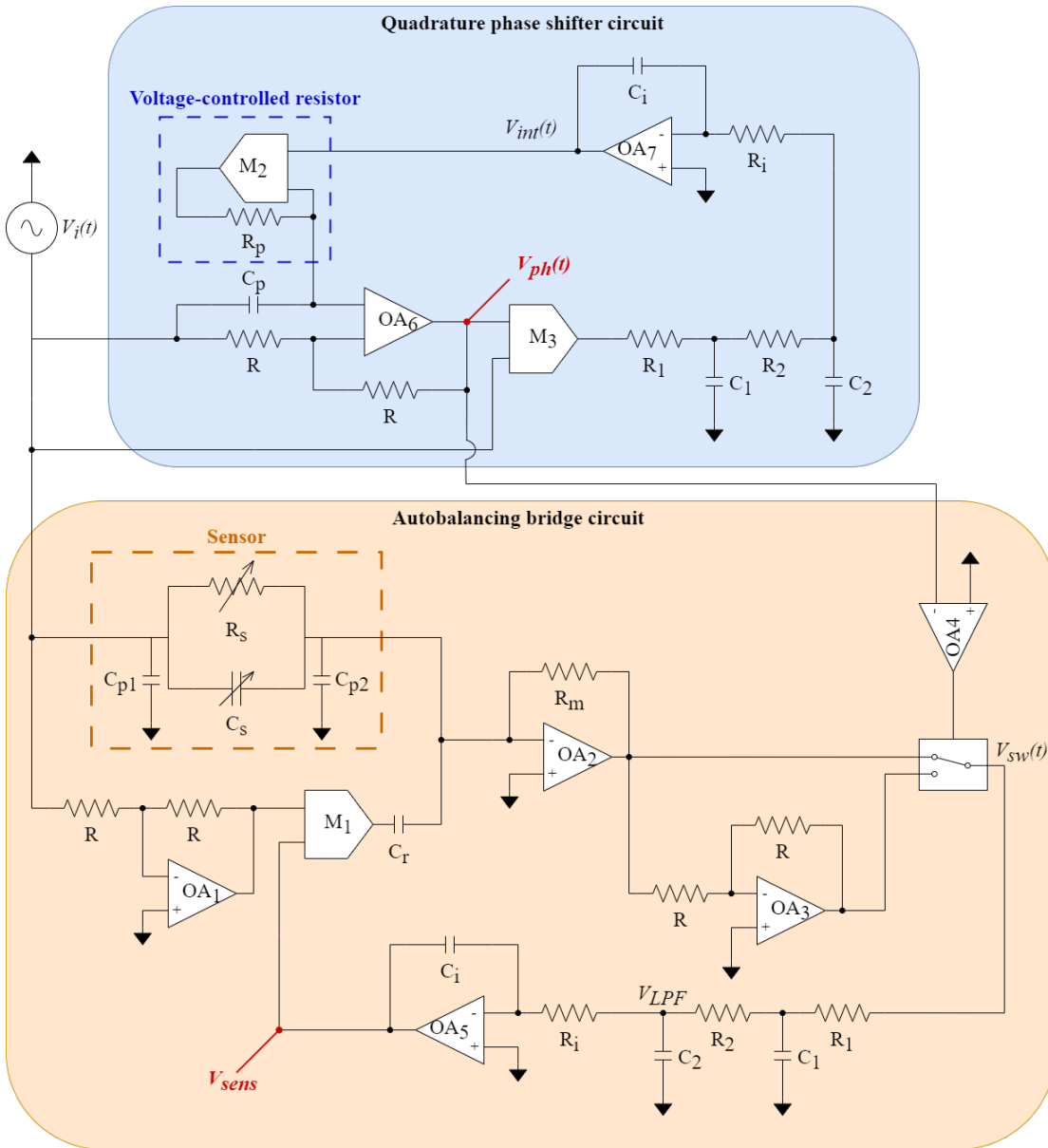
Figure 5.2: Schematic diagram of the signal conditioning circuit with a quadrature phase shifter, and auto-balancing bridge circuit. The quadrature phase shifter contains a voltage-controlled all-pass filter and a quadrature detector in a negative feedback loop. It is used to separate the sensing capacitor from the bridge output signal.

$$V_{LPF} = \frac{-2V_m R_m}{\pi}\left[\frac{1}{R_S}\cos\varphi + \omega\left(C_S - \frac{V_{sens}}{K_1}C_r\right)\sin\varphi\right].\tag{5.3}$$

The output signal of the low-pass filter is then fed to the feedback loop, and (at the null condition) the sensor capacitance is measured as [195]:

$$C_S = \frac{V_{sens}}{K_3} C_r. \tag{5.4}$$

Furthermore, the signal circuitry is designed in such a way that the parasitic capacitance, C_{p1}, does not affect the circuit performance as long as the circuit is driven with a low impedance excitation source, while the capacitor C_{p2} is at virtual ground.

In this study, the previously described method is adapted and modified to effectively compensate for the effect of the parasitic capacitance caused by the long cables. This addition is necessary when the measurand must be read out from distances of tens of meters.

To compensate for the parasitic capacitance, $C_{cables1}$, $C_{cables2}$, and $C_{cables3}$, the cable type has to be chosen properly. In the case of a typical cable, the parasitic capacitance is caused by an inner conductor core, acting as one of the capacitor plates, its insulation acting as a dielectric, and any random conductor that happens to be present in the vicinity of the cable core. The random conductor represents the second capacitor plate and it can be of unknown size and distance, and, hence, causing the unknown parasitic capacitance. The presence of the other signal-carrying cable in the vicinity may, also, couple into the capacitance measurements. In that regard, a proper candidate to minimize the effect of $C_{cables1}$, $C_{cables2}$, and $C_{cables3}$ is a coaxial cable. The coaxial cable consists of an inner conductor, surrounded by the inner insulation, and a second conductor, the shield, that encloses the inner insulation. The shield is electrically insulated by the outer insulation.

Fig. 5.3 (a) illustrates a way of connecting the sensor to the interface circuit using a pair of coaxial cables. The C_{cp1} and C_{cp2} represent the parasitic capacitance between the cable core and cable shielding, while C_{shiled} represents the parasitic capacitance between the shielding of the cables.

In our proposed configuration, one sensor end is at the virtual ground, and to nullify the effect C_{cp2}, the cable shield must be connected to the ground potential. This approach is called passive shielding (Fig. 5.3 (b)). However, this configuration is not useful in the case of the parasitic capacitance C_{cp1}. This capacitance considerably increases the parasitic capacitance to the ground, making passive shielding unsuitable.

To avoid these issues while maintaining shielding effectiveness, active shielding is applied [196], [197]. This involves driving the cable shield at the same potential as the inner conductor using a shield-driver circuit (SDC), as depicted in Fig. 5.3 (b). In this configuration, external interferences are driven to ground through the low output impedance of the SDC, and C_{cp1} should ideally not impact the measurement since both cable conductors (core and shield) are at the same potential. If the pair of coaxial cables are kept enough apart from each other, the effect of the C_{shiled} is negligible.

The described approach has been tested for various sensor capacitance, ranging from 100 pF

(a)

(b)
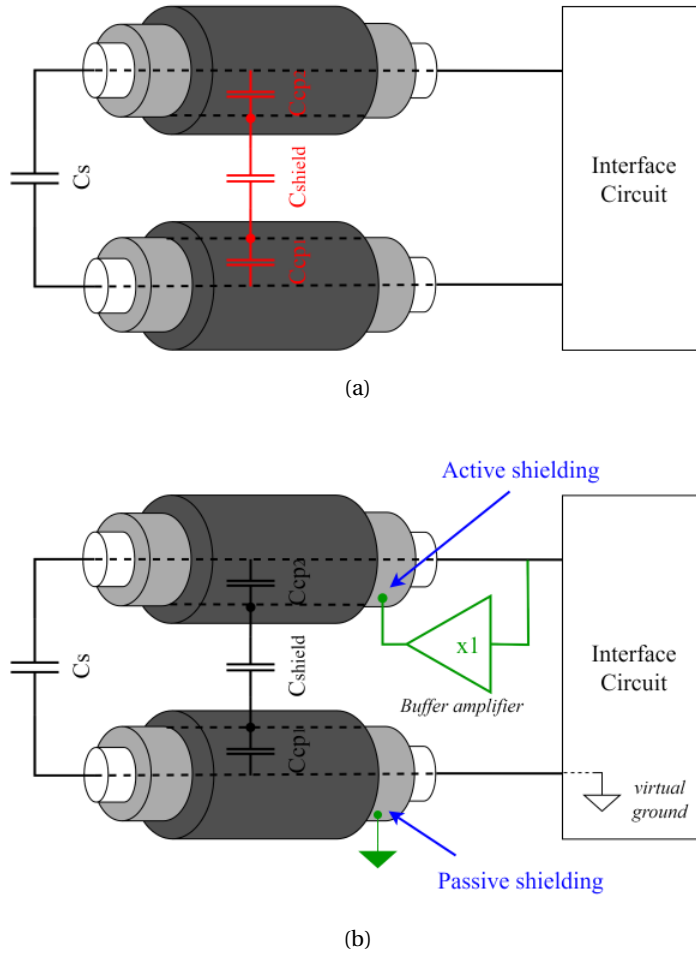
Figure 5.3: (a) Schematic representation of the cable parasitic effects on the sensor capacitance (C_S). (b) Configuration for nullifying the cable parasitic effects using passive and active shielding.

to 500 pF, with the presence of leakage resistance. Different lengths and types of cables were used and the results of the experiments are presented in section 5.4.

5.3.1   Error Analysis

Effect of the Input Offset Voltage of the Operational Amplifiers

The operational amplifiers possess a finite input offset voltage that can affect the performance of the proposed circuit. The operational amplifiers OA_1, OA_2, OA_3, and OA_5 introduce dc offset voltages V_{off1}, V_{off2}, V_{off3} and V_{off5}, respectively at the output of each op-amp.

The dc offset voltage V_{off1} at the output of $OA1$ is eventually filtered out by reference capacitor C_r. The PSD operation nullifies V_{off2} as it has the same amplitude but opposite polarity in $V_a(t)$ and $V_b(t)$. On the other hand, op-amp $OA5$ introduces a dc offset V_{off5}, which means

that V_{LPF} will not be zero at the balanced state but instead will be V_{off5}. By taking into account these offset voltages, the offset output voltage used to compute the sensor capacitor C_S is derived as follows:

$$V_{off} = \frac{\pi(V_{off5} - V_{off3})}{-2\omega V_m R_m},$$
(5.5)

The effective input offset voltage caused by OA_3 and OA_5 is reduced by a factor of $\omega V_m R_m$. In the prototype, the op-amps OA_3 and OA_5 are implemented with the LT6012 chip, which has a maximum input offset voltage of 60 μV. The values of V_m, R_m, and excitation frequency ($f = \omega/2\pi$) were 1 V, 20 kΩ, and 1 kHz, respectively. The worst-case error resulting from the (5.5) is less than 0.35 %. However, the use of more precise operational amplifiers can further reduce this effect.

Effect of the Gain-Bandwidth Product of the Operational Amplifiers

The practical op-amps are affected by the limited gain-bandwidth product (GBP) and they can affect some of the measurements of the sensor parameters. The op-amp is modeled as a single-pole system with an open-loop transfer function:

$$A(s) = \frac{A_0}{\left(1 + \frac{s}{\omega_0}\right)},$$
(5.6)

where A_0 is the open-loop dc gain and ω_0 is the dominant pole frequency. The product $A_0\omega_0$ is the GBP.

Taking into account the effect of the GBP, the amplitude and phase of the output voltage of inverting amplifiers OA_1 and OA_3 will be modified by a factor of $1/(1 + (2\omega/A_0\omega_0)^2)^{1/2}$ and $-tan^{-1}(2\omega/A_0\omega_0)$, respectively. In the prototype, the chosen op-amp has a GBP of 0.3 MHz, resulting in a magnitude error of 0.1 % and a phase error of -0.017 ° at an excitation frequency of 1 kHz for amplifier OA_1.

Similarly, the effect of GBP of op-amp OA_2 has been analyzed, and the magnitude error and phase error are 0.001 % and 0.04 °, respectively, for the worst-case measurement scenario.

For the integrator implemented using OA_5, capacitor C_i, and resistor R_i, the transfer function $T(s)$ with finite GBP of the op-amp is given as:

$$T(s) = \frac{-GBP}{sR_iC_i\left(s + GBP + \frac{1}{R_iC_i}\right)}, \tag{5.7}$$

which introduces a phase error and magnitude multiplying factor of $tan^{-1}(\omega/(GBP + 1/R_iC_i))$ and $1/(1 + (\omega/GBP)^2)^{1/2}$, respectively. For the prototype with GBP of 3 MHz and excitation signal of 1 kHz, the worst-case phase error and magnitude multiplying factor are 0.02 ° and 0.99993, respectively. The use of high-speed op-amps can further reduce the magnitude and phase error due to GBP.

Error Due to the Analog Multiplier

In the balanced condition, assuming the analog multiplier gain error as ΔA_m, the sensor capacitor is calculated as:

$$C_S = \frac{V_{sens}}{(K_1 \pm \Delta A_m)}C_r, \tag{5.8}$$

This indicates that the presence of a gain error in the analog multiplier can cause a measurement error in the sensor capacitance. For the prototype, a precise analog multiplier MPY634 from Texas Instruments was used, and the worst-case error was found to be less than 0.5 %. To estimate the value of the sensor capacitor, the analog multiplier gain error was taken into account. A highly accurate analog multiplier, such as the AD734 from Analog Devices, with an error rate of less than 0.1 %, can be used to avoid the need for calibration.

Effect Due to Errors in the Phase Shifter and Delay Time of the Zero-Crossing Detector

A quadrature-phase shifted signal was generated using an operational amplifier-based all-pass filter followed by a zero-crossing detector ($OA4$). However, small changes in the closed-loop gain of the op-amp or excitation frequency lead to variations in the phase of the quadrature-phase shifter. Furthermore, the delay time t_d of the $OA4$ contributes to the phase error. Assuming $\Delta\varphi_1$ is the phase error due to t_d, which is expressed as $\Delta\varphi_1 = \omega t_d$, and $\Delta\varphi_2$ as the phase error due to the quadrature-phase shifter, the total phase error $\Delta\varphi$ can be represented as the sum of $\Delta\varphi_1$ and $\Delta\varphi_2$. Since the total phase error $\Delta\varphi$ is small, the output of the low pass filter is simplified as follows:

$$V_{LPF} = -2V_mR_m\pi\left[\frac{1}{R_S}(-\Delta\varphi) + \omega(C_S - \frac{V_{sens}}{K_1}C_r)\right] \tag{5.9}$$

The sensor capacitance, considering the phase error $\Delta\varphi$, is written as follows:

$$C_S = \frac{\frac{1}{R_S}\Delta\varphi}{\omega} + \frac{V_{sens}}{K_1}C_r. \tag{5.10}$$

According to (5.10), errors in the measurement of C_S are introduced by R_S and ω. However, the use of a high-speed comparator to implement the $OA4$ can reduce these errors. In the prototype, an AD8599 op-amp with a slew rate of 10 V/μs was employed for this purpose. The delay or propagation time for the square wave signal, which changes amplitude from +10 V to -10 V and vice versa, is 0.63 μs for AD8599. For an excitation frequency of 1 kHz, the maximum phase error introduced by the $OA4$ is less than ±0.005°. The worst-case error in C_S measurement due to the phase error is less than ±0.03 %.

Mismatch Between the R-R Resistors of Operational Amplifiers

This analysis focuses on the mismatch of the $R-R$ resistors of the operational amplifiers OA_1, OA_3, and OA_5. Considering the R_1 and R_2 as the input and feedback resistors of OA_1, and R_3 and R_4 as the input and feedback resistors of OA_3, the voltage V_{LPF} is expressed as:

$$V_{LPF} = \frac{-2V_m R_m \omega}{\pi}\left(C_S - \frac{V_{sens}}{K_1}\frac{R_2}{R_1}C_r\right)\left(1 + \frac{R_4}{R_3}\right). \tag{5.11}$$

At the balance condition, the voltage V_{LPF} becomes zero and the sensor capacitance value is then estimated using the expression:

$$C_S = \frac{V_{sens}}{K_1}\frac{R_2}{R_1}C_r. \tag{5.12}$$

As such, the $R-R$ network of OA_1 has an impact on sensor capacitor measurement accuracy, while the imbalance of the $R-R$ resistors of OA_3 may cause $V_{SW}(t)$ distortion and impact V_{sens} output voltage. Therefore, matching these resistors is crucial. The imbalance of the $R-R$ network of the OA_6, while potentially affecting the signal $V_p(t)$ amplitude, does not affect the constant 90° phase shift φ due to auto-tuning feedback loop. One solution is to use matched (MPMT) resistors that come in one package. The MPMT resistors are matched in temperature and in case of temperature increase (or decrease), both resistors will drift the same and the gain will not be affected.

Effect of Switch Nonidealities

To ensure accurate measurement, the switch used in the circuit must be analyzed for its nonidealities, specifically the ON-resistance and charge injection. Charge injection causes a spike in the switch output, which can impact the LPF output. Choosing a switch with a low-charge injection can help minimize this effect. ON-resistance, on the other hand, reduces the LPF cutoff frequency and affects measurement time, but has minimal impact on sensor capacitance accuracy. Thus, a low ON-resistance switch is preferable. To address these nonidealities, a switch with both low charge injection and low ON-resistance, such as the Analog Devices ADG333, with 20 Ω ON-resistance and 2 pC charge injection for load capacitances up to 10 nF, is recommended. By selecting a switch based on these criteria, the error due to nonidealities will be negligible in the proposed circuit design.

Effect of the Parasitic Capacitance due to the Sensor Leads

To prevent any interference with the measurement, the signal conditioning circuit has been carefully designed to ensure that the parasitic capacitors, C_{p1} and C_{p2}, are not a factor. C_{p1} is attached to the load of the excitation source $V_i(t)$, and will only affect the interface circuit if the source internal impedance is larger than that of C_{p1}. Meanwhile, the other parasitic capacitance, C_{p2}, is not expected to impact the performance of the interface circuit, as one end is connected to the ground while the other is at virtual ground.

Noise/Interference due to the Cable

The performance analysis of active shielding is carried out by considering the circuit illustrated in Figure 5.4 a) and its corresponding electrical circuit shown in Figure 5.4 b), which takes into account the parasitic components of the interconnection cable. In this circuit, the capacitance between the inner conductor and the shield of the coaxial cable is denoted as C_p, while L_p represents the inductance of the current loop between the circuit and the sensor C_S. R_p represents the resistance of the interconnection conductors. It is assumed that all these parameters exhibit linear dependence on the length of the interconnection cable.

To include the operational amplifier (OpAmp) in the analysis, a macro-model with two voltage-controlled sources (VCVS) as depicted in Figure 5.5 is employed. The first VCVS has a gain of A_0, which represents the differential dc gain of the OpAmp, while the second VCVS has a unity gain. The frequency limitations of the OpAmp are modeled using the resistor R_{opa} and the capacitor C_{opa}, which give rise to a dominant pole $\omega_a = 2\pi f_a = (R_{opa}C_{opa})^{-1}$ and a unity-gain bandwidth $\omega_b = 2\pi f_b = A_0\omega_a$. The model also takes into account the output resistance R_o.

A systematic analysis of the circuit in Fig. 5.4 b) provides the following fourth-order transfer function between $V_p(s)$ and $V_{in}(s)$:

(a)   (b)
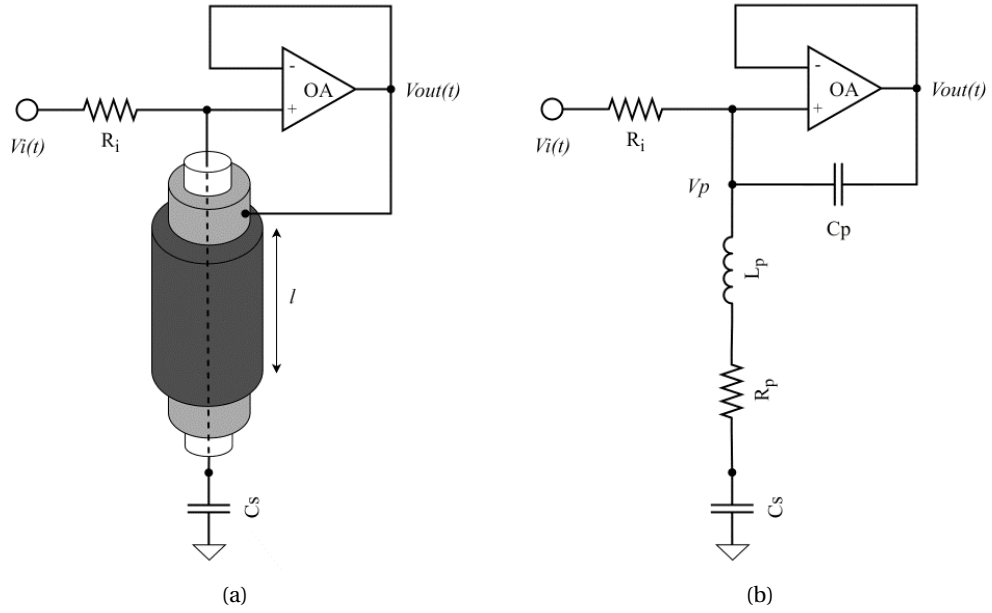
Figure 5.4: (a) Simplified circuit used to analyze the performance of active shielding. (b) The equivalent circuit includes the parasitic components of the interconnection cable.
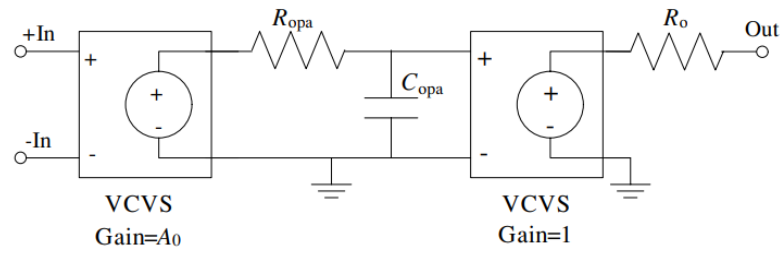
Figure 5.5: Macro-model of the OpAmp that considers the dominant-pole open-loop response and the output resistance R_o.

$$H(s) = \frac{V_p(s)}{V_{in}(s)} = \frac{Q(s)\left[(R_o C_p s + 1)(s + \omega_a) + \omega_b\right]}{P(s)(s + \omega_a) + (Q(s) + R_i C_S s)\omega_b},$$ (5.13)

where

$$Q(s) = C_S L_p s^2 + R_p C_S s + 1,$$ (5.14)

and

$$P(s) = C_p C_S L_p (R_o + R_i) s^3$$
$$+ C_S \left[L_p + C_p (R_o R_p + R_i R_p + R_i R_o) \right] s^2 \qquad (5.15)$$
$$+ (R_o C_p + R_p C_S + R_i C_S + R_i C_p) s + 1.$$

If we consider some practical relations between the parameters where $R_i \gg R_o$, $R_i \gg R_p$, $\omega_b \gg \omega_a$, then the denominator polynomial $d(s)$ of equation (5.13) is simplified to:

$$d(s) \approx R_i C_p C_S L_p s^4 + R_i C_p C_S (R_p + R_o) s^3$$
$$+ \left[R_i (C_p + C_S) + C_S L_p \omega_b \right] s^2 + (1 + R_i C_S \omega_b) s + \omega_b. \qquad (5.16)$$

By applying the Routh–Hurwitz stability criterion [198], in equation (5.16), we obtain the following stability condition:

$$f_b < f_{stab} = \frac{1}{2\pi} \frac{R_i (C_p + C_S)(R_p + R_o) - L_p}{C_S L_p (R_i - R_p - R_o)}, \qquad (5.17)$$

where the frequency f_{stab}, which is determined by the components of the circuit in Fig. 5.4 b), is defined as the maximal allowable bandwidth of the OpAmp to guarantee stability. The previous equation shows that practically f_{stab} is inversely proportional to the parasitic inductance L_p, indicating that decreasing the current loop area between the circuit and the sensor C_S can improve circuit stability. On the other hand, as either C_p or the factor $R_p + R_o$ increases, so does f_{stab}. Accordingly, a capacitor placed in parallel with C_p and/or a resistor added in series with either R_p or R_o should improve stability.

Considering the parameters $r_p = 1.0 \ \Omega\text{m}^{-1}$, $c_p = 100 \ \text{nFm}^{-1}$, and $l_p = 1.0 \ \mu\text{m}^{-1}$, which denote the characteristics of the interconnection cable used in the experimental configuration, and $R_i = 100 \ \text{k}\Omega$, and by employing the minimum value for $R_o = 50 \ \Omega$, according to eq. (5.17), we address the worst case in terms of stability. This results that the maximum allowable bandwidth for OpAmp must be $f_b < 6 \ \text{MHz}$ in order for the circuit to be stable.

5.4   Results and Discussion

A board prototype version was fabricated and various experiments were performed to validate the circuit performances. A photograph of the fabricated prototype is shown in Fig. 5.6. The measurements were obtained with a Textronix TDS 3032B digital oscilloscope and RS Pro LCR 1017 meter. In the bridge configuration, a 1 nF C0G capacitor was used as a reference capacitor

Figure 5.6: Single channel PCB prototype for capacitive humidity sensor readout.

Table 5.2: Overview of the used components and values.

Component	Model/Value
OA1, OA2, OA3, OA5	LT6012
O4, O6, O7	AD8599
M1, M2, M3	MPY634
Analog Switch	ADG333
R	10 kΩ
C_r	1 nF
R_m	20 kΩ
R_i	1 kΩ
C_i	1 µF
f	1 kHz
V_m	1 V$_{p-p}$

due to its low-temperature dependence and high stability. The LT6012 and AD8599 operational amplifiers were chosen, while for the analog switch and analog multipliers, ADG333 and MPY634 chips were used, respectively. The supply voltage was 9 V. Table 5.2 gives a summary of the used components and their values.

The following section about tests is split into three subsections. The first subsection presents the capacitance measurements with a fixed step capacitance change, while the second subsection presents the effects of the parasitic resistance on the capacitance measurements. The third subsection gives an analysis of the influence of various cable lengths and leakage resistances on capacitance measurements.
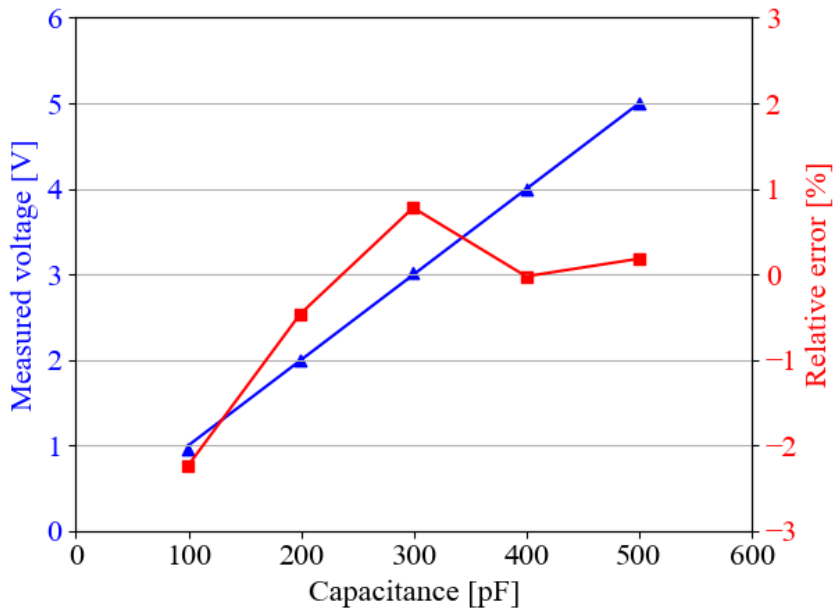
Figure 5.7: Relative error of capacitance measurements for the 100 pF to 500 pF range with a fixed step of capacitance change of 100 pF shown in red. The blue line represents the dependence of measured voltage on capacitance.

5.4.1   Relative Error on the Capacitance Measurements

To extract the imaginary part of the sensor complex impedance, the control signal of the switch must be delayed 90 degrees with respect to the input signal. From equation (5.1), a 90-degree delay is obtained by adjusting the values of frequency f, resistor R_p and capacitor C_p. In this case, the resistor value $R_p = 10 \, \text{k}\Omega$ was chosen, while the input signal has an amplitude of 1 V_{p-p} and a frequency of 1 kHz. Therefore, the C_p value must be in the 1 nF to 30 nF range. A delay of 92.7 degrees with respect to the input signal was measured with the chosen components. From equation (5.3) one can conclude that the absolute error shift of 2.7 degrees does not completely minimize the effect of the parasitic resistance, while the sine wave part of the equation can be approximated as equal to one. In this case, the shift deviation influences the circuit output allowing the leakage resistance to cause an error in the output signal. Lower values of the leakage resistance have a higher negative effect on the circuit output signal.

In these tests, the relative error between the reference and measured capacitors is evaluated. The reference capacitors were initially measured with the LCR meter. In the first test, the reference capacitor was varied from 100 pF to 500 pF in 100 pF steps and the results are shown in Fig. 5.7. The figure shows the linear change of the measured voltage with the change in capacitance. The maximum relative error of around -2 % was measured at 100 pF. The relative error of the measured capacitance with respect to the reference was lower than 1 % in the range from 200 pF to 500 pF.
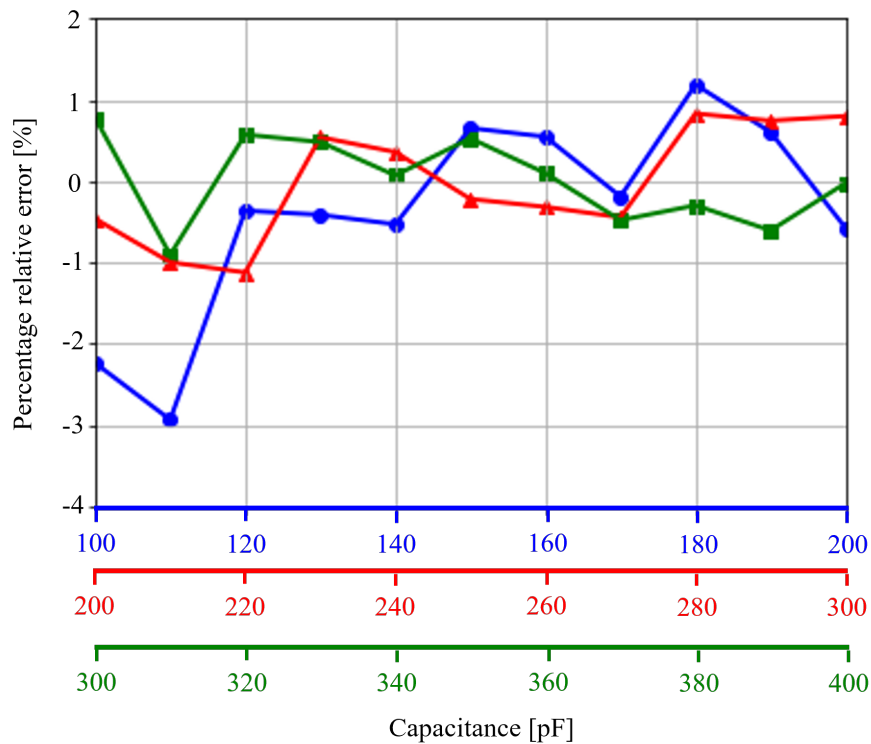
Figure 5.8: Relative error of capacitance measurements for the range from 100 pF to 500 pF with a step of capacitance change of 10 pF.

In the second group of tests, the circuit performances were evaluated by changing the value of the reference capacitor by 10 pF in the 100 pF to 400 pF range. Fig. 5.8 presents the relative error of the measurements. The maximum relative error has -3 % and it occurs for a capacitance of 110 pF. The relative error for the 120 pF to 400 pF range was less than 1.2 % with respect to the reference capacitance.

Considering the MK33-W sensor sensitivity to be 0.45 pF/%rh, a step change of around 5 %rh was emulated with the addition of a 2.2 pF capacitor. The results are presented in Fig. 5.9. The highest relative error was measured in the region between 100 pF and 110 pF and it was between 2 % and 4 %. The relative error reached 1.2% for the capacitance steps around 200 pF and 300 pF, while for the steps around 400 pF the relative error is lower than 0.5 %.

5.4.2   Effects of Leakage Resistance on Capacitance Measurements

The leakage resistance affects the capacitance measurements and, therefore, it needs to be taken into account. To evaluate the effects of leakage resistance on capacitive measurements, the measurements of the capacitance of 100 pF, 200 pF, 300 pF, and 400 pF with "leakage" resistors connected in parallel were taken. The resistance was varied from 910 kΩ to 2.7 MΩ and 3.61 MΩ. The relative errors of the measurements are presented in Fig. 5.10. The
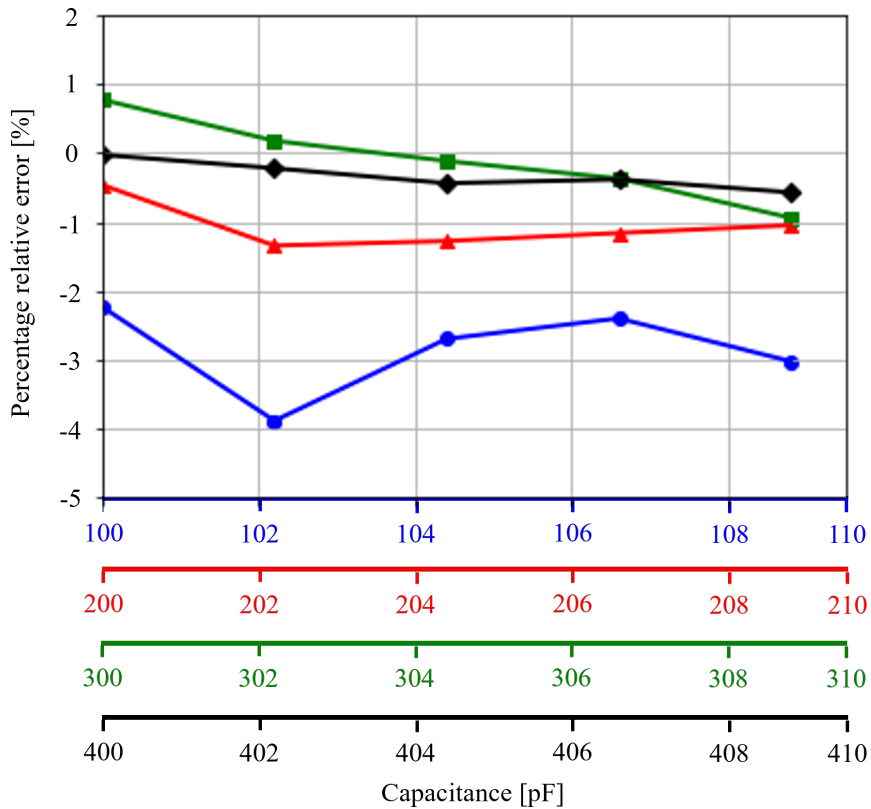
Figure 5.9: Relative error of capacitance measurements with a fixed capacitance step of 2.2 pF.

Table 5.3: Comparison of the signal delay at different frequencies

f [kHz]	C_p [nF]	φ	$\cos\varphi$
1	18	92.7	-0.047
6.2	1	90.5	-0.009

measurements confirm equations (5.3) which shows that lower leakage resistance has a more negative impact on the circuit output. A relative error of around 17% for the 100 pF capacitor and 910 kΩ parasitic resistance was measured with a tendency of increase for the lower values of capacitance and parasitic resistance and that is unacceptable for safety applications.

Additionally, equation (5.3) tells that the effect of the parasitic resistance is decreased at higher frequencies. To operate at higher frequencies, C_p was changed to 1 nF and new measurements were performed at 6.2 kHz. A 90.5 degree delay with respect to the input signal was obtained, also reducing the parasitic resistance effect on the measurements as shown in Table 5.3. The cosine part of the equation corresponds to the effect of the leakage resistance on the output signal. The relative error of the measurements is presented in Fig. 5.10 with dashed lines. The higher relative error of around 3 % was at 100 pF capacitance and leakage resistance of 2.7 MΩ. The smallest relative error was measured at 300 pF capacitance.
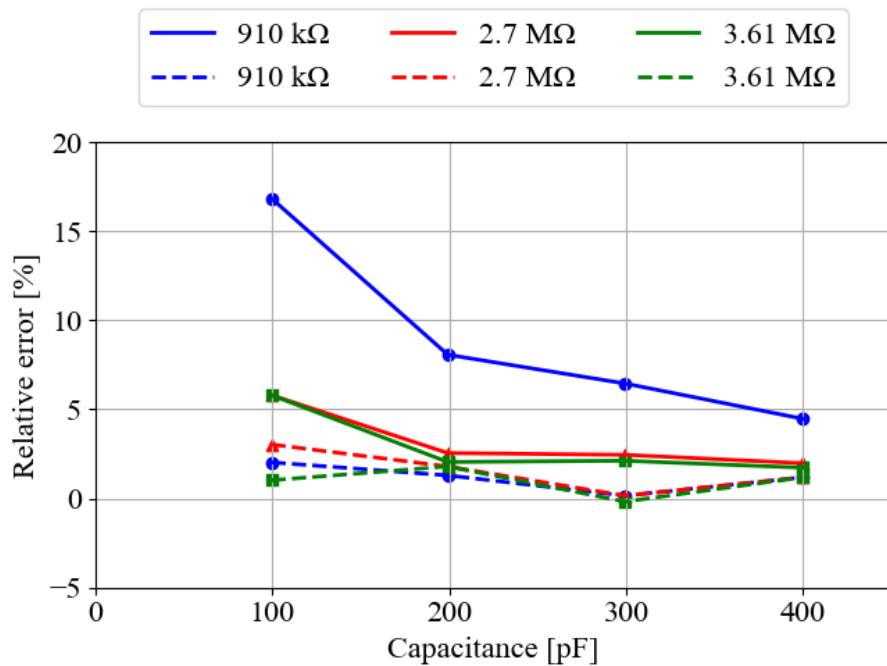
Figure 5.10: Relative error of capacitance measurements for different values of leakage resistance. Full lines present relative errors taken at a frequency of 1 kHz, while the dashed lines show the relative error at a frequency of 6.2 kHz.

5.4.3   Effects of Cable Length and Leakage Resistance on Capacitance Measurements

In industrial or harsh environments the space for the sensor is sometimes limited or the readout electronics performance might be degraded due to effects of the surrounding environment and, therefore, the electronics have to be placed far away from the sensor. Connecting the sensor with the electronics by a cable of a specific length introduces additional parasitic capacitance. In the case of longer cables, the parasitic capacitance might have much higher values than the sensor capacitance making the latter practically invisible to the readout electronics.

In these tests, different cable lengths are used. Two types of cables were considered: NEK RG 58 C/U and Bedea 0801 CA, and their specifications are presented in Table 5.4. The first test was conducted with cable NEK RG 58 C/U and different lengths of 10 m, 20 m and 50 m. Three different capacitors were tested (180 pF, 280 pF and 360 pF) and the results of the measurements are presented in Fig. 5.11. The proposed solution of driving the cable shield successfully minimized the parasitic capacitance effects. The measured relative error is compared with the measurements shown in Fig. 5.8 where the experiment was done without cable. The second test was performed to compare two different cables with different cross-sections. In this test, the cable lengths were 50 m and the measurements are presented in Table 5.5. A higher relative error was measured with the thinner coaxial cable and its maximum value is equal to 2.1 %.
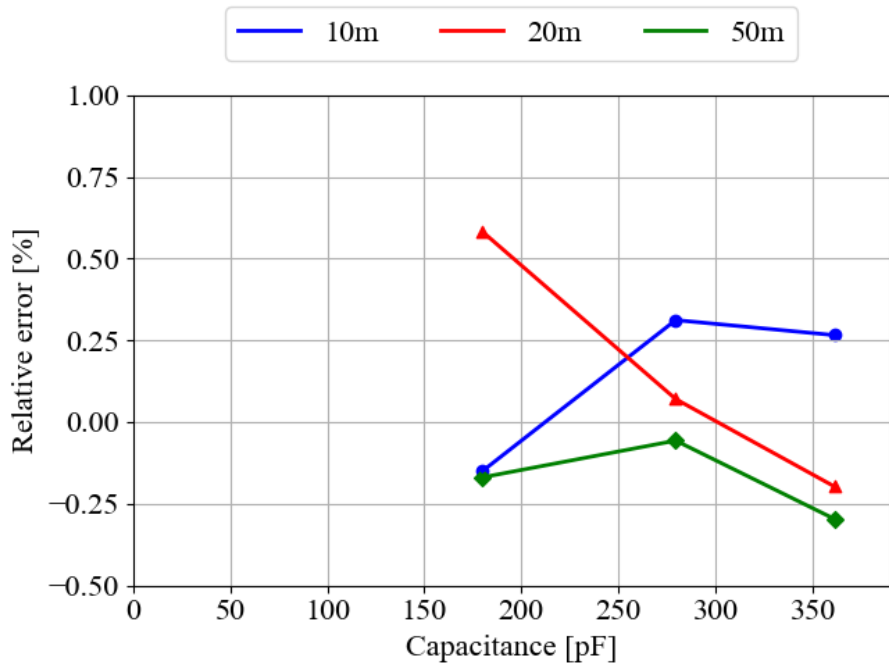
Figure 5.11: Relative error of capacitance measurements at a frequency of 1 kHz for different lengths of NEK RG 58 C/U coaxial cable between the sensor and the signal conditioning unit.

Table 5.4: The types and characteristics of two coaxial cables

Type	Conductor Stranding	Conductor Diameter [mm]	Cable Outer Diameter [mm]	Parasitic Capacitance [pF/m]
NEK RG 58 C/U	19	0.18	3.0	100
Bedea 0801 CA	10	0.1	2.2	100

Table 5.5: Comparison of two different cable types at 1 kHz

Type	Length [m]	Rel. Error [%] at 180 pF	Rel. Error [%] at 280 pF	Rel. Error [%] pF at 360 pF
NEK RG 58 C/U	50	-0.17	-0.06	-0.3
Bedea 0801 CA	50	1.5	2.1	1.09

In the following test, the measurements were conducted on a 180 pF capacitor and at a frequency of 1 kHz, with various resistor values. The same cable types and lengths were used. The results are shown in Fig 5.12 and they are similar to the results obtained without cables and with the presence of parasitic resistance. To minimize the parasitic resistance effects, new measurements were conducted at 6.2 kHz. It is noticeable that there is no change in the output signal due to the variation of the parasitic resistance. However, the relative error is increased at higher frequencies for the cable length of 50 m. The relative error, in the case of various cable lengths, is constant and it can be easily recompensated for further measurements.
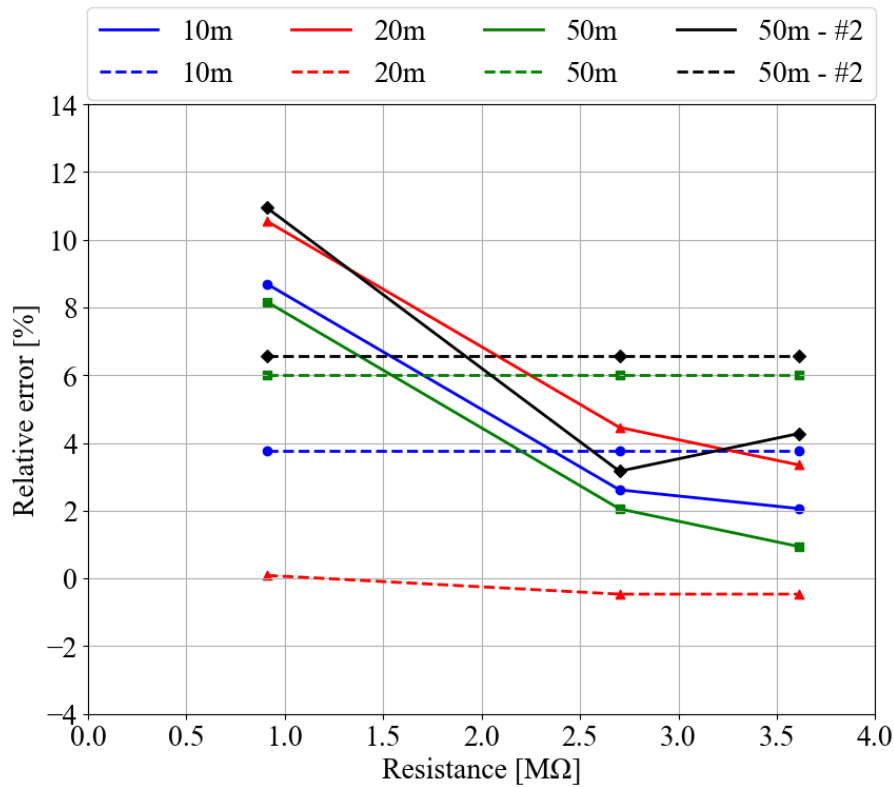
Figure 5.12: Relative error at different frequencies, lengths of NEK RG 58 C/U coaxial cable, and types of coaxial cables (Bedea 0801 CA labeled as #2). Leakage resistor values are also varied. The solid lines show the relative error of measurements obtained at 1 kHz, while the dashed lines present the measurement relative error at 6.2 kHz.

5.5 Multi-Channel Signal Conditioning Unit for Relative Humidity Sensors

The high granularity of the detector necessitates the distribution of a large number of humidity sensors across the detector to ensure valid humidity monitoring. Furthermore, in each sub-detector requiring dew point temperature monitoring, the same number of redundancy humidity sensors must be included, resulting in the need for thousands of sensors. Therefore, it is crucial to design a multi-channel readout unit capable of conditioning as many humidity sensors as possible.

5.5.1   4-channel Signal Conditioning Unit

In the previous section, we presented and analyzed a 1-channel solution that required an external signal generator. In the multi-channel prototype version, we integrated an oscillator into the board to generate a sine wave, eliminating the need for an external signal generator. Additionally, we proposed a solution to generate a quadrature phase-shifted signal, reducing
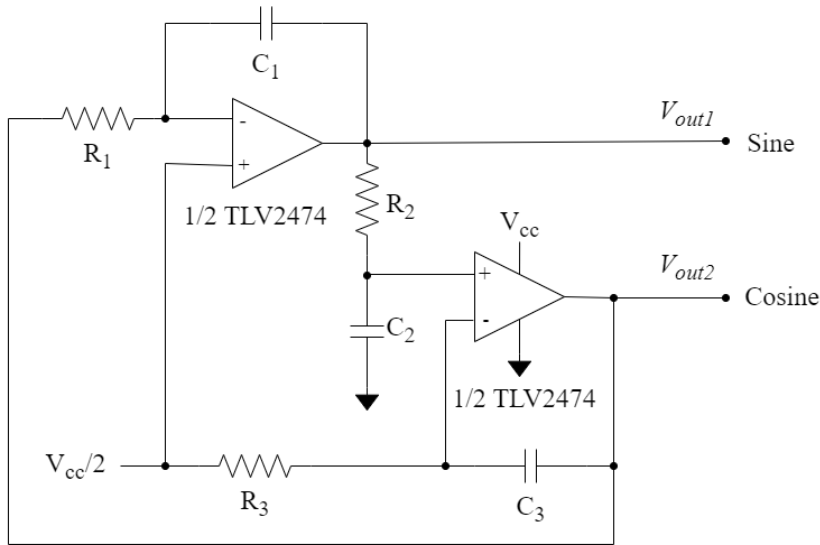
Figure 5.13: Quadrature oscillator based on the TLV2474 chip and three RC networks.

the number of components required in the first solution. The TLV2474 chip, [199], and three RC networks are used to generate the sine and cosine waves. The proposed design is illustrated in Figure 5.13.

The quadrature oscillator exploits the fact that the double integral of a sine wave is a negative sine wave of the same frequency and phase, which is 180° phase-shifted. The phase of the second integrator is inverted and applied as positive feedback to induce oscillation. The loop gain is calculated as follows:

$$A\beta = A\frac{1}{R_1 C_1 s}\frac{R_3 C_3 s + 1}{R_3 C_3 s (R_2 C_2 s + 1)}.$$ (5.18)

When $R_1 C_1 = R_2 C_2 = R_3 C_3$, equation (5.18) reduces to:

$$A\beta = A\left(\frac{1}{RCs}\right)^2.$$ (5.19)

When $\omega = 1/RC$, equation (5.18) reduces to $1\angle-180°$, and oscillation occurs at $\omega = 2\pi f = 1/RC$. Fig.5.14 depicts the output signals of the test circuit built with three 2 kΩ resistors and three 10 pF capacitors. The test circuit oscillated at 8.33 kHz rather than the calculated 7.96 kHz, while the phase difference between the output signals is 89.92 °. This discrepancy in frequency is attributed to component variations. Both outputs had relatively high distortion that can be reduced with a gain-stabilizing circuit. The sine output had 0.637% distortion and the cosine
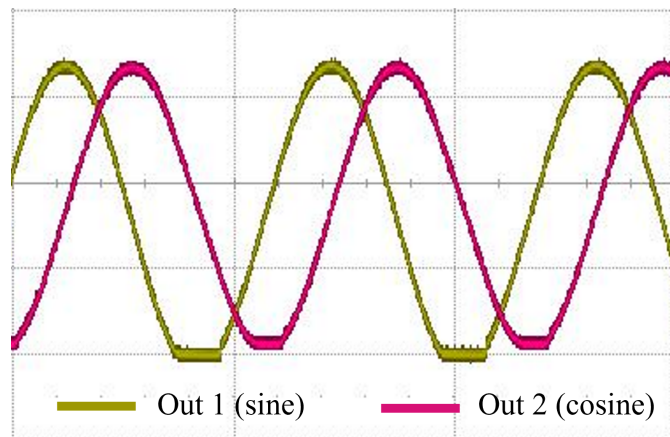
Figure 5.14: Output signals of the quadrature oscillator based on the TLV2474 chip and three RC networks. The phase difference between the output signals is 89.92 °.
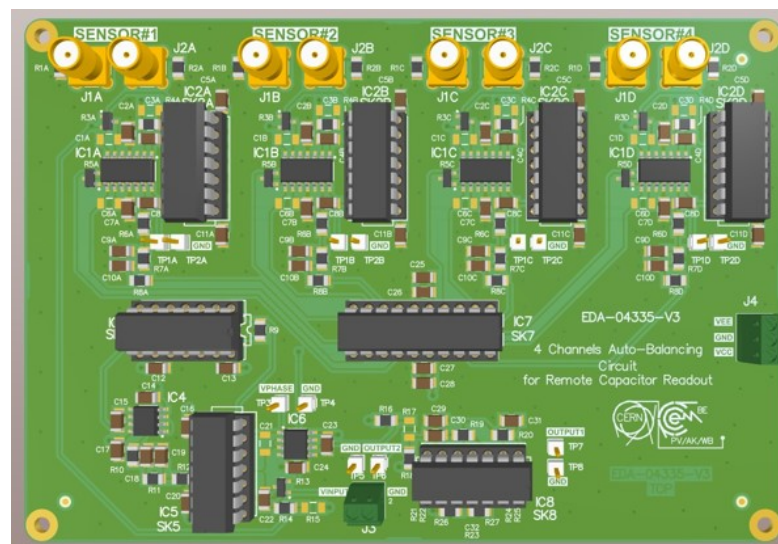
Figure 5.15: 4-channel PCB unit for conditioning capacitive humidity sensors designed using Altium software.

output had 0.43% distortion. Adjusting the gain can increase the amplitudes, but this results in reduced bandwidth.

The multi-channel board must conform to the standard industrial 3U Eurocrate dimensions. In the first multi-channel version, we designed a board with four channels, primarily using SOIC components. The designed PCB is shown in Fig. 5.15, with dimensions of 130 mm x 90 mm.

5.5.2   8-channel Signal Conditioning Unit

The next step is to design the 8-channel signal conditioning unit based on the previously analyzed approach using SMD components. This will allow for the housing of more components on the same board and the conditioning of up to 8 capacitive sensors simultaneously. The board will include two 4-differential channels 16-bit $\Sigma\Delta$ ADC chips (MCP3428 [200]).The digital signals will be selected and addressed by the microcontroller and the board will be equipped with the necessary communication protocols.

Further optimization of the readout will involve considering the integration of multiplexers (MUX) and demultiplexers (DEMUX). Ongoing R&D projects at CERN are working on developing radiation-hardened MUX and DEMUX, which will allow the conditioning of multiple sensors with one readout unit. This will significantly reduce the use of coaxial cables from the detector to the readout electronics, resulting in lower costs for the entire system.

5.6   Standalone Massive Channel System for Temperature Monitoring

In cooling systems, the temperature is a critical parameter that is measured by temperature sensors embedded in the readout chips of Si-based sub-detectors of CMS. However, more monitoring of the temperature is required around the periphery of the detector and detector-off side, demanding the use of more RTDs rather than temperature sensors embedded in readout chips. In the past, monitoring and control are carried out through PLC-based systems, which are robust for data acquisition, monitoring, and controlling processes. However, as the number of channels to be monitored increases, the cost per channel read by PLC increases as well as the occupied space.

To address this issue, we propose a cost-effective, multi-platform, easy-to-deploy RTD readout system that minimizes cost and occupied space as objective functions. The proposed readout system efficiently conditions the RTD 4-wired temperature sensors, as they are radiation-hard, reliable, compatible with detector conditions, and engageable in the detector safety system (DSS) and detector control system (DCS). RTDs are also readily available, affordable, and operate at temperatures from -200 °C to 850 °C. Furthermore, they provide high measurement accuracy by compensating for all series resistance due to engaging with lead connectors. Besides the RTD sensor, the proposed readout system can also house a different temperature sensor. Fig. 5.16 shows a picture of the actual card and the card is briefly discussed in the following subsections.

5.6.1   The LTC2984 chip

The card conditions up to 24 RTD sensors in a 3U Eurocrate format using four LTC2984 chips [201]. It is powered using 5 V and consumes about 100 mA all components included. The
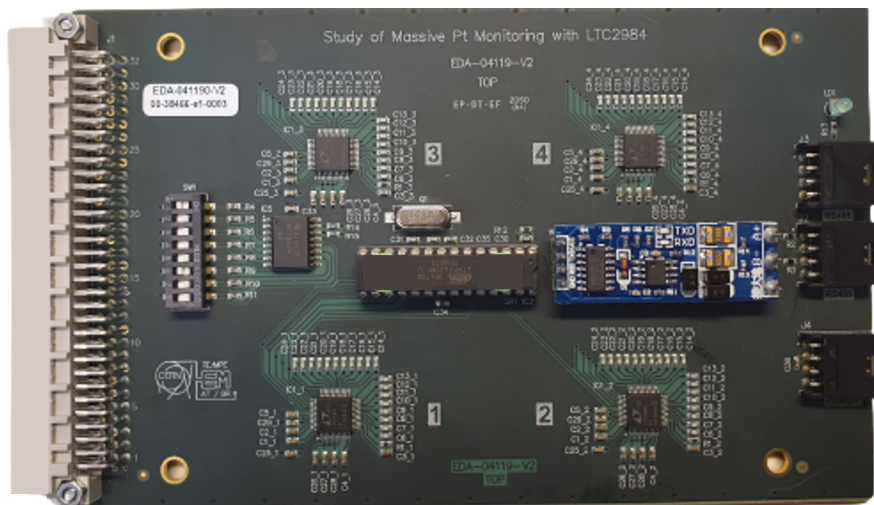
Figure 5.16: A photograph of the fabricated PCB prototype to readout up to 24 temperature sensors.

LTC2984 chip, produced by Analog Device, is widely used for temperature measurement and can measure a range of temperature sensors, including RTDs, thermocouples, diodes, and thermistors. The chip includes 20 channels for sensor connections and configurations (see Fig. 5.17). Buffers protect the inputs against external signals and filter them without drop errors. It also features three 24-bit $\Delta\Sigma$ ADCs, providing conversion of analog sensor input to digital output with high accuracy of 0.1 °C and resolution of 0.001 °C. Additionally, the LTC2984 includes electrically erasable programmable read-only memory (EEPROM), which stores custom coefficients in RAM for accommodating custom sensors. Standard coefficients are stored in ROM eliminating the lockup tables. Rotatable current sources eliminate thermocouple effects in resistive measurements. The serial protocol interface (SPI) provides convenient device configuration and sensor readout in °C and °F.

5.6.2   DAQ of the RTDs

Fig. 5.18 depicts a schematic of the communication protocols. An ATMEGA328P-U microcontroller [202], is used for selecting and addressing the LTC2984 chips. The data is read over the ATMEGA SPI bus. The ATMEGA I2C bus is used for reading the status of the board switches used for configuring the board and the ATMEGA UART is employed to communicate the information to the outside world but also to initiate the transfer of data over the RS485 protocol. With the multi-temperature readout system is planned to read several hundreds of RTDs both in the LS3 CMS as well as in massive detector tests before the installation.
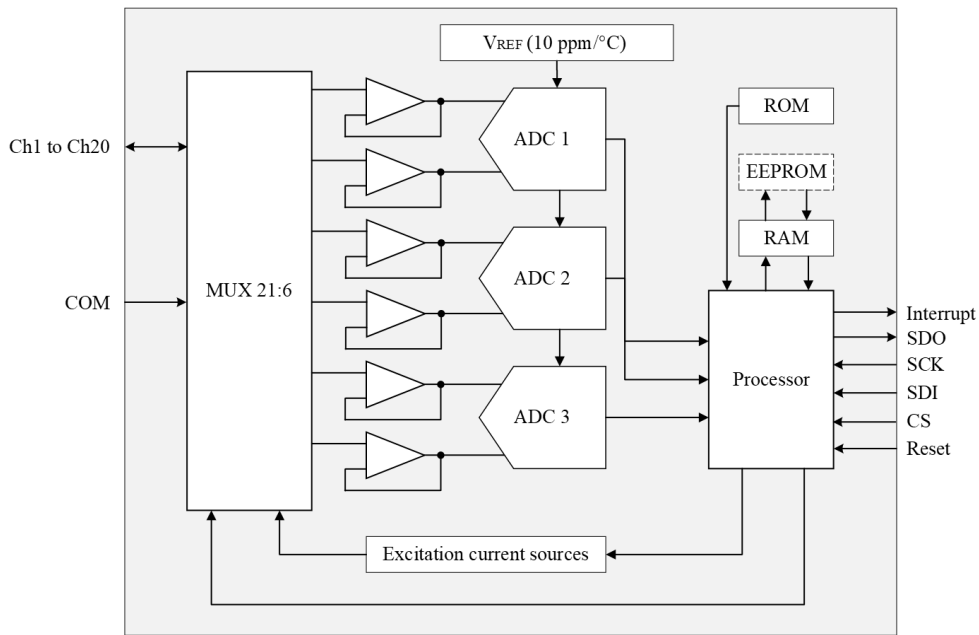
Figure 5.17: A block diagram of the LTC2984 chip.
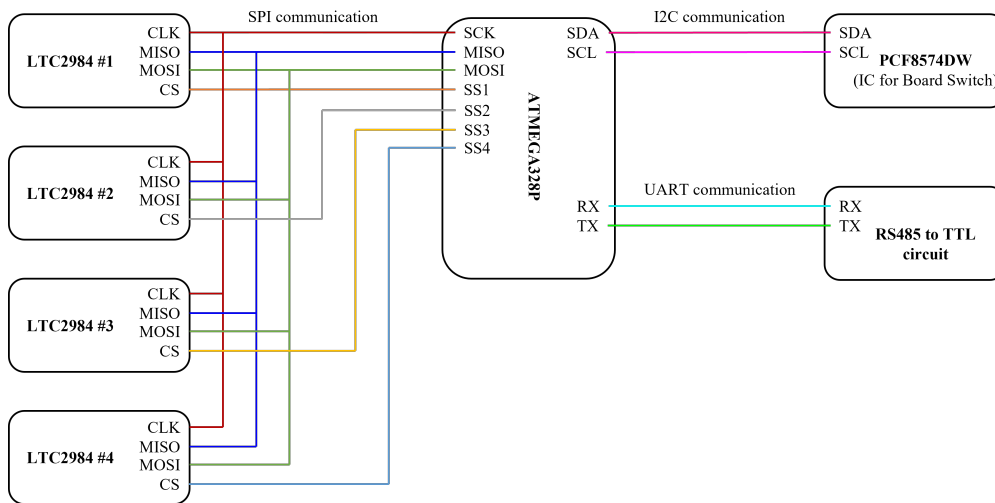
Figure 5.18: A schematics of the communication protocols.

5.7   Summary

Effective monitoring of temperature and humidity is a critical aspect of controlling the cold subdetector in the CMS detector, and its significance will only increase in the LS3 phase. In this regard, we developed and examined two dedicated systems that are specifically designed for this purpose and will be integrated into the cold subdetector DCS.

This chapter outlines an efficient analog signal conditioning circuit that facilitates the reading

of lossy capacitive sensors over long distances. The circuit employs an auto-balancing bridge architecture and a quadrature-phase shifter to generate a 90-degree phase delay with respect to the excitation signal. In the initial version of the system, an external signal generator was necessary to generate a sine excitation signal. In the second iteration, the external signal generator was replaced with an internal oscillator that generates a sine wave. Furthermore, three RC networks are used to generate and shift the sine wave to produce a cosine wave reducing the number of components required. Lastly, we proposed an 8-channel readout unit in conjunction with the microprocessor and the following communication protocols. Further optimization of the readout will involve considering the integration of rad-hard MUX and DMUX.

In previous years, temperature monitoring was provided through PLC-based systems that are not cost-effective and take up a lot of space on the off-detector side. Here, a new design for a temperature monitoring system is presented. The proposed design conditions up to 24 RTDs and can operate independently or as a part of the group. Additionally, it presents a cost-effective and easy-to-deploy solution compared to the current PLC-based solutions for massive temperature monitoring. The temperature monitoring system is currently operational in several testing facilities in preparation for the LS3 subdetectors.

6 Integration of Humidity and Temperature Monitoring Systems in the CMS [I]

Coming together is the beginning.
Keeping together is progress.
Working together is success.
— Henry Ford

This chapter discusses the integration of humidity and temperature sensors within the CMS detector, with a particular focus on the cold CMS sub-detectors. In order to understand the significance of sensor integration, we first discuss the cooling system employed in the parts of interest of the CMS detector, as well as the (indispensable) distribution of dry gas within the detector. The chapter then highlights the importance of dew point temperature monitoring, especially in the detector parts where the temperature can be lower than the dew point of the experimental cavern and with not completely closed sub-detectors (e.g. HGCAL). Furthermore, the situations where cooling or gas distribution system failures occur have to be considered. Based on this, an in-depth analysis is dedicated to the positioning of humidity and temperature sensors within the cold sub-detectors. Lastly, this chapter closes with the integration of the temperature and humidity monitoring systems into the CMS detector control system (DCS) and detector safety system (DSS).

6.1 Detector cooling system for the CMS experiment

For several years, smaller-size systems using the concept of pure CO_2 two-phase accumulator-controlled loop (2PACL) have been successfully implemented in various detectors such as

---

[I]Part of this chapter has been published in [180].
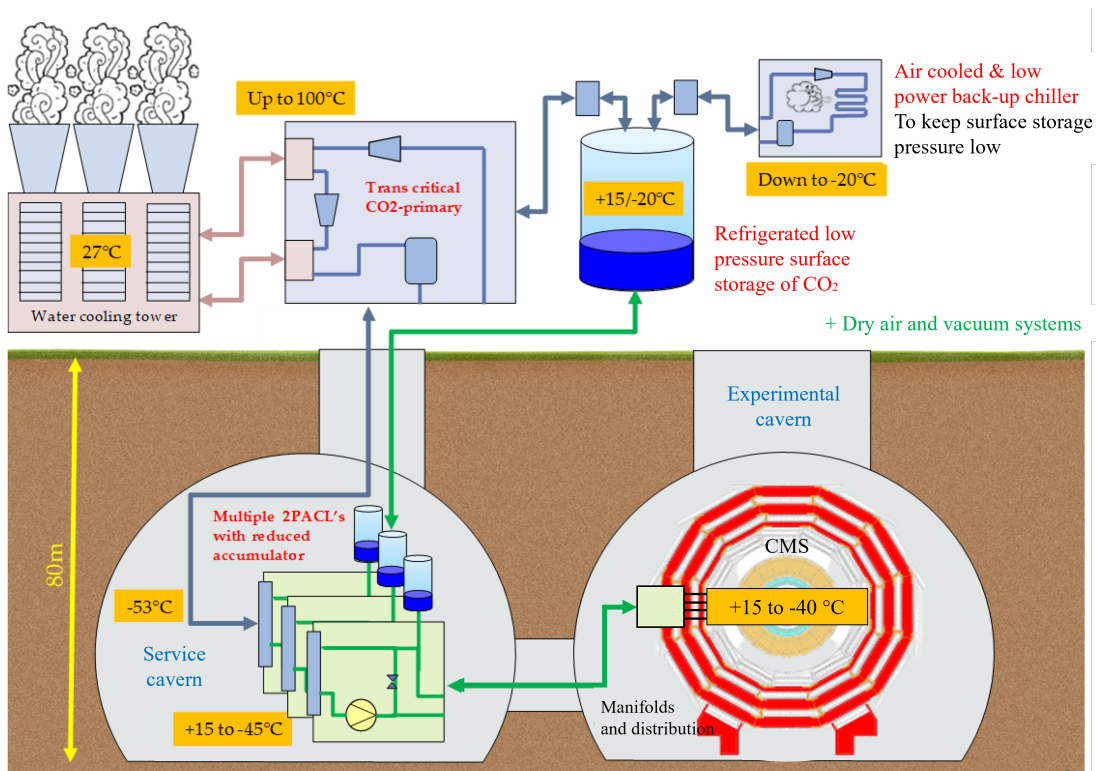
Figure 6.1: R744 and 2PACL system overview [206].

the ATLAS IBL [203], the CMS Pixel Phase I [204], and LHCb VELO [205]. These systems have demonstrated effective cooling power ranging up to several kilowatts.

The upcoming High Luminosity Program presents new challenges in terms of detector cooling capacity. The required capacity for CMS is reaching 550 kW. Additionally, the detector temperature requirements have shifted to a lower range of -35 °C. In response to these demands, CERN has chosen R744 as the primary working fluid for the first fully CO_2-based detector cooling system, together with the 2PACL in the secondary loop (see Fig. 6.1) [206]. The final installations of 2PACL in CMS will be located in the underground service caverns, approximately 100 m away from the manifold distribution system, with tri-axial vacuum-insulated transfer lines connecting them to the detectors. The R744[II] system [207], housed in new surface buildings, will be linked to the underground 2PACL systems through two warm transfer lines in vertical shafts. The R744 system pre-cools the 2PACL to approximately -53 °C, which is only a few degrees warmer than the freezing point of CO_2.

To ensure the uninterrupted flow of CO_2 to the detectors, it is crucial to have contingency plans in case of power outages or cooling plant failures. The CO_2 systems are designed with $N+1$ redundancy, with a backup from an uninterruptible power supply (UPS) and diesel

---

[II]The term R744 refers to CO_2 when it is used as a natural refrigerant in the refrigeration and air conditioning industry.

156
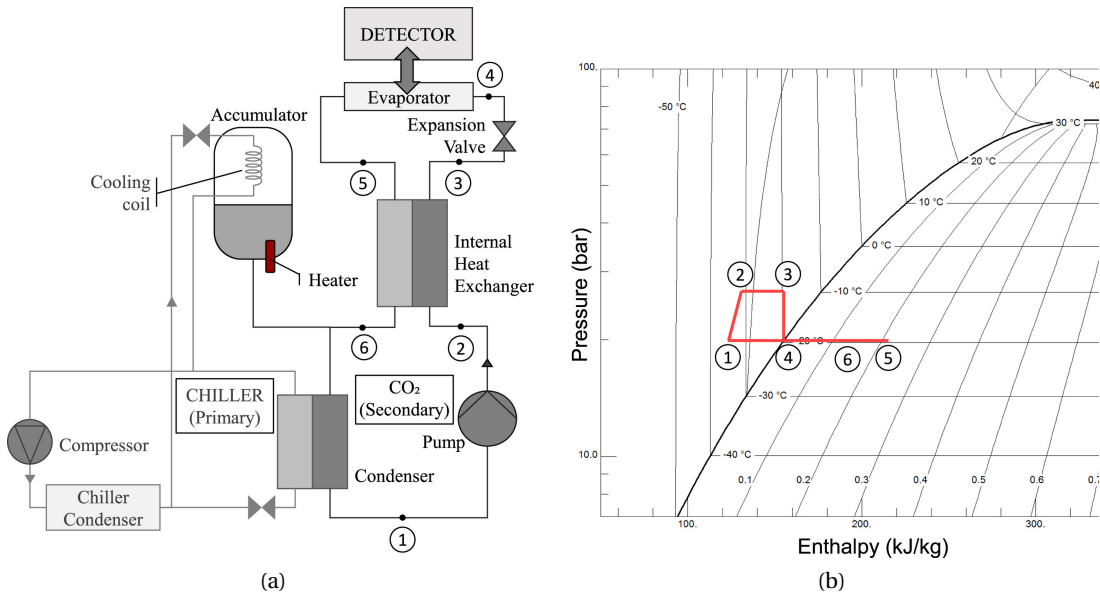
Figure 6.2: (a) 2PACL cooling system architecture, and (b) Operating principle in the pressure-enthalpy diagram of CO_2 [208].

support for both the 2PACL and a portion of the R744 system. This redundancy extends the lifetime of the detectors by removing ambient heat pickup even when the detector power is off. Overall, a total of 8+1 2PACL plants and 12+1 R744 slices will be installed as the detector cooling system for CMS.

To enhance reliability, the primary systems predominantly use air coolers to minimize potential downtime due to dependencies on other services. The large volume of the 2PACL detector cooling circuits, combined with their wide operational temperature range spanning from -45 °C to +15 °C, requires significant amounts of CO_2. Storing all the required fluid underground is impractical due to the size of the 2PACL accumulators, which would exceed the capacity of the service caverns. Alternatively, the surface tank will be pre-cooled either directly by R744 or with a small backup chiller. Cold transfer lines will connect the surface storage tank to the underground facilities, enabling the delivery or removal of 2PACL depending on the detector operational requirements.

6.1.1 2PACL cooling concept

The 2PACL concept is a cooling system that utilizes the unique thermodynamic properties of CO_2 in two-phase flow conditions. The system operates by controlling the pressure of the working fluid, which in turn determines the temperature at which evaporation occurs. A schematic diagram of the 2PACL system and a pressure-enthalpy diagram of CO_2 are shown in Figure 6.2.

In the 2PACL system, the secondary cooling loop (depicted in dark grey in Figure 6.2 (a)) consists of a condenser, a circulation pump, a heat exchanger, an evaporator connected to the thermal load, and an accumulator tank equipped with a cartridge heater and cooling coil. The chiller loop (shown in light grey) absorbs heat from the condenser and cools the accumulator, thereby reducing the operating pressure.

The process begins with subcooled liquid CO_2 exiting the condenser (state point 1) and being pressurized by the pump (state point 2). The CO_2 then passes through the heat exchanger, where it is heated to the evaporator temperature (state point 3). Next, the saturated liquid CO_2 expands through the expansion valve and enters the evaporator in a saturated liquid state (state point 4). Within the evaporator, the CO_2 gradually evaporates while absorbing heat from the detector electronics and sensors. The CO_2 exits the evaporator as a two-phase flow (state point 5), which is partially condensed in the heat exchanger (state point 6) and fully condensed and subcooled in the condenser (returning to state point 1). Thus, the CO_2 is in a liquid state from the condenser outlet to the expansion valve inlet, while it exists as a two-phase mixture in the evaporator, transfer line, and condenser.

The pressure of the CO_2 in two-phase flow conditions is regulated by the accumulator, where a mixture of liquid and vapor CO_2 is always present. By heating the liquid CO_2 inside the accumulator using the cartridge heater, the vapor pressure increases, pushing liquid CO_2 into the loop and raising both the loop pressure and the evaporator temperature. Conversely, cooling the vapor CO_2 in the accumulator causes partial condensation, thereby reducing the loop pressure and evaporator temperature. The cooling action is facilitated by a spiral coil heat exchanger located inside the accumulator and supplied by the chiller loop.

The 2PACL system offers precise control over the evaporation temperature by manipulating the pressure through the accumulator. By employing a standard vapor compression system, the chiller loop handles heat absorption from the condenser. For further details on the 2PACL concept, refer to the work by Petagna et al. [209].

Several CO_2 2PACL systems will be used for running all the cold sub-detectors. The cooling circuits form part of the Si-detector support system in the CMS structure, ensuring the efficient distribution of the cooling liquid/gas.

6.2   CMS environmental control dry gas system

As permanent flushing of the sub-detectors with dry gas is imperative, here we explain its functions and operations. The CMS dry gas system has 3 primary functions [210]:

i) Distribution of dry gas to CMS cold volumes operating below the environmental dew points to avoid condensation and ice formation. The cold volumes in CMS are divided into detector cold volumes (tracker and BTL, ECAL, HGCAL and ETL - see Fig. 6.3) and infrastructure cold volumes (2PACL cooling plants and stations).
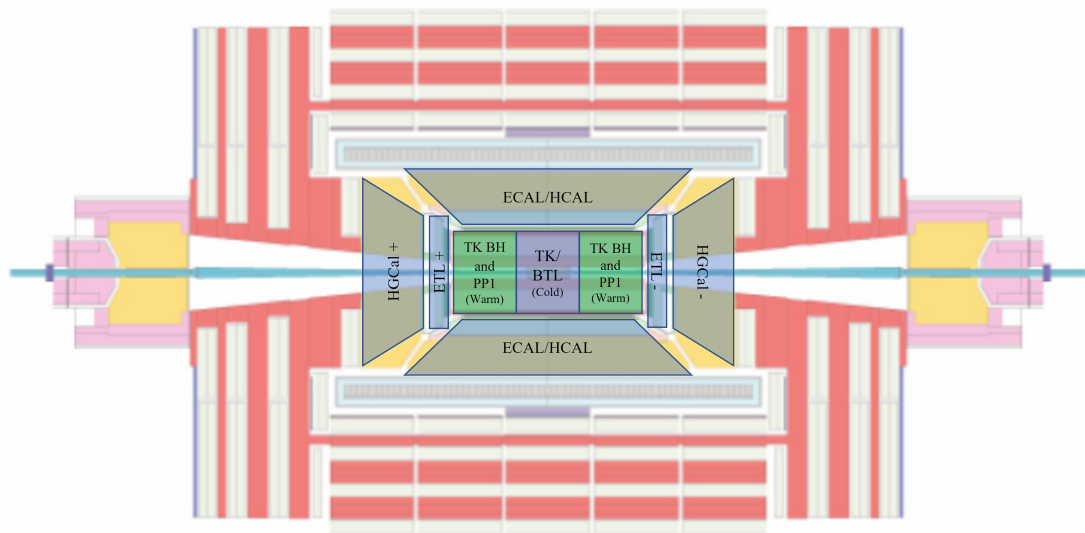
Figure 6.3: List of detectors flushed volumes based on action panel granularity.

  ii) Flushing of the ECAL and HCAL electronics boxes to eliminate the possibility of helium contamination[III].

 iii) Provision of an inert environment (N_2) to the whole CMS detector during regular running (CMS closed) as a precaution against fire.

6.2.1 Gas sources

The following gas sources are used in the system:

Hypoxic/dry air membrane plants

Two membrane separation plants working in parallel and operating in dual mode (hypoxic air when CMS is closed, dry air when CMS is open) will be used to flush the detector cold volumes. Each plant has two compressors that alternate cycles to feed the membrane separation unit where oxygen is filtrated so hypoxic air with a maximum O_2 content of 5% and a dew point of -70 °C is supplied to the detector, with both drying and inerting purposes. For safety reasons, the plants will operate on dry air mode during technical stops, and produce dry air with a dew point of -70 °C.

The plants are connected to two independent electrical networks. This configuration ensures a high degree of redundancy in case of electrical or equipment failure. Each plant is able to produce nominally 220Nm^3/h of hypoxic air when working on one compressor, and 400

[III]Helium is used in the CMS Magnet and the LHC magnets cryogenic systems (and of course, there are no leaks), but minuscule amounts still affect the phototubes used to monitor scintillation life in calorimeters [211].

Nm^3/h when working with two compressors. This way, the system is operated with only one of the two plants in case of maintenance/failure of the other.

Flushing dry air compressors

An array of three dryers and three air-cooled dry compressors working in cycles will be used to flush the cooling infrastructure cold volumes. Two Atlas-Copco dry compressors [212] model ZT55VSD+ are already in place and a third dry compressor ZT37VSD+ will be installed during 2023 to cope with the surface dry gas needs. This gas network is also used to back up the hypoxic/dry air plants in case of electrical or equipment failure, or if the hypoxic/dry gas properties flushed into the detector volumes are outside the acceptable range defined by users.

With all three compressors working, the maximum capacity of the network is 1210 Nm^3/h, enough to feed the cooling infrastructure and detector cold volumes simultaneously if needed. The dew point of the produced air is -70 °C.

Storage batteries/tanks

An emergency source of dry air is available in the form of batteries of compressed air bottles. As for today, 6 batteries of 12 bottles each provide autonomy of 8 hours of emergency flow to the cold tracker volume in case both the hypoxic network and the flushing dry air network fail. This gives the tracker cooling system enough time to warm up and reach dew point values over the cavern dew point.

In the future system, the increase of critical dry gas flow needs due to the connection of the new endcap cold detectors, together with the long time needed to warm up HGCAL due to its big thermal mass, will require an increase of the bottled air. At the moment, several options are being studied to cope with this new requirement:

- Increase the number of batteries, although the space is very limited.

- Rely on the batteries only in case of short maintenance (i.e., sensor calibration). The high level of redundancy provided by the hypoxic and flushing dry air networks adds redundancy to the present system.

6.2.2   Gas distribution

The dry gas distribution in Point 5[IV] is organized following the schematic depicted in Fig. 6.4. The three gas sources described in the previous subsection are located in Point 5 surface and distribute the dry gas to the underground service cavern (USC) with three independent pipes:

[IV]Point 5 refers to insertion region 5 of the LHC (see Fig. 1.3)
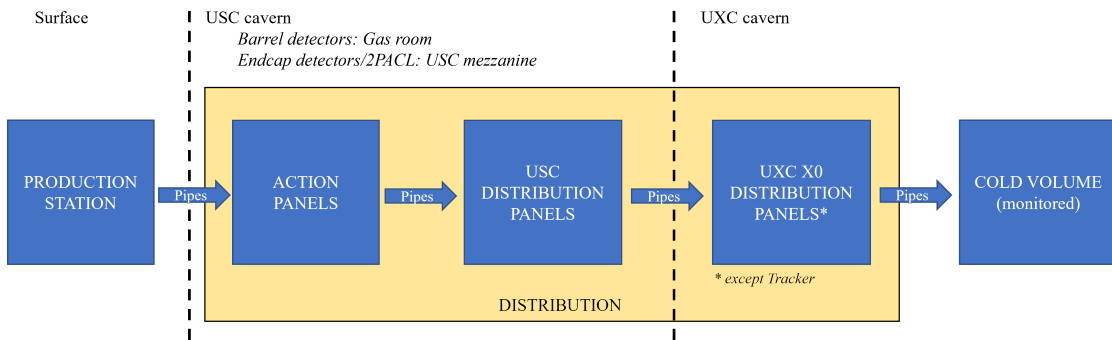
Figure 6.4: Schematic of the gas distribution in P5.

DN250 for hypoxic air, DN100 for flushing dry air, and DN40 for bottled air. In USC there will be two spaces allocated for the dry gas action panels and distribution racks: the 2PACL USC mezzanine for the racks dedicated to the flushing of new endcap sub-detectors (HGCAL, ETL) and 2PACL equipment; and the gas room for the racks dedicated to the flushing of the upgraded barrel detectors (Tracker, BTL, ECAL, HCAL). From these locations, pipes distribute the dry gas to the underground experimental cavern (UXC), where the last level of splitting will take place in distribution racks at X0 level (except for Tracker, where the last level of splitting is in YB0 patch panels located in the near and far balconies).

6.3   Integration of the humidity and temperature sensors in the CMS sub-detectors

Condensation formation on surfaces below the dew point temperature poses a significant challenge to the operation of electronic components. The risk becomes even more pronounced when the temperature drops below 0 °C, as ice formation can occur, leading to potential mechanical damage to electronic components and structures. Subsequently, when the iced components are getting warm, the ice melts, leaving all surfaces coated in water. Therefore, the monitoring of dew point temperature becomes crucial in the cold sub-detectors of the CMS experiment, as outlined in Chapter **1**. The dew point temperature monitoring is going to be a part of the detector control system and it will promptly provide a warning to the detector safety system to react in case of a sudden dew point temperature increase.

The CMS Phase-2 cold sub-detectors are the Tracker (Inner and Outer), MTD (BTL and ETL) and HGCAL, all of which are designed to operate at temperatures as low as -35 °C. Additionally, the ECAL sub-detector will lower its operating temperature to below the cavern dew point to manage the power dissipation originating from the Tracker and to cool the new ECAL readout electronics.

The Tracker sub-detector currently and in its upgrade does not require dew point temperature measurements across its entire volume. Instead, the existing sniffer system will be employed

for dew point temperature analysis. This system consists of 26 sniffing lines that extract gas samples from various positions within and outside the Tracker, which are then transferred to a gas analysis rack located in the underground service cavern, [213]. The dew point analysis is carried out using 26 industrial Vaisala DMT242 dew point transmitters [214] known for their reliable performance, even in extremely dry environments. For future operations, the sensor model will be upgraded but the main functionalities and operation model will remain the same.

On the other hand, the HGCAL and possibly the ECAL sub-detectors, although serviced by the sniffer system as well, due to their volume and exposure to the experimental cavern atmosphere require dew point temperature monitoring that does not "average" over large volumes systems. The integration of humidity and temperature sensors in these sub-detectors is discussed in the following sub-sections.

6.3.1   HGCAL sub-detector

In a simplified description, a large fraction of the HGCAL subdetector will be composed of alternating layers of absorber material (copper) and detector modules made of silicon wafers. In order to limit radiation damage to these silicon modules, a two-phase CO_2 cooling system will provide up to 140 kW of cooling power per endcap, maintaining the silicon sensors at -35 °C and prolonging their working life under high irradiation [28]. A thermal screen will surround the detector to separate the cold dry detector volume from the ambient conditions in the cavern (refer to Fig. 6.5).

Due to the complex shape of the detector, the thermal screen is composed of many smaller panels of different sizes and shapes, internally flushed with dry nitrogen gas. Due to space constraints, the thickness of the insulation panels is limited to 20 or 30 mm in most places. With this thickness, and a temperature difference of around 55 °C[V] across them, standard passive insulation is not sufficient to maintain the external surface above the 16 °C maximum dew point in the experimental cavern (and certainly not above the 21 °C dew point which may occur in the surface hall in the summer). Therefore, electrically powered heating foils and temperature sensors will be integrated into the thermal screen to heat and control the external surface temperature of the detector [28].

As the cassettes are equipped with the cooling structures on which the Si-detectors are positioned and the cassette volume is densely packed with Si-sensors, cables, readout fibres, piping and etc., the dew point temperature inside each cassette must be measured. There are two different cassette sizes: 60-degree cassettes that form CE-E (6 cassettes per layer), and 30-degree cassettes that form CE-H (12 cassettes per layer). One endcap of the HGCAL sub-detector comprises of 47 layers, with 26 layers of CE-E and 21 layers of CE-H, resulting in a total of 156 60-degree cassettes and 252 30-degree cassettes (see Fig. 6.6). Considering two HGCAL endcaps, the total number of 60-degree cassettes is 312 and 30-degree cassettes is 504.

[V]One end of the wedges will be at -35 °C while the other end will be at 18 °C.

(a)   (b)
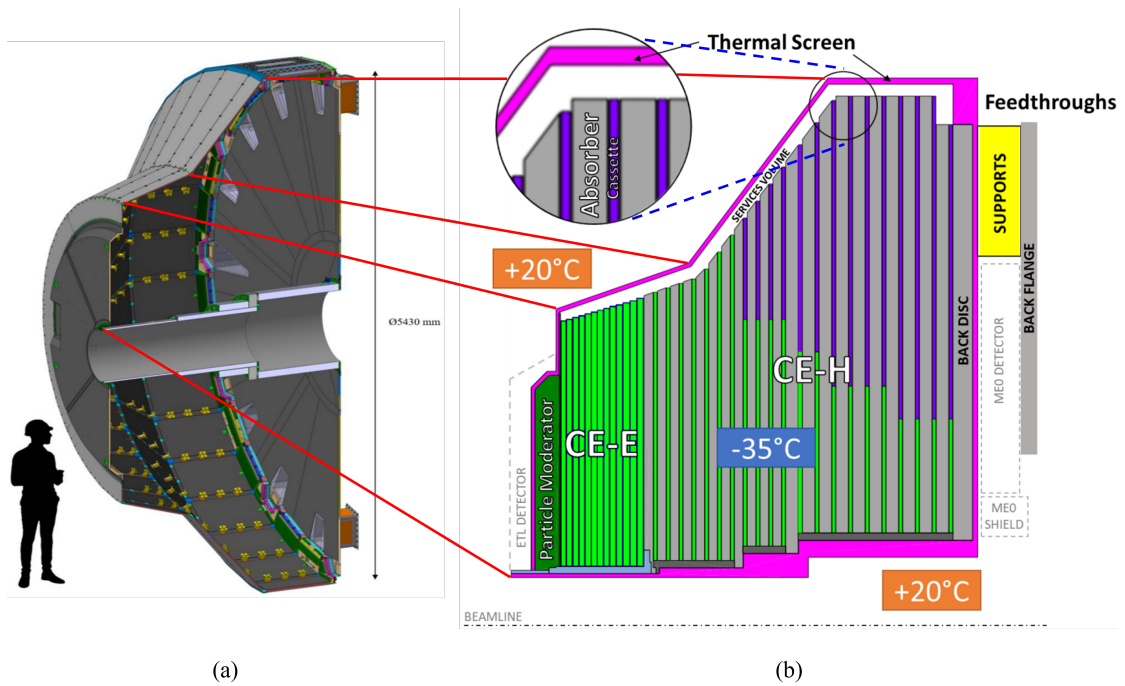
Figure 6.5: (a) A 3D drawing of the HGCAL Thermal Screen and (b) a cross-section of the HGCAL layers. The HGCAL Thermal Screen keeps the detector outer surface at a temperature higher than the cavern dew point in order to avoid condensation towards the outside.

(a)   (b)
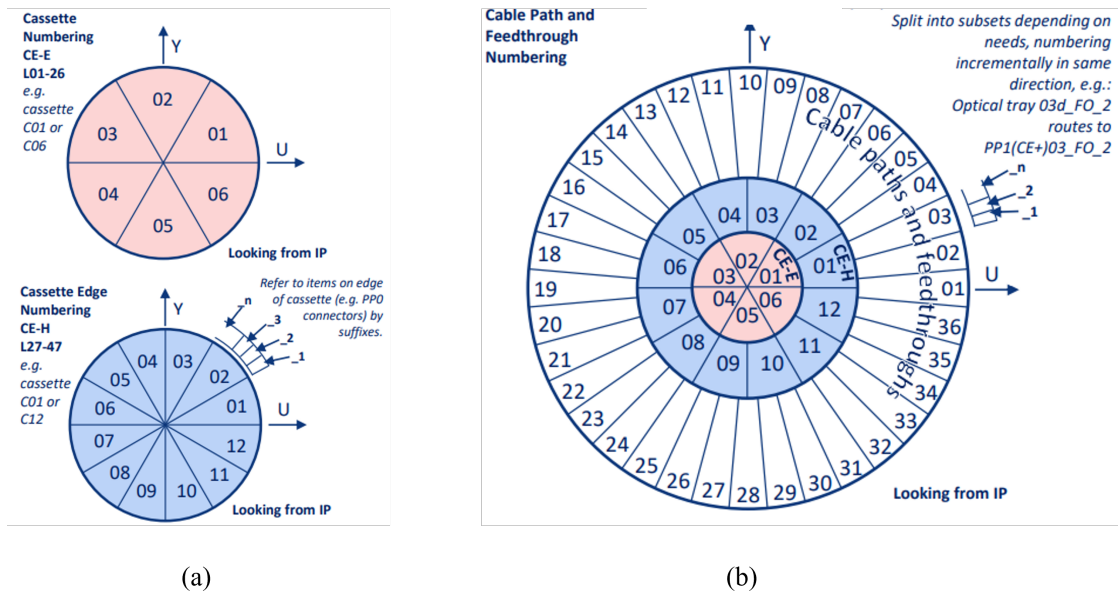
Figure 6.6: (a) A schematic representation of the cassettes and their corresponding numbering in the CE-E and CE-H. Additionally, the patch panel PP0, used for sensor connectors, is indicated on the edge of the CE-H. (b) A schematic of the positions of CE-E and CE-H in the HGCAL sub-detector.

163
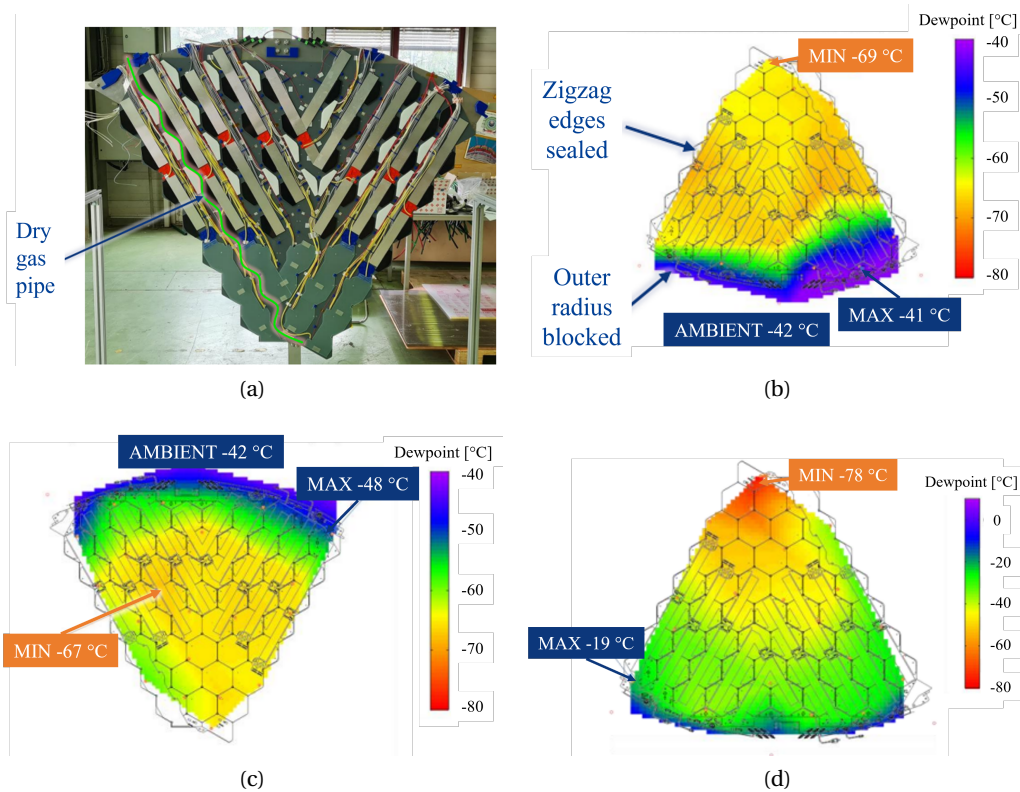
Figure 6.7: (a) A cassette-like setup for the cooling test. The results of the experiment with the environmental temperature fixed at (b) -35 °C, (c) -35 °C, and (d) 20 °C. In experiment (b) and (c) different cassette orientation was considered. During the entire experiment, the mass flow rate of the coolant was 0.094 kg/h.

To determine the number and position of the humidity and temperature sensors, a special cassette-like setup has been designed as shown in Fig. 6.7 a). The experiment was done with the inlet dry air at -78 °C dew point temperature and with a rate of approximately 6.5 vol/h. The specially designed cold room was used to control the external environment, with the temperature varying from 20 °C down to -35 °C. Fig. 6.7 b) and c) illustrate the results of the experiment with the environmental temperature fixed at -35 °C and at different cassette orientations. In both tests, the dew point temperature of the majority of the cassette was 20-30 °C below ambient temperature. The third test also confirmed the possibility of drying out the cassette at room temperature (Fig. 6.7 d)). In all three tests, the outer radius was not completely sealed due to some gaps for cables to come out. However, even a partially blocked edge of the cassette proved the ability to prevent ambient air from easily recirculating into the middle of the cassette from the service volume.

The tests revealed that the most critical points for dew point measurements are located next to the cassette edge. Therefore, the MK33-W sensors and Pt1000s will be placed in that area. Due to space limitations, we decided to have one humidity sensor for 30-degree cassettes and
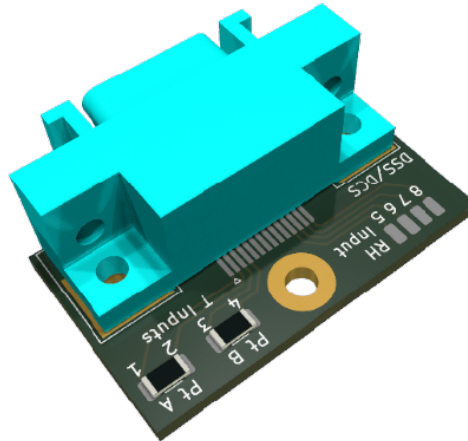
Figure 6.8: A 3D image of the PCB with two Pt1000 temperature sensors mounted on the board, along with four pads designated for the humidity sensor. The board also features a 14-pin connector, with 8 pins allocated for the two Pt1000 sensors (4 pins each), and 4 pins specifically designed for the RH sensor. Additionally, two spare pins are available.

two humidity sensors for 60-degree cassettes. The total number of humidity sensors required for both endcaps amounts to 1128. As for the Pt1000 temperature sensors, there will be twice as many as humidity sensors, totaling 2256.

Fig. 6.8 displays a PCB designed with two Pt1000 temperature sensors mounted on the board. The anticipated temperature sensors come in the form of SMD components with a size of 1206. The PCB includes four pads integrated for the humidity sensors, as there will be a pair of coaxial cables between the sensor and the PCB. Two pads are allocated for the conductors from each cable, and an additional two are provided for driving the shields of the cables. The PCB also features a 14-pin connector for further sensor wiring to the corresponding readout units. This connector will be part of the PP0 patch panel situated at the edge of CH-E cassettes (as depicted in Fig. 6.6 a).

6.3.2   ECAL sub-detector

Given the considerable power dissipation of approximately 200 kW of the CMS Tracker readout electronics in front of the ECAL crystals, the fulfillment of this requirement posed a technological challenge. After extensive analysis of various cooling systems and temperature stabilization options, the CMS ECAL Collaboration decided to implement a local water cooling system with the following key features [215]:

- The system must provide a water flow rate exceeding 70 liters per second to effectively remove thermal energy dissipated in the vicinity of the ECAL crystals and APD diodes.

- The cooling water temperature must be precisely regulated at $9.00 \pm 0.01\,^\circ$C to ensure
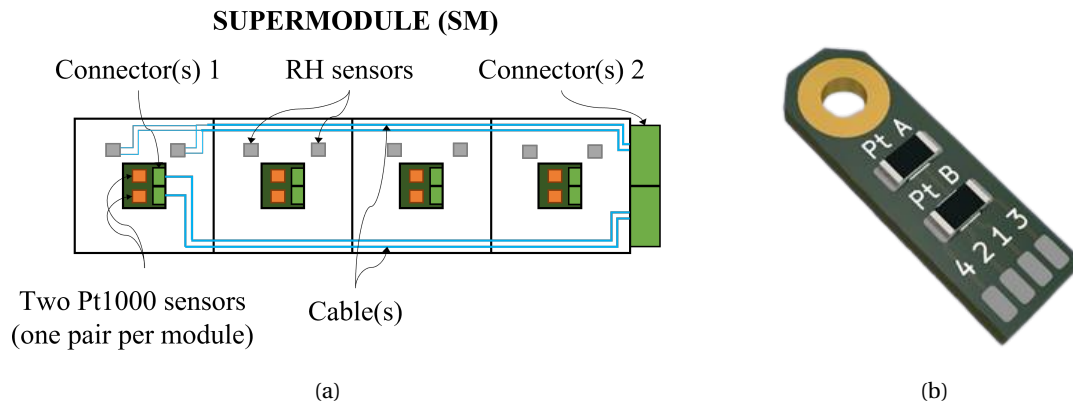
Figure 6.9: (a) A schematic representation of the ECAL supermodule. The supermodule is comprised of four individual modules, each of which accommodates a pair of Pt1000 temperature sensors and a pair of humidity sensors. (b) A 3D design on the PCB featuring two Pt1000 temperature sensors mounted on the same board.

> proper temperature stabilization of the crystals and APD diodes.

- Each ECAL Supermodule needs to be supplied with independent water cooling.

- The system should incorporate a thermal shield between the Tracker detector and the ECAL crystals, as well as between the ECAL crystals and the ECAL readout electronics.

- Additional cooling for the ECAL readout electronics should be provided.

The ECAL Cooling system was designed in accordance with these specifications, ensuring that each Supermodule, which consists of four modules, receives independent cooling with water as a coolant maintained at a temperature of 9.00 ± 0.01 °C. To ensure reliable cooling of the Supermodules and their electronics, temperature and humidity sensors will be integrated into each Supermodule. Specifically, four pairs of Pt1000 temperature sensors and four pairs of humidity sensors will be installed in each Supermodule (one pair of Pt1000s and one pair of RH per module), as depicted in Fig. 6.9 a). A PCB design featuring two Pt1000 temperature sensors, mounted in a 1206 size package, is illustrated in Fig. 6.9 b). The humidity sensor is going to be connected by a pair of coaxial cables to the connector located at the edge of the Supermodule. As the ECAL sub-detector comprises 36 supermodules (as mentioned in 1.2.3), the total required number of temperature and humidity sensors is 288 and 288, respectively.

6.4   Application scenario and integration in the CMS DSS/DCS

As stated before, to ensure adequate monitoring of the detector environmental parameters, temperature and humidity sensors will be massively distributed inside the cold sub-detectors. Therefore, the Cold sub-detector DCS for LS3 detectors must be equipped with independent, continuous and reliable readout and DAQ of temperature and humidity sensors.

166
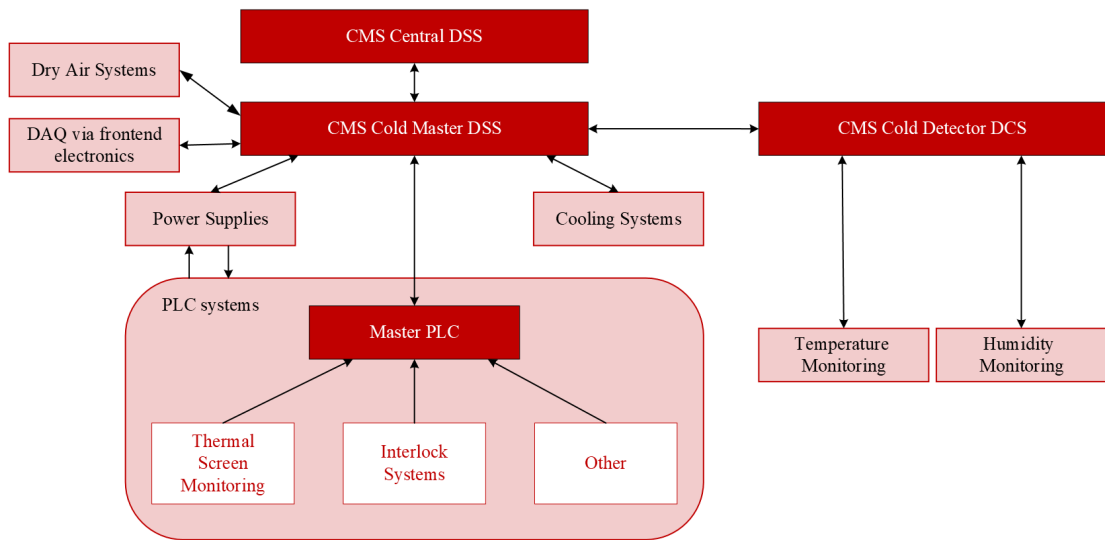
Figure 6.10: A simplified functional block diagram of the CMS Cold DSS/DCS (hardware blocks) including some interconnections between various subsystems and the temperature and humidity monitoring systems.

Humidity and temperature monitoring systems are going to be integrated in the CMS DSS/DCS and their future implementation is shown in Fig. 6.10. The figure presents the main hardware components and the internal structure of the CMS Cold Detector DSS/DCS. Each sub-detector has its own standalone detector control system operating with different parameter values in terms of temperature, voltage, current, or humidity. The humidity monitoring is also obligatory before switching on the cooling and certainly before switching on the front-end electronics, thus the readout of the humidity must be independent of the front-end electronics and from part of the DSS.

For obvious minimal redundancy reasons, each RTD has a "twin" attached to the same surface. The first sensor is integrated into the interlock PLC while the second is powered and read out via a novel standalone massive RTD monitoring system, discussed in Chapter 5.6. This system is developed for serving RTDs at a modest cost and with limited space requirements (around 400 channels can be housed in a 3U Eurocrate, while the same number of sensors attached to a PLC will require twenty times the volume). Furthermore, the humidity sensors are going to be read out by the multi-channel auto-balancing signal conditioning unit discussed in Chapter 5.5.

The safety systems are built using PLC components that form the core of the autonomous hardware DSS. The PLC systems are integrated as a slave into CMS Central DSS. Most information in the DSS systems is reported to the CMS DCS via CMS Cold Detector System specially designed for sub-detectors that require cooling. The CMS DCS applications are based on an industrial WinCC Open Architecture (WinCC OA) Supervisory Control And Data Acquisition (SCADA) software extended with a Joint Control Project (JCOP) framework developed at CERN.

The baseline communication protocol is Open Platform Communication Unified Architecture (OPC UA) [216].

6.5   Summary

This chapter has presented the integration principles of humidity and temperature sensors required for computing the dew point temperature. While the Tracker sub-detector will rely on the existing sniffer system for analyzing the dew point temperature, the HGCAL and ECAL sub-detectors require the installation of numerous humidity and temperature sensors.

The HGCAL sub-detector, comprising 916 cassettes, and the ECAL sub-detector, with 36 supermodules, will necessitate the installation of 1128 and 288 humidity sensors, respectively. Both sub-detectors require twice as many temperature sensors as humidity sensors to ensure effective monitoring.

Both systems will be integrated into the CMS DCS/DSS. The seamless integration of these systems enhances the overall efficiency, safety, and performance of the CMS detector, ensuring the reliability of experimental data and the protection of sensitive electronic components.

7 Conclusion and Research Perspectives

The High Luminosity LHC (HL-LHC) project is a major upgrade of the accelerator aimed at increasing its luminosity by a factor of ten compared to the original design value (from 300 to 3000 fb^{-1}). This upgrade will result in significantly higher levels of radiation. Additionally, with over a billion Si sensor and their readout channels required to achieve the high resolution needed for "imaging" charged tracks, the overall power consumption will reach hundreds of kilowatts, leading to additional heating. To mitigate the effects of radiation on the silicon sensors, and also to fight overheating due to the high current densities, the operating temperature of the detectors will be lowered to sub-zero temperatures. Under these conditions, accurate control of the dew point temperature, therefore thermal and hygrometric properties, is vital.

This thesis was focused on the selection, characterization, and integration of humidity and temperature sensors in high-energy physics (HEP) detectors designed to operate in HL-LHC conditions. As RTDs have demonstrated the ability to reliably work in the harsh detector environment, the research primarily addressed the challenges of humidity sensors operating at sub-zero temperatures, in radiation-exposed environments with strong magnetic fields. The results demonstrated the resilience of the tested sensors in such environments and their suitability for integration into the silicon-based sub-detectors.

Two irradiation campaigns were conducted, successfully identifying a radiation-tolerant MK33-W humidity sensor that exhibited a linear output dependence on accumulated fluence. The studies demonstrated a methodology that can be followed for other dew point sensor candidates. Radiation changes the structure of the matter; however, if the changes can be parametrized using a unique formula for all of them they can be used and accompany the detectors throughout their HL-LHC operations. In the case of the MK33-W sensor, it has been proven that the effect could be effectively compensated using a first-order polynomial function. The Pt1000 temperature sensors proved their ability to work confidently at doses expected in the future HL-LHC. They were minimally affected by radiation and can be reliable in such a HEP environment.

Temperature dependence tests of the selected humidity sensor were performed at tempera-

tures as low as -30 °C. The tests showed that the effects of negative temperatures on sensor sensitivity could be compensated using an inverse second-order polynomial. A magnetic test at a strong magnetic field of 2 T was conducted on both non-irradiated and irradiated sensors to assess their magnetic field dependence. In both cases, the output of the sensors remained insensitive to the magnetic field, including the ON/OFF phases.

The uncertainty of the measurements of the relative humidity sensor after receiving the highest expected dose and operating at negative temperatures is around 3 %rh, while for the temperature sensors, the uncertainty is 0.13 °C. According to (2.6), and taking into consideration the uncertainty of the selected sensor candidates, the uncertainty of the dew point temperature measurements at the ambient temperature of -35 °C is 4.5 °C for dry air conditions. At 30 %rh, the uncertainty of the dew point measurement is 0.9 °C, while at 50 %rh and 80 %rh, the uncertainty is 0.6 °C and 0.4 °C, respectively.

As commercial off-the-shelf (COTS) electronics are not radiation-hardened, the readout systems for the sensors must be placed far away from the sensors (~ 100 m). To facilitate the reading of capacitive-based humidity sensors over long distances, an appropriate analog signal conditioning circuit was developed to compensate for the parasitic effects. The circuit employed an auto-balancing bridge architecture and a quadrature-phase shifter to provide a 90-degree phase delay with respect to the excitation signal. The delayed signal was used as a switch control signal to demodulate the bridge output, extracting only the capacitive part of the sensor and eliminating internal sensor parasitic resistance. The effects of cable parasitic capacitance were minimized using active and passive shielding techniques. In the second prototype version, an internal oscillator for generating an excitation signal was integrated. The oscillator is based on three RC networks and the TLV2474 chip where the outputs of the TLV2474 chip are an excitation (sine) signal and a 90-degree shifted (cosine) signal. This architecture reduced the number of required external components, simplifying the final readout system.

A new design for a temperature monitoring system was also proposed, offering a cost-effective and easy-to-deploy solution compared to previous PLC-based systems. This system allowed the monitoring of up to 24 RTDs, with each sensor connected using a 4-wire configuration to the readout unit. It demonstrated operational capability in several testing facilities and will work in parallel with the already integrated PLC-based system for temperature monitoring. The combination of those two conditioning solutions allows for detailed dew point monitoring inside the Si-detector volumes.

The integration principles for humidity and temperature sensors required for computing the dew point temperature were outlined. The seamless integration of these systems into the CMS Detector Control System/Detector Safety System (DCS/DSS) would improve detector safety and protect the large investment in Si-sensor technology while guaranteeing reliable experimental data.

The future steps can be divided into four points:

Point 1: Design a multi-channel version of the humidity monitoring unit consisting of eight channels (in a 3U card format). Further iterations will include the implementation of an ADC chip and a microcontroller on the board, similar to the proposed multi-channel temperature monitoring system. The goal is to produce a cost-effective, multi-platform, and easy-to-deploy monitoring system.

Point 2: Optimize the proposed readout system by using multiplexers and demultiplexers. Ongoing R&D projects at CERN are working on developing radiation-hardened MUX and DEMUX, which will allow the conditioning of multiple sensors with one readout unit. This will significantly reduce the use of coaxial cables from the detector to the readout electronics, resulting in lower costs for the entire system. We note here that changes in dew point are processes that take seconds so short integration times are not an issue but reliability and repeatability are.

Point 3: The sensors and readout electronics are going to be separated by over 100-meter-long coaxial cables. Commercially available cables are usually not radiation-tolerant, or their radiation tolerance has not been investigated. However, after in-depth investigation and collaboration with companies, some possible candidates (made of radiation-tolerant Kapton material) suitable for the harsh detector environment have been identified. Before making the final decision, these cables must undergo various tests, including exposure to a gamma beam, thermal aging, and evaluation of their mechanical and electrical properties. The mechanical test will consider tensile testing and microscopy on defective samples, while electrical tests will evaluate signal transmission for different cable lengths. These examinations must be performed before, during, and after the irradiation procedure to ensure that the cables are suitable for the required conditions.

Point 4: Integrate the developed system into the real detector system as it will be tested before finalizing sensor calibration and verifying the performance of the readout system.

In conclusion, this dissertation presents the first complete study of dew point temperature monitoring based on commercially available humidity and temperature sensors. The findings and methodologies presented offer valuable insights for researchers and engineers to ensure the safe operation of HEP detectors. The selected sensors and monitoring systems can be easily employed in future experiments and integrated into the Phase-2 upgrade of the CMS detector. The continuous advancement and optimization of environmental sensors will be important for enhancing the performance and longevity of HEP detectors, ensuring the success of future experiments in understanding fundamental particles and their interactions. Moreover, the knowledge gained from this research can be extended to other scientific and industrial applications that require robust and reliable environmental sensing capabilities.

Bibliography

[1]   B. W. Carroll and D. A. Ostlie, *An introduction to modern astrophysics.* Cambridge University Press, 2017.

[2]   A. Rubbia, *Phenomenology of particle physics.* Cambridge University Press, 2022.

[3]   D. A. Edwards and M. J. Syphers, *An introduction to the physics of high energy accelerators.* John Wiley & Sons, 2008.

[4]   E Todesco, H Bajas, M Bajko, *et al.*, "The high luminosity lhc interaction region magnets towards series production", *Superconductor Science and Technology*, vol. 34, no. 5, p. 053 001, 2021.

[5]   E. Mobs, "The CERN accelerator complex - August 2018. Complexe des accélérateurs du CERN - Août 2018", 2018, General Photo. [Online]. Available: http://cds.cern.ch/record/2636343.

[6]   W. Herr and B Muratori, "Concept of luminosity", 2006. DOI: 10.5170/CERN-2006-002.361. [Online]. Available: https://cds.cern.ch/record/941318.

[7]   L. Evans and P. Bryant, "LHC machine", *JINST*, vol. 3, no. 08, S08001, 2008.

[8]   G. Aad, J. Butterworth, J Thion, *et al.*, "The ATLAS experiment at the cern large hadron collider", *JINST*, vol. 3, S08003, 2008.

[9]   ALICE collaboration, "The ALICE experiment at the CERN LHC", *JINST*, vol. 3, S08002,

[10]   R. Adolphi *et al.*, "The CMS experiment at the CERN LHC", *JINST*, vol. 803, S08004, 2008.

[11]   A. A. Alves Jr, L. Andrade Filho, A. Barbosa, *et al.*, "The LHCb detector at the LHC", *JINST*, vol. 3, no. 08, S08005, 2008.

[12]   LHCf collaboration, O Adriani, L Bonechi, *et al.*, "The LHCf detector at the CERN Large Hadron Collider", *JINST*, vol. 3, no. 08, S08006, 2008.

[13]   P. Lipari and M. Lusignoli, "Interpretation of the measurements of total, elastic, and diffractive cross sections at LHC", *The European Physical Journal C*, vol. 73, no. 11, p. 2630, 2013.

[14]   J. Pinfold, K Kinoshita, R Soluk, *et al.*, "Technical design report of the MoEDAL experiment", Tech. Rep., 2009.

[15] G. Apollinari, I Béjar Alonso, O Brüning, *et al.*, "High-Luminosity Large Hadron Collider (HL-LHC). Technical Design Report v. 0.1", Fermi National Accelerator Lab. (FNAL), Batavia, IL (United States), Tech. Rep., 2017.

[16] O Aberle, E Carlier, E Barzi, *et al.*, "Submitter: High-Luminosity Large Hadron Collider (HL-LHC): Technical design report", CERN, Tech. Rep., 2020.

[17] G. Bayatian, A Korablev, A Soha, *et al.*, "CMS Physics: Technical Design Report Volume 1: Detector Performance and Software", CMS-TDR-008-1, Tech. Rep., 2006.

[18] CMS collaboration, *Technical proposal for the phase-ii upgrade of the CMS detector*, 2015.

[19] D Contardo, M Klute, J Mans, L Silvestris, and J Butler, "Technical Proposal for the Phase-II Upgrade of the CMS Detector", Geneva, Tech. Rep., 2015. DOI: 10.17181/CERN. VU8I.D59J. [Online]. Available: https://cds.cern.ch/record/2020886.

[20] CMS collaboration, "The CMS tracker system project: technical design report", CERN-LHCC-98-006, Tech. Rep., 1997.

[21] CMS collaboration, "The CMS tracker: addendum to the Technical Design Report", CERN-LHCC-2000-016, Tech. Rep., 2000.

[22] A. Dierlamm, "Silicon sensor developments for the CMS Tracker upgrade", *JINST*, vol. 7, no. 01, p. C01110, 2012.

[23] A. La Rosa, "The Upgrade of the CMS Tracker at HL-LHC", in *Proceedings of the 29th International Workshop on Vertex Detectors (VERTEX2020)*, 2021, p. 010 006.

[24] "The Phase-2 Upgrade of the CMS Tracker", CERN, Geneva, Tech. Rep., 2017. DOI: 10.17181/CERN.QZ28.FLHW. [Online]. Available: https://cds.cern.ch/record/2272264.

[25] *Fluka cern*, https://fluka.cern/, Accessed: 2022-04-28.

[26] J. Ernenwein, CMS collaboration, *et al.*, "Overview of the CMS electromagnetic calorimeter", *Nuclear Physics B-Proceedings Supplements*, vol. 78, no. 1-3, pp. 186–191, 1999.

[27] V. Abramov, B. Acharya, N Akchurin, *et al.*, "Studies of the response of the prototype CMS hadron calorimeter, including magnetic field effects, to pion, electron, and muon beams", *Nuclear Instruments and Methods in Physics Research Section A: Accelerators, Spectrometers, Detectors and Associated Equipment*, vol. 457, no. 1-2, pp. 75–100, 2001.

[28] "The Phase-2 Upgrade of the CMS Endcap Calorimeter", CERN, Geneva, Tech. Rep., 2017. DOI: 10.17181/CERN.IV8M.1JY2. [Online]. Available: https://cds.cern.ch/record/2293646.

[29] CMS collaboration, "The CMS muon project: technical design report", *Technical Design Report CMS. CERN, Geneva*, vol. 51, 1997.

[30] CMS collaboration, "The CMS trigger system", *arXiv preprint arXiv:1609.02366*, 2016.

[31] P Milenovic, J Puzovic, D Jovanovic, D Maletic, G. Dissertori, and P Adzic, "Performance of the CMS ECAL safety system for Super Modules SM0 and SM1", *Nuclear Instruments and Methods in Physics Research Section A: Accelerators, Spectrometers, Detectors and Associated Equipment*, vol. 554, no. 1-3, pp. 427–436, 2005.

[32] *Datasheet: HIH-3610 humidity sensor*, https://www.mouser.com/catalog/specsheets/hih3610.pdf, Accessed: 2023-05-22.

[33] *Datasheet: HIH-4030 humidity sensor*, https://www.mouser.fr/datasheet/2/187/hwscs06478_1-2270788.pdf, Accessed: 2023-05-22.

[34] M. Fossa and P. Petagna, "Use and calibration of capacitive RH sensors for the hygrometric control of the CMS tracker", CERN-CMS-NOTE-2003-024, Tech. Rep., 2003.

[35] M Fossa and P Petagna, "Temperature influence on humidity measurements for CMS tracker control", *CMS IN-2006–03*, 2006.

[36] G. M. Berruti, "Radiation tolerant fiber optic humidity sensors for High Energy Physics applications", PhD thesis, 2015. [Online]. Available: https://cds.cern.ch/record/2143228.

[37] *Datasheet: Precon HS2000 humidity sensor*, https://preconusa.com/files/2018/08/HS-2000V-Data-Sheet.pdf, Accessed: 2023-05-22.

[38] A Makovec, G Berruti, M Consales, *et al.*, "Radiation hard polyimide-coated FBG optical sensors for relative humidity monitoring in the CMS experiment at CERN", *JINST*, vol. 9, no. 03, p. C03040, 2014.

[39] M. Consales, G. Berruti, A. Borriello, *et al.*, "Nanoscale TiO 2-coated LPGs as radiation-tolerant humidity sensors for high-energy physics applications", *Optics letters*, vol. 39, no. 14, pp. 4128–4131, 2014.

[40] A. Kapić, A. Tsirou, P. G. Verdini, and S. Carrara, "Humidity Sensors for High Energy Physics Applications: A Review", *IEEE Sensors Journal*, vol. 20, no. 18, pp. 1–4, May 2020.

[41] C. T. Okada, *Humidity Sensors: Types, Nanomaterials, and Environmental Monitoring*. Nova Science Publishers, 2011.

[42] N. Yamazoe and Y. Shimizu, "Humidity sensors: principles and applications", *Sensors and Actuators*, vol. 10, no. 3-4, pp. 379–398, 1986.

[43] C.-A. Ku and C.-K. Chung, "Advances in humidity nanosensors and their application: review", *Sensors*, vol. 23, no. 4, 2023, ISSN: 1424-8220.

[44] S. Pixton and S. Warburton, "Moisture content/relative humidity equilibrium of some cereal grains at different temperatures", *Journal of Stored Products Research*, vol. 6, no. 4, pp. 283–293, 1971.

[45] A. Jha and P. Tukkaraja, "Monitoring and assessment of underground climatic conditions using sensors and gis tools", *International Journal of Mining Science and Technology*, vol. 30, no. 4, pp. 495–499, 2020, ISSN: 2095-2686.

[46]   R. d. C. P. Santos, J. M. da Silva, W. A. Junior, C. L. Pinto, M. M. Oliveira, and D. B. Mazzinghy, "Development of a low-cost device for monitoring ventilation parameters (temperature, humidity and pressure) in underground environments to increase operational safety using iot", *Mining*, vol. 2, no. 4, pp. 746–756, 2022, ISSN: 2673-6489.

[47]   N. D'Uva, F. Camera, S. Amendola, *et al.*, "Batteryless wireless temperature/humidity sensor for item-level smart pharma packaging", in *2021 IEEE International Workshop on Metrology for Industry 4.0 IoT (MetroInd4.0IoT)*, 2021, pp. 145–149.

[48]   Z. Ma, T. Fei, and T. Zhang, "An overview: sensors for low humidity detection", *Sensors and Actuators B: Chemical*, vol. 376, p. 133 039, 2023, ISSN: 0925-4005.

[49]   B. Arman Kuzubasoglu, "Recent studies on the humidity sensor: a mini review", *ACS Applied Electronic Materials*, vol. 4, no. 10, pp. 4797–4807, 2022.

[50]   Z. Chen and C. Lu, "Humidity sensors: a review of materials and mechanisms", *Sensor letters*, vol. 3, no. 4, pp. 274–295, 2005.

[51]   M Sajid, Z. Khattak, K Rahman, G Hassan, and K. Choi, "Progress and future of relative humidity sensors: a review from materials perspective", *Bulletin of Materials Science*, vol. 45, no. 4, p. 238, 2022.

[52]   J.-M. Tulliani, B. Inserra, and D. Ziegler, "Carbon-based materials for humidity sensing: a short review", *Micromachines*, vol. 10, no. 4, p. 232, 2019.

[53]   J. Wernecke and R. Wernecke, *Industrial moisture and humidity measurement: a practical guide.* John Wiley & Sons, 2013.

[54]   J. Cooper and R. Dooley, "The international association for the properties of water and steam", *Proceedings of the International Association for the Properties of Water and Steam (IAPWS)*, 1993.

[55]   H. Preston-Thomas *et al.*, "The International Temperature Scale of 1990 (ITS-90)", *metrologia*, vol. 27, no. 1, pp. 3–10, 1990.

[56]   B. Hardy, "Its-90 formulations for vapor pressure, frostpoint temperature, dewpoint temperature, and enhancement factors in the range–100 to+ 100 c", in *The proceedings of the third international symposium on Humidity & Moisture, Teddington, London, England*, 1998, pp. 1–8.

[57]   A. Wexler, "Vapor pressure formulation for ice", *Journal of Research of the National Bureau of Standards. Section A, Physics and Chemistry*, vol. 81, no. 1, p. 5, 1977.

[58]   H.-E. Endres, H. D. Jander, and W. Göttler, "A test system for gas sensors", *Sensors and Actuators B: Chemical*, vol. 23, no. 2-3, pp. 163–172, 1995.

[59]   Z. M. Rittersma, *Microsensor applications of porous silicon: from humidity-sensitive sheet to sacrificial layer.* Shaker Publishing, 1999.

[60]   U. Kang and K. D. Wise, "A high-speed capacitive humidity sensor with on-chip thermal reset", *IEEE Transactions on Electron Devices*, vol. 47, no. 4, pp. 702–710, 2000.

[61]   J. Korvink, L Chandran, T Boltshauser, and H Baltes, "Accurate 3D capacitance evalua-
        tion in integrated capacitive humidity sensors", *Sensors and Materials*, vol. 4, pp. 323–
        323, 1993.

[62]   Z. Rittersma, "Recent achievements in miniaturised humidity sensors—a review of
        transduction techniques", *Sensors and Actuators A: Physical*, vol. 96, no. 2-3, pp. 196–
        210, 2002.

[63]   G. Korotcenkov, "Paper-Based Humidity Sensors as Promising Flexible Devices: State
        of the Art: Part 1. General Consideration", *Nanomaterials*, vol. 13, no. 6, 2023, ISSN:
        2079-4991.

[64]   A. G. Foster, "The sorption of condensible vapours by porous solids. Part I. The applica-
        bility of the capillary theory", *Transactions of the Faraday Society*, vol. 28, pp. 645–657,
        1932.

[65]   W. Qu and J.-U. Meyer, "A novel thick-film ceramic humidity sensor", *Sensors and
        Actuators B: Chemical*, vol. 40, no. 2-3, pp. 175–182, 1997.

[66]   W. Qu and W. Wlodarski, "A thin-film sensing element for ozone, humidity and tem-
        perature", *Sensors and Actuators B: Chemical*, vol. 64, no. 1-3, pp. 42–48, 2000.

[67]   A. Tripathy, S. Pramanik, A. Manna, *et al.*, "Design and development for capacitive
        humidity sensor applications of lead-free Ca, Mg, Fe, Ti-oxides-based electro-ceramics
        with improved sensing properties via physisorption", *Sensors*, vol. 16, no. 7, p. 1135,
        2016.

[68]   J. Mareš, J. Krištofik, and E. Hulicius, "Influence of humidity on transport in porous
        silicon", *Thin Solid Films*, vol. 255, no. 1-2, pp. 272–275, 1995.

[69]   A. M. A. Motohashi, M. R. M. Ruike, M. K. M. Kawakami, H. A. H. Aoyagi, A. K. A.
        Kinoshita, and A. S. A. Satou, "Identification of water molecules in low humidity and
        possibility of quantitative gas analysis using porous silicon gas sensor", *Japanese
        journal of applied physics*, vol. 35, no. 8R, p. 4253, 1996.

[70]   Z. Rittersma and W. Benecke, "A humidity sensor featuring a porous silicon capacitor
        with an integrated refresh resistor", *Sens. Mater*, vol. 12, no. 1, pp. 035–055, 2000.

[71]   Z. Rittersma, A Splinter, A Bödecker, and W Benecke, "A novel surface-micromachined
        capacitive porous silicon humidity sensor", *Sensors and Actuators B: Chemical*, vol. 68,
        no. 1-3, pp. 210–217, 2000.

[72]   M.-Q. Liu, C. Wang, and N.-Y. Kim, "High-sensitivity and low-hysteresis porous MIM-
        type capacitive humidity sensor using functional polymer mixed with TiO2 microparti-
        cles", *Sensors*, vol. 17, no. 2, p. 284, 2017.

[73]   H. Lee, S. Lee, S. Jung, and J. Lee, "Nano-grass polyimide-based humidity sensors",
        Sensors and Actuators B: Chemical, vol. 154, no. 1, pp. 2–8, 2011.

[74]   A. Rivadeneyra, J. Fernandez-Salmeron, M. Agudo-Acemel, J. A. Lopez-Villanueva, L. F.
        Capitan-Vallvey, and A. J. Palma, "Printed electrodes structures as capacitive humidity
        sensors: a comparison", *Sensors and Actuators A: Physical*, vol. 244, pp. 56–65, 2016.

[75] K. S. Choi, D. S. Kim, H. J. Yang, M. S. Ryu, and S. P. Chang, "A highly sensitive humidity sensor with a novel hole array structure using a polyimide sensing layer", *RSC Advances*, vol. 4, no. 61, pp. 32 075–32 080, 2014.

[76] J. Boudaden, M. Steinmaßl, H.-E. Endres, *et al.*, "Polyimide-based capacitive humidity sensor", *Sensors*, vol. 18, no. 5, p. 1516, 2018.

[77] H. Lensch, M. Bastuck, T. Baur, A. Schütze, and T. Sauerwald, "Impedance model for a high-temperature ceramic humidity sensor", *Journal of Sensors and Sensor Systems*, vol. 8, no. 1, pp. 161–169, 2019.

[78] J. Fraden, *Handbook of modern sensors: physics, designs, and applications*, 2016.

[79] T. Fei, H. Zhao, K. Jiang, and T. Zhang, "Synthesis and humidity sensitive property of cross-linked water-resistant polymer electrolytes", *Sensors and Actuators B: Chemical*, vol. 208, pp. 277–282, 2015.

[80] Z. Zhuang, Y. Li, D. Qi, C. Zhao, and H. Na, "Novel polymeric humidity sensors based on sulfonated poly (ether ether ketone) s: influence of sulfonation degree on sensing properties", *Sensors and Actuators B: Chemical*, vol. 242, pp. 801–809, 2017.

[81] S. Dey, S. Santra, S. K. Ray, and P. K. Guha, "Coral-like Cu x Ni (1- x) O-based resistive sensor for humidity and VOC detection", *IEEE Sensors Journal*, vol. 18, no. 15, pp. 6078–6084, 2018.

[82] Y. Feng, A. L. Cabezas, Q. Chen, L.-R. Zheng, and Z.-B. Zhang, "Flexible UHF resistive humidity sensors based on carbon nanotubes", *IEEE Sensors Journal*, vol. 12, no. 9, pp. 2844–2850, 2012.

[83] T. Hsueh, Y. Chen, W. Weng, *et al.*, "Nanocrystalline Si-based resistive humidity sensors prepared via HWCVD at various filament temperatures", *IEEE electron device letters*, vol. 33, no. 6, pp. 905–907, 2012.

[84] J. Xu, M. Bertke, H. S. Wasisto, and E. Peiner, "Piezoresistive microcantilevers for humidity sensing", *Journal of Micromechanics and Microengineering*, vol. 29, no. 5, p. 053 003, 2019.

[85] G Gerlach and K Sager, "A piezoresistive humidity sensor", *Sensors and Actuators A: Physical*, vol. 43, no. 1-3, pp. 181–184, 1994.

[86] T Waber, M Sax, W Pahl, *et al.*, "Fabrication and characterization of a piezoresistive humidity sensor with a stress-free package", *Journal of Sensors and Sensor Systems*, vol. 3, no. 2, pp. 167–175, 2014.

[87] J. Yang, J. Xu, W. Wu, M. Bertke, H. S. Wasisto, and E. Peiner, "Piezoresistive silicon cantilever covered by ZnO nanorods for humidity sensing", *Procedia Engineering*, vol. 168, pp. 1114–1117, 2016.

[88] S. Paul, A. Saikia, V. Majhi, and V. K. Pandey, *Introduction to Biomedical Instrumentation and Its Applications*. Academic Press, 2022.

[89] J. Lou, Y. Wang, and L. Tong, "Microfiber optical sensors: a review", *Sensors*, vol. 14, no. 4, pp. 5823–5844, 2014.

[90]   J. Ascorbe, J. M. Corres, F. J. Arregui, and I. R. Matias, "Recent developments in fiber optics humidity sensors", *Sensors*, vol. 17, no. 4, p. 893, 2017.

[91]   K. Peters, "Polymer optical fiber sensors—a review", *Smart materials and structures*, vol. 20, no. 1, p. 013 002, 2010.

[92]   K. O. Hill and G. Meltz, "Fiber bragg grating technology fundamentals and overview", *Journal of lightwave technology*, vol. 15, no. 8, pp. 1263–1276, 1997.

[93]   S. Magne, S. Rougeault, M. Vilela, and P. Ferdinand, "State-of-strain evaluation with fiber bragg grating rosettes: application to discrimination between strain and temperature effects in fiber sensors", *Applied optics*, vol. 36, no. 36, pp. 9437–9447, 1997.

[94]   S. W. James and R. P. Tatam, "Optical fibre long-period grating sensors: characteristics and application", *Measurement science and technology*, vol. 14, no. 5, R49, 2003.

[95]   T Venugopalan, T Sun, and K. Grattan, "Long period grating-based humidity sensor for potential structural health monitoring", *Sensors and Actuators A: Physical*, vol. 148, no. 1, pp. 57–62, 2008.

[96]   Y. Liu, L. Wang, M. Zhang, D. Tu, X. Mao, and Y. Liao, "Long-period grating relative humidity sensor with hydrogel coating", *IEEE Photonics Technology Letters*, vol. 19, no. 12, pp. 880–882, 2007.

[97]   K. M. Tan, C. M. Tay, S. C. Tjin, C. C. Chan, and H. Rahardjo, "High relative humidity measurements using gelatin coated long-period grating sensors", *Sensors and Actuators B: Chemical*, vol. 110, no. 2, pp. 335–341, 2005.

[98]   M. Konstantaki, S. Pissadakis, S. Pispas, N. Madamopoulos, and N. A. Vainos, "Optical fiber long-period grating humidity sensor with poly (ethylene oxide)/cobalt chloride coating", *Applied optics*, vol. 45, no. 19, pp. 4567–4571, 2006.

[99]   D Viegas, J Goicoechea, J. Corres, *et al.*, "A fibre optic humidity sensor based on a long-period fibre grating coated with a thin film of SiO2 nanospheres", *Measurement Science and Technology*, vol. 20, no. 3, p. 034 002, 2009.

[100]   F. J. Arregui, Y. Liu, I. R. Matias, and R. O. Claus, "Optical fiber humidity sensor using a nano Fabry–Perot cavity formed by the ionic self-assembly method", *Sensors and Actuators B: Chemical*, vol. 59, no. 1, pp. 54–59, 1999.

[101]   L. H. Chen, C. C. Chan, T. Li, *et al.*, "Chitosan-coated polarization maintaining fiber-based Sagnac interferometer for relative humidity measurement", *IEEE Journal of selected topics in Quantum electronics*, vol. 18, no. 5, pp. 1597–1604, 2012.

[102]   P. Kronenberg, B. Culshaw, and S. G. Pierce, "Development of a novel fiber optic sensor for humidity monitoring", in *Smart Structures and Materials 1999: Sensory Phenomena and Measurement Instrumentation for Smart Structures and Materials*, SPIE, vol. 3670, 1999, pp. 480–485.

[103]   Y. Wang, C. Shen, W. Lou, and F. Shentu, "Fiber optic humidity sensor based on the graphene oxide/PVA composite film", *Optics Communications*, vol. 372, pp. 229–234, 2016.

[104]   M Consales, A Buosciolo, A Cutolo, *et al.*, "Fiber optic humidity sensors for high-energy physics applications at CERN", *Sensors and Actuators B: Chemical*, vol. 159, no. 1, pp. 66–74, 2011.

[105]   L. Xu, J. C. Fanguy, K. Soni, and S. Tao, "Optical fiber humidity sensor based on evanescent-wave scattering", *Optics letters*, vol. 29, no. 11, pp. 1191–1193, 2004.

[106]   A. Gaston, I. Lozano, F. Perez, F. Auza, and J. Sevilla, "Evanescent wave optical-fiber sensing (temperature, relative humidity, and pH sensors)", *IEEE Sensors Journal*, vol. 3, no. 6, pp. 806–811, 2003.

[107]   S. K. Khijwania, K. L. Srinivasan, and J. P. Singh, "An evanescent-wave optical fiber relative humidity sensor with enhanced sensitivity", *Sensors and actuators B: Chemical*, vol. 104, no. 2, pp. 217–222, 2005.

[108]   K. Iniewski, *Optical Fiber Sensors: Advanced Techniques and Applications.* CRC Press, 2017.

[109]   D. Esperante Pereira and A. Vollhardt, "Design and development of the control board for the LHCb silicon tracker", Jan. 2008.

[110]   G. Korotcenkov, *Handbook of Humidity Measurement, Volume 3: Sensing Materials and Technologies.* CRC Press, 2020.

[111]   *Datasheet: CHS-UPS humidity sensor*, https://product.tdk.com/system/files/dam/doc / product / sensor / sensor / humidity / catalog / sensor _ humidity _ chs _ en . pdf, Accessed: 2023-05-22.

[112]   *Datasheet: SHT85 rh/t module*, https://sensirion.com/media/documents/4B40CEF3/640B2346/Sensirion_Humidity_Sensors_SHT85_Datasheet.pdf, Accessed: 2023-05-22.

[113]   *Datasheet: Humicap 180 humidity sensor*, https://qsgroup.it/wp-content/uploads/2021/03/HMP113-Datasheet-B211251EN.pdf, Accessed: 2023-05-22.

[114]   *The Rotronic Humidity Handbook*, http://www.southeastern-automation.com/PDF/Rotronic/Humidity_Handbook.pdf, Accessed: 2023-06-04.

[115]   A. Lechner, "Particle interactions with matter", *CERN Yellow Rep. School Proc.*, vol. 5, p. 47, 2018. DOI: 10.23730/CYRSP-2018-005.47. [Online]. Available: https://cds.cern.ch/record/2674116.

[116]   J.-L. Basdevant, J. Rich, and M. Spiro, *Fundamentals in nuclear physics: From nuclear structure to cosmology.* Springer Science & Business Media, 2005.

[117]   C. Patrignani, "Review of particle physics", *Chinese Physics C*, vol. 40, no. 10, p. 100 001, 2016. DOI: 10.1088/1674-1137/40/10/100001. [Online]. Available: https://dx.doi.org/10.1088/1674-1137/40/10/100001.

[118]   D. E. Groom and S. Klein, "Passage of particles through matter", *The European Physical Journal C-Particles and Fields*, vol. 15, no. 1-4, pp. 163–173, 2000.

[119]   D. E. GROOM, N. V. MOKHOV, and S. I. STRIGANOV, "Muon stopping power and range tables 10 mev–100 tev", *Atomic Data and Nuclear Data Tables*, vol. 78, no. 2, pp. 183–356, 2001, ISSN: 0092-640X. DOI: https://doi.org/10.1006/adnd.2001.0861. [Online]. Available: https://www.sciencedirect.com/science/article/pii/S0092640X01908617.

[120]   J. S. Bogard, D. J. Downing, R. L. Coleman, K. F. Eckerman, and J. E. Turner, *Atoms, radiation, and radiation protection*. John Wiley & Sons, 2022.

[121]   J. F. Ziegler and J. P. Biersack, "The stopping and range of ions in matter", in *Treatise on Heavy-Ion Science: Volume 6: Astrophysics, Chemistry, and Condensed Matter*, Springer, 1985, pp. 93–129.

[122]   F. Halzen and A. D. Martin, *Quark & Leptons: An introductory course in modern particle physics*. John Wiley & Sons, 2008.

[123]   B. M. Bolotovskii, "Vavilov–Cherenkov radiation: its discovery and application", *Physics-Uspekhi*, vol. 52, no. 11, p. 1099, 2009.

[124]   Y. Hatano, Y. Katsumura, and A Mozumder, "Charged particle and photon interactions with matter: recent advances, applications, and interfaces", 2010.

[125]   A. Holmes-Siedle and L. Adams, "Handbook of radiation effects", 1993.

[126]   C. W. Fabjan and H. Schopper, *Particle Physics Reference Library: Volume 2: Detectors for Particles and Radiation*. Springer Nature, 2020, vol. 2.

[127]   J Knaster, A Moeslang, and T Muroga, "Materials research for fusion", *Nature Physics*, vol. 12, no. 5, pp. 424–434, 2016.

[128]   M. Norgett, M. Robinson, and I. M. Torrens, "A proposed method of calculating displacement dose rates", *Nuclear engineering and design*, vol. 33, no. 1, pp. 50–54, 1975.

[129]   M. T. Robinson and I. M. Torrens, "Computer simulation of atomic-displacement cascades in solids in the binary-collision approximation", *Phys. Rev. B*, vol. 9, pp. 5008–5024, 12 1974. DOI: 10.1103/PhysRevB.9.5008. [Online]. Available: https://link.aps.org/doi/10.1103/PhysRevB.9.5008.

[130]   M. Moll, "Displacement damage in silicon detectors for high energy physics", *IEEE Transactions on Nuclear Science*, vol. 65, no. 8, pp. 1561–1582, 2018.

[131]   M. Huhtinen, "Simulation of non-ionising energy loss and defect formation in silicon", *Nuclear Instruments and Methods in Physics Research Section A: Accelerators, Spectrometers, Detectors and Associated Equipment*, vol. 491, no. 1-2, pp. 194–215, 2002.

[132]   I Dawson, F Faccio, M Moll, and A Weidberg, "Overview of radiation effects on detector systems", *CERN Yellow Reports: Monographs*, vol. 1, pp. 3–3, 2021.

[133]   G. Kramberger, "Solid state detectors for high radiation environments", in *Particle Physics Reference Library: Volume 2: Detectors for Particles and Radiation*, C. W. Fabjan and H. Schopper, Eds. Cham: Springer International Publishing, 2020, pp. 965–1034.

[134] T. Goudon, V. Miljanović, and C. Schmeiser, "On the Shockley–Read–Hall model: generation-recombination in semiconductors", *SIAM Journal on Applied Mathematics*, vol. 67, no. 4, pp. 1183–1201, 2007.

[135] S. M. Sze, *Semiconductor devices: physics and technology*. John wiley & sons, 2008.

[136] "Leakage current of hadron irradiated silicon detectors – material dependence", *Nuclear Instruments and Methods in Physics Research Section A: Accelerators, Spectrometers, Detectors and Associated Equipment*, vol. 426, no. 1, pp. 87–93, 1999, ISSN: 0168-9002. DOI: https://doi.org/10.1016/S0168-9002(98)01475-2.

[137] R Wunstorf, "Radiation hardness of silicon detectors: current status", *IEEE Transactions on Nuclear Science*, vol. 44, no. 3, pp. 806–814, 1997.

[138] Z. Li, B. Dezillie, M. Bruzzi, *et al.*, "HTLT oxygenated silicon detectors: radiation hardness and long-term stability", *Nuclear Instruments and Methods in Physics Research Section A: Accelerators, Spectrometers, Detectors and Associated Equipment*, vol. 461, no. 1, pp. 126–132, 2001, 8th Pisa Meeting on Advanced Detectors, ISSN: 0168-9002. DOI: https://doi.org/10.1016/S0168-9002(00)01187-6.

[139] M. M. Atalla, E. Tannenbaum, and E. Scheibner, "Stabilization of silicon surfaces by thermally grown oxides", *Bell System Technical Journal*, vol. 38, no. 3, pp. 749–783, 1959.

[140] D. L. Griscom, "Hydrogen model for radiation-induced interface states in Sio 2-on-Si Structures: A review of the evidence", *Journal of electronic materials*, vol. 21, pp. 763–767, 1992.

[141] A Goetzberger, V Heine, and E. Nicollian, "Surface states in silicon from charges in the oxide coating", *Applied Physics Letters*, vol. 12, no. 3, pp. 95–97, 1968.

[142] L. W. McKeen, *The Effect of Radiation on Properties of Polymers*. William Andrew, 2020.

[143] F. Guarino, M. Tavlet, and C. Hauviller, *Compilation of radiation damage test data*. CERN, 2001.

[144] J. R. Schwank, M. R. Shaneyfelt, D. M. Fleetwood, *et al.*, "Radiation effects in mos oxides", *IEEE Transactions on Nuclear Science*, vol. 55, no. 4, pp. 1833–1853, 2008. DOI: 10.1109/TNS.2008.2001040.

[145] F Faccio, S Michelis, D Cornale, A. Paccagnella, and S. Gerardin, "Radiation-induced short channel (risce) and narrow channel (rince) effects in 65 and 130 nm mosfets", *IEEE Transactions on Nuclear Science*, vol. 62, no. 6, pp. 2933–2940, 2015.

[146] G. Termo, G. Borghello, F. Faccio, S. Michelis, A. Koukab, and J.-M. Sallese, "Fab-to-fab and run-to-run variability in 130nm and 65nm cmos technologies exposed to ultra-high tid", *JINST*, vol. 18, no. 01, p. C01061, 2023.

[147] E. Petersen, *Single event effects in aerospace*. John Wiley & Sons, 2011.

[148] A. Kapić, A. Tsirou, P. G. Verdini, and S. Carrara, "Radiation Tolerance of Capacitive Humidity Sensor for High-Energy Physics Applications", *IEEE Sensors Letters*, vol. 3, no. 12, pp. 1–9, Dec 2019.

[149]   A. Kapić, A. Tsirou, P. G. Verdini, and S. Carrara, "Uncertainty analysis of polymer-based capacitive relative humidity sensor at negative temperatures and low humidity levels", *Measurement*, vol. 209, p. 112 468, 2023, ISSN: 0263-2241. DOI: https://doi.org/10.1016/j.measurement.2023.112468. [Online]. Available: https://www.sciencedirect.com/science/article/pii/S0263224123000325.

[150]   CMS collaboration, "Precise mapping of the magnetic field in the cms barrel yoke using cosmic rays", *JINST*, vol. 5, no. 03, T03021, 2010.

[151]   B Gkotse, M Glaser, M Moll, and F Ravotti, *IRRAD: The New 24 Gev/c Proton Irradiation Facility at CERN, in proceedings of the 12th international topical meeting on nuclear applications of accelerators (accapp 2015)*, 2015.

[152]   J Mekki, M Brugger, R. G. Alia, A Thornton, N. D. S. Mota, and S Danzeca, "CHARM: a mixed field facility at CERN for radiation tests in ground, atmospheric, space and accelerator representative environments", *IEEE Transactions on Nuclear Science*, vol. 63, no. 4, pp. 2106–2114, 2016.

[153]   D. Pfeiffer, G. Gorine, H. Reithler, *et al.*, "The radiation field in the Gamma Irradiation Facility GIF++ at CERN", *Nuclear Instruments and Methods in Physics Research Section A: Accelerators, Spectrometers, Detectors and Associated Equipment*, vol. 866, pp. 91–103, 2017, ISSN: 0168-9002.

[154]   M. Menouni, M. Barbero, F. Bompard, *et al.*, "1-Grad total dose evaluation of 65 nm CMOS technology for the HL-LHC upgrades", *JINST*, vol. 10, no. 05, p. C05009, 2015.

[155]   M Dosanjh, B Jones, and S Myers, "A possible biomedical facility at the European Organization for Nuclear Research (CERN)", *The British journal of radiology*, vol. 86, no. 1025, p. 20 120 660, 2013.

[156]   B. Gkotse, E. Matli, and F. Ravotti, "System architecture and data processing capabilities of the beam profile monitor for the CERN IRRAD facility", in *2016 IEEE Nuclear Science Symposium, Medical Imaging Conference and Room-Temperature Semiconductor Detector Workshop (NSS/MIC/RTSD)*, 2016, pp. 1–4.

[157]   M. Glaser, F. Ravotti, and M. Moll, "Dosimetry assessments in the irradiation facilities at the CERN-PS accelerator", in *2005 8th European Conference on Radiation and Its Effects on Components and Systems*, 2005, PI5–1.

[158]   P Allport, F Bögelspacher, K Bruce, *et al.*, "Experimental determination of proton hardness factors at several irradiation facilities", *JINST*, vol. 14, no. 12, P12004, 2019.

[159]   *MK33-W mini – datasheet*, https://www.ist-ag.com/en/products/capacitive-humidity-sensor-mk33-w-mini-200pf-40-pf, Accessed: 2023-06-01.

[160]   F. Hartmann, *Evolution of silicon sensor technology in particle physics*. Springer, 2009, vol. 43.

[161]   V. Neverov and Y. L. Revyakin, "Investigation of the integrated effects of irradiating platinum resistance thermometers", *Atomic Energy (New York)*, vol. 74, no. 1, pp. 73–76, 1993.

[162] P. Zajtsev, S. Prijmak, P. Olejnikov, *et al.*, "Models of the drift of the calibration curves of thermocouples and resistance thermometers under reactor conditions", *Atomic Energy*, vol. 113, no. 3, p. 219, 2013.

[163] H. Li, Y. Zhou, Y. Liu, L. Li, Y. Liu, and Q. Wang, "Dielectric polymers for high-temperature capacitive energy storage", *Chem. Soc. Rev.*, vol. 50, pp. 6369–6400, 11 2021.

[164] M.-Q. Liu, C. Wang, and N.-Y. Kim, "High-sensitivity and low-hysteresis porous mim-type capacitive humidity sensor using functional polymer mixed with TiO2 microparticles", *Sensors*, vol. 17, no. 2, 2017, ISSN: 1424-8220.

[165] V. Fernicola, M. Banfo, L. Rosso, and D. Smorgon, "Investigation of capacitive-based relative humidity sensors and their stability at high temperature", *Int J Thermophys*, vol. 29, 1668–1677, 2008.

[166] G. Buonanno, M. Dell'isola, V. Fernicola, and C. Frattolillo, "High temperature humidity sensor calibration", *in Proceedings of 4th International Symposium on Humidity and Moisture*, 2002.

[167] T. Lu and C. Chen, "Uncertainty evaluation of humidity sensors calibrated by saturated salt solutions", *Measurement*, vol. 40, no. 6, pp. 591–599, 2007.

[168] N. Ishiwata, T. Niwa, and H. Abe, "Accurate and precise dew-point control system based on active pressure control in two-pressure humidity generator", *Review of Scientific Instruments*, vol. 90, no. 7, p. 076 104, 2019.

[169] M. G. Ahmed, S. Mazen, D. El-Gelil, and N. I. El Sayed, "Realization of relative humidity scale using nis two-temperature humidity generator", *J. Phys. Sci. Appl*, vol. 4, pp. 484–487, 2014.

[170] P.-G. Su and R.-J. Wu, "Uncertainty of humidity sensors testing by means of divided-flow generator", *Measurement*, vol. 36, no. 1, pp. 21–27, 2004.

[171] L.-H. Chen and C. Chen, "Uncertainly analysis of two types of humidity sensors by a humidity generator with a divided-flow system", *Sensors*, vol. 18, no. 2, 2018.

[172] K. Jardine, W. Henderson, T. Huxman, and L Abrell, "Dynamic solution injection: a new method for preparing pptv–ppbv standard atmospheres of volatile organic compounds", *Atmospheric Measurement Techniques*, vol. 3, no. 6, pp. 1569–1576, 2010.

[173] *ESPEC climatic chamber – datasheet*, https://www.espec.co.jp/english/products/env-test/pj/, Accessed: 2022-04-28.

[174] D Grientschnig, "Relation between prediction errors of inverse and classical calibration", *Fresenius' journal of analytical chemistry*, vol. 367, no. 5, pp. 497–498, 2000.

[175] V. Centner, D. Massart, and S De Jong, "Inverse calibration predicts better than classical calibration", *Fresenius' journal of analytical chemistry*, vol. 361, no. 1, pp. 2–9, 1998.

[176] ISOGUM, "Guide to the expression of uncertainty in measurement", 1995.

[177] M. Heinonen, "Uncertainty in humidity measurements", *EUROMET Workshop*, 2006.

[178]   *SHT30 humidity module – datasheet*, https://sensirion.com/media/documents/
        213E6A3B/63A5A569/Datasheet_SHT3x_DIS.pdf, Accessed: 2023-06-01.

[179]   A. Kapić, A. Tsirou, P. G. Verdini, and S. Carrara, "Robust Analog Multisensory Array
        System for Lossy Capacitive Sensors Over Long Distances", *IEEE Transactions on
        Instrumentation and Measurement*, vol. 72, pp. 1–8, 2023. DOI: 10.1109/TIM.2022.
        3225041.

[180]   A. Kapic, A. Tsirou, P. Verdini, and S. Carrara, "Thermal and humidity monitoring in
        "cold" silicon-based high energy physics detectors", *JINST*, vol. 18, no. 02, p. C02066,
        2023. DOI: 10.1088/1748-0221/18/02/C02066. [Online]. Available: https://dx.doi.org/
        10.1088/1748-0221/18/02/C02066.

[181]   F. Reverter, X. Li, and G. C. Meijer, "Liquid-level measurement system based on a
        remote grounded capacitive sensor", *Sensors and Actuators A: Physical*, vol. 138, no. 1,
        pp. 1–8, 2007, ISSN: 0924-4247.

[182]   P. Mantenuto, A. De Marcellis, and G. Ferri, "Novel Modified De-Sauty Autobalancing
        Bridge-Based Analog Interfaces for Wide-Range Capacitive Sensor Applications", *IEEE
        Sensors Journal*, vol. 14, no. 5, pp. 1664–1672, 2014.

[183]   Z. Ignjatovic and M. Bocko, "An interface circuit for measuring capacitance changes
        based upon capacitance-to-duty cycle (CDC) converter", *IEEE Sensors Journal*, vol. 5,
        no. 3, pp. 403–410, 2005.

[184]   L. Somappa, S. Malik, S. Aeron, S. Sonkusale, and M. S. Baghini, "High resolution
        frequency measurement techniques for relaxation oscillator based capacitive sensors",
        IEEE Sensors Journal, vol. 21, no. 12, pp. 13 394–13 404, 2021.

[185]   S. Malik, L. Somappa, M. Ahmad, T. Islam, and M. S. Baghini, "An accurate digital
        converter for lossy capacitive sensors", *Sensors and Actuators A: Physical*, vol. 331,
        p. 112 958, 2021.

[186]   Z. Czaja, "A measurement method for lossy capacitive relative humidity sensors
        based on a direct sensor-to-microcontroller interface circuit", *Measurement*, vol. 170,
        p. 108 702, 2021, ISSN: 0263-2241.

[187]   G. Meijer, *Smart Sensor Systems*. J. Wiley & Sons, October 2008.

[188]   O. Kanoun, A. Yahia Kallel, and A. Fendri, "Measurement of lossy capacitances in the
        range of 1pf - 1nf: a review", *Measurement*, p. 111 067, 2022.

[189]   S. Malik, K. Kishore, T. Islam, Z. H. Zargar, and S. Akbar, "A time domain bridge-based
        impedance measurement technique for wide-range lossy capacitive sensors", *Sensors
        and Actuators A: Physical*, vol. 234, pp. 248–262, 2015, ISSN: 0924-4247.

[190]   A. Ulla Khan, T. Islam, and J. Akhtar, "An oscillator-based active bridge circuit for
        interfacing capacitive sensors with microcontroller compatibility", *IEEE Transactions
        on Instrumentation and Measurement*, vol. 65, no. 11, pp. 2560–2568, 2016.

[191] S. Malik, M. Ahmad, L. S, T. Islam, and M. S. Baghini, "Impedance-to-time converter circuit for leaky capacitive sensors with small offset capacitance", *IEEE Sensors Letters*, vol. 3, no. 7, pp. 1–4, 2019.

[192] S. Malik, K. Kishore, L. Somappa, *et al.*, "A dual-slope-based capacitance-to-time signal conditioning circuit for leaky capacitive sensors", *IEEE Transactions on Instrumentation and Measurement*, vol. 70, pp. 1–8, 2021.

[193] V. Sreenath and B. George, "A Switched-Capacitor Circuit-Based Digitizer for Efficient Interfacing of Parallel R-C Sensors", *IEEE Sensors Journal*, vol. 17, no. 7, pp. 2109–2119, 2017.

[194] R. Yang, M. A. P. Pertijs, and S. Nihtianov, "A Precision Capacitance-to-Digital Converter With 16.7-bit ENOB and 7.5-ppm/°C Thermal Drift", *IEEE Journal of Solid-State Circuits*, vol. 52, no. 11, pp. 3018–3031, 2017.

[195] S. Malik, L. Somappa, M. Ahmad, and M. S. Baghini, "AN-C2V: An Auto-Nulling Bridge-Based Signal Conditioning Circuit for Leaky Capacitive Sensors", *IEEE Sensors Journal*, vol. 20, no. 12, pp. 1–4, June 2020.

[196] F. Reverter, X. Li, and G. C. M. Meijer, "Stability and accuracy of active shielding for grounded capacitive sensors", *Measurement Science and Technology*, vol. 17, no. 11, p. 2884, 2006.

[197] E. M. Spinelli and F. Reverter, "On the stability of shield-driver circuits", *IEEE Transactions on Instrumentation and Measurement*, vol. 59, no. 2, pp. 458–462, 2010.

[198] T. Roskilly and R. Mikalsen, "Chapter five - closed-loop stability", in *Marine Systems Identification, Modeling and Control*, T. Roskilly and R. Mikalsen, Eds., Oxford: Butterworth-Heinemann, 2015, pp. 97–122, ISBN: 978-0-08-099996-8.

[199] *TLV2474 – datasheet*, https://www.ti.com/lit/ds/symlink/tlv2474.pdf?ts=1685604270054, Accessed: 2023-06-01.

[200] *MCP3428 – datasheet*, https://ww1.microchip.com/downloads/aemDocuments/documents/OTH/ProductDocuments/DataSheets/22226a.pdf, Accessed: 2023-06-01.

[201] *LTC2984 – datasheet*, https://www.analog.com/media/en/technical-documentation/data-sheets/2984fb.pdf, Accessed: 2023-06-01.

[202] *ATmega328P – datasheet*, https://ww1.microchip.com/downloads/en/DeviceDoc/Atmel-7810-Automotive-Microcontrollers-ATmega328P_Datasheet.pdf, Accessed: 2023-06-01.

[203] B. Verlaat, M Ostrega, L Zwalinski, *et al.*, "The ATLAS IBL CO2 cooling system", *JINST*, vol. 12, no. 02, p. C02064, 2017.

[204] P. Tropea, P. Petagna, S. Pavis, *et al.*, "Design, construction and commissioning of a 15 kW CO _2 evaporative cooling system for particle physics detectors: lessons learnt and perspectives for further development", *PoS*, p. 223, 2014.

[205] O. A. de Aguiar Francisco, J. Buytaert, P Collins, *et al.*, "Evaporative CO2 microchannel cooling for the LHCb VELO pixel upgrade", *JINST*, vol. 10, no. 05, p. C05014, 2015.

[206]   P. Barroca, A. Hafner, B. Verlaat, *et al.*, "An Ultra-Low Temperature Transcritical R744 Refrigeration System for Future Detectors at CERN LHC", *Applied Sciences*, vol. 11, no. 16, 2021, ISSN: 2076-3417.

[207]   P. Barroca, A. Hafner, Á. Álvarez Pardiñas, *et al.*, "Evaporative cooling system with natural refrigerant at -50°C and 100 m underground", in *Proceedings of the 14th IIR-Gustav Lorentzen Conference on Natural Refrigerants*, International Institute of Refrigeration, 2020.

[208]   V. Bhanot, P. Petagna, A. Cioncolini, and H. Iacovides, "Development and validation of a simulation tool for next generation detector cooling systems", *Nuclear Instruments and Methods in Physics Research Section A: Accelerators, Spectrometers, Detectors and Associated Equipment*, vol. 955, p. 163 264, 2020, ISSN: 0168-9002.

[209]   P. Petagna, B. Verlaat, and A. Francescon, "Two-phase thermal management of silicon detectors for high energy physics", in *Encyclopedia of Two-Phase Heat Transfer and Flow III: Macro and Micro Flow Boiling and Numerical Modeling Fundamentals Volume 4: Special Boiling Topics*, World Scientific, 2018, pp. 335–412.

[210]   S Chatrchyan, G Hmayakyan, V Khachatryan, *et al.*, "The CMS experiment at the CERN LHC", *JINST*, vol. 3, 2008.

[211]   J. Incandela, S. Ahlen, J. Beatty, *et al.*, "The performance of photomultipliers exposed to helium", *Nuclear Instruments and Methods in Physics Research Section A: Accelerators, Spectrometers, Detectors and Associated Equipment*, vol. 269, no. 1, pp. 237–245, 1988, ISSN: 0168-9002. DOI: https://doi.org/10.1016/0168-9002(88)90885-6.

[212]   *Oil-free screw air compressors ZT (VSD)*, https://www.atlascopco.com/it-ch/compressors/products/air-compressor/oil-free-air-compressors/rotary-screw-air-compressors-zr-zt, Accessed: 2023-06-04.

[213]   E. M. Butz and CMS collaboration, "CMS Strip Detector: Operational Experience and Run1 to Run2 Transition", CERN, Geneva, Tech. Rep., 2014. [Online]. Available: https://cds.cern.ch/record/1971428.

[214]   *Vaisala DMT242 dewpoint transmitter - datasheet*, https://www.vaisala.com/sites/default/files/documents/DMT242-Datasheet-B210765EN-E.pdf, Accessed: 2023-06-04.

[215]   O. Teller, "The design of the cooling system for the CMS barrel electromagnetic calorimeter", in *2006 IEEE Nuclear Science Symposium Conference Record*, IEEE, vol. 1, 2006, pp. 430–434.

[216]   W. Karimeh, M. Chammoun, I. Shvetsov, A. Tsirou, and P. G. Verdini, "Status and Future of the CMS Tracker DCS", in *EPJ Web of Conferences*, EDP Sciences, vol. 245, 2020, p. 01 005.

List of Publications

Journal publications:

- **A. Kapić**, A. Tsirou, P. G. Verdini and S. Carrara, "Multichannel Radiation-Compensated Systems for Temperature and Humidity Monitoring for High Energy Physics Detectors", *under review.*

- **A. Kapić**, A. Tsirou, P. G. Verdini and S. Carrara, "Analysis of Proton Radiation-induced Effects on Polymer-based Relative Humidity Sensor", *under review.*

- **A. Kapić**, A. Tsirou, P. G. Verdini and S. Carrara, "Uncertainty Analysis of Polymer-based Capacitive Relative Humidity Sensor at Negative Temperatures and Low Humidity Levels," *Measurement*, vol. 209, pp. 112468, 2023.

- **A. Kapić**, A. Tsirou, P. G. Verdini and S. Carrara, "Thermal and Humidity Monitoring in "Cold" Silicon-based High Energy Physics Detectors," *Journal of Instrumentation (JINST)*, vol. 18, no. 2, pp. C02066, 2023.

- **A. Kapić**, A. Tsirou, P. G. Verdini and S. Carrara, "Robust Analog Multisensory Array System for Lossy Capacitive Sensors Over Long Distances," *IEEE Transactions on Instrumentation and Measurement*, vol. 72, pp. 1-8, 2023.

- **A. Kapić**, A. Tsirou, P. G. Verdini and S. Carrara, "Humidity Sensors for High Energy Physics Applications: A Review," *IEEE Sensors Journal*, vol. 20, no. 18, pp. 10335-10344, 2020.

- **A. Kapić**, A. Tsirou, P. G. Verdini and S. Carrara, "Radiation Tolerance of Capacitive Humidity Sensor for High-Energy Physics Applications," *IEEE Sensors Letters*, vol. 3, no. 12, pp. 1-4, 2019.

Journal publications not related to the thesis:

- A. A. A. Abbas, J. Qian, G. L. Barbruni, A. Golparvar, **A. Kapić** and S. Carrara, "A Novel Piezoresistive Microcantilever Structure for Free-Valproic Acid Sensing in Personalized Epilepsy Management", *IEEE Sensors Journal*, in press.

Conference publications not related to the thesis:

- C. Delgrange, A. Fulciniti, T. Veske, R. Peseux, **A. Kapić**, A. Golparvar, G. L. Barbruni and S. Carrara, "Amperometric Urine Biosensor for Rapid Point-of-Care Tuberculosis Diagnosis", *IEEE Sensors*, in press.

- A. Chevrot, J. Venckute, S. Cuesta, A. Golparvar, **A. Kapić**, G. L. Barbruni, and S. Carrara, "Portable Breathalyzer for Exhaled Volatile Organic Compounds Monitoring in Lung Diseases," *2022 IEEE International Symposium on Medical Measurements and Applications (MeMeA)*, Messina, Italy, 2022, pp. 1-5.

Conference/Workshop presentations:

- **A. Kapić**, A. Tsirou, P. G. Verdini, and S. Carrara, "Multichannel Radiation-Tolerant Humidity Monitoring System for the CMS Inner Cold Sub-detectors", *Topical Workshop on Electronics for Particle Physics*, Geremeas (Sardinia), Italy, 2023.

- **A. Kapić**, A. Tsirou, P. G. Verdini, and S. Carrara, "Radiation-tolerant humidity monitoring system for the CMS Phase-2 Upgrade", *CMS Upgrade Days*, Geneva, Switzerland, 2023.

- **A. Kapić**, A. Tsirou, P. G. Verdini, and S. Carrara, "Thermal and Humidity Monitoring in "Cold" Silicon-based High Energy Physics Detectors," *Topical Workshop on Electronics for Particle Physics*, Bergen, Norway, 2022.

- **A. Kapić**, A. Tsirou, P. G. Verdini, and S. Carrara, "Cold detectors - Monitoring environmental parameters for operational purposes and integration in the control scheme", *Forum on Tracking Detector Mechanics*, online, 2021.

- **A. Kapić**, A. Tsirou, P. G. Verdini, and S. Carrara, "Radiation Tolerant Humidity Sensor for High Energy Physics Applications", *6th EIROforum School on Instrumentation*, Noordwijk, The Netherlands, 2019.

🎓 EDUCATION

2019-present EPFL	**Doctor of Philosophy (Ph.D.) in Microsystems and Micro-electronics** **École Polytechnique Fédérale de Lausanne (EPFL)** *Institute of Microengineering* 📍 Lausanne, Switzerland PhD thesis: Radiation-tolerant Multichannel Dew Point Temperature Monitoring System for High-Energy Physics Applications
2017-2017	**Master of Science (M.Sc.) in Control Engineering** **University of Sapienza** *Faculty of Electrical Engineering* 📍 Rome, Italy Erasmus+ Exchange Student Programme
2015-2018	**Master of Science (M.Sc.) in Control Engineering** **University of Montenegro** *Faculty of Electrical Engineering* 📍 Podgorica, Montenegro Master thesis: Proposal of Maximum Power Point Tracking Algorithms for Photovoltaic Panels **GPA: 10/10, ECTS: 120**
2012-2015	**Bachelor of Science (B.Sc.) in Power Systems and Control Engineering** **University of Montenegro** *Faculty of Electrical Engineering* 📍 Podgorica, Montenegro **GPA: 9.91/10, ECTS: 180**

💼 WORK EXPERIENCE

2020-present	**Teaching Assistant** **École Polytechnique Fédérale de Lausanne (EPFL)** 📍 Lausanne, Switzerland • EE-517: Bio-nano-chip design (Master-level course) - Assisted in exercise sessions and provided mentorship to students during their semester projects.

2017-present	**Research Assistant**
	
	European Organisation for Nuclear Research (CERN)
	📍 Geneva, Switzerland
	
	• Designed and conducted tests to:
	  (i) Assess radiation tolerance of environmental (humidity and temperature) sensors under controlled environmental conditions, subjecting the sensors to an accumulated fluence of $3 \times 10^{16} \frac{protons}{cm^2}$,
	  (ii) Evaluate sensor sensitivity to a strong magnetic field of $2\ T$,
	  (iii) Evaluate sensor performance at sub-zero temperatures and low relative humidity levels;
	• Critically analyzed data obtained from the conducted tests;
	• Designed, simulated and produced signal conditioning unit for reading lossy capacitive (humidity) and resistive (temperature) sensors over long distances ($100\ m$);
	• Designed, simulated and produced a multi-channel readout system for processing data from hundreds of humidity and temperature sensors;
	• Successfully integrated humidity and temperature monitoring systems into the CMS DCS/DSS environment.

2016-2017	**Electrical Engineer** **Hidroenergija Montenegro** 📍 Podgorica, Montenegro • Lead engineer in maintaining and operating six small hydro-power plants (sHPPs), • Supervised equipment installation in new facilities, • Enrolled in the design and preparation of project documentation for sHPPs and facilitated their connection to the distribution grid, • Improved the functionality of the existing SCADA system.

Amar Kapić

Ph.D. candidate | *EPFL / CERN*

──── **About me** ────

Ph.D. researcher specialized in the design of hardware and software interfaces for sensor characterization. Expert in the design, realization, and characterization of sensor readout front-end circuits and in the development of embedded software. Master's degree in control engineering. Published his research work in top-tier peer-reviewed international journals and conferences. Strong analytical and communication skills, very fast learner, team worker, highly curious, open-minded, and passionate about science and technology. At ease in working in multicultural and multidisciplinary teams.

──── **Contact** ────

🧍 Born on 11/9/1993

✉ amar.kapic@cern.ch

✉ amar.kapic@epfl.ch

📞 +41 75 411 52 06

📍 Rue des Champs Fussy 3
01630 Saint-Genis Pouilly, France

in Amar Kapic

g Amar Kapic

iD ORCID: 0000-0003-3389-1324

Languages

- 🔴 Montenegrin - Native Language
- 🏴 English - Professional Knowledge
- 🟢 Italian - Basic Knowledge
- 🔵 French - Basic Knowledge

Programming Languages

Matlab: *Advanced*	**Python:** *Advanced*
C/C++: *Advanced*	**Java:** *Advanced*

🖥 INFORMATION TECHNOLOGY SKILLS

Data Analysis	**MATLAB**: *Advanced*
	Jupyter Notebook: *Advanced*
	SQL: *Intermediate*
Design, Modeling and Simulation	**Simulink** : *Advanced*
	LTSpice: *Advanced*
	Altium: *Intermediate*
	COMSOL Multiphysics: *Intermediate*
Automation	**SIMATIC Step 7** : *Advanced*
	LabVIEW : *Advanced*
	WinCC OA : *Intermediate*
Object Design	**AutoCAD** : *Intermediate*
Office Automation	**MS Office (Excel, Word, PowerPoint)**: *Advanced*
	LaTeX: *Advanced*

🎖 AWARDS

2017	Scholarship from Engineering Chamber of Montenegro (2016/2017) for the best student of technical faculties in the field of spatial planning, design and construction of facilities
2016	Award for finishing all third year exams with an average mark 10, The Student Awards Committee of Capital City – Podgorica – The Committee of Capital City awards the best student from each faculty
2016	Award for the best student of the study program Power Systems and Control, Faculty of Electrical Engineering – Faculty of Electrical Engineering awards the best student of the generation
2015	Award for the best student of the Faculty of Electrical Engineering, University of Montenegro (2014/2015) – University of Montenegro awards the best student from each faculty

✳ CERTIFICATES AND TRAINING

- OxML 2023: Oxford Machine Learning Summer School (*online, 2023*)
- 5th Barcelona Techno Week: Semiconductor Radiation Detectors (*online, 2021*)
- 6th EIROforum School on Instrumentation (*European Space Research and Technology Centre (ESTEC), Nordwajk, The Netherlands, 2019*)
- Siemens – STEP7 : level 2 (*CERN, Geneva, Switzerland, 2018*)
- Siemens – STEP7 : level 1 (*CERN, Geneva, Switzerland, 2018*)
- Cosylab Summer School (*Cosylab Headquarters, Ljubljana, Slovenia, 2018*)
- CERN Summer School (*CERN, Geneva, Switzerland, 2017*)

⚛ ACTIVITIES

- Member of the organizing committee of the 1st Heavy Ion Therapy School, 2021, online.
- Member of the organizing committee and lecturer at the Particle Therapy MasterClass for high school students, 2020, online.
- Presenter at CERN Open Days 2019, Geneva, Switzerland.
- Member of the organizing committee and lecturer at the IPPCE MasterClass for high school students, 2019, Podgorica, Montenegro.
- SEEIIST presentation at Open Science Days 2019, Podgorica, Montenegro.
- CERN presentation at Open Science Days 2017, Podgorica, Montenegro.